

## ABSTRACT

HAN, SANG-DON. Delving into the Properties and Solution Structure of Solvent-Lithium Salt Electrolytes for Li-ion Batteries. (Under the direction of Dr. Wesley A. Henderson).

In spite of the critical importance of understanding the molecular interactions in solvent-salt electrolyte systems which is essential for the optimization of advanced lithium battery electrolytes, a molecular-level systematic approach to determine such interactions within electrolytes and the link between these interactions and the electrolyte properties does not exist. In addition, widely used polarization parameters (e.g., donor/acceptor numbers, dielectric constant, etc.) are actually ineffective for gauging these molecular interactions and describing the solvate species present within the electrolyte, as shown as part of this work. Here we demonstrate that a combination of methods—i.e., the determination of the electrolyte thermal phase behavior (phase diagram and the corresponding solvate crystal structures), a Raman spectroscopic evaluation of the solvation/ionic association interactions and molecular dynamics (MD) simulations—can provide detailed insight into the coordination interactions of the solvent and anions and thus explanations for the solution behavior and variability in the transport properties (viscosity and ionic conductivity) of concentrated electrolytes.

As a preliminary study, Raman vibrational spectroscopy was used to explore the distribution of anion...Li<sup>+</sup> cation coordination modes and readily discern how solvent structural features govern Li<sup>+</sup> cation solvation. The anion Raman vibrational bands of lithium trifluoromethanesulfonate (LiCF<sub>3</sub>SO<sub>3</sub>), lithium difluoro(oxalato)borate (LiDFOB) and lithium hexafluorophosphate (LiPF<sub>6</sub>) were characterized in detail to evaluate the anion...Li<sup>+</sup>

cation interactions within known and newly reported crystalline  $\text{LiCF}_3\text{SO}_3$ ,  $\text{LiDFOB}$  and  $\text{LiPF}_6$  solvates. The information obtained from these analyses provides key guidance to correctly assign the observed vibrational bands to specific forms of anion coordination in electrolytes containing the  $\text{LiCF}_3\text{SO}_3$ ,  $\text{LiDFOB}$  and  $\text{LiPF}_6$  salts.

Utilizing a combination of methods, the degree of solvation and ionic association have been determined for a wide variety of electrolyte mixtures with acetonitrile (AN, a model solvent) and new and conventional lithium salts ( $\text{LiDFOB}$ ,  $\text{LiFSI}$ ,  $\text{LiPF}_6$ ,  $\text{LiTFSI}$ ,  $\text{LiClO}_4$ ,  $\text{LiBF}_4$ ,  $\text{LiCF}_3\text{SO}_3$  and  $\text{LiCF}_3\text{CO}_2$ ). Once the solution structure was well understood, the transport properties (viscosity and ionic conductivity) of the electrolyte mixtures were correlated with the structural information to obtain insight into the origin of the transport property variations for the different electrolytes. MD simulations for the  $(\text{AN})_n\text{-LiX}$  mixtures have been performed to obtain additional insight into the solution structure and to explore the limitations of the experimental work and simulations for electrolyte characterization. This research provides a detailed understanding of electrolyte mixtures, including how interactions at the molecular-level are affected by factors such as solvent/ion structure, temperature and concentration and how these interactions govern the properties of electrolytes. Furthermore, this study is expected to contribute to a better understanding and control of electrolyte-electrode interfacial interactions, which directly influence battery performance and safety, and to the optimization of multi-solvent electrolytes, thus enabling the rational design of electrolytes for a wide variety of battery chemistries and applications.

© Copyright 2013 by Sang-Don Han

All Rights Reserved

Delving into the Properties and Solution Structure  
of Solvent-Lithium Salt Electrolytes  
for Li-ion Batteries

by  
Sang-Don Han

A dissertation submitted to the Graduate Faculty of  
North Carolina State University  
in partial fulfillment of the  
requirements for the Degree of  
Doctor of Philosophy

Chemical Engineering

Raleigh, North Carolina

2013

APPROVED BY:

---

Dr. Wesley Henderson  
Committee Chair

---

Dr. Saad Khan

---

Dr. Michael Dickey

---

Dr. Edmond Bowden

## **DEDICATION**

*This dissertation is dedicated to my parents,*

*All of my family, advisors, friends and colleagues*

*Without whom none of my success would be possible.*

## **BIOGRAPHY**

Sang-Don Han was born in Seoul, South Korea to parents Jong-Soo Han and Hye-Won Son. At age 1, he moved to Busan, South Korea, where he was raised with his sister, Seo-Kyung Han. After graduating from Busan Jungang High School in 1998, he attended Ajou University in Suwon, South Korea in 1999. In the summer of 2000, he started military service at Osan Air Base and completed in 2002. He came back to university in 2003 and earned Bachelor of Engineering degree in Environmental Engineering in 2006. In the summer of 2006, he attended Gwangju Institute of Science and Technology (GIST) in Gwangju, South Korea and joined the Membrane and Electrochemistry Laboratory (MEL), advised by Dr. Seung-Hyeon Moon. After receiving his Master of Science degree in Environmental Science and Engineering in 2008, Sang-Don attended the Department of Chemical and Biomolecular Engineering at North Carolina State University. In the winter of 2009, he joined the Ionic Liquids and Electrolytes for Energy Technologies (ILEET) research group, advised by Dr. Wesley Henderson.

## ACKNOWLEDGMENTS

I am sincerely grateful to my advisor, Dr. Wesley Henderson, who has provided invaluable guidance. I would like to thank his continuous encouragement, daily involvement in research, assistance with academic writing and my future career mentoring. I greatly look forward to him as a prudent future research collaborator.

I would like to thank my colleagues and friends for their help and time. To Daniel Seo, Dennis McOwen, Eric Fox, Ezinne Achinivu, James Daubert, Josh Allen, Sam Delp, Sung-Hyun Yun and Xinglian Geng, I thank you for your support and assistance with research. The vacation, get-togethers, birthday parties, coffee breaks... with my best friends, Alex, Moataz, Mohammed and Rohan, are something I will never forget. To my love Vin, I truly could not have done this without your constant love and support. Thanks to all of you, I have enjoyed my graduate school experience more than I could have ever expected.

Finally, I would like to thank my family for their continuous support: To my father and mother, always thank you for your support and encouragement; I love you so much. To my sister Seo-Kyung, your advice and comments are really helpful and can be a good stepping stone for my career; Thank you and I love you...

## TABLE OF CONTENTS

LIST OF TABLES.....	ix
LIST OF FIGURES.....	x
CHAPTER 1: Introduction.....	1
1.1. Battery Technologies in Plug-in Hybrid Electric Vehicles (PHEVs).....	1
1.2. Li-ion Batteries.....	2
1.3. Electrolyte in Li-ion Batteries.....	5
1.3.1. A New Approach to Electrolyte Studies.....	7
1.3.2. Electrolyte Properties Characterization.....	9
1.4. Motivation for This Study.....	11
1.5. References.....	15
CHAPTER 2: Experimental Methods.....	21
2.1. Materials.....	21
2.1.1. Lithium Salts.....	21
2.1.2. Solvents.....	23
2.2. Sample Preparation.....	27
2.3. Instruments and Techniques.....	29
2.3.1. Differential Scanning Calorimetry (DSC).....	29
2.3.2. X-Ray Diffraction.....	29
2.3.3. Raman Spectroscopy.....	30
2.3.4. Density/Viscosity Measurements.....	31
2.3.5. Conductivity Measurements.....	32
2.3.6. Molecular Dynamics (MD) Simulations and Quantum Chemistry (QC) Calculations.....	32
2.4. References.....	35

CHAPTER 3: Reassessing Polarization Parameters and Li <sup>+</sup> Cation Solvation.....	37
3.1. Introduction.....	37
3.2. CF <sub>3</sub> SO <sub>3</sub> <sup>-</sup> Anion Raman Vibrational Band Characterization.....	43
3.2.1. Solvate Structures and Li <sup>+</sup> Cation Coordination.....	44
3.2.2. Raman Spectroscopic Analysis of Crystalline Solvates.....	46
3.3. Raman Spectroscopic Analysis of Anion Bands for Lithium Salts.....	49
3.3.1. Ether Solvents.....	49
3.3.2. Cyclic and Acyclic Carbonate/Ester Solvates.....	51
3.4. Conclusions.....	53
3.5. References.....	55
 CHAPTER 4: Crystalline Solvate Structures and Ionic Association Interactions.....	 64
4.1. Introduction.....	64
4.2. DFOB <sup>-</sup> Anion Raman Vibrational Band Characterization.....	68
4.2.1. Solvate Structures and Li <sup>+</sup> Cation Coordination.....	70
4.2.2. Raman Band Assignments.....	73
4.2.3. Raman Spectroscopic Analysis of Crystalline Solvates.....	77
4.3. PF <sub>6</sub> <sup>-</sup> Anion Raman Vibrational Band Characterization.....	83
4.3.1. Solvate Structures and Li <sup>+</sup> Cation Coordination.....	83
4.3.2. Raman Spectroscopic Analysis of Crystalline Solvates.....	86
4.4. Conclusions.....	92
4.5. References.....	93
 CHAPTER 5: Electrolyte Solvation and Ionic Association. I. Acetonitrile-Lithium Salt Mixtures.....	 100
5.1. Introduction.....	101
5.2. Solvent-Lithium Salt Phase Behavior.....	102
5.2.1. Pure Acetonitrile (AN).....	102

5.2.2. (AN) <sub>n</sub> -Lithium Salt Mixtures: Intermediate and Associated Salts.....	104
5.2.3. (AN) <sub>n</sub> -Lithium Salt Mixtures: Dissociated Salts.....	108
5.3. Raman Characterization of AN-Li <sup>+</sup> Cation Solvation.....	112
5.4. Raman Characterization of Ionic Association.....	119
5.4.1. (AN) <sub>n</sub> -Lithium Salt Mixtures: Intermediate and Associated Salts.....	119
5.4.2. (AN) <sub>n</sub> -Lithium Salt Mixtures: Dissociated Salts.....	127
5.5. MD Simulations of (AN) <sub>n</sub> -Lithium Salt Mixtures.....	135
5.5.1. (AN) <sub>n</sub> -Lithium Salt Mixtures: Intermediate and Associated Salts.....	135
5.5.2. (AN) <sub>n</sub> -Lithium Salt Mixtures: Dissociated Salts.....	140
5.6. Transport Properties of (AN) <sub>n</sub> -Lithium Salt Mixtures.....	146
5.6.1. Concentration and Density of (AN) <sub>n</sub> -LiX Mixtures.....	147
5.6.2. Viscosity of (AN) <sub>n</sub> -LiX Mixtures.....	147
5.6.3. Conductivity of (AN) <sub>n</sub> -LiX Mixtures.....	151
5.6.4. Dynamics of Solvate Formation.....	160
5.7. Conclusions.....	164
5.8. References.....	167
CHAPTER 6: Electrolyte Solvation and Ionic Association. II. Acetonitrile-Lithium Difluoro(oxalato)borate (LiDFOB) Mixtures.....	174
6.1. Introduction.....	174
6.2. Solvent-Lithium Salt Phase Behavior of (AN) <sub>n</sub> -LiDFOB Mixtures.....	175
6.3. Raman Characterization of AN-Li <sup>+</sup> Cation Solvation.....	178
6.4. Raman Characterization of Ionic Association.....	181
6.5. Force Field Development and MD Simulations of (AN) <sub>n</sub> -LiDFOB Mixtures.....	185
6.6. Transport Properties of (AN) <sub>n</sub> -LiDFOB Mixtures.....	194
6.7. Conclusions.....	201
6.8. References.....	202

CHAPTER 7: Electrolyte Solvation and Ionic Association. III. Acetonitrile-Lithium Bis(oxalato)borate (LiFSI) Mixtures.....	207
7.1. Introduction.....	207
7.2. Solvent-Lithium Salt Phase Behavior of (AN) <sub>n</sub> -LiFSI Mixtures.....	208
7.3. Raman Characterization of AN-Li <sup>+</sup> Cation Solvation.....	211
7.4. Raman Characterization of Ionic Association.....	213
7.5. MD Simulations of (AN) <sub>n</sub> -LiFSI Mixtures.....	220
7.6. Transport Properties of (AN) <sub>n</sub> -LiFSI Mixtures.....	223
7.7. Conclusions.....	227
7.8. References.....	229
CHAPTER 8: Conclusions.....	235
APPENDICES.....	238
Appendix A.....	239
Appendix B.....	251
Appendix C.....	255

## LIST OF TABLES

### CHAPTER 3

**Table 3.1.** Solvent structures and solvent polarization parameters—relative permittivity (or dielectric constant) ( $\epsilon$ ), donor number (DN), acceptor number (AN) and  $E_T(30)$ .....39

### CHAPTER 4

**Table 4.1.** Calculated (uncoordinated DFOB<sup>-</sup> from M06-2X) vibration mode frequencies ( $\text{cm}^{-1}$ ), Raman ( $\text{\AA}^4 \text{amu}^{-1}$ ) and IR ( $\text{km mol}^{-1}$ ) intensities and tentative assignments (no scaling) ( $\text{freq}_{\text{expt}}$  refers to the LiDFOB salt—Figure 4.6).....76

### CHAPTER 5

**Table 5.1.** Composition of the ion coordination shell from MD simulations of  $(\text{AN})_n\text{-LiClO}_4$  and  $(\text{AN})_n\text{-LiBF}_4$  mixtures at 60 °C (Note: some of the percentages do not sum to 100% due to the rounding off of the values). Experimental density values in parentheses were extrapolated from experimental data.....136

**Table 5.2.** Composition of the ion coordination shell from MD simulations of  $(\text{AN})_n\text{-LiPF}_6$  mixtures at 60 °C (Note: some of the percentages do not sum to 100% due to the rounding off of the values).....141

**Table 5.3.** Composition of the ion coordination shell from MD simulations of  $(\text{AN})_n\text{-LiTFSI}$  mixtures at 60 °C (Note: some of the percentages do not sum to 100% due to the rounding off of the values).....143

### CHAPTER 6

**Table 6.1.** Binding energies of DFOB<sup>-</sup>/Li<sup>+</sup> complexes ( $\text{kcal mol}^{-1}$ ) (see Fig. 6.1).....187

**Table 6.2.** MD simulation data for the  $(\text{AN})_n\text{-LiDFOB}$  mixtures at 60 °C.....188

**Table 6.3.** Probability matrix for DFOB<sup>-</sup> anion coordination to Li<sup>+</sup> cations through the anion carbonyl oxygen and/or fluorine donor atoms.....189

**Table 6.4.** Fraction of uncoordinated AN (i.e.,  $r_{\text{Li-N}} > 2.40 \text{ \AA}$ ) in the MD simulations. Data for other salts shown for comparison.....196

**Table 6.5.** Comparison of experimental (from Raman spectroscopic data) and computational (from MD simulations) solvation numbers for the  $(\text{AN})_n\text{-LiX}$  mixtures at 60 °C.....197

### CHAPTER 7

**Table 7.1.** MD simulations data for the  $(\text{AN})_n\text{-LiFSI}$  mixtures at 60 °C.....221

## LIST OF FIGURES

### CHAPTER 1

- Figure 1.1.** Schematic representation of a typical Li-ion battery.....4
- Figure 1.2.**  $\text{Li}^+$  cation solvates in THF mixtures (X is the anion and Li is the  $\text{Li}^+$  cation) (from known crystal structures).....8
- Figure 1.3.** The ion coordination in the crystal and chemical structures of (a) LiDFOB, (b) LiBOB, (c)  $\text{LiBF}_4$  and (d) LiFSI. The elemental color key is: B (tan), C (grey), F (light green), Li (purple), N (blue), O (red) and S (yellow).....14

### CHAPTER 2

- Figure 2.1.** Ion structures and acronyms of the lithium salts studied.....22
- Figure 2.2.** Synthesis of LiDFOB by direct reaction of  $\text{BF}_3$ -etherate and dilithium oxalic acid.....23
- Figure 2.3.** Structures and acronyms of the solvents studied.....24

### CHAPTER 3

- Figure 3.1.** Examples of  $\text{Li}^+$  cation solvates with THF and  $\text{Et}_2\text{O}$  from crystalline solvate structures (X is the anion).....40
- Figure 3.2.** Fraction of "solvate species" (actually anion coordination modes) in solvent- $\text{LiClO}_4$  mixtures from Raman spectroscopic band analyses: (a)  $932\text{-}934\text{ cm}^{-1}$  (SSIP), (a)  $938\text{-}939\text{ cm}^{-1}$  (CIP), (c)  $944\text{-}948\text{ cm}^{-1}$  (AGG) and (d)  $958\text{-}961\text{ cm}^{-1}$  (more concentrated AGGs).42
- Figure 3.3.** Varying modes of  $\text{CF}_3\text{SO}_3^- \dots \text{Li}^+$  cation coordination: (a) SSIP, (b) CIP-I, (c) AGG-I, (d) AGG-II and (e) AGG-III.....44
- Figure 3.4.**  $\text{CF}_3\text{SO}_3^- \dots \text{Li}^+$  cation coordination in solvates which have previously been reported: (a) SSIP  $(2,9\text{-DMPHEN})_2:\text{LiCF}_3\text{SO}_3$ , (b) CIP-I  $(\text{G3})_1:\text{LiCF}_3\text{SO}_3$ , (c) CIP-I  $(\text{PHEN})_2:\text{LiCF}_3\text{SO}_3$ , (d) AGG-I  $(\text{TMEDA})_1:\text{LiCF}_3\text{SO}_3$  (partial structure), (e) AGG-I  $(\text{G2})_1:\text{LiCF}_3\text{SO}_3$ , (f) AGG-I  $(\text{PMDETA})_1:\text{LiCF}_3\text{SO}_3$ , (g) AGG-II  $(\text{THF})_1:\text{LiCF}_3\text{SO}_3$ , (h) AGG-II  $(\text{G3})_{1/2}:\text{LiCF}_3\text{SO}_3$ , (i) AGG-II  $(\text{AN})_1:\text{LiCF}_3\text{SO}_3$ , (j) AGG-II  $(\text{DMC})_1:\text{LiCF}_3\text{SO}_3$ , (k) AGG-II  $(\text{DEC})_1:\text{LiCF}_3\text{SO}_3$ , (l) AGG-II  $(\text{GBL})_1:\text{LiCF}_3\text{SO}_3$ , (m) AGG-II  $(\text{EC})_1:\text{LiCF}_3\text{SO}_3$  and (n) AGG-III pure  $\text{LiCF}_3\text{SO}_3$ .....45
- Figure 3.5.**  $\text{CF}_3\text{SO}_3^- \dots \text{Li}^+$  cation coordination in the newly reported  $\text{LiCF}_3\text{SO}_3$  solvates: (a) SSIP  $(12\text{C4})_2:\text{LiCF}_3\text{SO}_3$ , (b) AGG-II  $(\text{BN})_1:\text{LiCF}_3\text{SO}_3$  and (c) AGG-II  $(\text{MA})_1:\text{LiCF}_3\text{SO}_3$ ...46
- Figure 3.6.** Raman spectrum of  $\text{LiCF}_3\text{SO}_3$  (at  $20^\circ\text{C}$ ).....47
- Figure 3.7.** Raman band peak positions for the  $\text{CF}_3\text{SO}_3^-$  anion vibrational bands for various crystalline solvates.....48

**Figure 3.8.** Raman spectra of the CF<sub>3</sub> symmetric bending mode ( $\delta_s$ CF<sub>3</sub>) for (solvent)<sub>n</sub>-LiCF<sub>3</sub>SO<sub>3</sub> mixtures with ether solvents. The spectra for the pure salt (black) and pure solvents (dashed) are shown for comparison.....50

**Figure 3.9.** Raman spectra (at 20 °C) of the CF<sub>3</sub> symmetric bending mode ( $\delta_s$ CF<sub>3</sub>) for (solvent)<sub>n</sub>-LiCF<sub>3</sub>SO<sub>3</sub> mixtures with cyclic and acyclic carbonate/ester solvents. The spectra for the pure salt (black) and pure solvents (dashed) are shown for comparison.....52

## CHAPTER 4

**Figure 4.1.** PF<sub>6</sub><sup>-</sup>...Li<sup>+</sup> cation coordination: (a) SSIP, (b) CIP-I, (c) CIP-II, (d) AGG-Ia, (e) AGG-Ib, (f) AGG-II and (g) AGG-III (other forms of coordination may also occur) (Li<sup>+</sup> cations are colored black).....65

**Figure 4.2.** DFOB<sup>-</sup>...Li<sup>+</sup> cation coordination: (a) SSIP, (b) CIP-I, (c) CIP-II, (d) AGG-Ia, (e) AGG-Ib, (f) AGG-Ic, (g) AGG-Id, (h) AGG-IIa, (i) AGG-IIb, (j) AGG-IIIa and (k) AGG-IIIb (other forms of coordination may also occur) (Li<sup>+</sup> cations are colored black).....66

**Figure 4.3.** DFOB<sup>-</sup>...Li<sup>+</sup> cation coordination in the crystalline solvates: (a) (G1)<sub>2</sub>:LiDFOB and (b) (Et-G1)<sub>3/2</sub>:LiDFOB (Li-purple, O-red, B-tan, F-light green).....69

**Figure 4.4.** DFOB<sup>-</sup>...Li<sup>+</sup> cation coordination in crystalline LiDFOB and the crystalline solvates studied: (a) AGG-IIIb LiDFOB, (b) AGG-Ic (H<sub>2</sub>O)<sub>1</sub>:LiDFOB, (c) CIP-I (TMS)<sub>2</sub>:LiDFOB, (d) CIP-II (G1)<sub>2</sub>:LiDFOB, (e) CIP-I/CIP-II (Et-G1)<sub>3/2</sub>:LiDFOB, (f) AGG-Ia (DMC)<sub>3/2</sub>:LiDFOB, (g) AGG-Ib (SN)<sub>1</sub>:LiDFOB, (h) AGG-Ia (AN)<sub>3</sub>:LiDFOB and (i) AGG-IIa (AN)<sub>1</sub>:LiDFOB.....71

**Figure 4.5.** DFOB<sup>-</sup>...Li<sup>+</sup> cation coordination in the crystalline solvates studied: (a) AGG-IIb (ADN)<sub>1</sub>:LiDFOB, (b) AGG-Ia (PMDETA)<sub>1</sub>:LiDFOB, (c) CIP-I/CIP-II/AGG-Id (CRYPT-222)<sub>2/3</sub>:LiDFOB and (d) AGG-IIIa (PC)<sub>1</sub>:LiDFOB.....72

**Figure 4.6.** Raman spectrum of LiDFOB (at 20 °C).....74

**Figure 4.7.** Principal bonds/angles contributing to the DFOB<sup>-</sup> anion vibrational modes as determined from the DFT calculations.....75

**Figure 4.8.** Raman spectra of the DFOB<sup>-</sup> anion vibrational band variation for the (speculative) SSIP crystalline solvates: (12C4)<sub>2</sub>:LiDFOB, (G2)<sub>2</sub>:LiDFOB and (HMTETA)<sub>1</sub>:LiDFOB (bold spectra indicate that the solvate has melted at this temperature).....78

**Figure 4.9.** Raman spectra of the DFOB<sup>-</sup> anion vibrational band variation for the CIP crystalline solvates: (TMS)<sub>2</sub>:LiDFOB, (G1)<sub>2</sub>:LiDFOB and (Et-G1)<sub>3/2</sub>:LiDFOB (bold spectra indicate that the solvate has melted at this temperature).....79

**Figure 4.10.** Summary of the Raman band peak position for the DFOB<sup>-</sup> anion ring breathing vibrational band for various crystalline solvates (see Appendix B for the assignments of the data to specific solvates).....81

<b>Figure 4.11.</b> Stable ion pairs obtained for LiDFOB from the DFT calculations (while C and E look the same superficially, C has the Li <sup>+</sup> cation in the FBO plane, while E has the cation in the oxalate plane).....	82
<b>Figure 4.12.</b> PF <sub>6</sub> <sup>-</sup> ...Li <sup>+</sup> cation coordination in the solvates which have been previously reported: (a) SSIP (AN) <sub>5</sub> :LiPF <sub>6</sub> , (b) SSIP (EC) <sub>4</sub> :LiPF <sub>6</sub> , (c) AGG-Ia (DMC) <sub>2</sub> :LiPF <sub>6</sub> , and (d) AGG-Ia (PMDETA) <sub>1</sub> :LiPF <sub>6</sub> .....	84
<b>Figure 4.13.</b> PF <sub>6</sub> <sup>-</sup> ...Li <sup>+</sup> cation coordination in the newly reported LiPF <sub>6</sub> solvates: (a) CIP-I (G3) <sub>1</sub> :LiPF <sub>6</sub> and (b) AGG-Ib (DEC) <sub>2</sub> :LiPF <sub>6</sub> .....	85
<b>Figure 4.14.</b> Raman spectrum of LiPF <sub>6</sub> (at 20 °C).....	86
<b>Figure 4.15.</b> Raman spectra vs. temperature (°C - shown on the left) of the PF <sub>6</sub> <sup>-</sup> anion vibrational bands for the crystalline solvates: (a) SSIP (AN) <sub>5</sub> :LiPF <sub>6</sub> , (b) SSIP (EC) <sub>4</sub> :LiPF <sub>6</sub> , (c) (speculative SSIP) (G2) <sub>2</sub> :LiPF <sub>6</sub> , (d) (speculative SSIP) (G1) <sub>3</sub> :LiPF <sub>6</sub> , (e) (speculative SSIP) (PN) <sub>4</sub> :LiPF <sub>6</sub> , (f) CIP-I (G3) <sub>1</sub> :LiPF <sub>6</sub> , (g) (speculative CIP-I) (DMC) <sub>3</sub> :LiPF <sub>6</sub> , (h) AGG-Ia (DMC) <sub>2</sub> :LiPF <sub>6</sub> , (i) AGG-Ia (PMDETA) <sub>1</sub> :LiPF <sub>6</sub> , (j) AGG-Ib (DEC) <sub>2</sub> :LiPF <sub>6</sub> and (k) AGG-III LiPF <sub>6</sub> (the dark lines indicate that a phase transition has occurred—e.g., melting).....	88
<b>Figure 4.16.</b> Summary of the PF <sub>6</sub> <sup>-</sup> anion Raman band peak positions for the different crystalline solvates (each line is for a separate solvate).....	91

## CHAPTER 5

<b>Figure 5.1.</b> DSC heating traces (5 °C min <sup>-1</sup> ) and the corresponding phase diagrams for (a) (1-x) AN-(x) LiClO <sub>4</sub> and (b) (1-x) AN-(x) LiBF <sub>4</sub> mixtures.....	103
<b>Figure 5.2.</b> DSC heating trace (5 °C min <sup>-1</sup> ) of the (AN) <sub>1</sub> :LiCF <sub>3</sub> SO <sub>3</sub> crystalline solvate... 107	107
<b>Figure 5.3.</b> DSC heating traces (5 °C min <sup>-1</sup> ) of (1-x) AN-(x) LiCF <sub>3</sub> CO <sub>2</sub> mixtures..... 107	107
<b>Figure 5.4.</b> DSC heating traces (5 °C min <sup>-1</sup> ) and the corresponding phase diagrams of (a) (1-x) AN-(x) LiTFSI and (b) (1-x) AN-(x) LiPF <sub>6</sub> mixtures..... 111	111
<b>Figure 5.5.</b> Raman spectra at 60°C of the AN C–C stretching mode (918 cm <sup>-1</sup> ) and C≡N stretching mode (2254 cm <sup>-1</sup> ) bands for (a) (AN) <sub>n</sub> -LiBF <sub>4</sub> and (b) (AN) <sub>n</sub> -LiCF <sub>3</sub> CO <sub>2</sub> mixtures (AN/LiX ratio indicated)..... 113	113
<b>Figure 5.6.</b> Raman spectra at 60°C of AN C–C stretching mode (920 cm <sup>-1</sup> ) and C≡N stretching mode (2250 cm <sup>-1</sup> ) bands for (a) (AN) <sub>n</sub> -LiTFSI and (b) (AN) <sub>n</sub> -LiPF <sub>6</sub> mixtures (AN/LiX ratio indicated)..... 114	114
<b>Figure 5.7.</b> Raman spectroscopic analysis at 60 °C of solvent bands for uncoordinated AN and Li <sup>+</sup> cation coordinated AN in (a) (AN) <sub>n</sub> -LiPF <sub>6</sub> , (b) (AN) <sub>n</sub> -LiTFSI, (c) (AN) <sub>n</sub> -LiClO <sub>4</sub> , (d) (AN) <sub>n</sub> -LiBF <sub>4</sub> and (e) (AN) <sub>n</sub> -LiCF <sub>3</sub> CO <sub>2</sub> mixtures. The calculated Li <sup>+</sup> cation average solvation number ( <i>N</i> ) is shown at the top. The dark solid line corresponds to the average of the two sets of data from Figs. 5.5 and 5.6 (no scaling factor was applied) ..... 116	116

<b>Figure 5.8.</b> ClO <sub>4</sub> <sup>-</sup> anion band variation with concentration in the (AN) <sub>n</sub> -LiClO <sub>4</sub> mixtures at -80 °C.....	120
<b>Figure 5.9.</b> BF <sub>4</sub> <sup>-</sup> anion band variation with concentration in the (AN) <sub>n</sub> -LiBF <sub>4</sub> mixtures at (a) -80 °C and (b) 60 °C.....	121
<b>Figure 5.10.</b> Solvate species distribution in the (AN) <sub>n</sub> -LiBF <sub>4</sub> mixtures at 60 °C.....	123
<b>Figure 5.11.</b> Temperature dependence of the BF <sub>4</sub> <sup>-</sup> anion bands in the (AN) <sub>n</sub> -LiBF <sub>4</sub> mixtures for (a) n = 8 and (b) n = 4.....	124
<b>Figure 5.12.</b> TFSI <sup>-</sup> anion band variation with concentration in (AN) <sub>n</sub> -LiTFSI mixtures at (a) -80 °C and (b) 60 °C. The mixtures with n = 3.0, 2.5, 2.0 and 1.55 are in the crystallinity gap and remain either fully amorphous liquids or glassy solids at -80 °C.....	127
<b>Figure 5.13.</b> TFSI <sup>-</sup> anion band variation with temperature in (AN) <sub>n</sub> -LiTFSI mixtures with (a) n = 6.0 (crystalline in the -80 to -45 °C range) and (b) n = 4.0 (crystalline in the -100 to -35 °C range).....	128
<b>Figure 5.14.</b> Solvate species distribution in (AN) <sub>n</sub> -LiTFSI mixtures at 60 °C.....	130
<b>Figure 5.15.</b> Variable-temperature TFSI <sup>-</sup> anion band variation with concentration in (AN) <sub>n</sub> -LiTFSI mixtures with (a) n = 4.0, (b) n = 3.0, (c) n = 2.0 and (d) n = 1.0.....	132
<b>Figure 5.16.</b> PF <sub>6</sub> <sup>-</sup> anion band variation with concentration in (AN) <sub>n</sub> -LiPF <sub>6</sub> mixtures at (a) -80 °C and (b) 60 °C.....	134
<b>Figure 5.17.</b> Representative Li <sup>+</sup> cation solvate species (i.e., coordination shells) extracted from the MD simulations for the (AN) <sub>n</sub> -LiBF <sub>4</sub> mixtures (n = 30, 20 and 10) at 60 °C: (a) SSIP, (b) CIP-I, CIP-II, (c) CIP-I, (d) CIP-II, (e) CIP-I, AGG-I, (f) AGG-I, (g) CIP-I, AGG-I (×3), (h) CIP-I, AGG-I (×3), AGG-III, (i) CIP-I, AGG-I (×2), (j) CIP-I (×2), AGG-I and (k) AGG-I (×3). Solvent and BF <sub>4</sub> <sup>-</sup> anions within 3.33 Å of a Li <sup>+</sup> cation are shown (Li-purple, N-blue, B-tan, F-light green).....	139
<b>Figure 5.18.</b> Representative Li <sup>+</sup> cation solvate species (i.e., coordination shells) extracted from the MD simulations for the (AN) <sub>n</sub> -LiPF <sub>6</sub> mixtures (n = 30, 20 and 10) at 60 °C: (a) SSIP, (b) CIP-I, (c) AGG-I, (d) CIP-I (×2), (e) CIP-I, AGG-I and (f) CIP-I, CIP-II (Li-purple, N-blue, P-orange, F-light green).....	142
<b>Figure 5.19.</b> Representative Li <sup>+</sup> cation solvate species (i.e., coordination shells) extracted from the MD simulations for the (AN) <sub>n</sub> -LiTFSI mixtures (n = 30, 20 and 10) at 60 °C: (a) C <sub>1</sub> -SSIP, (b) C <sub>1</sub> -CIP-I, (c) C <sub>2</sub> -AGG-I, (d) C <sub>2</sub> -CIP-I, C <sub>1</sub> -CIP-II (e) C <sub>2</sub> -CIP-I (×2), C <sub>1</sub> -AGG-I, (f) C <sub>2</sub> -CIP-II (×2), (g) C <sub>1</sub> -CIP-II, (h) C <sub>1</sub> -AGG-I (×2), (i) C <sub>1</sub> -AGG-I, C <sub>2</sub> -AGG-I and (j) C <sub>1</sub> -CIP-I (×2), C <sub>1</sub> -AGG-I, C <sub>2</sub> -AGG-I, C <sub>2</sub> -AGG-II (Li-purple, N-blue, O, red, S-yellow, F-light green).....	145
<b>Figure 5.20.</b> (a) Density of (AN) <sub>n</sub> -LiX mixtures at 60 °C (AN/LiX (n) noted in plots) and (b) relationship between molarity vs. AN/LiX (n) for (AN) <sub>n</sub> -LiX mixtures.....	148

<b>Figure 5.21.</b> (a) Viscosity of (AN) <sub>n</sub> -LiX mixtures at 60 °C (AN/LiX (n) noted in plots) and (b) the same data for the dilute mixtures alone. Data for concentrated mixtures with LiPF <sub>6</sub> and LiClO <sub>4</sub> was not gathered as these samples crystallize during the measurements.....	149
<b>Figure 5.22.</b> Ionic conductivity of (AN) <sub>n</sub> -LiX mixtures: (a) LiPF <sub>6</sub> , (b) LiTFSI, (c) LiClO <sub>4</sub> , (d) LiBF <sub>4</sub> and (e) LiCF <sub>3</sub> CO <sub>2</sub> (AN/LiX (n) noted in plot).....	152
<b>Figure 5.23.</b> Ionic conductivity of (AN) <sub>n</sub> -LiX mixtures at 60 °C (AN/LiX (n) noted at the top of the plot).....	153
<b>Figure 5.24.</b> Molecular simulation snapshots of (AN) <sub>n</sub> -LiBF <sub>4</sub> mixtures with (a) n = 30, (b) n = 20 and (c) n = 10 (Li-purple, N-blue, B-tan, F-light green). Uncoordinated AN has been removed to aid in discerning the solvates present.....	155
<b>Figure 5.25.</b> Molar conductivity of (a) (AN) <sub>n</sub> -LiX mixtures (60 °C) for varying AN/LiX (n) and (b) (AN) <sub>n</sub> -LiX mixtures (n = 20 - filled circles are average values, individual measurements shown as small open circles and n = 4 - larger open circles) with varying temperature.....	159
<b>Figure 5.26.</b> Dynamics of solvate formation for a Li <sup>+</sup> cation (No. 2973) in the MD simulation of the (AN) <sub>n</sub> -LiBF <sub>4</sub> (n = 30) mixture at 60 °C. Full coordination for the "other Li <sup>+</sup> " cations not shown (i.e., full solvate structure).....	161
<b>Figure 5.27.</b> Anion...Li <sup>+</sup> and AN...Li <sup>+</sup> cation residence times in the (AN) <sub>n</sub> -LiX mixtures from the MD simulations: (a) filled symbols are anions, open symbols are AN and (b) filled symbols are anions.....	164
<b>CHAPTER 6</b>	
<b>Figure 6.1.</b> (a) DSC heating traces (5 °C min <sup>-1</sup> ) and the corresponding phase diagram for (1-x) AN-(x) LiDFOB mixtures and DFOB <sup>-</sup> ...Li <sup>+</sup> cation coordination in the crystalline solvates: (b) AGG-Ia (AN) <sub>3</sub> :LiDFOB <sup>6</sup> and (c) AGG-IIa (AN) <sub>1</sub> :LiDFOB.....	176
<b>Figure 6.2.</b> Raman spectra at 60°C of the AN C–C stretching mode (918 cm <sup>-1</sup> ) and C≡N stretching mode (2254 cm <sup>-1</sup> ) bands for (AN) <sub>n</sub> -LiDFOB mixture (AN/LiX ratio indicated) and Raman spectroscopic analysis at 60 °C of the solvent bands for uncoordinated AN and Li <sup>+</sup> cation coordinated AN in the (AN) <sub>n</sub> -LiDFOB mixtures. The calculated Li <sup>+</sup> cation average solvation number ( <i>N</i> ) is shown at the top.....	179
<b>Figure 6.3.</b> DFOB <sup>-</sup> anion band variation with concentration for the (AN) <sub>n</sub> -LiDFOB mixtures at (a) -80 °C and (b) 60 °C.....	181
<b>Figure 6.4.</b> Temperature dependence of the DFOB <sup>-</sup> anion bands for the (AN) <sub>n</sub> -LiDFOB mixtures for (a) n = 7 and (b) n = 4 (the measurements were obtained while cooling the samples, thus the n = 4 mixture at -20 °C is a supercooled liquid).....	184
<b>Figure 6.5.</b> Optimized geometries from G4MP2 calculations (bold) and the force field for the (a), (b) and (c) coordination noted in Table 6.1.....	187

<b>Figure 6.6.</b> Representative $\text{Li}^+$ cation solvate species extracted from the MD simulations for the $(\text{AN})_n\text{-LiDFOB}$ mixtures ( $n = 30, 20$ and $10$ ) at $60\text{ }^\circ\text{C}$ (Li-purple, N-blue, O-red, B-tan, F-light green).....	191
<b>Figure 6.7.</b> Relationship between molarity and AN/LiX (i.e., $n$ ) for $(\text{AN})_n\text{-LiX}$ mixtures. Data for salts other than LiDFOB reported for comparison.....	194
<b>Figure 6.8.</b> Viscosity of the $(\text{AN})_n\text{-LiX}$ mixtures at $60\text{ }^\circ\text{C}$ (AN/LiX ratio noted in plots). Data for salts other than LiDFOB reported for comparison.....	195
<b>Figure 6.9.</b> Ionic conductivity of the (a) $(\text{AN})_n\text{-LiDFOB}$ mixtures (AN/LiX ratio ( $n$ ) noted in plot) and the (b) $(\text{AN})_n\text{-LiX}$ mixtures at $60\text{ }^\circ\text{C}$ . Data for salts other than LiDFOB reported for comparison.....	198
<b>Figure 6.10.</b> Molar conductivity of the (a) $(\text{AN})_n\text{-LiX}$ mixtures ( $60\text{ }^\circ\text{C}$ ) for varying AN/LiX ( $n$ ) concentrations and (b) $(\text{AN})_n\text{-LiX}$ mixtures with varying temperature. Data for salts other than LiDFOB reported for comparison.....	199

## CHAPTER 7

<b>Figure 7.1.</b> DSC heating traces ( $5\text{ }^\circ\text{C min}^{-1}$ ) and the corresponding phase diagrams for $(1-x)\text{AN-(}x\text{) LiFSI}$ mixtures.....	209
<b>Figure 7.2.</b> Raman spectra at $60\text{ }^\circ\text{C}$ of the AN C–C ( $920\text{ cm}^{-1}$ ) and $\text{C}\equiv\text{N}$ ( $2250\text{ cm}^{-1}$ ) stretching mode bands for the $(\text{AN})_n\text{-LiFSI}$ mixtures (AN/LiX ratio indicated) and Raman spectroscopic analysis at $60\text{ }^\circ\text{C}$ of the solvent bands for the uncoordinated and coordinated (to $\text{Li}^+$ cations) AN in the $(\text{AN})_n\text{-LiFSI}$ mixtures. The calculated $\text{Li}^+$ cation average solvation number ( $N$ ) is shown at the top.....	212
<b>Figure 7.3.</b> FSI $^-$ anion band variation with concentration in the $(\text{AN})_n\text{-LiFSI}$ mixtures at (a) $-80\text{ }^\circ\text{C}$ and (b) $60\text{ }^\circ\text{C}$ (The mixtures with $n = 2.8, 2.5, 1.50$ and $1.00$ are in the crystallinity gap and remain either fully amorphous liquids or glassy solids at $-80\text{ }^\circ\text{C}$ ).....	214
<b>Figure 7.4.</b> Variable-temperature FSI $^-$ anion band variation with concentration in the $(\text{AN})_n\text{-LiFSI}$ mixtures with (a) $n = 3.5$ , (b) $n = 3.0$ , (c) $n = 2.8$ , (d) $n = 2.5$ , (e) $n = 2.4$ and (f) $n = 2.3$ .....	216
<b>Figure 7.5.</b> Temperature dependence of the FSI $^-$ anion bands in the $(\text{AN})_n\text{-LiFSI}$ mixtures for (a) $n = 8$ and (b) $n = 4$ .....	219
<b>Figure 7.6.</b> Representative $\text{Li}^+$ cation solvate species extracted from the MD simulations for the $(\text{AN})_n\text{-LiFSI}$ mixtures ( $n = 30, 20$ and $10$ ) at $60\text{ }^\circ\text{C}$ (Li-purple, N-blue, O-red, S-yellow, F-light green).....	223
<b>Figure 7.7.</b> Relationship between molarity and AN/LiX (i.e., $n$ ) for the $(\text{AN})\text{-LiX}$ mixtures. Data for salts other than LiFSI are reported for comparison.....	224

**Figure 7.8.** Ionic conductivity of the (a)  $(AN)_n$ -LiFSI mixtures with varying temperature (AN/LiX ratio (n) noted in plot) and (b)  $(AN)_n$ -LiX mixtures with varying concentration at 60C. Data for salts other than LiFSI are reported for comparison.....225

**Figure 7.9.** Molar conductivity of the (a)  $(AN)_n$ -LiX mixtures (60 °C) for varying AN/LiX (n) concentrations and (b)  $(AN)_n$ -LiX mixtures with varying temperature. Data for salts other than LiFSI reported for comparison.....226

*The objectives of this research were to (1) demonstrate new or improved methods/approaches to electrolyte characterization and (2) discover how ion and solvent structure influence the physicochemical/transport/electrochemical properties and solution behavior in nitrile-LiDFOB/LiFSI electrolyte mixtures.*

### **1.1. Battery Technologies in Plug-in Hybrid Electric Vehicles (PHEVs)**

Recent increasing concerns about energy security, oil dependence, and climate change have led to tremendous changes in energy production and use. In response to these issues, the electrification of transportation with electrical energy storage (i.e., batteries) has received considerable attention because this will reduce fuel consumption, lower the dependence on imported oil, decrease greenhouse gas emissions, and provide fuel flexibility.<sup>1</sup> The examples of electrified transportation are hybrid electric vehicles (HEVs—combination of a regular internal combustion engine with a complementary electric energy source), plug-in hybrid electric vehicles (PHEVs—combination of a primary electric energy source with a back-up

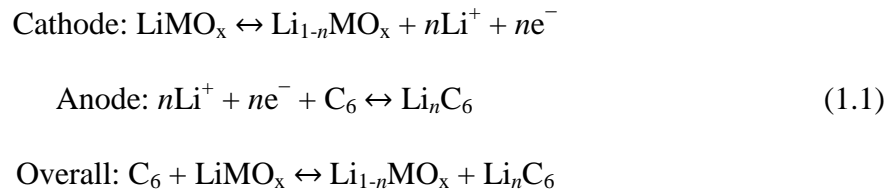
combustion engine) and electric vehicles (EVs—all electric energy source). Initially, HEVs were not able to be commercialized due to the limitations of available battery technologies. Advances in batteries in recent decades, however, resulted in the commercialization of HEVs (e.g., Toyota Prius in 1997), whereas PHEVs (e.g., Chevy Volt in 2007) and EVs (e.g., Nissan Leaf in 2010) are still in the early stages of full-scale commercialization. Significant battery improvements, therefore, are required to realize the wide-spread commercialization and utilization of PHEVs (and then EVs) including a/an: (1) much lower cost, (2) longer cycle/calendar life, (3) higher safety/abuse tolerance, and (4) improved operation over a wider temperature range.<sup>2-4</sup> Different types of batteries have been adopted for vehicle applications, but Li-ion batteries have drawn the greatest attention for most commercial vehicles due to their high energy density attributed to the large potential difference between the electrodes and use of high capacity electrode materials with nonaqueous electrolytes. Significant further advances in the development of Li-ion battery technologies, however, are required for this application, in particular with regard to safety and cost.

## **1.2. Li-ion Batteries**

The Li-ion battery is one of the most promising energy storage technologies currently available. Such batteries are widely used in portable electronics due to their high energy density and long-term cycling performance which other energy storage technologies cannot match.<sup>5</sup> Recently, great interest has been shown for the energy and environmental sustainability of larger scale Li-ion battery systems for (hybrid) electric vehicles and

complimentary (grid-level or stationary) energy storage linked with renewable energy resources.<sup>5</sup>

Li-ion batteries are typically composed of three main components—an anode, a cathode and an electrolyte (which is dispersed within a separator) as shown in Fig. 1.1. Eqn. 1.1 below shows the reactions for a Li-ion battery (with  $\text{MO}_x$  being a metal oxide and  $\text{C}_6$  being graphite). As the battery is charged, electrons are extracted from the cathode active material (oxidizing the cathode) and transferred to the anode active material (reducing the anode). This results in the deintercalation of  $\text{Li}^+$  cations from the cathode and intercalation of  $\text{Li}^+$  cations into the anode ( $\text{Li}^+$  cations are transferred from the cathode through the electrolyte to the anode):



Once the Li-ion battery has been charged, the electrode materials are maintained in a thermodynamically unstable state. During the discharge process, the electrodes are driven to return to their thermodynamically favorable state resulting in the reverse reactions (deintercalation of  $\text{Li}^+$  cations from the anode and the intercalation of  $\text{Li}^+$  cations into the cathode) and the generation of a current through the external circuit (allowing useful work to be done). These multi-step reactions occur simultaneously within the Li-ion battery and are limited primarily by the  $\text{Li}^+$  cation delivery rate of the electrolyte between the electrodes.

Commercially available cathode materials are lithiated layered transition metal oxides—

$\text{Li}_x\text{MO}_2$  ( $M = \text{Co}, \text{Ni}, \text{Mn}$ , or their mixtures), transition metal spinel oxides— $\text{LiM}_2\text{O}_4$  ( $M = \text{Mn}$  or mixtures of  $\text{Mn}, \text{Co}$ , and  $\text{Ni}$ ) and transition metal phosphates— $\text{LiMPO}_4$  ( $M = \text{Fe}$ ),<sup>6</sup> which can be oxidized/reduced and retain a structure which permits the deintercalation /intercalation of the  $\text{Li}^+$  cations (for charge balance). New cathode active materials with a significantly higher specific energy have been developed which can result in a total cost reduction of a vehicle's battery pack by reducing the number of batteries needed.<sup>7,8</sup> The

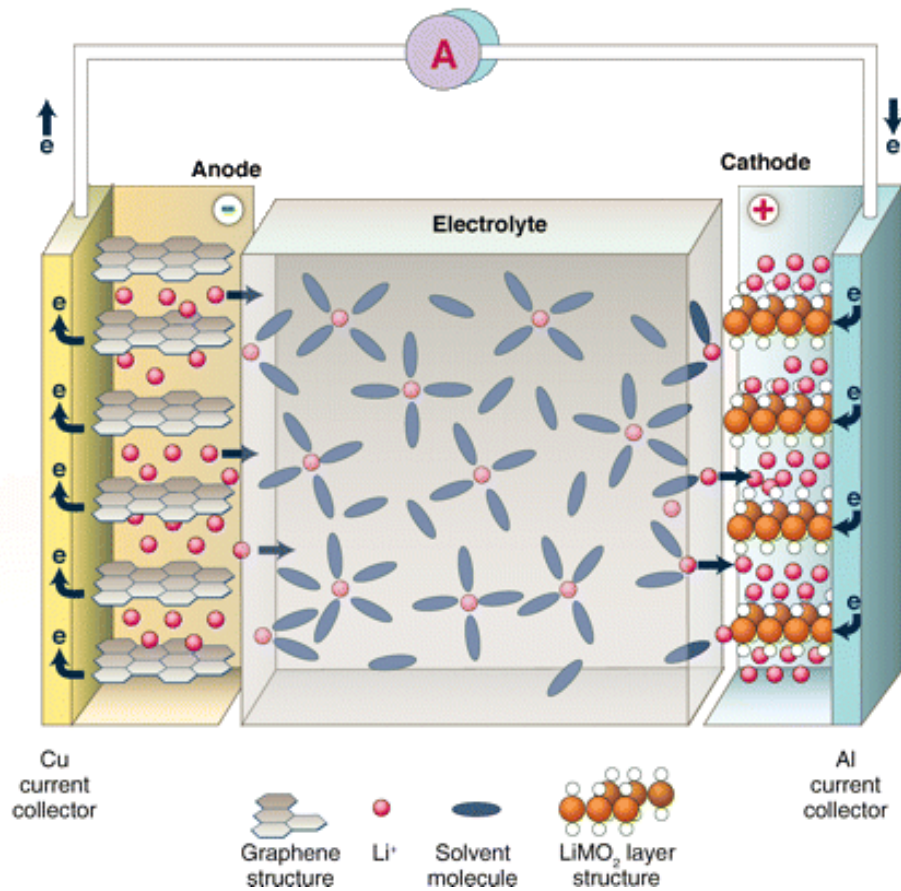


**Figure 1.1.** Schematic representation of a typical Li-ion battery.<sup>15</sup>

anode material in all commercial Li-ion batteries is graphite due to its low cost, high availability and the possibility of ready modifications.<sup>5</sup> Alternative anode material (e.g., silicon, germanium and other metal alloys of lithium) are also being developed for higher-capacity anodes.<sup>5,6,9,10</sup> The rational design of new electrolytes, therefore, for a wide variety of battery chemistries and applications is required to enable stable cycling of such high capacity alternative cathode and anode materials. In addition, the electrolyte itself is a critical component in Li-ion batteries, and thus PHEVs, due to its crucial role in device power, low/high temperature performance, lifetime, safety and cost, which are significant challenging factors for the development of PHEVs. As higher voltage electrode technologies emerge, stagnant battery electrolyte formulations, which prevent the use of such electrodes, become the limiting factor for the utilization of next generation Li-ion batteries.

### **1.3. Electrolyte in Li-ion Batteries**

An electrolyte in a Li-ion battery serves not only as an ionic conductor to transfer  $\text{Li}^+$  cations between the electrodes, but also as an electronic insulator to prevent internal self-discharge and/or short-circuit (the direct reaction between the electrodes). Aqueous electrolytes, which are often used in electrochemistry, are not suitable for Li-ion battery applications because of the reactivity of water with the electrodes and the resulting water electrolysis,<sup>11</sup> whereas nonaqueous electrolytes, which are usually organic solvents with a lithium salt, have been utilized in Li-ion batteries due to the high ionic conductivity and stability of such electrolytes.<sup>5</sup>

Current state-of-the-art liquid electrolytes in Li-ion batteries consist of mixtures of ethylene carbonate (EC) and a non-cyclic carbonate such as diethylcarbonate (DEC), dimethyl carbonate (DMC) or ethylmethyl carbonate (EMC) with a lithium salt.<sup>12,13</sup> Lithium hexafluorophosphate ( $\text{LiPF}_6$ ) is almost exclusively used due to its favorable battery electrolyte properties including high solubility in aprotic solvents, high conductivity, excellent electrochemical stability and formation of a stable solid electrolyte interface (SEI).<sup>12,14,15</sup> However, this salt also has several disadvantages such as voltage limitations ( $\sim 4.3 \text{ V vs. Li/Li}^+$ ), temperature limitations ( $-10 \text{ }^\circ\text{C} - 60 \text{ }^\circ\text{C}$ ), high cost, storage difficulty (due to hydrolysis), and formation of toxic byproducts upon decomposition in the presence of positive-electrode materials ( $\text{Li}_x\text{MO}_2$ , where M is Co, Ni or Mn).<sup>12,15,16</sup> Therefore, the preparation and characterization of new electrolyte formulations are required for advanced rechargeable Li-ion batteries targeted for PHEVs. Such electrolytes are expected to be composed of less expensive materials, be stable to  $> 4.5 \text{ V vs. Li/Li}^+$  for high energy density Li-ion batteries, have exceptional inherent thermal and electrochemical stability, continuously self-heal the SEI layers on the electrodes for longer cycle life and improved safety, retain significant fluidity and conductivity at  $< -10 \text{ }^\circ\text{C}$  and be stable in contact with active electrode materials for both low and high temperature operations.<sup>3,12</sup>

Despite these needs, Li-ion battery electrolytes remain a poorly understood topic relative to the research devoted to battery electrodes. For example, electrode materials have made great improvements in capacity, stability, and cost since the introduction of the Li-ion battery 25 years ago, but the electrolyte has undergone only minor changes since then, holding back

the progression of these batteries. Abraham *et al.* noted that “recent advances in cathode and anode materials have refocused attention on electrolytes as the technological bottleneck limiting the operation and performance of lithium-battery systems”.<sup>17</sup> The development of a comprehensive understanding of electrolyte interactions (something which at present is largely nonexistent) and the exploration of new electrolyte solvents/salts are therefore urgently required to advance new Li-ion battery technologies.

### **1.3.1. A New Approach to Electrolyte Studies**

Instead of the ‘empirical’ Edisonian approach extensively used by battery researchers, a ‘molecular-level systematic’ approach is required to provide a comprehensive understanding of Li-ion battery electrolytes: how solvent and anion structure determine the solvation state of  $\text{Li}^+$  cations in solvent-lithium salt ( $\text{LiX}$ ) mixtures and how this, in turn, dictates the electrolyte properties which govern, in part, battery performance. Ultimately, the fundamental information on molecular-level interactions will provide strong guidance for selecting next-generation electrolytes for future advanced Li-ion batteries.

In solvent-salt electrolyte systems, ionic association is a key feature.<sup>12,18-20</sup> It is widely cited that there are three different general forms of ionic species: solvent-separated ion pairs (SSIPs), in which the anions remain uncoordinated to a  $\text{Li}^+$  cation; contact ion pairs (CIPs), in which the anions are coordinated to a single cation; and aggregates (AGGs), in which the anions are coordinated to two or more cations (Fig. 1.2). This will be demonstrated in the following chapters to be an overly simplistic categorization of solvate species. The solvate

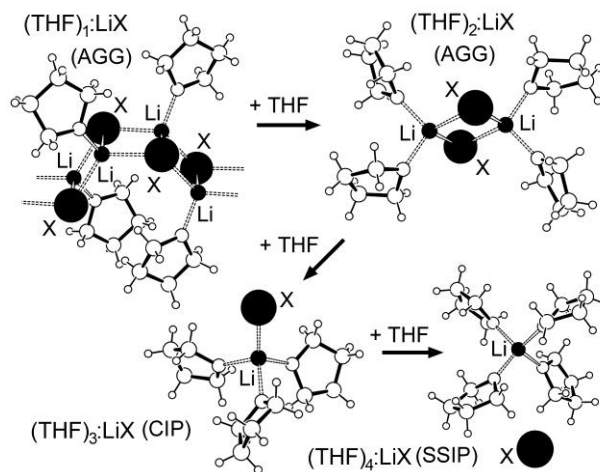


**Figure 1.2.**  $\text{Li}^+$  cation solvates in THF mixtures (X is the anion and Li is the  $\text{Li}^+$  cation) (from known crystal structures).<sup>12</sup>

species, nonsolvated anions and strongly solvated/coordinated cations, in an electrolyte depend on the structure of the solvents and anions, temperature and salt concentration. The ionic solvation is determined by the properties of both the solvent and the anion. Influencing properties of the solvent include (1) the type of solvent donor atom(s) (e.g., N, O or S), which influences the strength of the  $\text{D}\cdots\text{Li}^+$  (D: donor atom) coordination bond, (2) steric effects, which may limit the ability of the solvent donor atom (or neighboring solvent molecules) to approach a  $\text{Li}^+$  cation to form a coordination bond, (3) temperature, which influences thermal motion thus affecting steric hindrance and the efficiency of molecule packing, and (4) multidentate ligands, which have the ability for a single solvent molecule to coordinate to a  $\text{Li}^+$  cation with more than one donor atom.<sup>12,21</sup> Influencing properties of the anion are (1) the coordinating ability, which is determined by the anion donor atoms (e.g., O, N or F), steric

effects and flexibility, (2) negative charge delocalization (resonance), which spreads the negative charge across several atoms and reduces the interaction between any one atom of the anion and a single  $\text{Li}^+$  cation, (3) size, which may become a factor when it is significant enough to prevent solvent molecules or other anions from approaching a  $\text{Li}^+$  cation, and (4) proximity to other ions.<sup>12</sup>

In spite of the significant importance of understanding solvation/ionic association in solvent-salt electrolyte system to aid in optimizing advanced lithium battery electrolytes, a molecular-level systematic approach to determining such interactions within the electrolyte and the link between these interactions and the electrolyte properties does not exist. Thus, it is necessary to study the molecular-level ion/solvent structure, macro-level physicochemical, transport and electrochemical properties, and solution behavior of electrolytes to understand the relationship between them.

### **1.3.2. Electrolyte Properties Characterization**

To examine the link between molecular-level ion/solvent structure and the macro-level physicochemical/transport/electrochemical properties and solution behavior that determine, in part, the performance of Li-ion batteries, a synergistic experimental approach was employed with the following 3 research thrusts.

*Thrust 1. Thermal Phase Behavior and Crystalline Solvate Structure Analysis.*—An in-depth analysis of the thermal phase behavior<sup>22-25</sup> and solvate crystal structures<sup>26-34</sup> of nitrile solvent-lithium salt (LiX) mixtures can give important insight into the molecular-level

interactions that exist within an electrolyte system. Based upon differential scanning calorimetry (DSC) data, phase diagrams with various solvents can be prepared to determine whether crystalline solvates form and the operational liquid range for nitrile solvent-lithium salt mixtures with varying lithium salt concentrations. Moreover, the crystalline solvates obtained from nitrile solvent-lithium salt mixtures may be structurally characterized to explore how the solvent molecules and anions interact with the  $\text{Li}^+$  cations. Crystal structures not only provide the type of solvate (i.e., SSIP, CIP and AGG) formed in dilute electrolytes, thus aiding in the Raman characterization of Thrust 2, but also suggest a link between the anion association tendency and the melting point of the crystalline solvates. In addition, complementary variable-temperature powder XRD analysis can be conducted to aid in phase diagram preparation, although this has not been done in the present study.

*Thrust 2. Ion Solvation and Ionic Association Analysis.*—The ion solvation (solvent... $\text{Li}^+$  cation) and ionic association (anion... $\text{Li}^+$  cation) behavior of lithium salts with various nitrile solvents and anions was explored utilizing Raman spectroscopic analysis. By examining the solvent vibrational bands, it is possible to determine the fraction of coordinated solvent molecules (i.e., solvation number).<sup>23-25</sup> The analysis of anion vibrational bands can provide the explanation for how the anions influence the ionic association and fraction of coordinated solvent molecules.<sup>23-25,29-32</sup> These Raman spectroscopic analyses therefore provide indirect, but detailed information regarding the solvate species present in the solid-state and liquid phases.

*Thrust 3. Transport Properties Analysis.*—Electrolyte transport properties were determined

for comparison with the phase behavior, solvate structures and ion solvation/ionic association behavior. These electrolyte properties are crucial because they govern, in part, the performance of Li-ion batteries. Ionic conductivity, viscosity and density were measured at various temperatures and compositions of nitrile solvent-LiX mixtures. The ionic conductivity<sup>4,25,35-37</sup> and viscosity/density<sup>25,35,36</sup> can be determined by using a potentiostat/galvanostat (potentiostatic electrochemical impedance spectroscopy) and Stabinger viscometer, respectively.

The present work focuses on the link between molecular-level ion/solvent structure and the macro-level physicochemical/transport/electrochemical properties and solution behavior that govern, in part, the performance of Li-ion batteries. Once this was done, the obtained properties data were utilized to optimize/validate detailed computational simulations by collaborators to have additional knowledge/insight unavailable through experimental techniques alone, such as the structural interactions for individual solvates and their influence on the electrolyte properties and kinetics of Li<sup>+</sup> cation transport at electrolyte-electrode interfaces.<sup>23-25,29-33,35</sup> Ultimately, the fundamental information on molecular-level interactions from the present work will provide strong guidance for ‘directed’ electrolyte composition optimization instead of the previous ‘empirical’ approach. This, in turn, will suggest criteria for alternative electrolytes for future advanced Li-ion batteries.

## **1.4. Motivation for This Study**

In the development of next-generation Li-ion batteries, electrolyte development is not just

an option but a necessity with higher-voltage, higher-capacity cathode and anode materials critically needed for new batteries. The previous ‘trial-and-error’ Edisonian method widely utilized by battery researchers limits the ability to identify new promising electrolyte formulations. Within electrolyte mixtures, there is a competition between the solvent molecules (solvation) and anions (ionic association) for the coordination of the  $\text{Li}^+$  cations, which crucially influences the electrolyte properties. These molecular interactions in a battery electrolyte, however, remain a poorly understood and hardly studied topic due to the strong limitations currently available for characterizing solution structure. Most of the previous studies for electrolyte interactions have provided inaccurate information due to the poor assumptions made or lack of rigorous characterization methods.

The present study, therefore, has focused on utilizing a combination of methods including thermal phase behavior characterization (phase diagram from DSC data), XRD solvate crystal structure determination (working with several crystallographers) and Raman vibrational spectroscopic analyses. These combined experimental methods have been applied to determine the degree of solvation and ionic association for the mixtures including model or newly used solvents (i.e., nitriles or dinitriles) and new or conventional lithium salts (i.e., LiDFOB, LiFSI or  $\text{LiPF}_6$ , LiTFSI,  $\text{LiBF}_4$ ,  $\text{LiClO}_4$ ,  $\text{LiCF}_3\text{SO}_3$ ). The resulting knowledge of the electrolyte solution structure obtained then provides mechanistic explanations for the link between the molecular-level interactions and electrolyte properties such as ionic conductivity and viscosity. This research provides a detailed understanding of electrolyte mixtures including how interactions at the molecular-level are affected by factors such as solvent/ion

structure, temperature and concentration and how the interactions govern the properties of electrolytes. Furthermore, this study is expected to provide, in future studies, the foundations for a comprehensive understanding and control of electrode-electrolyte interfaces and the optimization of electrolyte formulations for greatly improved battery performance and safety.

Among a number of potential replacements for the state-of-the-art lithium salt (i.e.,  $\text{LiPF}_6$ ), lithium difluoro(oxalato)borate ( $\text{LiDFOB}$ , Fig. 3a) is of principal interest in the present body of research because  $\text{LiDFOB}$ —a hybrid salt of lithium bis(oxalato)borate ( $\text{LiBOB}$ , Fig. 3b)<sup>38-41</sup> and lithium tetrafluoroborate<sup>42-45</sup> ( $\text{LiBF}_4$ , Fig. 3c)—possesses beneficial properties of both parent anions. These properties include (1) a relatively high ionic conductivity over a wide temperature range, (2) the ability to not only support metallic lithium cycling reversibly on the surface of a copper anode current collector, but to also passivate the aluminum cathode current collector at high voltage, (3) the active formation of a SEI layer, and (4) the possibility to increase battery safety protection and overcharge tolerance.<sup>46-52</sup> In addition, lithium bis(fluorosulfonyl)imide ( $\text{LiFSI}$ , Fig. 3d) is another strong potential candidate for the replacement of  $\text{LiPF}_6$  due to its various advantages: (1) superior thermal and chemical stability, (2) a relatively high ionic conductivity over a wide temperature range, (3) high  $\text{Li}^+$  cation transference number, and (4) high solubility in most polar solvents.<sup>53-64</sup> In the work presented in subsequent chapters, the experimental methodology noted above (complemented by computational work) was employed to fully characterize the  $\text{LiDFOB}$  and  $\text{LiFSI}$  salts to aid in determining their potential as either primary salts or salt additives for newly formulated Li-ion battery electrolytes.

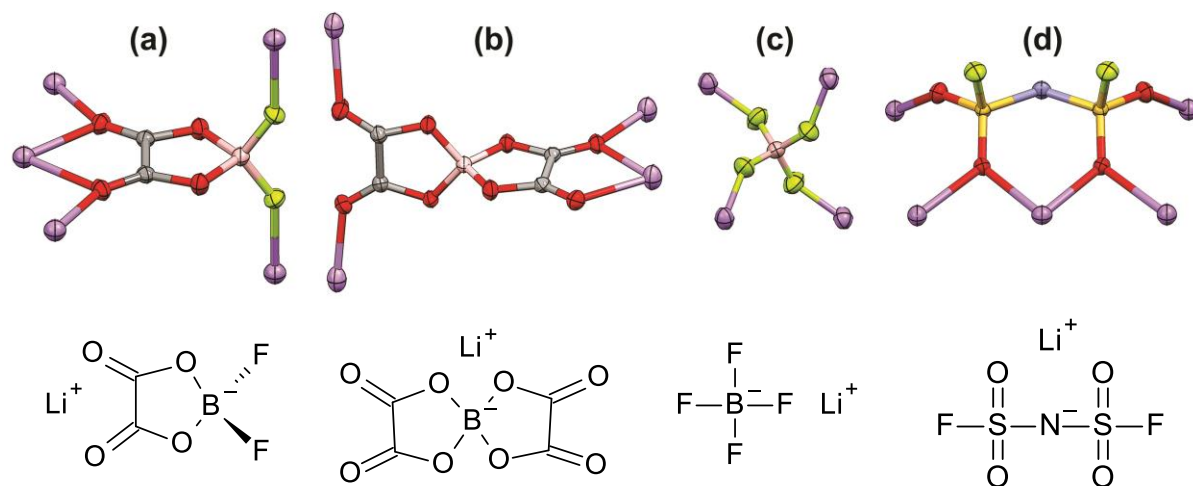


**Figure 1.3.** The ion coordination in the crystal and chemical structures of (a) LiDFOB,<sup>4,28,29</sup> (b) LiBOB,<sup>4</sup> (c) LiBF<sub>4</sub><sup>44</sup> and (d) LiFSI.<sup>65</sup> The elemental color key is: B (tan), C (grey), F (light green), Li (purple), N (blue), O (red) and S (yellow).

## 1.5. References

1. A. Pesaran and T. Markel, *Battery Requirements and Cost-Benefit Analysis for Plug-In Hybrid Vehicles* presented at The 24th International Battery Seminar & Exhibit, National Renewable Energy Laboratory, Fort Lauderdale, FL (2007).
2. FreedomCAR and Vehicle Technologies Program: *Plug-In Hybrid Electric Vehicle R&D Plan*, Working Draft, The Office of Energy Efficiency & Renewable Energy (EERE), Washington, DC (2007).
3. T. Markel, A. Brooker, J. Gonder, M. O’Keefe, A. Simpson, and M. Thornton, *Plug-In Hybrid Vehicle Analysis*, Milestone Report, NREL/MP-540-40609, National Renewable Energy Laboratory, Golden, CO (2006).
4. S. S. Zhang, *Electrochem. Commun.*, **8**, 1423 (2006).
5. X. Yuan, H. Liu, and J. Zhang, eds., *Lithium-Ion Batteries: Advanced Materials and Technologies*, CRC Press, Boca Raton, FL (2012).
6. B. Scrosati, K. M. Abraham, W. A. van Schalkwijk, and J. Hassoun, eds., *Lithium Batteries: Advanced Technologies and Applications*, John Wiley & Sons, Inc., Hoboken, NJ (2013).
7. J. W. Fergus, *J. Power Sources*, **195**, 939 (2010).
8. A. Patil, V. Patil, D. W. Shin, J.-W. Choi, D.-S. Paik, and S.-J. Yoon, *Materials Research Bulletin*, **43**, 1913 (2008).
9. M. Yoshio, R. J. Brodd, and A. Kozawa, eds., *Lithium-Ion Batteries: Science and Technologies*, Springer, New York, NY (2009).

10. C.-M. Park, J.-H. Kim, H. Kim, and H.-J. Sohn, *Chem. Soc. Rev.*, **39**, 3115 (2010).
11. D. Linden and T. B. Reddy, eds., *Handbook of Batteries*, 3rd ed., McGraw-Hill, New York, NY (2002).
12. W. A. Henderson, *Linking Ion Solvation and Lithium Battery Electrolyte Properties*, Proposal awarded by DOE, RFP#: DE-PS02-09ER09-01 (2009).
13. S. S. Zhang, T. R. Jow, K. Amine, and G. L. Henriksen, *J. Power Sources*, **107**, 18 (2002).
14. S. S. Zhang, K. Xu, and T. R. Jow, *J. Electrochem. Soc.*, **149**, A586 (2002).
15. K. Xu, *Chem. Rev.*, **104**, 4303 (2004).
16. S. S. Zhang, K. Xu, and T. R. Jow, *J. Power Sources*, **154**, 276 (2006).
17. D. P. Abraham, M. M. Furczon, S.-H. Kang, D. W. Dees, and A. N. Jansen, *J. Power Sources*, **180**, 612 (2008).
18. M. Ue and S. Mori, *J. Electrochem. Soc.*, **142**, 2577 (1995).
19. A. Webber, *J. Electrochem. Soc.*, **138**, 2586 (1991).
20. P. K. Muhuri, B. Das, and D. K. Hazra, *J. Phys. Chem. B*, **101**, 3329 (1997).
21. L. M. Jackman and L. M. Scarmoutzos, *J. Am. Chem. Soc.*, **109**, 5348 (1987).
22. W. A. Henderson, *J. Phys. Chem. B*, **110**, 13177 (2006).
23. D. M. Seo, O. Borodin, S.-D. Han, Q. Ly, P. D. Boyle, and W. A. Henderson. *J. Electrochem. Soc.*, **159**, A553 (2012).
24. D. M. Seo, O. Borodin, S.-D. Han, P. D. Boyle, and W. A. Henderson. *J. Electrochem. Soc.*, **159**, A1489 (2012).

25. S.-D. Han, O. Borodin, J. L. Allen, D. M. Seo, D. W. McOwen, and W. A. Henderson, *J. Electrochem. Soc.*, in-press (2013).
26. W. A. Henderson, N. R. Brooks, W. W. Brennessel, and V. G. Young Jr., *Chem. Mater.*, **15**, 4679 (2003).
27. W. A. Henderson, N. R. Brooks, W. W. Brennessel, and V. G. Young Jr., *J. Phys. Chem. A*, **108**, 225 (2004).
28. J. L. Allen, S.-D. Han, P. D. Boyle, and W. A. Henderson, *J. Power Sources*, **196**, 9737 (2011).
29. S.-D. Han, J. L. Allen, E. Jónsson, P. Johansson, D. W. McOwen, P. D. Boyle, and W. A. Henderson, *J. Phys. Chem. C*, **117**, 5521 (2013).
30. D. M. Seo, P. D. Boyle, J. L. Allen, S.-D. Han, E. Jónsson, P. Johansson, and W. A. Henderson, *J. Phys. Chem. C.*, in-press (2013).
31. D. M. Seo, P. D. Boyle, R. D. Sommer, J. S. Daubert, O. Borodin, and W. A. Henderson, submitted (2013).
32. S.-D. Han, S.-H. Yun, D. M. Seo, O. Borodin, R. D. Sommer, V. G. Young Jr., and W. A. Henderson, in-preparation (2013).
33. D. M. Seo, P. D. Boyle, O. Borodin, and W. A. Henderson, *RSC Adv.*, **2**, 8014 (2012).
34. D. M. Seo, P. D. Boyle, and W. A. Henderson, *Acta Crystallogr.*, **E67**, m1148 (2011).
35. D. M. Seo, O. Borodin, D. Balogh, M. O'Connell, Q. Ly, S.-D. Han, S. Passerini, and W. A. Henderson. *J. Electrochem. Soc.*, **160**, A1061 (2013).
36. Y. Abu-Lebdeh and I. Davidson, *J. Electrochem. Soc.*, **156**, A60 (2009).

37. S. Zugmann, D. Moosbauer, M. Amereller, C. Schreiner, F. Wudy, R. Schmitz, R. Schmitz, P. Isken, C. Dippel, R. Müller, M. Kunze, A. Lex-Balducci, M. Winter, and H. Gores, *J. Power Sources*, **196**, 1417 (2011).
38. K. Xu, S. S. Zhang, U. Lee, J. L. Allen, and T. R. Jow, *J. Power Sources*, **146**, 79 (2005).
39. S. S. Zhang, K. Xu, and T. R. Jow, *J. Power Sources*, **154**, 276 (2006).
40. S. S. Zhang, K. Xu, and T. R. Jow, *J. Power Sources*, **156**, 629 (2006).
41. S. Dalavi, M. Xu, B. Knight, and B. L. Lucht, *Electrochem. Solid-State Lett.*, **15**, A28 (2011).
42. S. S. Zhang, K. Xu, and T. R. Jow, *Electrochem. Commun.*, **4**, 928 (2002).
43. S. S. Zhang, K. Xu, and T. R. Jow, *J. Electrochem. Soc.*, **149**, A586 (2002).
44. Y. G. Andreev, V. Seneviratne, M. Khan, W. A. Henderson, R. E. Frech, and P. G. Bruce, *Chem. Mater.*, **17**, 767 (2005).
45. R. Jow, S.S. Zhang, K. Xu, and J. Allen, *ECS Trans.*, **3**, 51 (2007).
46. J. Liu, Z. Chen, S. Busking, and K. Amine, *Electrochem. Commun.*, **9**, 475 (2007).
47. Z. Chen, J. Liu, and K. Amine, *Electrochem. Solid-State Lett.*, **10**, A45 (2007).
48. M. H. Fu, K. L. Huang, S. Q. Liu, J. S. Liu, and Y. K. Li, *J. Power Sources*, **195**, 862 (2010).
49. J. Li, K. Xie, Y. Lai, Z. Zhang, F. Li, X. Hao, X. Chen, and Y. Liu, *J. Power Sources*, **195**, 5344 (2010).

50. A. Lex-Balducci, R. Schmitz, R.W. Schmitz, R.A. Müller, M. Amereller, D. Moosbauer, H. J. Gores, and M. Winter, *ECS Trans.*, **25**, 13 (2010).
51. S. Zugmann, D. Moosbauer, M. Amereller, C. Schreiner, F. Wudy, R. Schmitz, R. Schmitz, P. Isken, C. Dippel, R. Müller, M. Kunze, A. Lex-Balducci, M. Winter, and H.J. Gores, *J. Power Sources*, **196**, 1417 (2011).
52. M. Hu, J. Wei, L. Xing, and Z. Zhou, *J. Appl. Electrochem.*, **42**, 291 (2012).
53. J. L. Allen, D. W. McOwen, S. A. Delp, E. T. Fox, J. S. Dickmann, S.-D. Han, Z.-B. Zhou, T. R. Jow, and W. A. Henderson, *J. Power Sources*, **237**, 104 (2013).
54. Y. Liu, S. Zhou, H. Han, H. Li, J. Nie, Z. Zhou, L. Chen, and X. Huang, *Electrochim. Acta*, **105**, 524 (2013).
55. G. G. Eshetu, S. Grugeon, G. Gachot, D. Mathiron, M. Armand, and S. Laruelle, *Electrochim. Acta*, **102**, 133 (2013).
56. K. Zaghib, M. Dontigny, A. Guerfi, J. Trottier, J. Hamel-Paquet, V. Gariépy, K. Galoutov, P. Hovington, A. Mauger, H. Groult, and C. M. Julien, *J. Power. Sources*, **216**, 192 (2012).
57. J. Reiter, M. Nádhern á and R. Dominko, *J. Power. Sources*, **205**, 402 (2012).
58. H.-B. Han, S.-S. Zhou, D.-J. Zhang, S.-W. Feng, L.-F. Li, K. Liu, W.-F. Feng, J. Nie, H. Li, X.-J. Huang, M. Armand, and Z.-B. Zhou, *J. Power. Sources*, **196**, 3623 (2011).
59. L. Li, S. Zhou, H. Han, H. Li, J. Nie, M. Armand, Z. Zhou, and X. Huang, *J. Electrochem. Soc.*, **158**, A74 (2011).
60. J. Huang and A. F. Hollenkamp, *J. Phys. Chem. C*, **114**, 21840 (2010).

61. A. Abouimrane, J. Ding, and I. J. Davidson, *J. Power Sources*, **189**, 693 (2009).
62. E. Paillard, Q. Zhou, W. A. Henderson, G. B. Appetecchi, M. Montanino, and S. Passerini, *J. Electrochem. Soc.*, **156**, A891 (2009).
63. G. D. Smith, O. Borodin, S. P. Russo, R. J. Rees, and A. F. Hollenkamp, *Phys. Chem. Chem. Phys.*, **11**, 9884 (2009).
64. A. Guerfi, M. Dontigny, Y. Kobayashi, A. Vijh, and K. Zaghib, *J. Solid State Electrochem.*, **13**, 1003 (2009).
65. M. Beran, J. Příhoda, Z. Žák, and M. Černík, *Polyhedron*, **25**, 1292 (2006).

---

## Experimental Methods

---

Using a combination of methods including thermal phase diagrams (from DSC data), XRD solvate structure determination (single crystal x-ray diffraction) and Raman vibrational spectroscopic analysis, the degree of solvation and ionic association have been determined for a wide variety of electrolyte mixtures including model or newly used solvents (i.e., nitriles or dinitriles) and new or conventional lithium salts (LiDFOB, LiFSI, LiPF<sub>6</sub>, LiTFSI, LiBF<sub>4</sub>, LiClO<sub>4</sub> and LiCF<sub>3</sub>SO<sub>3</sub>). Once the solution structure was well understood, the transport properties (viscosity and ionic conductivity) of the electrolyte mixtures were correlated with the structural information to obtain insight into the origin of the transport property variations for the different electrolytes.

## 2.1. Materials

### 2.1.1. Lithium Salts

The lithium salts (LiX) used in the present study and their acronyms are noted in Fig. 2.1. LiPF<sub>6</sub> (electrolyte grade), LiClO<sub>4</sub> (battery grade, 99.998%) and LiBF<sub>4</sub> (anhydrous, 99.99%) were purchased from Novolyte and used as-received. LiFSI (> 99.5%, Suzhou Fluolyte

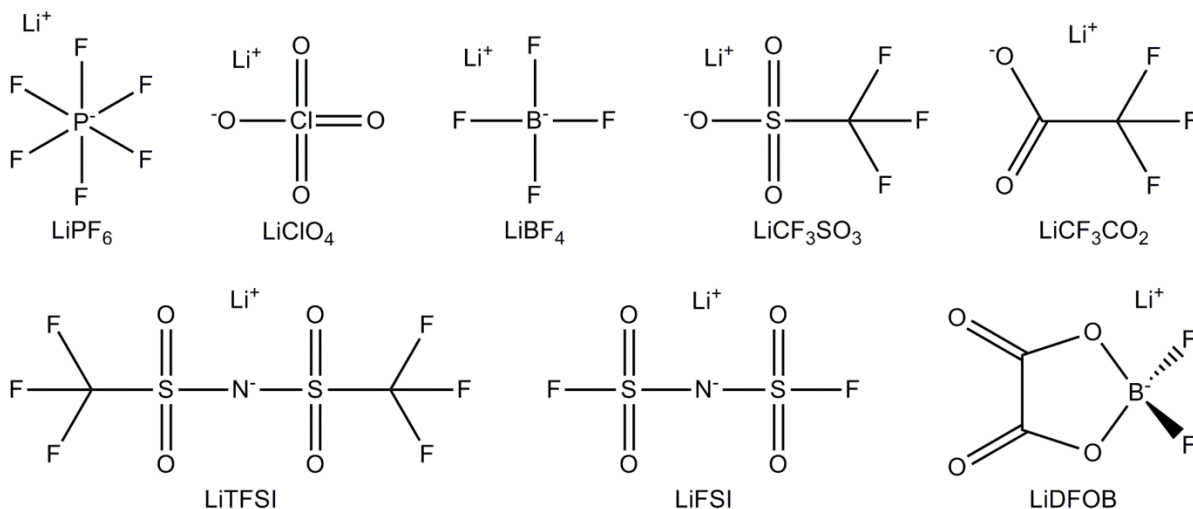


**Figure 2.1.** Ion structures and acronyms of the lithium salts studied.

Company) was used as-received. LiTFSI (electrolyte grade, 3M), LiCF<sub>3</sub>SO<sub>3</sub> (99.995%, Sigma-Aldrich) and LiCF<sub>3</sub>CO<sub>2</sub> (95%, Sigma-Aldrich) were dried under high vacuum at 120 °C for 24 h prior to use.

LiDFOB (≥ 99.9%) was synthesized by the direct reaction of excess boron trifluoride diethyl etherate (BF<sub>3</sub>-ether) with lithium oxalate (oxalic acid dilithium salt or Li<sub>2</sub>Ox), both used as-received from Sigma-Aldrich (Fig. 2.2). The ether solvent, one of the reaction byproducts, was filtered off along with the unreacted BF<sub>3</sub>-ether. Residual ether was then evaporated at room temperature under high vacuum. The resulting solids, a mixture of LiF, unreacted Li<sub>2</sub>Ox and LiDFOB, were mixed with DMC at 80 °C. The LiDFOB dissolved in the DMC solvent, while the LiF and Li<sub>2</sub>Ox were insoluble. These solids were filtered off and the solution was cooled to crystallize the LiDFOB as a (DMC)<sub>3/2</sub>:LiDFOB solvate. The

LiDFOB was purified by multiple recrystallization steps. The LiDFOB solvate was dried in a vacuum oven at 105 °C for 48 h to remove the DMC. The resulting pure LiDFOB salt was stored in a sealed container in a N<sub>2</sub>-filled Vacuum Atmospheres inert atmosphere glovebox (< 1 ppm H<sub>2</sub>O). In order to verify the purity of the LiDFOB, the salt was analyzed by <sup>11</sup>B and <sup>19</sup>F-NMR.<sup>1</sup>

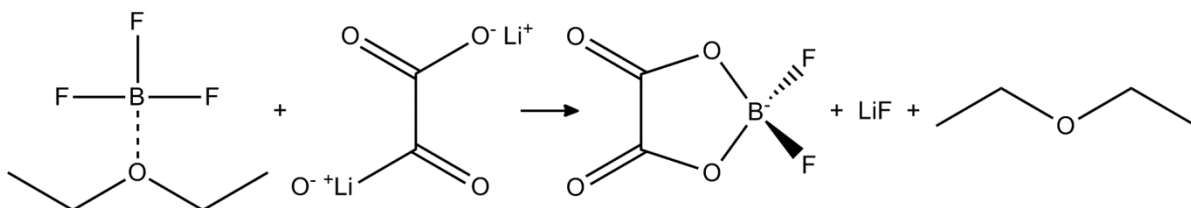
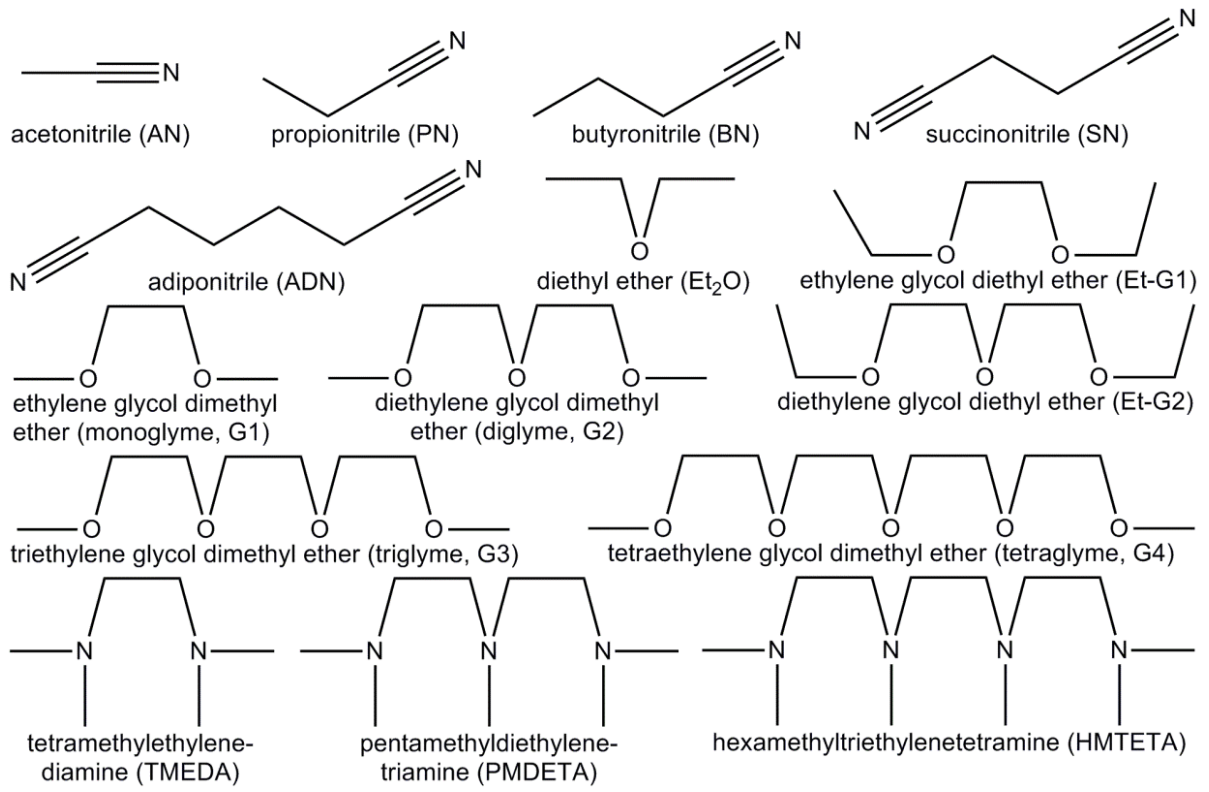


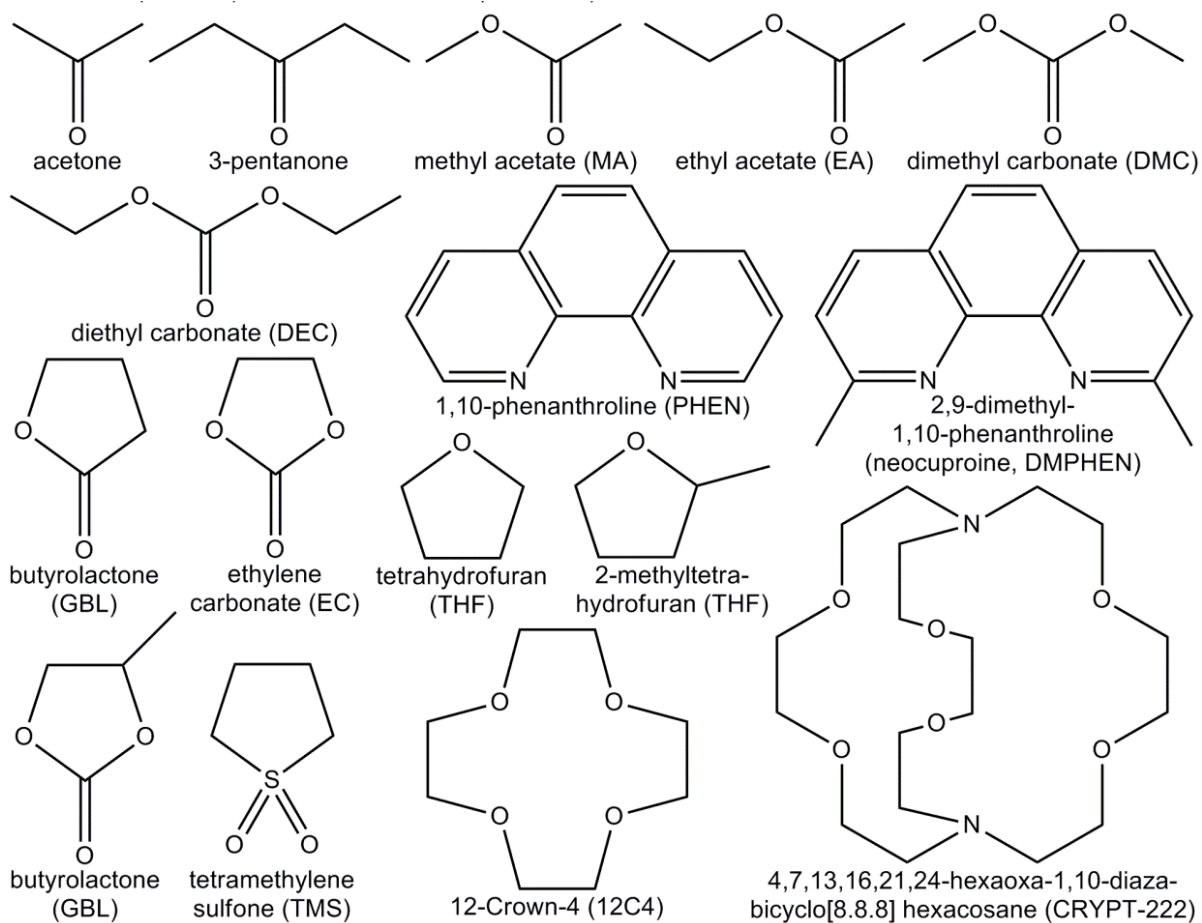
**Figure 2.2.** Synthesis of LiDFOB by direct reaction of BF<sub>3</sub>-etherate and dilithium oxalic acid.<sup>1</sup>

### 2.1.2. Solvents

The solvent used in the present study and their acronyms are noted in Fig. 2.3. Acetonitrile (AN, extra dry, 99.9%), propionitrile (PN, 99%), butyronitrile (BN, ≥ 99%), succinonitrile (SN, 99%), adiponitrile (ADN, 99%), diethyl ether (Et<sub>2</sub>O, anhydrous, ≥ 99%), ethylene glycol dimethyl ether or 1,2-dimethoxyethane (monoglyme or G1, anhydrous, 99.5%), diethylene glycol dimethyl ether or 2-methoxyethyl ether (diglyme or G2, anhydrous, 99.5%), triethylene glycol dimethyl ether or triglyme (G3, 99%), tetraethylene glycol dimethyl ether or tetraglyme (G4, 99%), ethylene glycol diethyl ether or 1,2-diethoxyethane (Et-G1, 98%), diethylene glycol diethyl ether or 2-ethoxyethyl ether (Et-G2,

**Figure 2.3.** Structures and acronyms of the solvents studied.





reagent grade,  $\geq 98\%$ ), *N,N,N',N'*-tetramethylethylenediamine (TMEDA, 99%), *N,N,N',N'',N''*-pentamethyl-diethylenetriamine (PMDETA, 99%), 1,1,4,7,10,10-hexamethyltriethylenetetramine (HMTETA, 97%), ethylene carbonate (EC, anhydrous, 99%), propylene carbonate (PC, anhydrous, 99.7%),  $\gamma$ -butyrolactone (GBL,  $\geq 99\%$ ), tetramethylene sulfone or sulfolane (TMS, 99%), acetone ( $\geq 99.9\%$ ), 3-pentanone ( $\geq 99\%$ ), methyl acetate (MA,  $\geq 98\%$ ), ethyl acetate (EA, 99.8%), dimethyl carbonate (DMC, anhydrous,  $\geq 99\%$ ), diethyl carbonate (DEC, anhydrous,  $\geq 99\%$ ), tetrahydrofuran (THF, anhydrous,  $\geq 99.9\%$ ), 2-methyltetrahydrofuran (2-MeTHF,  $\geq 99.5\%$ ), 1,10-phenanthroline (PHEN,  $\geq 99\%$ ), 2,9-dimethyl-1,10-phenanthroline or neocuproine (DMPHEN,  $\geq 98\%$ ), 1,4,7,10-tetraoxacyclododecane (12-crown-4 or 12C4, 98%), 4,7,13,16,21,24-hexaoxa-1,10-diazabicyclo[8.8.8]hexacosane (CRYPT-222, 98%) were purchased from either Sigma-Aldrich, Novolyte or Fisher Scientific. The solvents were dried over 3 Å molecular sieves, if necessary, until the water content was verified to be negligible ( $< 30$  ppm) using a Mettler Toledo DL39 Karl Fischer coulometer.

## 2.2. Sample Preparation

Mixtures were prepared in the glovebox by combining appropriate amounts of the lithium salts with solvents in hermetically-sealed glass vials and then heated/stirred on a hot plate to form homogenous solutions. The compositions of each mixture/solvate are described using the following three notations:  $(1-x)$  solvent- $(x)$  LiX,  $(\text{solvent})_n\text{-LiX}$  and  $(\text{solvent})_n\text{:LiX}$  for discussions focusing on mole fraction, ratio of AN/Li and specific crystalline solvates,

respectively. A slightly different notation has been used for the quantum chemical (QC) and molecular dynamic (MD) simulation calculations.

To obtain single crystals from a given mixture, compositions for the mixture were typically slightly more dilute than the solvate composition of interest. Single crystals grew from the mixtures upon standing either at room temperature, at 4 °C (in a refrigerator), at -23 °C (in a freezer) or at -20 °C to -40 °C (in a Binder environmental chamber) which is below the single crystal melting point (as obtained from a DSC analysis). The single crystal solvate structures obtained with LiCF<sub>3</sub>SO<sub>3</sub>, LiPF<sub>6</sub> and LiDFOB will be discussed in Chapters 3 and 4. Solvate single crystals were used for the determination of the structures via single-crystal X-ray diffraction, for the analysis of the thermal phase behavior (i.e., solid-solid phase transitions melt transition ( $T_m$ ), glass transition ( $T_g$ ), etc.) via differential scanning calorimetry (DSC), and for the characterization of ion solvation/ionic association behavior via Raman spectroscopy. For the DSC analysis, the single crystals were directly added to the hermetically-sealed sample pans and tested. For the Raman analysis, the solvate crystals were either ground in the glovebox into a powder using a mortar and pestle (if the  $T_m$  of the solvate is greater than room temperature) or used directly. For solvates with a  $T_m$  at or below room temperature, liquid samples of the appropriate composition were instead prepared in the glovebox and the crystalline solvate phases were grown directly in the Linkam heating/cooling stage during the Raman measurements.

## **2.3. Instruments and Techniques**

### **2.3.1. Differential Scanning Calorimetry (DSC)**

TA Instruments Q100 and Q2000 differential scanning calorimeters with liquid N<sub>2</sub> cooling were used for the DSC measurements. The instruments were calibrated with cyclohexane (solid-solid phase transition at -87.06 °C,  $T_m$  at 6.54 °C) and indium ( $T_m$  at 156.60 °C). Two or three droplet of sample was added to an aluminum pan and hermetically-sealed in the glovebox. Typically, sample pan were cooled to -150 °C and then heated to 100-200 °C at a rate of 5 °C min<sup>-1</sup>, depending upon the temperature necessary for melting and/or decomposition. In many cases, it was necessary to cycle and repeatedly anneal the sample pans at subambient temperature to ensure complete crystallization of the samples. Once the samples were crystallized, the pans were cooled to -150 °C and then heated (5 °C min<sup>-1</sup>) to fully melt the samples. If crystallization was not achieved after 3-5 cycles, it was assumed that the sample could not be crystallized (with the procedures used). Neat lithium salts and single crystals were not annealed, but rather cooled to -150 °C and heated until melting and/or decomposition was observed. Peak temperature values were recorded from the final heating thermograms and these data were used to construct the reported phase diagrams.

### **2.3.2. X-Ray Diffraction**

The structural determination and analysis for the single crystals were performed by Drs. Paul D. Boyle and Roger D. Sommer in the Department of Chemistry at North Carolina State University. In general, samples were mounted on a nylon loop with a small amount of

Paratone N oil. X-ray measurements were performed on a Bruker-Nonius Kappa Axis X8 Apex2 diffractometer at a temperature of -163 °C. The unit cell dimensions were determined from symmetry constrained fits of the reflections. The frame integrations were performed using SAINT.<sup>2</sup> The resulting raw data were scaled and absorption corrected using a multiscan averaging of symmetry equivalent data using SADABS or TWINABS (if twinning was present).<sup>2</sup> The structures were solved by direct methods using either the XS or SIR92 programs.<sup>3-4</sup> All non-hydrogen atoms were obtained from the initial solutions. The hydrogen atoms were introduced at idealized positions and were allowed to ride on the parent atom. The structural models were fit to the data using full matrix least-squares based on  $F^2$ . The calculated spectra factors included corrections for anomalous dispersion from the usual tabulation. The structures were refined using the XL program from SHELXTL.<sup>4</sup>

### **2.3.3. Raman Spectroscopy**

A Horiba Jobin-Yvon LabRAM HR VIS high resolution confocal Raman microscope was used to collect Raman vibrational spectra using a 632 nm<sup>-1</sup> He-Ne laser as the exciting source and a hermetically-sealed Linkam heating/cooling stage for temperature control. The instrument was calibrated with a two point calibration of the Raman laser line at 0.0 nm and a monocrystalline Si wafer at 520.7 cm<sup>-1</sup>. Samples were added to a machined well cut into an aluminum plate with a vacuum grease-sealed glass cover slide used to seal the well. The aluminum plate with the sample was then added to a Linkam stage in the glovebox before transferring the stage to the spectrometer. Spectra were typically collected with a 50X long-

range objective using a 10-70 s exposure time and 10-20 accumulations to ensure high resolution spectra were obtained. Raman spectra were evaluated with LabSpec software.

#### **2.3.4. Density/Viscosity Measurements**

An Anton Paar SVM 3000 Stabinger viscometer was used for the viscosity and density measurements. The instrument was calibrated at three different temperatures (20 °C, 60 °C and 100 °C) using Cannon viscosity and density reference standard oils: APS3 (3.689 mPa s<sup>-1</sup>/0.8150 g cm<sup>-3</sup>), APN7.5 (9.995 mPa s<sup>-1</sup>/0.8159 g cm<sup>-3</sup>), APN26 (50.02 mPa s<sup>-1</sup>/0.8209 g cm<sup>-3</sup>) and APN415 (1105 mPa s<sup>-1</sup>/0.8456 g cm<sup>-3</sup>) (values at 20 °C). To improve the accuracy of the measurements in the very low viscosity range, an ultra low viscosity adjustment also performed at three different temperatures (20 °C, 60 °C and 100 °C) with n-heptane (0.412 mPa s<sup>-1</sup>/0.6838 g cm<sup>-3</sup>), n-octane (0.545 mPa s<sup>-1</sup>/0.7027 g cm<sup>-3</sup>), n-nonane (0.708 mPa s<sup>-1</sup>/0.7177 g cm<sup>-3</sup>) and n-decane (0.906 mPa s<sup>-1</sup>/0.7301 g cm<sup>-3</sup>) (values at 20 °C). After the instrument calibration, the sample measurements were conducted in 10 °C steps from 0 °C to 60 °C with a 1 °C min<sup>-1</sup> heating rate. All of the samples were tested in duplicate with a fresh sample after each analysis. Approximately 2.6 ml of a sample was injected into the instrument with care taken to prevent the sample exposure to water from ambient air prior to and during the measurements. The instrument was cleaned before and after each set of measurements with ethyl acetate and isopropyl alcohol, and flushed with N<sub>2</sub> gas (> 99.99%, water concentration 2-5 ppm). The moisture content of the samples was tested before and after each measurement to ensure the absence of water contamination.

### 2.3.5. Conductivity Measurements

A Biologic VMP3 Potentiostat/Galvanostat/EIS analyzer was used for the ionic conductivity ( $\kappa$ ) measurements using AMEL Instruments two electrode cells with Pt electrodes. The cells were assembled inside the glovebox and transferred into a Binder MK53 environmental chamber for testing. Cell constants were calculated for each cell with a 11.67 mS cm<sup>-1</sup> aqueous KCl standard at 25 °C (Sigma-Aldrich). Each experiment was performed from 1 MHz to 20 Hz with a 10 mV AC perturbation. Conductivity values were measured in 10 °C steps from 100 °C to -40 °C with the samples equilibrated at each temperature in an environmental chamber for approximately 60 min prior to the measurements. A Nyquist plot was generated for each measurement and the conductivity was evaluated using the point where the impedance curve intersected the real axis.<sup>4-6</sup> Molar concentration  $C$  (mol dm<sup>-3</sup>) values were calculated from the concentration  $m$  (mol-salt kg<sup>-1</sup>-solution) and density  $\rho$  (g cm<sup>-3</sup>) of each solution by  $C = m\rho$ . These values were then used to calculate the molar conductivity values by  $\Lambda = \kappa/C$ .

### 2.3.6. Molecular Dynamics (MD) Simulations and Quantum Chemistry (QC) Calculations

MD simulations were performed by Dr. Oleg Borodin at the U.S. Army Research Laboratory (ARL) on AN doped with LiX (LiPF<sub>6</sub>, LiTFSI, LiClO<sub>4</sub>, LiBF<sub>4</sub>, LiDFOB and LiFSI) employing a recently developed, many-body polarizable APPLE&P force field for AN and AN/Li<sup>+</sup>.<sup>5-7</sup> The force fields for the DFOB<sup>-</sup> or FSI<sup>-</sup> anions have been developed and

validated for this work.<sup>8</sup> The APPLE&P functional form was used for all of the bonded and non-bonded interactions, as described elsewhere.<sup>7</sup> The repulsion-dispersion parameters for the Li<sup>+</sup>...solvent and Li<sup>+</sup>...anion interactions were taken from previous work.<sup>6</sup> Simulations were performed for solvent:salt ratios (n) of 30, 20, 10, 5 and 2 at 60 °C with the corresponding number of salt units in the simulation box of 16, 32, 64, 128, 256 resulting in various simulation box size lengths. Extensive details regarding the force field development and MD simulation methodology are provided in the published manuscripts.<sup>8-11</sup>

The solvent and anion residence times in the Li<sup>+</sup> cation solvation shells have been analyzed in order to better understand the Li<sup>+</sup> cation transport mechanisms in (AN)<sub>n</sub>-LiX solutions.<sup>11</sup> The distribution of residence times for the AN molecules and anions present in the cation's primary solvation shell were calculated using:

$$P_{X-Li}(t) = \langle H(t) * H(0) \rangle$$

where H(t) is 1 if a given atom—i.e., N(AN), B(BF<sub>4</sub>), Cl(ClO<sub>4</sub>), P(PF<sub>6</sub>), etc.—is within the previously specified proximity for solvent/anion coordination to a given Li<sup>+</sup> cation<sup>9,10</sup> and zero otherwise. The brackets indicate averaging over all of the Li<sup>+</sup> cations and multiple time origins, as well as normalization such that P<sub>X-Li</sub>(0) = 1. The residence time for each species in the Li<sup>+</sup> cation solvation shell was calculated as the time integral of stretched exponential exp(-(t/τ)<sup>β</sup>) fits to the P<sub>X-Li</sub>(t) distribution functions.

Density functional theory (DFT) calculations were performed by Erlendur Jónsson and Dr. Patrik Johansson at Chalmers University of Technology.<sup>12</sup> The DFOB<sup>-</sup> anion and its various ion pairs with Li<sup>+</sup> cations were constructed manually and geometries were optimized

using the 6-311+G\* basis set employing two different DFT functionals: B3LYP<sup>13-15</sup> and M06-2X<sup>16</sup>—the former to support backward compatibility (significant previous work has been done using only the B3LYP functional) and the latter to make use of the recent development of better functionals (M06-2X). Utilizing both serves as an internal calibration/verification of the results. Subsequently, the structures were all verified as energy minima by computing their Hessians and the Raman spectral data (frequencies, activities) were obtained from the partial third derivatives of the energy. In addition to the above calculations, all done for ionic species in vacuum, a solvent effect was added (with the structures reoptimized) using a solvent self-consistent reaction field (SCRF-SMD) methodology<sup>17</sup> with AN as the parametrized solvent. This was done to in some way account for the reduced ion-ion interactions in the crystalline and/or liquid environment, and thus to mimic the experimental analysis to some extent. As the DFOB<sup>-</sup> anion is able to adopt a multitude of different forms of Li<sup>+</sup> cation coordination, the same strategy as noted above was also employed to scrutinize various ion pairs for numerous DFOB<sup>-</sup>...Li<sup>+</sup> cation combinations. All calculations were made using Gaussian 09.<sup>18</sup> To assist the comparison with the experimental data, artificial Raman spectra were created by convolution of the spectral data using a Lorentzian band shape and a FWHM of 5 cm<sup>-1</sup>.

## 2.4. References

1. J. L. Allen, S.-D. Han, P. D. Boyle, and W. A. Henderson, *J. Power Sources*, **196**, 9737 (2011).
2. Bruker-Nonius, *SAINTE, SADABS and TWINABS*, Bruker AXS Inc., Madison, WI (2009).
3. A. Altomare, G. Cascarano, C. Giacovazzo, A. Guagliardi, M. C. Burla, G. Polidori, and M. Camalli, *J. Appl. Crystallogr.*, **27**, 435 (1994).
4. G. M. Sheldrick, *Acta Crystallogr.*, **A64**, 112 (2008).
5. J. B. Hooper and O. Borodin, *Phys. Chem. Chem. Phys.*, **12**, 4635 (2010).
6. O. Borodin, *J. Phys. Chem. B*, **113**, 11463 (2009).
7. O. Borodin and G. D. Smith, *J. Phys. Chem. B*, **113**, 1763 (2009).
8. S.-D. Han, O. Borodin, J. L. Allen, D. M. Seo, D. W. McOwen, and W. A. Henderson, *J. Electrochem. Soc.*, in-press (2013).
9. D. M. Seo, O. Borodin, S.-D. Han, Q. Ly, P. D. Boyle, and W. A. Henderson, *J. Electrochem. Soc.*, **159**, A553 (2012).
10. D. M. Seo, O. Borodin, S.-D. Han, P. D. Boyle, and W. A. Henderson, *J. Electrochem. Soc.*, **159**, A1489 (2012).
11. D. M. Seo, O. Borodin, D. Balogh, M. O'Connell, Q. Ly, S.-D. Han, S. Passerini, and W. A. Henderson, *J. Electrochem. Soc.*, **160**, A1061 (2013).
12. S.-D. Han, J. L. Allen, E. Jónsson, P. Johansson, D. W. McOwen, P. D. Boyle, and W. A. Henderson, *J. Phys. Chem. C*, **117**, 5521 (2013).

13. S. H. Vosko, L. Wilk, and M. Nusair. *Can. J. Phys.*, **58**, 1200 (1980).
14. C. Lee, W. Yang, and R. G. Parr, *Phys. Rev. B*, **37**, 785 (1988).
15. A. D. Becke, *J. Chem. Phys.*, **98**, 5648 (1993).
16. Y. Zhao and D. G. Truhlar, *Theor. Chem. Acc.*, **120**, 215 (2008).
17. A. V. Marenich, C. J. Cramer, and D. G. Truhlar, *J. Phys. Chem. B*, **113**, 6378 (2009).
18. M. J. Frisch, G. W. Trucks, H. B. Schlegel, G. E. Scuseria, M. A. Robb, J. R. Cheeseman, G. Scalmani, V. Barone, B. Mennucci, and G. A. Petersson, *et al.*, *Gaussian 09, Revision B.01.*, Gaussian Inc., Wallingford, CT (2010).

---

## Reassessing Polarization Parameters and Li<sup>+</sup> Cation Solvation

---

Polarization parameters are widely utilized to gauge solvation interactions, yet here it is shown that the most widely used parameters are ineffective at describing the solvate species present in solution for dissolved lithium salts. For solutions with aprotic solvents, the solvent molecules and anions directly compete with one another for coordination to the Li<sup>+</sup> cations. The distribution of anion...Li<sup>+</sup> cation coordination modes is directly and unambiguously accessible from vibrational spectroscopy. The use of this anion coordination information readily enables the discernment of how solvent structural features govern Li<sup>+</sup> cation solvation.

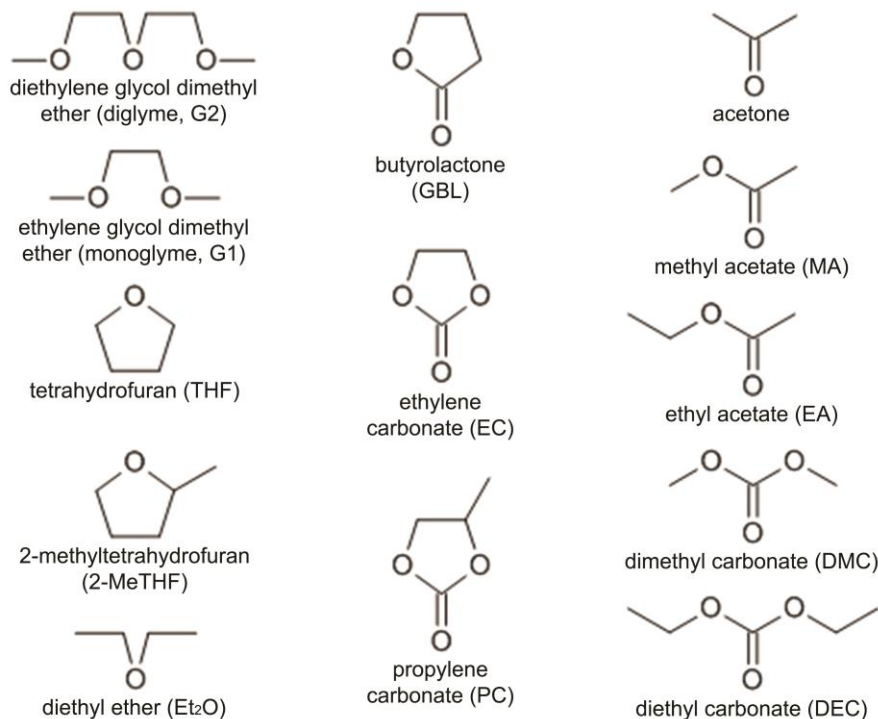
### 3.1. Introduction

Solvation and ionic association interactions are key features of solvent-salt systems. Although it has long been known that different forms of ionic species govern the ionic conductivity and physical properties of electrolytes,<sup>1-18</sup> it is only in recent years that a knowledge of the ionic association behavior of lithium reagents (organolithium reagents, LiAlH<sub>4</sub>, LiEt<sub>3</sub>BH, LiCuR<sub>2</sub>, LiNR<sub>2</sub>, lithium enolates, etc.) has been widely recognized as crucial for understanding their reactivity and reaction rates.<sup>19-76</sup> Knowledge regarding how

the solvent used influences the outcome of a reaction or an electrolyte's physical properties is usually lacking and the choice of solvent is frequently based upon empirical experience or what is readily accessible. The subtleties of the solvent's role in the process are missed.

Typically, solvent-ion interactions are characterized in terms of the solvent's polarity.<sup>19,77</sup> Katritzky *et al.* noted that "the term 'polarity' is usually related to the capacity of a solvent for solvating dissolved charged or dipolar species. 'Polarity' is easy to comprehend qualitatively, but substantial difficulties arise with (i) its precise definition and (ii) its quantitative measurement.....The term "solvent polarity".....is generally used to encompass all of the intermolecular interactions of which the solvent is capable."<sup>77</sup> There are many ways to categorize such a parameter, but one widely used measure of solvent polarity is the dielectric constant or permittivity (Table 3.1). Another widely utilized polarity parameter is the donor number, DN (Table 3.1).<sup>78-80</sup> This indicates the Lewis base donor power of a solvent and reflects the solvent's ability to solvate cations and other Lewis acids (e.g., to 'donate' electrons) (Table 3.1). Carbonate and ether solvents tend to solvate cations through the carbonyl or ether oxygen (EO) electron lone-pairs, respectively. The converse of the DN is the acceptor number, AN (note that this acronym is used in subsequent chapters for the solvent acetonitrile), which measures the ability of a solvent to accept electrons as a Lewis acid (Table 3.1).<sup>81</sup> The AN indicates the degree with which the solvent will interact with anions. Anions tend to be solvated by hydrogen bonding and in aprotic solvents this is not possible. The relatively high DN's and low AN's of polyether and related solvents (Table 3.1), therefore, suggest that solvate formation will be dictated largely by the balance/competition

**Table 3.1.** Solvent structures and solvent polarization parameters—relative permittivity (or dielectric constant) ( $\epsilon$ ), donor number (DN), acceptor number (AN) and  $E_T(30)$ .



Solvent	$\epsilon$	DN	AN	$E_T(30)$
diglyme (G2)	7.2	24	9.9	38.6
monoglyme (1,2-DME or G1)	7.1	20	10.2	38.2
tetrahydrofuran (THF)	7.4	20.0	8.0	37.4
2-methyltetrahydrofuran (2-MeTHF)	7.0	18	-	36.5
diethyl ether ( $\text{Et}_2\text{O}$ )	4.2	19.2	3.9	34.6
$\gamma$ -butyrolactone (GBL)	39.1	18	(18.6)	-
ethylene carbonate (EC) <sup>†</sup>	90.4	16.4	-	-
propylene carbonate (PC)	65.0	15.1	18.3	46.6
acetone (ACET)	20.6	17.0	12.5	42.2
methyl acetate (MA)	6.7	16.3	-	40.0
ethyl acetate (EA)	6.0	17.1	-	38.1
dimethyl carbonate (DMC)	3.1	15.1	-	-
diethyl carbonate (DEC)	2.8	16.0	-	36.2

<sup>†</sup>at 40 °C

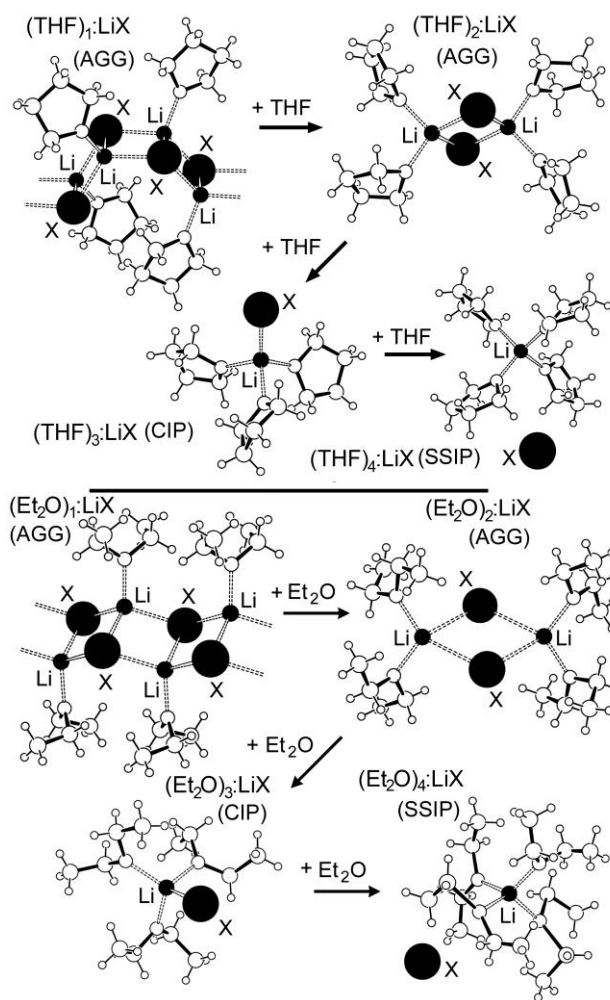


**Figure 3.1.** Examples of Li<sup>+</sup> cation solvates with THF and Et<sub>2</sub>O from crystalline solvate structures (X is the anion).

between solvent...Li<sup>+</sup> cation (roughly indicated by the solvent DN) and anion...Li<sup>+</sup> cation interactions.

For a given salt (e.g., LiX) to be soluble in a solvent S, energy must be expended to break apart the interionic, (X<sup>-</sup>...Li<sup>+</sup>)<sub>n</sub>, forces (represented by a salt's lattice energy). The lattice energy of the salt is compensated by exothermic solvent...ion (i.e., S...Li<sup>+</sup> and/or S...X<sup>-</sup>)

interactions. In simple crystalline lithium salts, the  $\text{Li}^+$  cations are coordinated by four to six anions and vice versa.<sup>82-87</sup> If some of the coordinating anions are replaced by solvent molecules, AGG or CIP solvate species form (Fig. 3.1). AGGs consist of ions coordinated to several counterions, such as  $[\text{X}^-\dots(\text{D})_n\text{Li}^+\dots\text{X}^-]^-$  or  $[(\text{D})_n\text{Li}^+\dots\text{X}^-\dots(\text{D})_n\text{Li}^+]^+$  (where D is a solvent donor atom such as oxygen) for the simplest cases, while CIPs consist of ions coordinated to a single counterion,  $[(\text{D})_n\text{Li}^+\dots\text{X}^-]$ . If the  $\text{Li}^+$  cations are fully solvated by the solvent molecules (the anions remain uncoordinated), then SSIP solvate species result (or perhaps even 'free' well-separated ions in dilute mixtures). Examples of these types of solvates are shown in Fig. 3.1 for tetrahydrofuran (THF)<sub>n</sub>:LiX solvates—SSIP (THF)<sub>4</sub>:LiX,<sup>88-</sup><sup>96</sup> CIP (THF)<sub>3</sub>:LiX,<sup>97-100</sup> AGG (THF)<sub>2</sub>:LiX<sup>101-105</sup> and AGG (THF)<sub>1</sub>:LiX.<sup>106,107</sup> Note that in each case, the  $\text{Li}^+$  cations have 4-fold coordination, but with increasing aggregation the THF molecules are incrementally replaced with anions.

FTIR and Raman spectroscopy are powerful techniques for identifying the ionic aggregation state of solvent-salt solutions (and solid solvates). Fig. 3.2 indicates the reported fraction of different solvate species found in  $\text{LiClO}_4$  solutions with dimethylformamide (DMF), acetone ( $\text{Me}_2\text{CO}$ ) or diethyl ether ( $\text{Et}_2\text{O}$ ) solvents, respectively.<sup>108-111</sup> It will be shown in later chapters, however, that this actually represents the distribution of various modes of  $\text{ClO}_4^- \dots \text{Li}^+$  coordination, rather than providing direct information about the solvates. For all of the solutions, anion aggregation is seen to increase with increasing salt concentration due to the lower number of solvent molecules available for  $\text{Li}^+$  coordination and the closer proximity of the ions. But dramatic differences in aggregation are noted for

different solvents, even for dilute solutions. All three solvents should have only weak interactions with the anions (low AN). An examination of Table 3.1 indicates that the DN fails to explain the aggregations state of the solutions, but the dielectric constant ( $\epsilon$ ) may

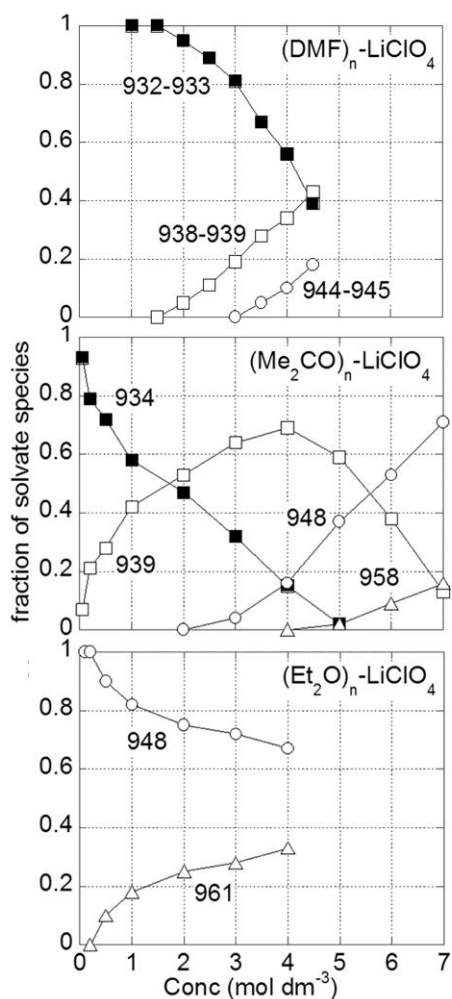
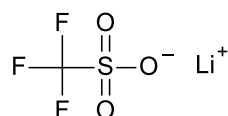


**Figure 3.2.** Fraction of "solvate species" (actually anion coordination modes) in solvent-LiClO<sub>4</sub> mixtures from Raman spectroscopic band analyses: (a) 932-934 cm<sup>-1</sup> (SSIP), (a) 938-939 cm<sup>-1</sup> (CIP), (c) 944-948 cm<sup>-1</sup> (AGG) and (d) 958-961 cm<sup>-1</sup> (more concentrated AGGs).<sup>108-111</sup>

offer a possible explanation. In fact, it will be shown below for various solvents mixed with the salt lithium trifluoromethanesulfonate ( $\text{LiCF}_3\text{SO}_3$ ) that these polarity parameters are, in fact, poor indicators of the solvation interactions with  $\text{Li}^+$  cations.

### 3.2. $\text{CF}_3\text{SO}_3^-$ Anion Raman Vibrational Band Characterization

$\text{LiCF}_3\text{SO}_3$  (lithium trifluoromethanesulfonate or triflate):



is, in general, not a practical electrolyte salt due to the poor transport properties of the electrolytes with  $\text{LiCF}_3\text{SO}_3$ , but it is an extremely useful model lithium salt for Raman spectroscopic studies because it has two strong single  $\text{CF}_3\text{SO}_3^-$  anion Raman bands attributed to the  $\text{CF}_3$  symmetric bending and  $\text{SO}_3^-$  stretching modes, respectively.<sup>112</sup> In addition, as will be shown below, the Raman spectroscopic results for electrolytes with this salt provide relatively unambiguous peak positions corresponding to the specific types of  $\text{CF}_3\text{SO}_3^- \dots \text{Li}^+$  cation coordination interactions.<sup>113</sup> The known and newly determined crystalline solvates with  $\text{LiCF}_3\text{SO}_3$  have therefore been used in this study to identify the Raman band positions for the  $\text{CF}_3\text{SO}_3^-$  anion bands for varying  $\text{CF}_3\text{SO}_3^- \dots \text{Li}^+$  cation interaction modes (Fig. 3.3). The present analysis serves as a key evaluation tool for deciphering the Raman spectroscopic data for electrolytes with  $\text{LiCF}_3\text{SO}_3$  and correlating this to the liquid-phase molecular interactions within such electrolytes.

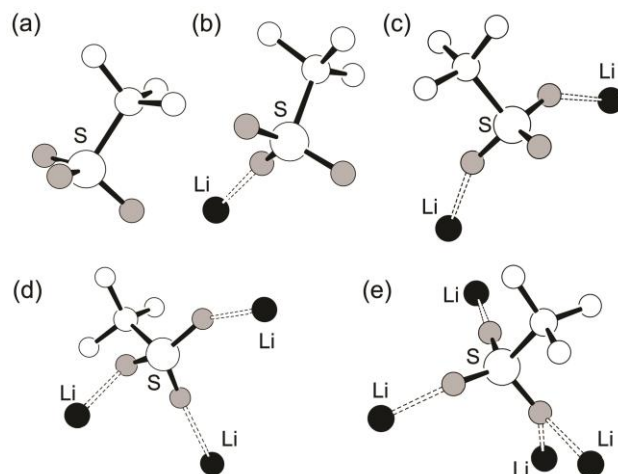


**Figure 3.3.** Varying modes of  $\text{CF}_3\text{SO}_3^- \dots \text{Li}^+$  cation coordination: (a) SSIP, (b) CIP-I, (c) AGG-I, (d) AGG-II and (e) AGG-III.

### 3.2.1. Solvate Structures and $\text{Li}^+$ Cation Coordination

Figs. 3.4 and 3.5 show the schematic illustrations of the  $\text{CF}_3\text{SO}_3^- \dots \text{Li}^+$  cation coordination in the crystalline solvates. Among them, the structures of the crystalline solvates  $(2,9\text{-DMPHEN})_2:\text{LiCF}_3\text{SO}_3$ ,  $(\text{G3})_1:\text{LiCF}_3\text{SO}_3$ ,  $(\text{PHEN})_2:\text{LiCF}_3\text{SO}_3$ ,  $(\text{TMEDA})_1:\text{LiCF}_3\text{SO}_3$ ,  $(\text{PMDETA})_1:\text{LiCF}_3\text{SO}_3$ ,  $(\text{G2})_1:\text{LiCF}_3\text{SO}_3$ ,  $(\text{THF})_1:\text{LiCF}_3\text{SO}_3$ ,  $(\text{G3})_{1/2}:\text{LiCF}_3\text{SO}_3$ ,  $(\text{AN})_1:\text{LiCF}_3\text{SO}_3$ ,  $(\text{DMC})_1:\text{LiCF}_3\text{SO}_3$ ,  $(\text{DEC})_1:\text{LiCF}_3\text{SO}_3$ ,  $(\text{GBL})_1:\text{LiCF}_3\text{SO}_3$ ,  $(\text{EC})_1:\text{LiCF}_3\text{SO}_3$  and pure  $\text{LiCF}_3\text{SO}_3$  have been previously reported (Fig. 3.4).<sup>114-125</sup> The structures of the crystalline solvates  $(12\text{C4})_2:\text{LiCF}_3\text{SO}_3$ ,  $(\text{BN})_1:\text{LiCF}_3\text{SO}_3$  and  $(\text{MA})_1:\text{LiCF}_3\text{SO}_3$  were determined as part of the present study (Fig. 3.5). In all of the solvate structures, if the  $\text{CF}_3\text{SO}_3^-$  anions coordinated, they have at least one of the oxygen atoms coordinated to a  $\text{Li}^+$  cation. Each sulfonyl oxygen atoms can coordinate up to two  $\text{Li}^+$  cations using the available two electron lone-pairs (Fig. 3.4n), although this is rarely found to occur.

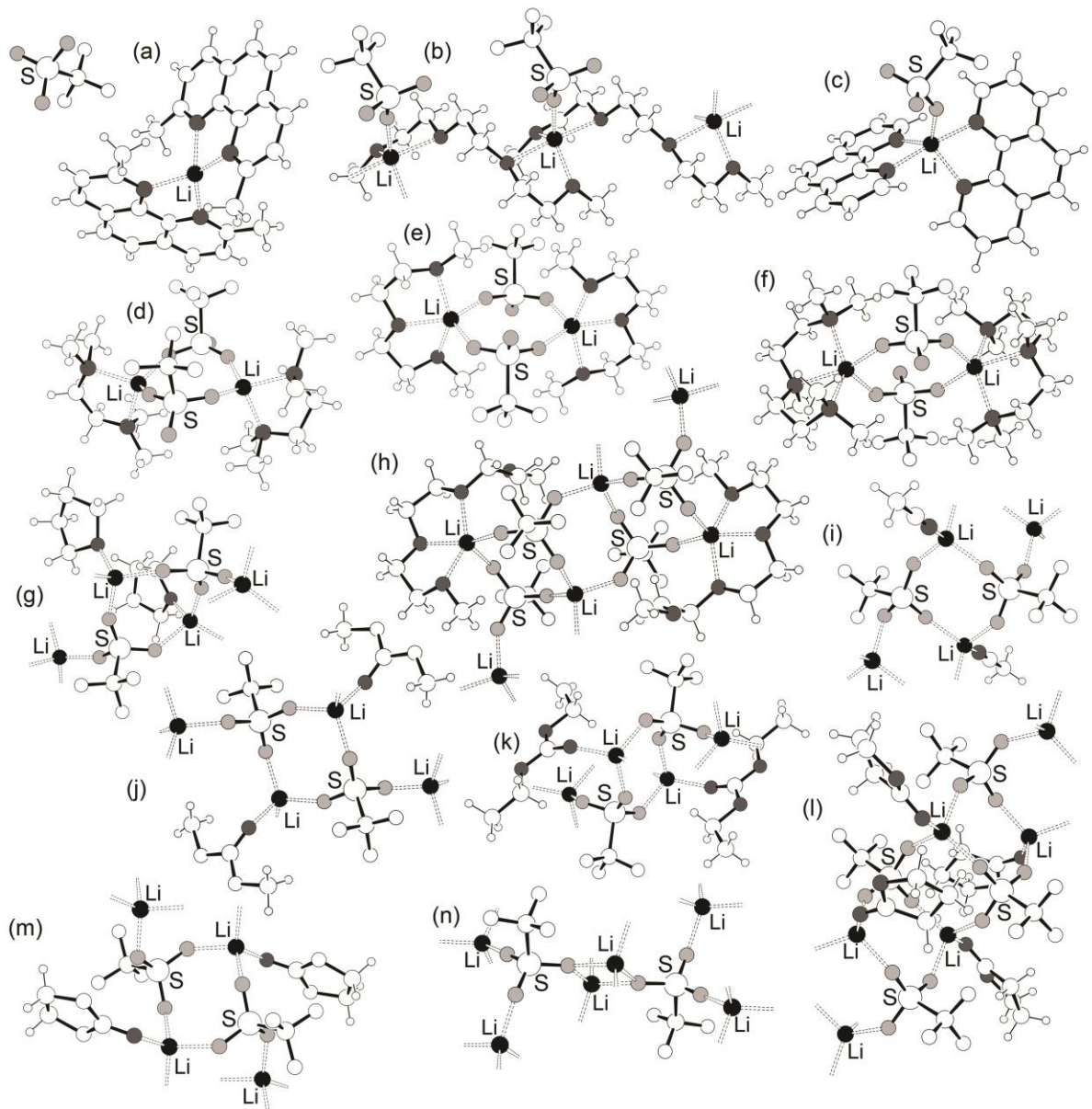


**Figure 3.4.**  $\text{CF}_3\text{SO}_3^- \dots \text{Li}^+$  cation coordination in solvates which have previously been reported: (a) SSIP  $(2,9\text{-DMPHEN})_2:\text{LiCF}_3\text{SO}_3$ , (b) CIP-I  $(\text{G3})_1:\text{LiCF}_3\text{SO}_3$ , (c) CIP-I  $(\text{PHEN})_2:\text{LiCF}_3\text{SO}_3$ , (d) AGG-I  $(\text{TMEDA})_1:\text{LiCF}_3\text{SO}_3$  (partial structure), (e) AGG-I  $(\text{G2})_1:\text{LiCF}_3\text{SO}_3$ , (f) AGG-I  $(\text{PMDETA})_1:\text{LiCF}_3\text{SO}_3$ , (g) AGG-II  $(\text{THF})_1:\text{LiCF}_3\text{SO}_3$ , (h) AGG-II  $(\text{G3})_{1/2}:\text{LiCF}_3\text{SO}_3$ , (i) AGG-II  $(\text{AN})_1:\text{LiCF}_3\text{SO}_3$ , (j) AGG-II  $(\text{DMC})_1:\text{LiCF}_3\text{SO}_3$ , (k) AGG-II  $(\text{DEC})_1:\text{LiCF}_3\text{SO}_3$ , (l) AGG-II  $(\text{GBL})_1:\text{LiCF}_3\text{SO}_3$ , (m) AGG-II  $(\text{EC})_1:\text{LiCF}_3\text{SO}_3$  and (n) AGG-III pure  $\text{LiCF}_3\text{SO}_3$ .

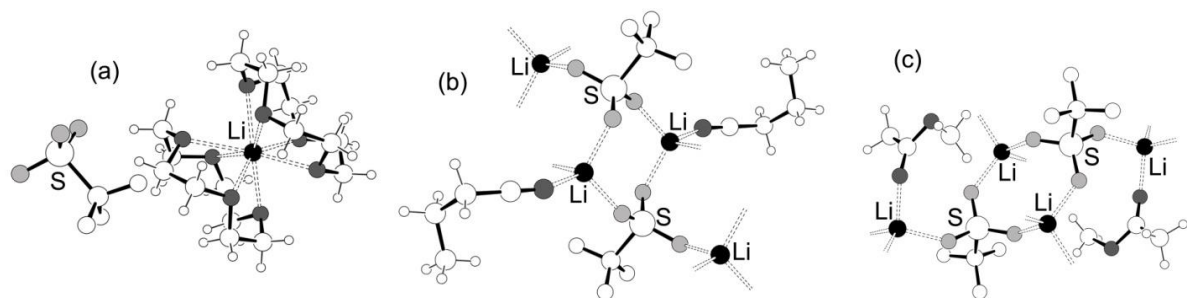


**Figure 3.5.**  $\text{CF}_3\text{SO}_3^- \dots \text{Li}^+$  cation coordination in the newly reported  $\text{LiCF}_3\text{SO}_3$  solvates: (a) SSIP  $(12\text{C}4)_2:\text{LiCF}_3\text{SO}_3$ , (b) AGG-II  $(\text{BN})_1:\text{LiCF}_3\text{SO}_3$  and (c) AGG-II  $(\text{MA})_1:\text{LiCF}_3\text{SO}_3$ .

AGG-II coordination to three  $\text{Li}^+$  cations using all three oxygen atoms is a common feature for the anion... $\text{Li}^+$  cation interactions in the solid-state structures, as found in nine of the crystalline solvates:  $(\text{THF})_1:\text{LiCF}_3\text{SO}_3$ ,  $(\text{G}3)_{1/2}:\text{LiCF}_3\text{SO}_3$ ,  $(\text{AN})_1:\text{LiCF}_3\text{SO}_3$ ,  $(\text{DMC})_1:\text{LiCF}_3\text{SO}_3$ ,  $(\text{DEC})_1:\text{LiCF}_3\text{SO}_3$ ,  $(\text{GBL})_1:\text{LiCF}_3\text{SO}_3$ ,  $(\text{EC})_1:\text{LiCF}_3\text{SO}_3$ ,  $(\text{BN})_1:\text{LiCF}_3\text{SO}_3$  and  $(\text{MA})_1:\text{LiCF}_3\text{SO}_3$  (Figs. 3.4 and 3.5). None of the structures have  $\text{Li}^+$  cations coordination by the anion fluorine atoms. The various forms of  $\text{CF}_3\text{SO}_3^-$  anion coordination (i.e., SSIP, CIP-I, AGG-I, AGG-II and AGG-III) in these crystalline solvates and the pure lithium salt results in different Raman band positions which thereby serves as fingerprint for each  $\text{CF}_3\text{SO}_3^- \dots \text{Li}^+$  cation interaction mode.

### 3.2.2. Raman Spectroscopic Analysis of Crystalline Solvates

Crystalline solvates of the known and newly determined solvates were characterized by Raman spectroscopy to determine the  $\text{CF}_3\text{SO}_3^-$  anion band position variation with varying coordination and temperature. As a preliminary study, the Raman spectrum for the anhydrous

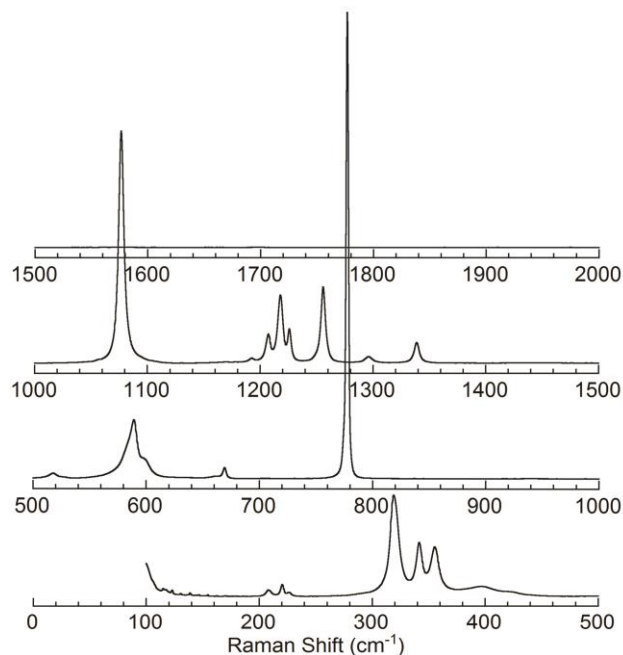


**Figure 3.6.** Raman spectrum of LiCF<sub>3</sub>SO<sub>3</sub> (at 20 °C).

LiCF<sub>3</sub>SO<sub>3</sub> crystalline salt (i.e., AGG-III) was determined, as shown in Fig. 3.6. Amongst the five regions of the spectrum with anion bands (i.e., 280-420 cm<sup>-1</sup>, 540-620 cm<sup>-1</sup>, 760-800 cm<sup>-1</sup>, 1040-1120 cm<sup>-1</sup> and 1180-1280 cm<sup>-1</sup>), relatively strong single anion bands are found near 775 and 1075 cm<sup>-1</sup>, which are attributed to the CF<sub>3</sub> symmetric bending mode ( $\delta_s$ CF<sub>3</sub>) and SO<sub>3</sub><sup>-</sup> stretching mode ( $\nu_s$ SO<sub>3</sub>), respectively.<sup>126</sup> These two bands were analyzed in depth. The Raman spectroscopic data for both regions are provided in Appendix A.

Fig. 3.7 shows a summary of the 745-785 cm<sup>-1</sup> and 1025-1085 cm<sup>-1</sup> results for the CF<sub>3</sub>SO<sub>3</sub><sup>-</sup> anion Raman vibrational band positions as a function of temperature for the various crystalline LiCF<sub>3</sub>SO<sub>3</sub> solvates and pure LiCF<sub>3</sub>SO<sub>3</sub>. Using this evaluation tool, it is possible to deconvolute the spectra for the CF<sub>3</sub>SO<sub>3</sub><sup>-</sup> anion in the liquid phase to identify specific forms

of anion coordination. There are two noteworthy points which may be drawn from the summary. First, as the  $\text{CF}_3\text{SO}_3^- \dots \text{Li}^+$  cation interactions increase (i.e.,  $\text{SSIP} < \text{CIP-I} < \text{AGG-I} < \text{AGG-II} < \text{AGG-III}$ ), the Raman bands shift to higher wavenumber. Second, at around  $755 \text{ cm}^{-1}$ , one of the bands corresponding to CIP-I coordination—black circle symbols (i.e., anion coordinated to a single  $\text{Li}^+$  cation via a single oxygen atom) overlaps with one of the bands corresponding to SSIP coordination—empty triangle symbols (i.e., uncoordinated anions). In addition, at around  $759 \text{ cm}^{-1}$ , one of the bands corresponding to AGG-I coordination—empty square symbols (i.e., anion coordinated to two  $\text{Li}^+$  cations via two oxygen atoms) overlaps with one of the bands corresponding to CIP-I coordination—black circle symbols. Despite

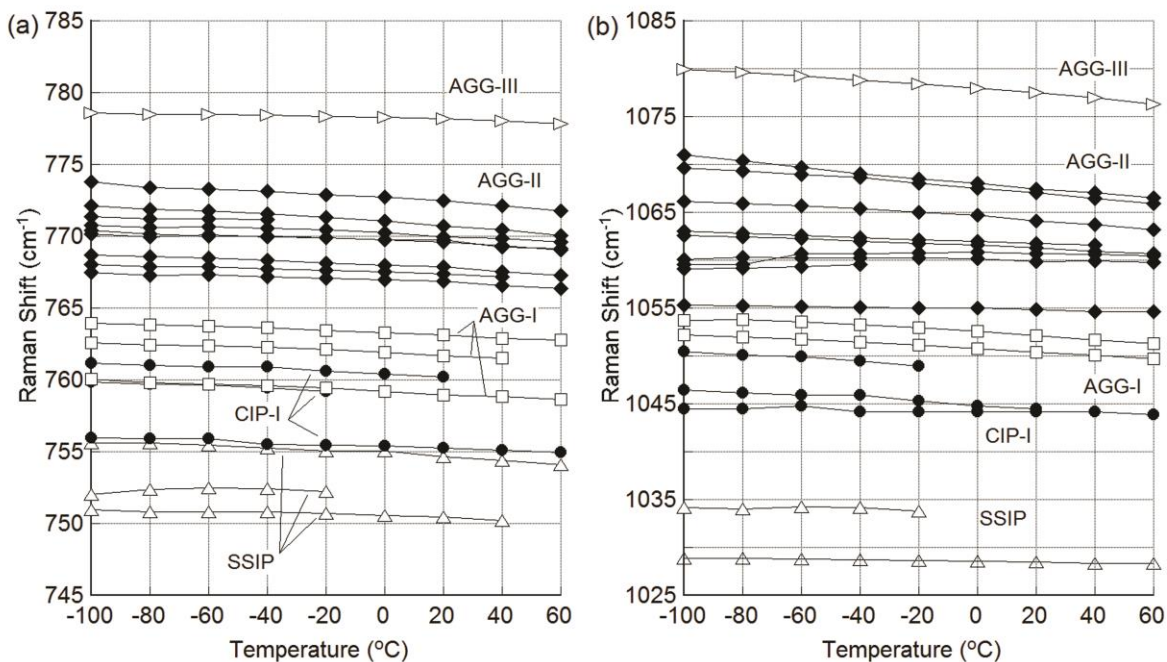


**Figure 3.7.** Raman band peak positions for the  $\text{CF}_3\text{SO}_3^-$  anion vibrational bands for various crystalline solvates.

this, it is relatively easy to distinguish the anions bands for the specific anion modes of coordination, as will be demonstrated below.

### 3.3. Raman Spectroscopic Analysis of Anion Bands for Lithium Salts

#### 3.3.1 Ether Solvents

Fig. 3.8 shows the Raman spectra ( $740\text{-}790\text{ cm}^{-1}$ ) of the  $\text{CF}_3\text{SO}_3^-$  anion  $\text{CF}_3$  symmetric bending mode ( $\delta_s\text{CF}_3$ ) for the  $(\text{solvent})_n\text{-LiCF}_3\text{SO}_3$  mixtures ( $n = 10$  and  $20$ ) with ether solvents at  $20\text{ }^\circ\text{C}$  and  $60\text{ }^\circ\text{C}$ . At both temperatures, all of the mixtures are liquids. The Raman spectra ( $1010\text{-}1110\text{ cm}^{-1}$ ) of the  $\text{SO}_3^-$  stretching mode ( $\nu_s\text{SO}_3$ ) for ether solvents with  $\text{LiCF}_3\text{SO}_3$  at  $20\text{ }^\circ\text{C}$  and  $60\text{ }^\circ\text{C}$  are provided in Appendix A. Based upon the Raman evaluation tools generated for electrolytes with  $\text{LiCF}_3\text{SO}_3$  (Fig. 3.7), each peak position can be assigned to identify the types and distribution of the anion coordination (i.e., SSIP, CIP, AGG-I, AGG-II and AGG-III). At  $20\text{ }^\circ\text{C}$ , both the  $n = 10$  and  $n = 20$  mixtures have almost the same peak positions, but variations in the peak intensities are observed (Fig. 3.8).

Given the similarity in the polarization parameter values for the DN, AN,  $E_T(30)$  and, in particular, dielectric constant ( $\epsilon$ ) for the ether solvents (i.e., G2, G1, THF, 2-MeTHF and  $\text{Et}_2\text{O}$  in Table 3.1), one would expect that electrolyte solutions with these solvents—in which the salt identity/concentration and temperature were the same—would have a similar aggregation state, but the data in Fig. 3.8 clearly indicate that is not the case. Instead, the peak positions for each ether solvent indicate the following order for decreasing  $\text{Li}^+$  cation solvation (increasing ionic association) in the liquid phase:

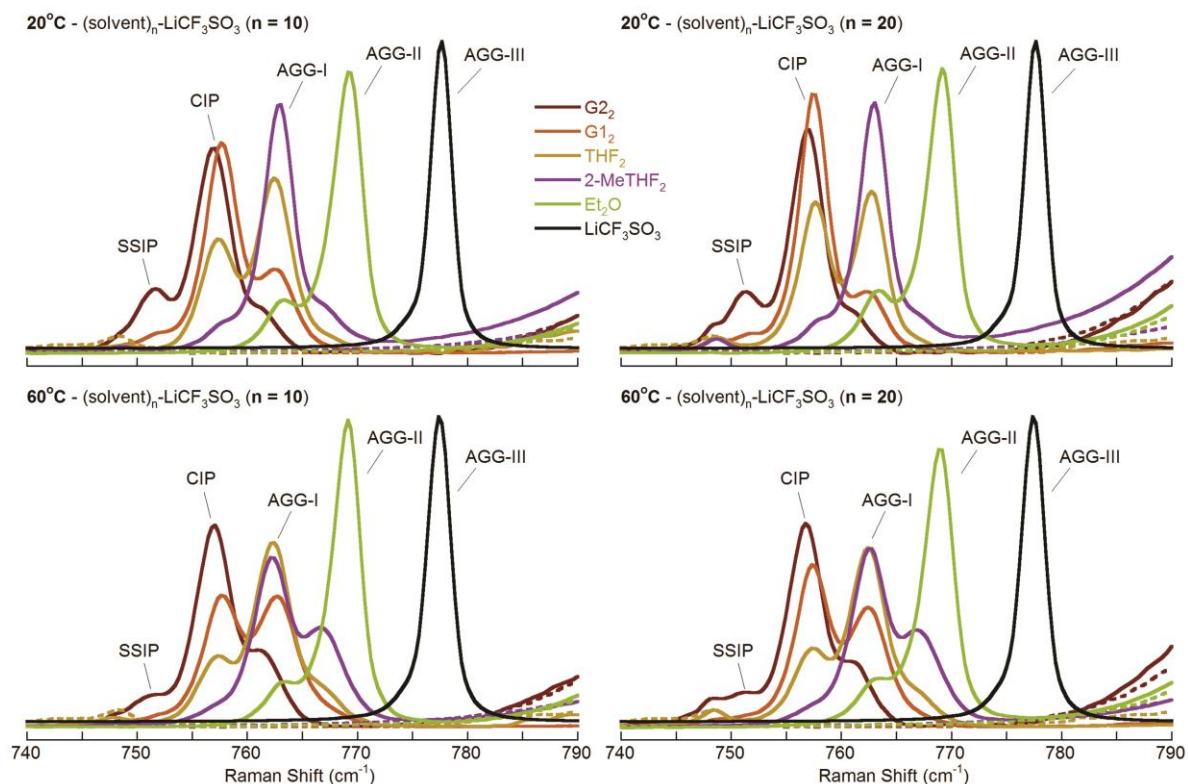


**Figure 3.8.** Raman spectra of the  $\text{CF}_3$  symmetric bending mode ( $\delta_s\text{CF}_3$ ) for  $(\text{solvent})_n\text{-LiCF}_3\text{SO}_3$  mixtures with ether solvents. The spectra for the pure salt (black) and pure solvents (dashed) are shown for comparison.

$$\text{G2} < \text{G1} < \text{THF} < \text{2-MeTHF} < \text{Et}_2\text{O}$$

This order is also found for the Raman spectra of the  $\text{SO}_3^-$  stretching mode ( $\nu_s\text{SO}_3$ ) for  $(\text{solvent})_n\text{-LiCF}_3\text{SO}_3$  mixtures with ether solvents (Fig. A1—Appendix A). One might argue that the G2 and G1 solvents have multiple ether donor atoms available relative to the monodentate solvents, but a comparison of the G1 mixtures with  $n = 10$  and the THF mixtures with  $n = 20$  still indicates that G1 is the better solvent (i.e., less ionic association is present). Fig. 3.8 also indicates that increasing the temperature results in increased ionic

association. For the ether solvents with  $\text{LiCF}_3\text{SO}_3$ , therefore, all of the widely utilized polarity parameters noted in Table 3.1 are poor indicators of the effectiveness of the solvents in coordinating  $\text{Li}^+$  cations within the  $(\text{ether solvent})_n\text{-LiCF}_3\text{SO}_3$  mixtures. This study was then extended to examine the anion coordination interactions within mixtures of cyclic and acyclic carbonate/ester solvents with  $\text{LiCF}_3\text{SO}_3$ .

### 3.3.2. Cyclic and Acyclic Carbonate/Ester Solvents

At 20 °C, the Raman spectra ( $740\text{-}790\text{ cm}^{-1}$ ) of the  $\text{CF}_3\text{SO}_3^-$  anion  $\text{CF}_3$  symmetric bending mode ( $\delta_s\text{CF}_3$ ) for  $(\text{solvent})_n\text{-LiCF}_3\text{SO}_3$  mixtures ( $n = 10$  and  $20$ ) with cyclic and acyclic carbonate/ester solvents were obtained, as shown in Fig. 3.9. The remaining Raman spectra of the  $\text{CF}_3$  symmetric bending mode ( $\delta_s\text{CF}_3$ ,  $740\text{-}790\text{ cm}^{-1}$ ) at 60 °C and the  $\text{SO}_3^-$  stretching mode ( $\nu_s\text{SO}_3$ ,  $1010\text{-}1110\text{ cm}^{-1}$ ) at 20 °C and 60 °C for cyclic and acyclic carbonate/ester solvents with  $\text{LiCF}_3\text{SO}_3$  are provided in Appendix A. Similar to the  $(\text{ether solvents})_n\text{-LiCF}_3\text{SO}_3$  mixtures, variations in the peak intensities are observed with changing the concentration (Fig. 3.9) or temperature (Fig. A4—Appendix A). However, the anion band peak positions for the mixtures of the cyclic and acyclic carbonate/ester solvents with  $\text{LiCF}_3\text{SO}_3$  are affected by neither the  $\text{LiCF}_3\text{SO}_3$  concentration nor temperature (see Fig. A2—Appendix A), as was also found in the Raman spectra of the  $\text{SO}_3^-$  stretching mode ( $\nu_s\text{SO}_3$ ,  $1010\text{-}1110\text{ cm}^{-1}$ ) at 20 °C and 60 °C in Appendix A (Figs. A3 and A4).

Repeated Raman measurements confirmed that the anion bands for the mixtures with both EC and PC have a reproducible peak shift for the  $\text{CF}_3$  symmetric bending mode, but this is

not the case for the  $\text{SO}_3^-$  stretching mode (Fig. A3—Appendix A). For the mixtures with the cyclic carbonate solvents and  $\text{LiCF}_3\text{SO}_3$ , the data (Fig. 3.9) indicate the following order for decreasing  $\text{Li}^+$  cation solvation (increasing ionic association):

$$\text{GBL} \leq \text{EC} < \text{PC}$$

In Table 3.1, the DN for GBL, EC and PC are 16.4, 15.1 and 18, while the ANs for PC and GBL are 18.3 and 18.6, respectively. These similar DN/AN values suggest that the same aggregation state for the solutions should be expected, but the mixtures with GBL are clearly

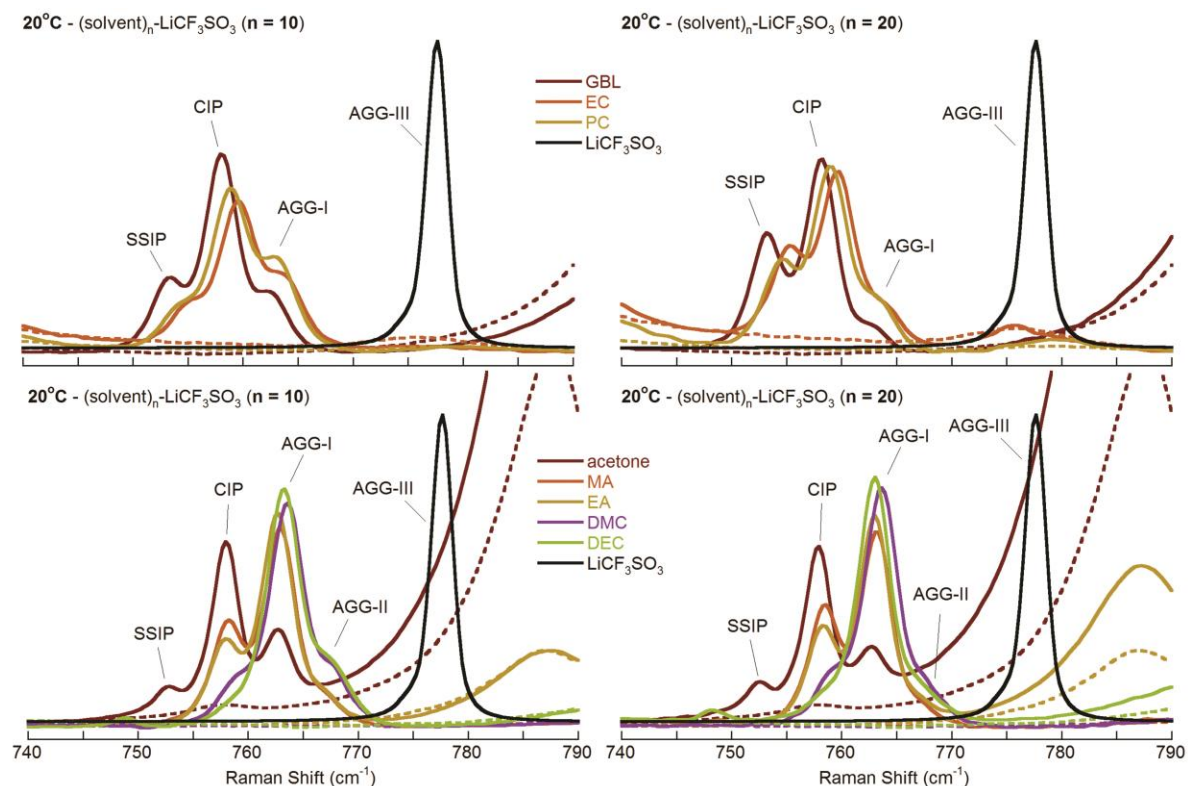


**Figure 3.9.** Raman spectra (at 20 °C) of the  $\text{CF}_3$  symmetric bending mode ( $\delta_s\text{CF}_3$ ) for  $(\text{solvent})_n\text{-LiCF}_3\text{SO}_3$  mixtures with cyclic and acyclic carbonate/ester solvents. The spectra for the pure salt (black) and pure solvents (dashed) are shown for comparison.

less associated (more extensive  $\text{Li}^+$  cation solvation) than those with EC or PC. It is noteworthy that each dielectric constant ( $\epsilon$ ) for GBL, EC and PC (i.e., 39.1, 90.4 and 65.0, respectively) suggests that GBL should be the least effective solvent of the three.

The data for the acyclic carbonate/ester solvent mixtures with  $\text{LiCF}_3\text{SO}_3$  (Fig. 3.9) indicates the following order for decreasing  $\text{Li}^+$  cation solvation (increasing ionic association) in the liquid phase:



Table 3.1, however, shows that these solvents have similar DN's. However, the dielectric constants ( $\epsilon$ ) for acetone, MA, EA, DMC and DEC do differ (20.6, 6.7, 6.0, 3.1 and 2.8, respectively) in the order one would expect, the data for the other solvents indicates that this is just happenstance. Polarization parameters, therefore, are poor indicators of the effectiveness of solvents to coordinated  $\text{Li}^+$  cations.

### 3.4. Conclusions

Crystal structures of  $\text{LiCF}_3\text{SO}_3$  solvates provide significant insight into the manner in which the  $\text{CF}_3\text{SO}_3^-$  anion coordinates  $\text{Li}^+$  cations. These crystalline solvates have been extensively characterized with Raman spectroscopy to link the vibrational bands with specific forms of  $\text{CF}_3\text{SO}_3^- \dots \text{Li}^+$  cation coordination. Based upon this Raman spectroscopic analysis, the ionic interactions (anion coordination—SSIP, CIP, AGG-I, AGG-II and AGG-III) within electrolyte mixtures with various solvents and  $\text{LiCF}_3\text{SO}_3$  can be readily identified. The characterization results indicate that the most commonly used polarity parameters (i.e.,

DN, AN,  $E_T(30)$ ,  $\epsilon$ ) are poor indicators of the solvation interactions for solvent mixtures with lithium salts.

### 3.5. References

1. D. Aurbach, eds., *Nonaqueous Electrochemistry*, Marcel Dekker, Inc., New York, NY (1999).
2. J. Barthel and H. J. Gores, in *Handbook of Battery Materials*, J. O. Besenhard, eds., Wiley-VCH, New York, NY (1999).
3. D. Saar, J. Brauner, H. Farber, and S. Petrucci, *J. Phys. Chem.*, **84**, 341 (1980).
4. M. Delsignore, H. Farber, and S. Petrucci, *J. Phys. Chem.*, **90**, 66 (1986).
5. M. Salomon, *J. Solution Chem.*, **22**, 715 (1993).
6. M. Salomon, *Electrochim. Acta*, **30**, 1021 (1985).
7. Z. Chen and M. Hojo, *J. Phys. Chem. B*, **101**, 10896 (1997).
8. M. Ue, *J. Electrochem. Soc.*, **141**, 3336 (1994).
9. M. Ue and S. Mori, *J. Electrochem. Soc.*, **142**, 2577 (1995).
10. A. Chagnes, B. Carré P. Willmann, and D. Lemordant, *J. Power Sources*, **109**, 203 (2002).
11. M. Ue, *Denki Kagaku*, **62**, 620 (1994).
12. A. Webber, *J. Electrochem. Soc.*, **138**, 2586 (1991).
13. M. Ue and S. Mori, in *Rechargeable Lithium and Lithium-Ion Batteries*, S. Megahead, B. M. Barnett, L. Xie, eds., Electrochem. Soc. Proc. Series, PV 94-28, Electrochem. Soc.: Pennington, NJ (1995).
14. D. Nandi, M. N. Roy, and D. K. Hazra, *J. Indian Chem. Soc.*, **70**, 305 (1993).
15. S. Onishi, H. Farber, and S. Petrucci, *J. Phys. Chem.*, **84**, 2922 (1980).

16. H. E. Maaser, M. Delsignore, M. Newstein, and S. Petrucci, *J. Phys. Chem.*, **88**, 5100 (1984).
17. H. Farber, D. E. Irish, and S. Petrucci, *J. Phys. Chem.*, **87**, 3515 (1983).
18. P. K. Muhuri, B. Das, and D. K. Hazra, *J. Phys. Chem. B*, **101**, 3329 (1997).
19. C. Reichardt and T. Welton, *Solvents and Solvent Effects in Organic Chemistry*, Wiley-VCH, Weinheim, Germany (2010).
20. B. L. Lucht, *Acc. Chem. Res.*, **32**, 1035 (1999).
21. K. W. Henderson, A. E. Dorigo, Q.-Y. Liu, and P. G. Williard, *J. Am. Chem. Soc.*, **119**, 11855 (1997).
22. H. Nöth, S. Thomas, and M. Schmidt, *Chem. Ber.*, **129**, 451 (1996).
23. M. John, C. Auel, C. Behrens, M. Marsch, K. Harms, F. Bosold, R. M. Gschwind, P. R. Rajamohanan, and G. Boche, *Chem. Eur. J.*, **6**, 3060 (2000).
24. A. Yakimansky and A. H. E. Müller, *J. Am. Chem. Soc.*, **123**, 4932 (2001).
25. B. L. Lucht, M. P. Bernstein, J. F. Remenar, and D. B. Collum, *J. Am. Chem. Soc.*, **118**, 10707 (1996).
26. J. Pauls and B. Neumüller, *Inorg. Chem.*, **40**, 121 (2001).
27. H.-H. Giese, H. Nöth, H. Schwenk, and S. Thomas, *Eur. J. Inorg. Chem.*, **1998**, 941 (1998).
28. F. Casado, L. Pisano, M. Farriol, I. Gallardo, J. Marquet, and G. Melloni, *J. Org. Chem.*, **65**, 322 (2000).

29. H. J. Reich, D. P. Green, M. A. Medina, W. S. Goldenberg, B. Ö. Gudmundsson, R. R. Dykstra, and N. H. Phillips, *J. Am. Chem. Soc.*, **120**, 7201 (1998).
30. J. S. Wang, R. Jérôme, R. Warin, H. Zhang, and Ph. Teyssié, *Macromolecules*, **27**, 3376 (1994).
31. D. Seebach, *Angew. Chem. Int. Ed. Engl.*, **27**, 1624 (1988).
32. A. Ramirez, E. Lobkovsky, and D. B. Collum, *J. Am. Chem. Soc.*, **125**, 15376 (2003).
33. D. Li, C. Sun, and P. G. Williard, *J. Am. Chem. Soc.*, **130**, 11726 (2008).
34. L. M. Pratt, S. C. Nguyen, and B. T. Thanh, *J. Org. Chem.*, **73**, 6086 (2008).
35. T. Tatic, H. Ott, and D. Stalke, *Eur. J. Inorg. Chem.*, **2008**, 3765 (2008).
36. P. A. Chase, M. Lutz, A. L. Spek, R. A. Gossage, and G. van Koten, *Dalton Trans.*, **2008**, 5783 (2008).
37. H. K. Khartabil, P. C. Gros, Y. Fort, and M. F. Ruiz-López, *J. Org. Chem.*, **73**, 9393 (2008).
38. H. K. Khartabil, M. T. C. Martins-Costa, P. C. Gros, Y. Fort, and M. F. Ruiz-López, *Theor. Chem. Account*, **121**, 321 (2008).
39. D. Hoffmann and D. B. Collum, *J. Am. Chem. Soc.*, **120**, 5810 (1998).
40. X. Sun and D. B. Collum, *J. Am. Chem. Soc.*, **122**, 2452 (2000).
41. X. Sun and D. B. Collum, *J. Am. Chem. Soc.*, **122**, 2459 (2000).
42. F. Xu, R. A. Reamer, R. Tillyer, J. M. Cummins, E. J. J. Grabowski, P. J. Reider, D. B. Collum, and J. C. Huffman, *J. Am. Chem. Soc.*, **122**, 11212 (2000).
43. J. L. Rutherford, D. Hoffmann, and D. B. Collum, *J. Am. Chem. Soc.*, **124**, 264 (2002).

44. P. Zhao and D. B. Collum, *J. Am. Chem. Soc.*, **125**, 4008 (2003).
45. P. Zhao and D. B. Collum, *J. Am. Chem. Soc.*, **125**, 14411 (2003).
46. P. Zhao, B. L. Lucht, S. L. Kenkre, and D. B. Collum, *J. Org. Chem.*, **69**, 242 (2004).
47. A. Ramírez, E. Lobkovsky, and D. B. Collum, *J. Am. Chem. Soc.*, **125**, 15376 (2003).
48. S. Liao and D. B. Collum, *J. Am. Chem. Soc.*, **125**, 15114 (2003).
49. S. H. Wiedemann, A. Ramírez, and D. B. Collum, *J. Am. Chem. Soc.*, **125**, 15893 (2003).
50. T. F. Briggs, M. D. Winemiller, D. B. Collum, R. L. Parsons Jr., A. H. Davulcu, G. D. Harris, J. M. Fortunak, and P. N. Confalone, *J. Am. Chem. Soc.*, **126**, 5427 (2004).
51. B. Qu and D. B. Collum, *J. Am. Chem. Soc.*, **127**, 10820 (2005).
52. S. J. Zuend, A. Ramírez, E. Lobkovsky, and D. B. Collum, *J. Am. Chem. Soc.*, **128**, 5939 (2006).
53. B. Qu and D. B. Collum, *J. Am. Chem. Soc.*, **128**, 9355 (2006).
54. A. Ramírez, X. Sun, and D. B. Collum, *J. Am. Chem. Soc.*, **128**, 10326 (2006).
55. B. Qu and D. B. Collum, *J. Org. Chem.*, **71**, 7117 (2006).
56. Y. Ma, A. Ramírez, K. J. Singh, I. Keresztes, and D. B. Collum, *J. Am. Chem. Soc.*, **128**, 15399 (2006).
57. K. J. Singh and D. B. Collum, *J. Am. Chem. Soc.*, **128**, 13753 (2006).
58. P. F. Godenschwager and D. B. Collum, *J. Am. Chem. Soc.*, **129**, 12023 (2007).
59. Y. Ma and D. B. Collum, *J. Am. Chem. Soc.*, **129**, 14818 (2007).

60. L. R. Liou, A. J. McNeil, A. Ramírez, G. E. S. Toombes, J. M. Gruver, and D. B. Collum, *J. Am. Chem. Soc.*, **130**, 4859 (2008).
61. P. F. Godenschwager and D. B. Collum, *J. Am. Chem. Soc.*, **130**, 8726 (2008).
62. J. M. Gruver, L. R. Liou, A. J. McNeil, A. Ramírez, and D. B. Collum, *J. Org. Chem.*, **73**, 7743 (2008).
63. J. C. Riggs, K. J. Singh, and D. B. Collum, *J. Am. Chem. Soc.*, **130**, 13709 (2008).
64. L. R. Liou, A. J. McNeil, G. E. S. Toombes, and D. B. Collum, *J. Am. Chem. Soc.*, **130**, 17334 (2008).
65. B. Qu and D. B. Collum, *J. Am. Chem. Soc.*, **128**, 9355 (2008).
66. J. Corset, M. Castellà-Ventura, F. Froment, T. Strzalko, and L. Wartski, *Spectrochim. Acta A*, **58**, 1971 (2002).
67. J. Corset, M. Castellà-Ventura, F. Froment, T. Strzalko, and L. Wartski, *J. Org. Chem.*, **68**, 3902 (2003).
68. J. Corset, M. Castellà-Ventura, F. Froment, T. Strzalko, and L. Wartski, *Spectrochim. Acta A*, **68**, 1340 (2007).
69. J. Corset, F. Froment, M.-F. Lautié N. Ratovelomanana, J. Seyden-Penne, T. Strzalko, and M.-C. Roux-Schmitt, *J. Am. Chem. Soc.*, **115**, 1684 (1993).
70. J. Corset, M. Castellà-Ventura, F. Froment, T. Strzalko, and L. Wartski, *J. Raman Spectrosc.*, **33**, 652 (2002).
71. J. C. G. Ruiz, H. Noth, and M. Warchhold, *Eur. J. Inorg. Chem.*, **2008**, 251 (2008).
72. J. Knizek, H. Noth, and M. Warchhold, *Z. Naturforsch. B*, **61**, 1079 (2006).

73. M. Westerhausen, T. Rotter, H. Goerls, C. Birg, M. Warchhold, and H. Noeth, *Z. Naturforsch. B*, **60**, 766 (2005).
74. H. Noeth, S. Rojas-Lima, and A. Troll, *Eur. J. Inorg. Chem.*, **2005**, 1895 (2005).
75. R. M. Gschwind, X. Xie, P. R. Rajamohanan, C. Auel, and G. Boche, *J. Am. Chem. Soc.*, **123**, 7299 (2001).
76. R. M. Gschwind, P. R. Rajamohanan, M. John, and G. Boche, *Organometallics*, **19**, 2868 (2000).
77. A. R. Katritzky, D. C. Fara, H. Yang and K. T ämm, *Chem. Rev.*, **104**, 175 (2004).
78. V. Gutmann, *Coordination Chemistry in Non-Aqueous Solvents*, Springer-Verlag, Wien, NY (1968).
79. V. Gutmann, *Coord. Chem. Rev.*, **18**, 225 (1976).
80. V. Gutmann, G. Resch and W. Linert, *Coord. Chem. Rev.*, **43**, 133 (1982).
81. U. Mayer, V. Gutmann, and W. Gerger, *Monatsh. Chem.*, **106**, 1235 (1975).
82. X. Wu, F. R. Fronczek, and L. G. Butler, *Inorg. Chem.*, **33**, 1363 (1994).
83. J. H. Burns, *Acta Crystallogr.*, **15**, 1098 (1962).
84. M. Tremayne, P. Lightfoot, M. A. Mehta, P. G. Bruce, K. D. M. Harris, K. Shankland, C. J. Gilmore, and G. Bricogne, *J. Solid State Chem.*, **100**, 191 (1992).
85. M. Bolte and H.-W. Lerner, *Acta Crystallogr.*, **E57**, m231 (2001).
86. W. A. Henderson and N. R. Brooks, *Inorg. Chem.*, **42**, 4522 (2003).
87. J. L. Nowinski, P. Lightfoot and P. G. Bruce, *J. Mater. Chem.*, **4**, 1579 (1994).
88. C.-S. Huang and P. P. Power, *Organometallics*, **18**, 697 (1999).

89. M. Tayebani, S. Conoci, K. Feghali, and S. Gambarotta, *Organometallics*, **19**,4568 (2000).
90. H. Bock, M. Ansari, M. Nagel, and R. F. C. Claridge, *J. Organomet. Chem.*, **521**, 51 (1996).
91. T. Habereeder and H. Nöth, *Z. Anorg. Allg. Chem.*, **627**, 789 (2001).
92. H. Link, A. Decker, and D. Fenske, *Z. Anorg. Allg. Chem.*, **626**, 1567 (2000).
93. C.-S. Hwang and P. P. Power, *J. Organomet. Chem.*, **589**, 234 (1999).
94. D. Vagedes, G. Erker, and R. Fröhlich, *J. Organomet. Chem.*, **641**, 148 (2002).
95. H. S. Chan, Q. Yang, T. C. W. Mak, and Z. Xie, *J. Organomet. Chem.*, **601**, 160 (2000).
96. G. Linti, A. Rodig, and W. Köstler, *Z. Anorg. Allg. Chem.*, **627**, 1465 (2001).
97. H. Nöth and R. Waldhör, *Z. Naturforsch, Teil. B*, **53b**, 1525 (1998).
98. H.-H. Giese, H. Nöth, H. Schwenk, and S. Thomas, *Eur. J. Inorg. Chem.*, **1998**, 941 (1998).
99. W. Zarges, M. Marsch, K. Harms, W. Koch, G. Frenking, and G. Boche, *Chem. Ber.*, **124**, 543 (1991).
100. C. J. Cardin, D. J. Cardin, W. Clegg, S. J. Coles, S. P. Constantine, J. R. Rowe, and S. J. Teat, *J. Organomet. Chem.*, **573**, 96 (1999).
101. F. E. Hahn and S. Rupprecht, *Z. Naturforsch*, **46b**,143 (1991).
102. M. A. Beswick, Y. G. Lawson, P. R. Raithby, J. A. Wood, and D. S. Wright, *J. Chem. Soc., Dalton Trans.*, **1999**, 1921 (1999).

103. T. Chivers, A. Downard, and M. Parvez, *Inorg. Chem.*, **38**, 5565 (1999).
104. R. A. Bartlett, M. M. Olmstead, and P. P. Power, *Inorg. Chem.*, **25**, 1243 (1986).
105. A. Downard, M. Nieuwenhuyzen, K. R. Seddon, J.-A. van den Berg, M. A. Schmidt, J. F. S. Vaughan, and U. Welz-Biermann, *Cryst. Growth Des.*, **2**, 111 (2002).
106. H. Schumann, J. A. Meese-Marktscheffel, and J. Loebel, *Z. Naturforsch, Teil. B*, **45**, 1304 (1990).
107. N. Kongprakaiwoot, R. L. Luck, and E. Urnezis, *Acta Crystallogr.*, **E58**, m735 (2002).
108. D. W. James, R. E. Mayes, W. H. Leong, I. M. Jamie, and G. Zhen, *Faraday Discuss. Chem. Soc.*, **85**, 269 (1988).
109. D. E. James and R. E. Mayes, *J. Phys. Chem.*, **88**, 637 (1984).
110. D. E. James and R. E. Mayes, *Aust. J. Chem.*, **35**, 1775 (1982).
111. D. E. James and R. E. Mayes, *Aust. J. Chem.*, **35**, 1785 (1982).
112. W. Huang, *Ion-Ion and Ion-Polymer Interactions in Polyether-Salt Complexes*. Ph.D. Thesis, The University of Oklahoma (1994).
113. W. A. Henderson, Proposal awarded by DOE, RFP#: DE-PS02-09ER09-01 (2009).
114. J. H. N. Buttery, Effendy, S. Mutrofin, N. C. Plackett, B. W. Skelton, N. Somers, C. R. Whitaker, and A. H. White, *Z. Anorg. Allg. Chem.*, **632**, 1839 (2006).
115. W. A. Henderson, N. R. Brooks, W. W. Brennessel, and V. G. Young Jr., *Chem. Mater.*, **15**, 4679 (2003).
116. S. W. Lee and W. C. Troglor, *Acta Crystallogr.*, **C45**, 1152 (1989).

117. J. H. N. Buttery, Effendy, G. A. Koutsantonis, S. Mutrofin, N. C. Plackett, B. W. Skelton, C. R. Whitaker, and A. H. White, *Z. Anorg. Allg. Chem.*, **632**, 1829 (2006).
118. R. A. Sanders, R. Frech, and M. A. Khan, *J. Phys. Chem. B*, **107**, 8310 (2003).
119. C. P. Rhodes and R. Frech, *Macromolecules*, **34**, 2660 (2001).
120. R. Frech, C. P. Rhodes, and M. Khan, *Macromol. Symp.*, **186**, 41 (2002).
121. N. R. Brooks, W. A. Henderson, and W. H. Smyrl, *Acta Crystallogr.*, **E58**, m176 (2002).
122. P. G. Bekiarian, M. Doyle, W. B. Farnham, and A. E. Feiring, *J. Fluor. Chem.*, **125**, 1187 (2004).
123. R. Dinnebier, N. Sofina, and M. Jansen, *Z. Anorg. Allg. Chem.*, **630**, 1613 (2004).
124. M. Bolte and H.-W. Lerner, *Acta Crystallogr.*, **E57**, m231 (2001).
125. H. Schumann, J. A. Meese-Marktscheffel, J. Loebel, and Z. Naturforsch, *J. Chem. Sci. B*, **B45**, 1304 (1990).
126. B. Sandner, J. Tübke, S. Wartewig, and S. Shashkov, *Solid State Ionics*, **83**, 87 (1996).

---

## Crystalline Solvate Structures and Ionic Association Interactions

---

Lithium hexafluorophosphate ( $\text{LiPF}_6$ ) is the primary salt used in commercial Li-ion and related battery electrolytes. Lithium difluoro(oxalato)borate ( $\text{LiDFOB}$ ) is a relatively new salt designed for battery electrolyte usage. Limited information is currently available, however, regarding the ionic interactions of these salts (i.e., solvate formation) when they are dissolved in aprotic solvents. Raman vibrational spectroscopy is a particularly powerful tool for identifying the ion-ion interactions, but only if the vibrational band assignment for the specific anion coordination modes can be accurately deciphered. The following work characterizes the anion Raman vibrational bands for the evaluation of the anion... $\text{Li}^+$  cation interactions within known and newly reported crystalline  $\text{LiDFOB}$  or  $\text{LiPF}_6$  solvates. The information obtained from these analyses provides key guidance to correctly link the vibrational bands to specific forms of anion coordination in electrolytes containing the  $\text{LiDFOB}$  or  $\text{LiPF}_6$  salts.

### 4.1. Introduction

The difluoro(oxalato)borate ( $\text{DFOB}^-$ ) anion, also known as oxalyldifluoroborate

(ODFB<sup>-</sup>), has drawn significant attention in recent years for Li-ion battery electrolytes.<sup>1-37</sup> The hexafluorophosphate anion (PF<sub>6</sub><sup>-</sup>), in contrast, is the most widely used anion for lithium battery applications. Little is known at present, however, about the solvate structures formed by salts with these anions and the spectroscopic evaluation of the molecular-level ionic interactions present once these salts are dissolved in the aprotic solvents used for electrolytes. Solvate crystal structures not only provide detailed insight into the molecular-level solvent...Li<sup>+</sup> and anion...Li<sup>+</sup> cation coordination, thus serving as both useful models for the solvates present in liquid electrolytes and aiding in deducing the anion...Li<sup>+</sup> cation coordination in both the solid and liquid phases from spectroscopic data. This information is

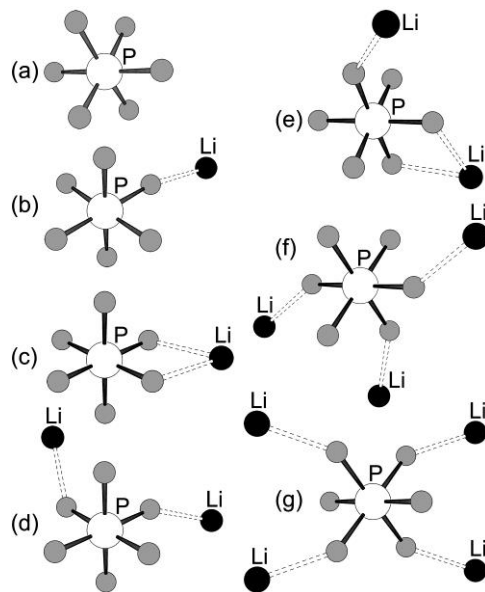


**Figure 4.1.** PF<sub>6</sub><sup>-</sup>...Li<sup>+</sup> cation coordination: (a) SSIP, (b) CIP-I, (c) CIP-II, (d) AGG-Ia, (e) AGG-Ib, (f) AGG-II and (g) AGG-III (other forms of coordination may also occur) (Li<sup>+</sup> cations are colored black).<sup>42</sup>

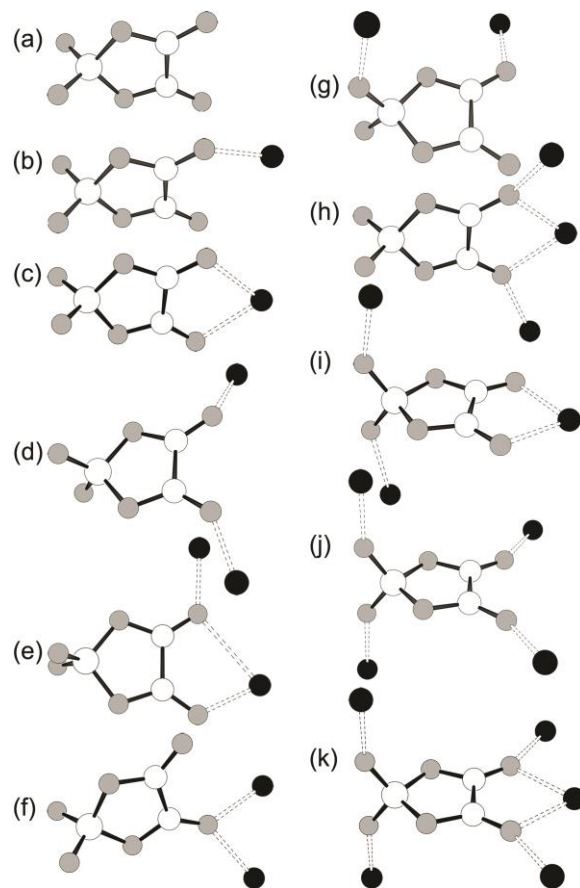


**Figure 4.2.** DFOB<sup>-</sup>...Li<sup>+</sup> cation coordination: (a) SSIP, (b) CIP-I, (c) CIP-II, (d) AGG-Ia, (e) AGG-Ib, (f) AGG-Ic, (g) AGG-Id, (h) AGG-IIa, (i) AGG-IIb, (j) AGG-IIIa and (k) AGG-IIIb (other forms of coordination may also occur) (Li<sup>+</sup> cations are colored black).<sup>43</sup>

necessary to understand the origin of electrolyte properties as solvent-salt mixtures consist of a diverse range of solvate species.<sup>38-41</sup>

The solvates present in electrolytes may be broadly classified as solvent-separated ion pair (SSIP), contact ion pair (CIP) or aggregate (AGG) solvates depending upon whether the anions form coordinate bonds with zero, one, or more than one Li<sup>+</sup> cations, respectively (Figs. 4.1 and 4.2).<sup>42,43</sup> These may be further differentiated as CIP-I, CIP-II and CIP-III for a

contact ion pair in which the anions are coordinated to a single  $\text{Li}^+$  cation through one, two or three fluorine atoms, respectively. AGG-I, AGG-II and AGG-III coordination then refers to the anions coordinated to two, three or more than three  $\text{Li}^+$  cations, respectively (Figs. 4.1 and 4.2). Each of these different forms of coordination results in a different vibrational spectral fingerprint. These solvate types are categorized in terms of the anion instead of the  $\text{Li}^+$  cation interactions because the anion coordination modes can be characterized using spectroscopic methods, while the cation coordination modes cannot. Note that spectroscopic methods therefore are only able to provide indirect insight into the solvates which form and their distribution. The combination of spectroscopic data with information from other methods, however, enables one to explore the solution structure of a given electrolyte and thus directly correlate with the electrolyte's transport and other properties.<sup>38-41</sup>

Vibrational spectroscopy (Raman and FTIR) is the predominant method to determine the extent of ionic association in electrolytes by examining the variation in anion vibrational band position.<sup>42,43</sup> When an anion coordinates one or more  $\text{Li}^+$  cations, the anion's electron density distribution changes, leading to changes in the bond lengths and angles which induce vibrational band variation. A Raman spectroscopic analysis of electrolytes is therefore able to determine the variability of the anion coordination present in solution. Such data typically consists of broad overlapping anion Raman bands, making it difficult to deconvolute them correctly and interpret them properly to distinguish the specific forms of anion... $\text{Li}^+$  cation coordination. Computational simulations may be utilized to assign the band positions for varying forms of coordination,<sup>44-48</sup> but they do not always provide a definitive validation for

the assignments. From previous studies,<sup>49-55</sup> however, it has been demonstrated that crystalline solvates with known structures can be utilized as models for the spectroscopic characterization of different forms of anion and  $\text{Li}^+$  cation coordination. Such evaluations indicate that many of the vibrational assignments previously published are either incorrect or oversimplifications of the true ionic association state present in the  $\text{LiClO}_4^-$  and  $\text{LiBF}_4^-$ -based electrolytes.

The known and newly determined crystalline solvate structures with  $\text{LiDFOB}$  or  $\text{LiPF}_6$  have been used in the present study to identify the Raman band positions for the  $\text{DFOB}^-$  and  $\text{PF}_6^-$  anion bands for varying  $\text{DFOB}^-$  or  $\text{PF}_6^- \dots \text{Li}^+$  cation interaction modes. In addition, density functional theory (DFT) calculations for the uncoordinated  $\text{DFOB}^-$  anion (i.e., SSIP) and the CIP-II form of the  $\text{DFOB}^- \dots \text{Li}^+$  cation coordination (Fig. 4.2) are described to explain the vibrational modes which contribute to the vibrational bands and their correlation with the spectra for the crystalline solvates. The present analysis is thus a key tool for deciphering the Raman spectroscopic data for electrolytes with  $\text{LiDFOB}$  or  $\text{LiPF}_6$  and correlating these data to the molecular interactions within such electrolytes.

## 4.2. $\text{DFOB}^-$ Anion Raman Vibrational Band Characterization

Vibrational spectroscopy, despite being a powerful tool for delineating the anion interactions with  $\text{Li}^+$  cations, has limitations for analyzing the ionic association interactions in a solution. Fig. 4.3 shows two different forms of anion CIP coordination found in the  $(\text{G1})_2:\text{LiDFOB}$  and  $(\text{Et-G1})_{3/2}:\text{LiDFOB}$  crystalline solvates.<sup>43</sup> As noted above, vibrational

spectroscopy can provide only indirect information about the  $\text{Li}^+$  cation interactions. For the  $(\text{Et-G1})_{3/2}:\text{LiDFOB}$  crystalline solvate (Fig. 4.3b), the spectroscopic data indicate a mixture of CIP-I and CIP-II solvates (anion coordination), whereas the structure instead consists of SSIP and AGG solvates from the viewpoint of the  $\text{Li}^+$  cation coordination. Similarly, the spectroscopic data for the  $(\text{CRYPT-222})_{2/3}:\text{LiDFOB}$  solvate are attributed to CIP-I/CIP-II/

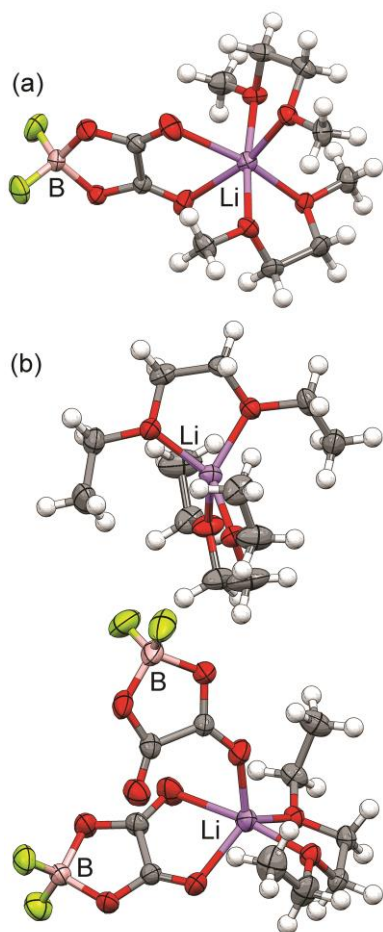


**Figure 4.3.**  $\text{DFOB}^- \dots \text{Li}^+$  cation coordination in the crystalline solvates: (a)  $(\text{G1})_2:\text{LiDFOB}$  and (b)  $(\text{Et-G1})_{3/2}:\text{LiDFOB}$  (Li-purple, O-red, B-tan, F-light green).<sup>43</sup>

AGG-Id coordination (three symmetrically independent anions), whereas the  $\text{Li}^+$  cation coordination is SSIP/SSIP/AGG. MD simulations for electrolyte mixtures show a further complexity.<sup>38-41</sup> In the liquid mixtures, the different solvates and aggregate clusters of ions are distributed and may contain one or more anions coordination to one  $\text{Li}^+$  cation (i.e., CIP), but the cluster itself may be large with many ions (i.e., the  $\text{Li}^+$  cation may be bonded to additional anions). Therefore, the spectroscopic data does not necessarily indicate the true state of ionic association. Caution is therefore needed when the information from a spectroscopic analysis for an electrolyte is translated into a direct interpretation of the solvate distribution. Such an analysis, however, can provide highly informative insight when the spectroscopic data is used in concert with other methods.<sup>38-41</sup>

#### 4.2.1. Solvate Structures and $\text{Li}^+$ Cation Coordination

Schematic illustrations of the  $\text{DFOB}^- \dots \text{Li}^+$  cation coordination in the crystalline solvates are shown in Figs. 4.4 and 4.5.<sup>43</sup> The structures of pure  $\text{LiDFOB}$ ,  $(\text{H}_2\text{O})_1:\text{LiDFOB}$  and  $(\text{TMS})_2:\text{LiDFOB}$  have been previously reported.<sup>9,14</sup> The remaining structures were determined as part of the present study.<sup>43</sup> The  $\text{DFOB}^-$  anion can have a range of different forms of  $\text{Li}^+$  cation coordination, as shown in Fig. 4.2. In all of the solvate structures, all of the  $\text{DFOB}^-$  anions have at least one of the carbonyl oxygen atoms coordinated to a  $\text{Li}^+$  cation. The two carbonyl oxygen atoms can coordinate up to three  $\text{Li}^+$  cations using the available four electron lone-pairs. Bidentate coordination to a  $\text{Li}^+$  cation using both carbonyl oxygen atoms is a common feature for the anion... $\text{Li}^+$  cation interactions in the crystal

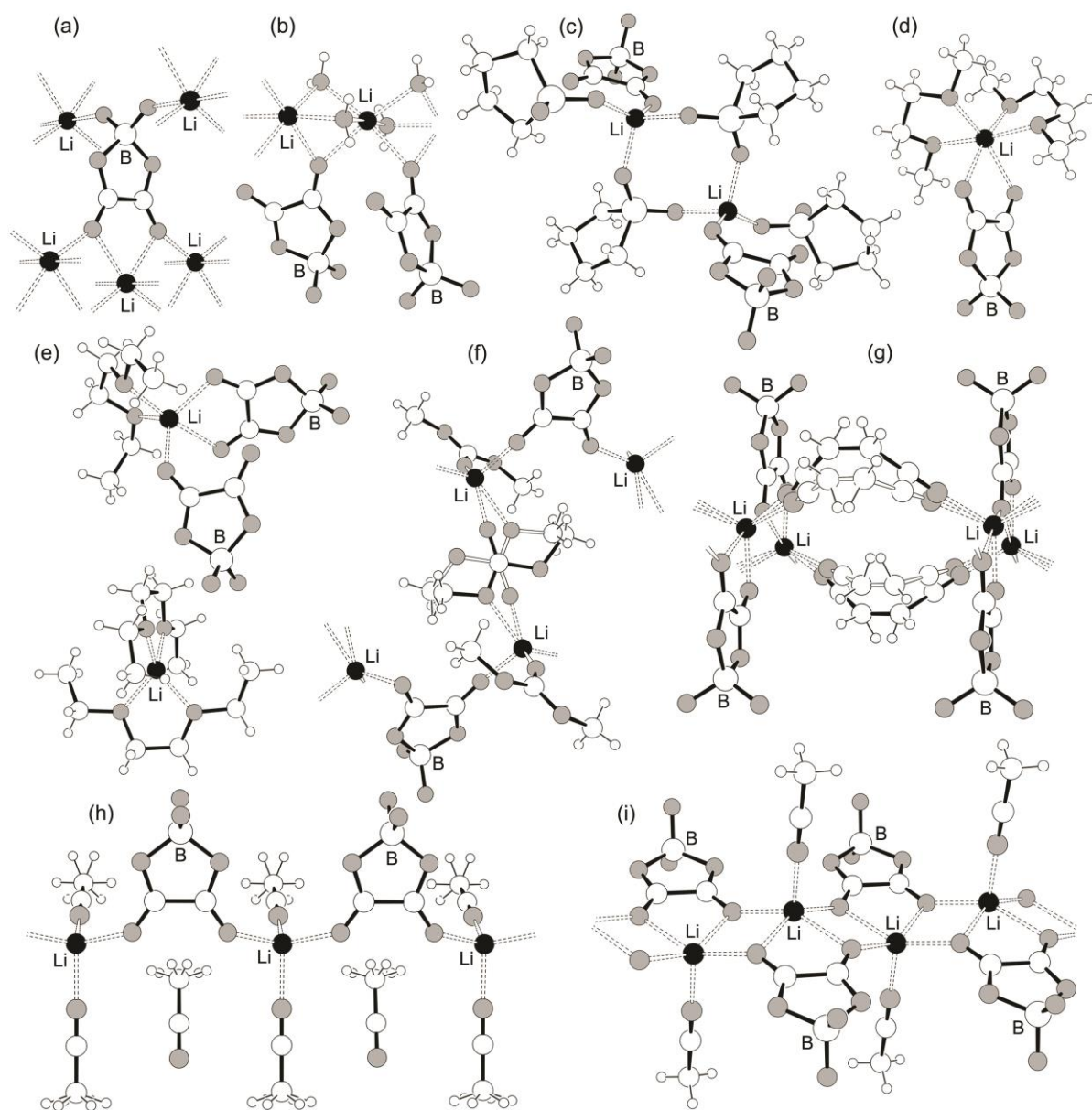


**Figure 4.4.** DFOB<sup>-</sup>...Li<sup>+</sup> cation coordination in crystalline LiDFOB and the crystalline solvates studied: (a) AGG-IIIb LiDFOB,<sup>9</sup> (b) AGG-Ic (H<sub>2</sub>O)<sub>1</sub>:LiDFOB,<sup>14</sup> (c) CIP-I (TMS)<sub>2</sub>:LiDFOB,<sup>9</sup> (d) CIP-II (G1)<sub>2</sub>:LiDFOB, (e) CIP-I/CIP-II (Et-G1)<sub>3/2</sub>:LiDFOB, (f) AGG-Ia (DMC)<sub>3/2</sub>:LiDFOB, (g) AGG-Ib (SN)<sub>1</sub>:LiDFOB, (h) AGG-Ia (AN)<sub>3</sub>:LiDFOB and (i) AGG-IIa (AN)<sub>1</sub>:LiDFOB.<sup>43</sup>

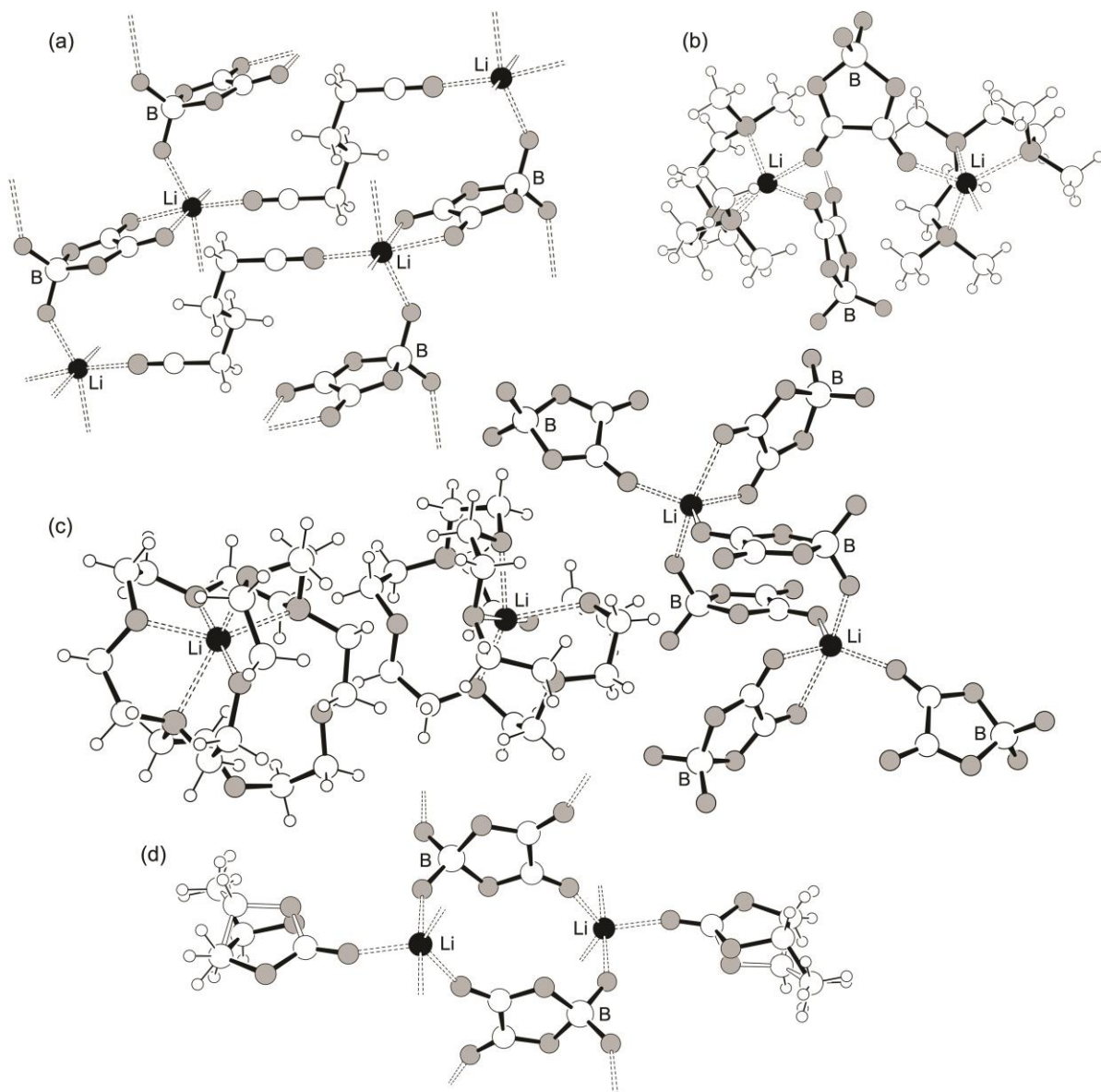


**Figure 4.5.** DFOB<sup>-</sup>...Li<sup>+</sup> cation coordination in the crystalline solvates studied: (a) AGG-IIb (ADN)<sub>1</sub>:LiDFOB, (b) AGG-Ia (PMDETA)<sub>1</sub>:LiDFOB, (c) CIP-I/CIP-II/AGG-Id (CRYPT-222)<sub>2/3</sub>:LiDFOB and (d) AGG-IIIa (PC)<sub>1</sub>:LiDFOB.<sup>43</sup>

structures, as found in seven of the structures: LiDFOB, (G1)<sub>2</sub>:LiDFOB, (Et-G1)<sub>3/2</sub>:LiDFOB,

(ADN)<sub>1</sub>:LiDFOB, (SN)<sub>1</sub>:LiDFOB, (AN)<sub>1</sub>:LiDFOB and (CRYPT-222)<sub>2/3</sub>:LiDFOB. Some anions such as bis(oxalatoborate) (BOB<sup>-</sup>),<sup>46</sup> dicyanotriazolate (DCTA<sup>-</sup> or TADC<sup>-</sup>)<sup>47</sup> and bis(trifluoromethanesulfonyl)imide (TFSI<sup>-</sup>)<sup>39</sup> may also have a tendency to form bidentate coordination, but other anions such as ClO<sub>4</sub><sup>-</sup>, BF<sub>4</sub><sup>-</sup> and PF<sub>6</sub><sup>-</sup> instead typically coordinate to Li<sup>+</sup> cation via monodentate coordination in crystalline solvate structures and in solution (the latter from MD simulations).<sup>38,39,52,56</sup> Only four of the structures have Li<sup>+</sup> cations coordination through fluorine atoms: LiDFOB, (ADN)<sub>1</sub>:LiDFOB, (CRYPT-222)<sub>2/3</sub>:LiDFOB and (PC)<sub>1</sub>:LiDFOB. The fluorine atom coordination in all of these solvates plays a role as a bridge to weld the structure together, which indicates that fluorine atom coordination to Li<sup>+</sup> cations is much less prevalent than the carbonyl oxygen atoms coordination.

#### 4.2.2. Raman Band Assignments

Fig. 4.6 shows the experimental Raman spectrum for the anhydrous LiDFOB crystalline salt (AGG-III).<sup>43</sup> Table 4.1 shows the DFT computed vibrational modes for the uncoordinated DFOB<sup>-</sup> anion to aid in the assignment of the peaks.<sup>43</sup> Note that differences are to be expected between the experimental vibrational band positions for the anions in the highly aggregated salt and the calculated vibrational band positions (from MD simulations) for the uncoordinated anion.

The two strong peaks found at about 1760 and 1800 cm<sup>-1</sup> in Fig. 4.6 correspond to the antisymmetric and symmetric C=O stretching vibrations, respectively (Table 4.1 and Fig. 4.7—the DFT calculations predict too high a frequency for these by ~100 cm<sup>-1</sup>).<sup>43</sup> As these

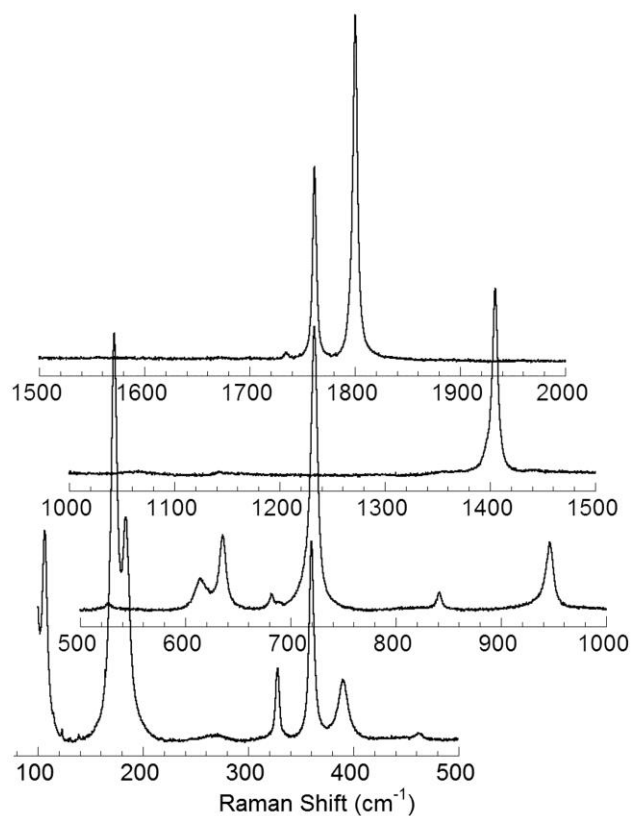


**Figure 4.6.** Raman spectrum of LiDFOB (at 20°C).<sup>43</sup>

two peaks are principally attributed to the anion carbonyl groups, these bands were expected to be excellent probes for the  $\text{DFOB}^- \dots \text{Li}^+$  cation interactions. Based upon a summary of the symmetric  $\text{C}=\text{O}$  stretching band positions for the crystalline solvates (Appendix B), however, the band positions for these  $\text{DFOB}^-$  anion carbonyl vibrational modes do not enable the facile discrimination of the different forms of anion coordination. It is noteworthy that the carbonyl bands for solvent... $\text{Li}^+$  cation interactions (i.e., with  $\gamma$ -butyrolactone and dimethyl carbonate) also often do not well reflect the coordination of the solvents to  $\text{Li}^+$  cations using

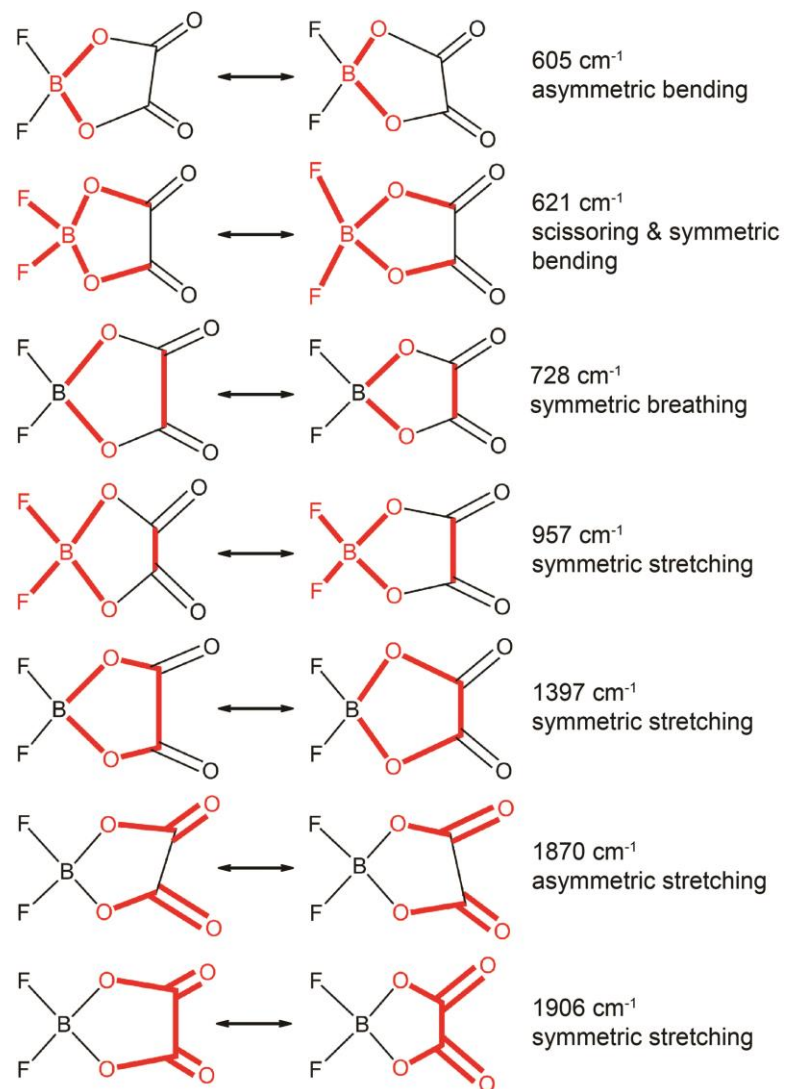


**Figure 4.7.** Principal bonds/angles contributing to the  $\text{DFOB}^-$  anion vibrational modes as determined from the DFT calculations.<sup>43</sup>

the carbonyl oxygen electron lone-pairs.<sup>57</sup>

The peak observed at  $1405 \text{ cm}^{-1}$  (Fig. 4.6) corresponds to the combination band of the C–C and symmetric C–O stretching modes (Table 4.1 and Fig. 4.7), while the peak near  $942$

**Table 4.1.** Calculated (uncoordinated DFOB<sup>-</sup> from M06-2X) vibration mode frequencies (cm<sup>-1</sup>), Raman (Å<sup>4</sup> amu<sup>-1</sup>) and IR (km mol<sup>-1</sup>) intensities and tentative assignments (no scaling) (freq<sub>expt</sub> refers to the LiDFOB salt—Figure 4.6)<sup>43</sup>

freq <sub>expt</sub>	Vacuum			SMD			tentative assignments
	freq	I <sub>Raman</sub>	I <sub>IR</sub>	freq	I <sub>Raman</sub>	I <sub>IR</sub>	
	81	1.61	2.10	82	2.55	2.53	B centered torsion
	114	0.72	0	110	1.09	0	torsion of O=C-C=O + ring + F-B-F
325	331	0.28	~0	328	0.38	~0	ring twisting + torsion of F-B-F
360	334	2.22	0.09	338	3.46	0.63	symm bend O=C-O in-plane + F-B-F bend out-of-phase
390	363	1.60	11.49	365	2.55	25.11	symm bend O=C-O in-plane + F-B-F bend in-phase
	373	0.05	7.34	371	0.06	15.52	∂(C-C) + π(F-B)
	468	0.12	19.63	467	0.42	33.07	π symm C-C
	522	0.30	25.05	517	0.44	40.49	∂(O=C-O)×2 + ρ rock B-F
615	605	2.24	14.92	608	3.15	19.20	∂(O-C-C)
635	621	2.33	0.68	619	3.85	1.00	B-F scissoring + O-B symm bend
680	690	0.44	2.78	695	0.96	2.95	ring rotation
723	728	9.55	7.41	739	15.53	9.95	ring breathing
840	856	0.53	~0	854	1.25	0.01	bend C-C (out of plane) + displacements of O
942	957	2.82	0.49	964	5.33	2.10	symm B-O stretch + C-C stretch + B-F stretch
	987	0.04	240.71	989	0.14	358.15	antisymm B-O stretch
	1119	0.30	785.88	1078	0.63	1288.27	symm B-F stretch
	1177	0.29	382.10	1113	0.47	534.47	antisymm B-F stretch
	1290	0.01	197.31	1278	0.18	264.56	in-plane C-C bending + antisymm C-O stretch
1405	1397	6.39	478.92	1386	7.61	677.46	symm C-O stretch + C-C stretch
1769	1870	13.75	172.05	1865	25.17	223.30	antisymm C=O stretch
1800	1906	19.19	713.11	1900	45.02	912.41	symm C=O stretch

cm<sup>-1</sup> (Fig. 4.6) is attributed to the combination of symmetric B-O, C-C and B-F stretching modes (Table 4.1 and Fig. 4.7). The very strong sole peak near 723 cm<sup>-1</sup> (Fig. 4.6)

corresponds to a ring breathing mode (Table 4.1 and Fig. 4.7), which is predicted to be the third strongest peak in the Raman spectra by the calculations. The two or more peaks observed at  $\sim 600\text{-}620\text{ cm}^{-1}$  (Fig. 4.6) are most likely due to a combination of different O–C–C bending modes and B-F scissoring from the other half of the  $\text{DFOB}^-$  anion (Table 4.1 and Fig. 4.7), which are difficult to use as probes for specific  $\text{DFOB}^- \dots \text{Li}^+$  cation interactions. Considering that boron isotopes have a natural abundance of 19.9%  $^{10}\text{B}$  and 80.1%  $^{11}\text{B}$ , it is noteworthy that vibrational modes which involve the displacement of the boron nucleus will give two different bands, which adds a further level of complexity to the band analysis for the  $\text{DFOB}^-$  anion.

#### 4.2.3. Raman Spectroscopic Analysis of Crystalline Solvates

Raman spectroscopic characterization was performed for the majority of the solvates with known crystal structures to determine the anion band position variation with varying  $\text{Li}^+$  cation coordination and temperature. The AGG-Ic  $(\text{H}_2\text{O})_1:\text{LiDFOB}$  solvate was not analyzed due to the hydrogen bond between the water molecules and anions (which is expected to perturb the vibrational bands). The analysis of the CIP-I/CIP-II/AGG-Id  $(\text{CRYPT-222})_{2/3}:\text{LiDFOB}$  solvate was also not done because of the low melting point (below ambient temperature) of the crystals and the fact that it was not possible to prepare the correct liquid composition (i.e., dissolve the appropriate amount of  $\text{LiDFOB}$  salt directly in the solvent). The anion bands near  $945$  and  $1405\text{ cm}^{-1}$  could not be used due to the significant overlap with the peaks from many common solvents. The bands in the  $600\text{-}650$ ,  $705\text{-}725$  and  $1780\text{-}$

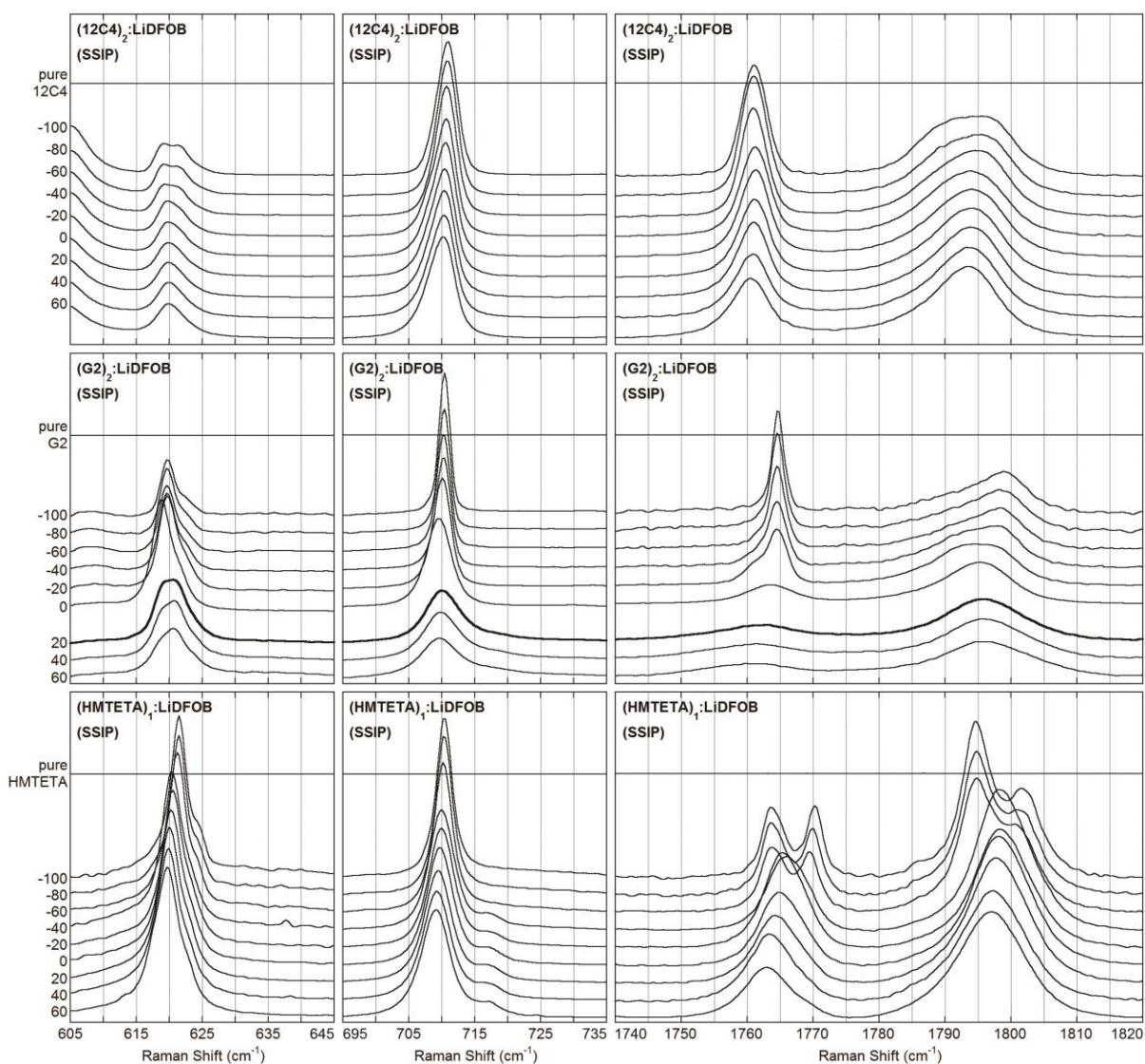


**Figure 4.8.** Raman spectra of the DFOB<sup>-</sup> anion vibrational band variation for the (speculative) SSIP crystalline solvates: (12C4)<sub>2</sub>:LiDFOB, (G2)<sub>2</sub>:LiDFOB and (HMTETA)<sub>1</sub>:LiDFOB (bold spectra indicate that the solvate has melted at this temperature).<sup>43</sup>

1820 cm<sup>-1</sup> region of the spectra did not generally overlap with solvents. Thus, these were analyzed in depth. Figs. 4.8 and 4.9 show the representative data for these regions. The

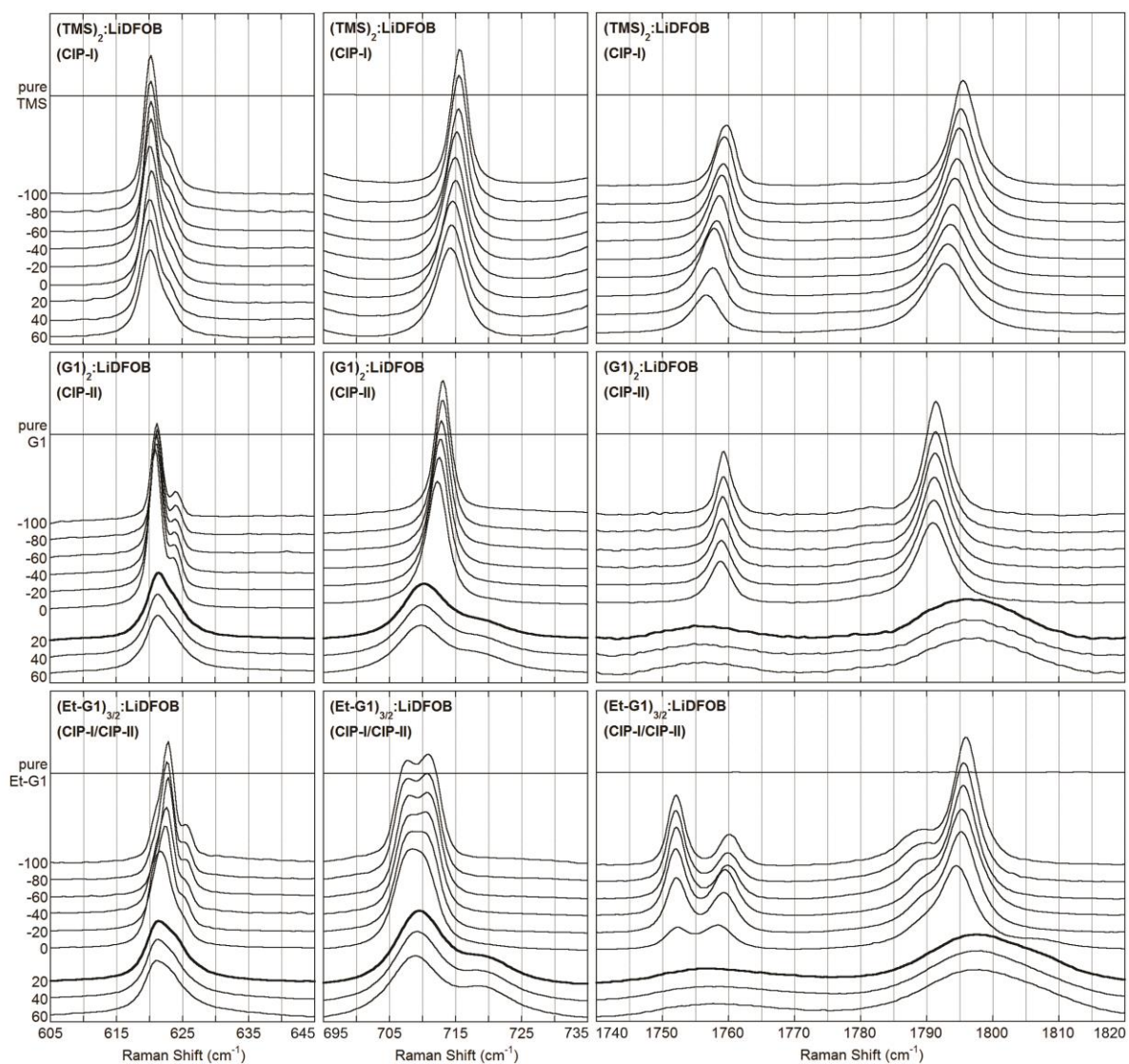


**Figure 4.9.** Raman spectra of the  $\text{DFOB}^-$  anion vibrational band variation for the CIP crystalline solvates:  $(\text{TMS})_2:\text{LiDFOB}$ ,  $(\text{G1})_2:\text{LiDFOB}$  and  $(\text{Et-G1})_{3/2}:\text{LiDFOB}$  (bold spectra indicate that the solvate has melted at this temperature).<sup>43</sup>

remaining sets of data are provided in Appendix B.<sup>43</sup> Fig. 4.10 shows a summary of the 705-725  $\text{cm}^{-1}$  results for the  $\text{DFOB}^-$  anion Raman vibrational band positions as a function of

temperature for the various crystalline LiDFOB solvates.<sup>43</sup>

No crystal structures are yet known for a SSIP solvate with LiDFOB, so the data in Fig 4.8 is for speculative SSIP solvates. The determination of the crystal structures for the (12C4)<sub>2</sub>:LiDFOB, (G2)<sub>2</sub>:LiDFOB and (HMTETA)<sub>1</sub>:LiDFOB solvates from single crystals was attempted, but these efforts were not successful due to the very energetic solid-solid phase transitions which occur for these solvates at low temperature and the presence of significant disorder within the solvate structures in the higher temperature phases.<sup>43</sup> No crystal structures for the solvates with HMTETA and LiX salts have been reported, but crystalline (12C4)<sub>2</sub>:LiX<sup>57-61</sup> and (G2)<sub>2</sub>:LiX<sup>52,62-65</sup> solvate phases are well known—all of them having uncoordinated anions (i.e., SSIP solvates). For all three speculative SSIP solvates, the band positioned near 710 cm<sup>-1</sup> remains relatively fixed over the entire temperature range (Figs. 4.8 and 4.10), whereas multiple bands are present near 620 cm<sup>-1</sup> which differ for the three solvates, as do the bands near 1760 and 1800 cm<sup>-1</sup> (Fig 4.8).

The spectra in Fig. 4.9 were obtained for the CIP solvates with known crystal structures, which show rather poor conformity in the band positions for all three regions. Note that both CIP-I and CIP-II anions have a very similar geometry based upon the bond lengths/angles comparison (Table 4.2).<sup>43</sup> There is a discrepancy, however, in the anion band positions for each region. For example, if the bands near 1760 and 1796 cm<sup>-1</sup> in the spectrum for the (Et-G1)<sub>3/2</sub>:LiDFOB solvate correspond to the CIP-I anion (rather than the CIP-II anion), then there is quite good agreement with the same bands in the (TMS)<sub>2</sub>:LiDFOB spectrum, but there is then poor agreement between the solvates for the bands near 620 cm<sup>-1</sup> and 710 cm<sup>-1</sup>

(Fig. 4.9). It is noteworthy that each of the anion bands originates from the combination of multiple vibrations: the symmetric C=O band near  $1800\text{ cm}^{-1}$  ( $1906\text{ cm}^{-1}$  from the calculations) also includes the C–O bonds (Fig. 4.7). It is not surprising, therefore, that the anion geometry variation results in widely different spectra.

The summary of the Raman band peak positions for the  $\text{DFOB}^-$  anion ring breathing vibrational mode near  $710\text{ cm}^{-1}$  shown in Fig. 4.10 indicates that it is quite challenging to accurately deconvolute the complex spectra for the  $\text{DFOB}^-$  anion in the liquid phase to

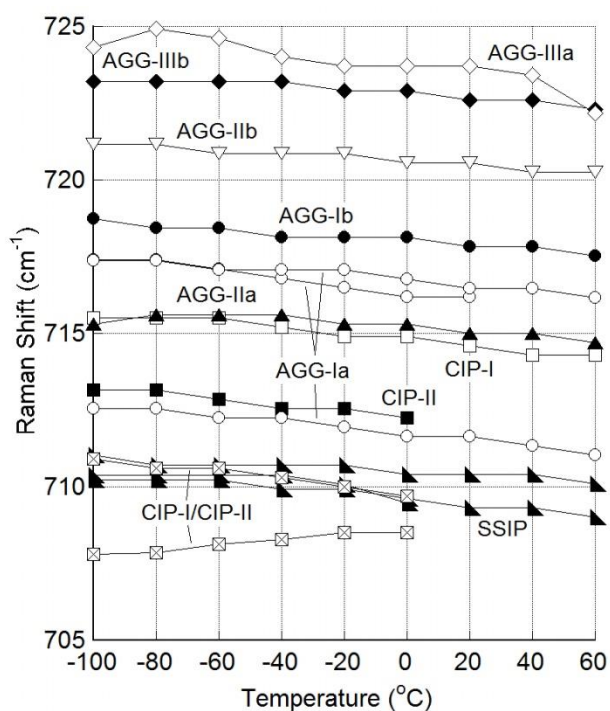


**Figure 4.10.** Summary of the Raman band peak position for the  $\text{DFOB}^-$  anion ring breathing vibrational band for various crystalline solvates (see Appendix B for the assignments of the data to specific solvates).<sup>43</sup>

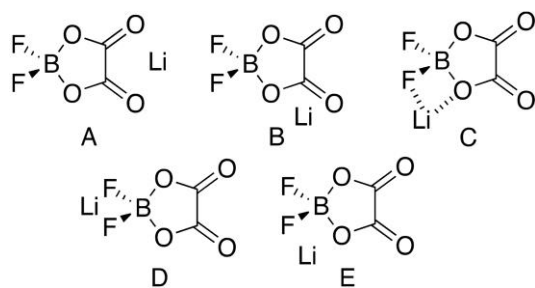


**Figure 4.11.** Stable ion pairs obtained for LiDFOB from the DFT calculations (while C and E look the same superficially, C has the  $\text{Li}^+$  cation in the FBO plane, while E has the cation in the oxalate plane).<sup>43</sup>

identify specific forms of anion coordination. This is attributed to both the numerous forms of  $\text{DFOB}^- \dots \text{Li}^+$  cation coordination and the various band positions for a given form of anion coordination. In particular, the latter point is true for the AGG solvates which have considerable variability in the anion geometry.<sup>43</sup> Relative to other regions of the spectra, however, the band positions in the  $710\text{-}725\text{ cm}^{-1}$  region can provide an indication of the relative fraction of SSIP, CIP, and AGG anion coordination (Fig. 4.10). For example, upon melting, remarkable changes in the spectra occur for both the  $(\text{G1})_2\text{:LiDFOB}$  and  $(\text{Et-G1})_{3/2}\text{:LiDFOB}$  solvates (Fig. 4.9). The similarity of the spectra when compared with that of the melted  $(\text{G2})_2\text{:LiDFOB}$  solvate (Fig. 4.8) indicate that the liquid from the melted crystalline CIP solvates may consist of a significant fraction of SSIP and CIP solvates with a lesser amount of AGG-I and perhaps AGG-II solvates. Considering the previous studies suggesting that melting of solvates often results in increased association (desolvation) of the solvate species rather than increased solvation (i.e., formation of SSIP solvates),<sup>38,39</sup> this is quite interesting.

For liquid electrolytes, other forms of  $\text{DFOB}^- \dots \text{Li}^+$  cation coordination than those found in the crystalline solvates (Fig. 4.2) are possible/plausible. Fig. 4.11 shows five distinct CIP forms of coordination as energy minima (A-E) obtained from DFT calculations.<sup>43</sup> Based upon the four different calculation methods shown in Table 4.3, only the  $\text{LiDFOB-A}$  ion pair was found to be strongly energetically favored.<sup>43</sup> As noted above, this type of bidentate coordination via the  $\text{DFOB}^-$  carbonyl oxygen atoms is readily found in many of the crystalline solvates. Both the computational and experimental results indicate, therefore, that there is a strong preference for this type of coordination.

### 4.3. $\text{PF}_6^-$ Anion Raman Vibrational Band Characterization

#### 4.3.1. Solvate Structures and $\text{Li}^+$ Cation Coordination

There are a number of previously reported  $\text{LiPF}_6$  solvate crystal structures, but most of these have rather exotic solvents/ligands.<sup>66-74</sup> There are exceptions, however, such as the  $\text{SSIP (EC)}_4:\text{LiPF}_6$  (Fig. 4.12b),<sup>75</sup>  $\text{SSIP (SN)}_2:\text{LiPF}_6$ <sup>76</sup> and  $\text{AGG-Ia (PMDETA)}_1:\text{LiPF}_6$  (Fig. 4.12d)<sup>77</sup> solvates. In addition, the crystal structure of  $\text{LiPF}_6$  is also known.<sup>78</sup> Recently several additional crystalline solvates have been reported including  $\text{SSIP (AN)}_6:\text{LiPF}_6$ ,<sup>79</sup>  $\text{SSIP (AN)}_5:\text{LiPF}_6$  (Fig. 4.12a),<sup>80</sup>  $\text{SSIP (GBL)}_4:\text{LiPF}_6$ <sup>81</sup> and  $\text{AGG-Ia (DMC)}_2:\text{LiPF}_6$  (Fig. 4.12c).<sup>81</sup> In the present study, the crystal structures of two new CIP-I  $(\text{G3})_1:\text{LiPF}_6$  and AGG-Ib  $(\text{DEC})_2:\text{LiPF}_6$  solvates are reported to complement these solvates.<sup>42</sup>

Fig. 4.13a shows the ion and solvent coordination within the CIP-I  $(\text{G3})_1:\text{LiPF}_6$  solvate.<sup>42</sup> The solvate has a similar crystal structure with other  $(\text{G3})_1:\text{LiX}$  solvates with  $\text{AsF}_6^-$ ,  $\text{ClO}_4^-$ ,

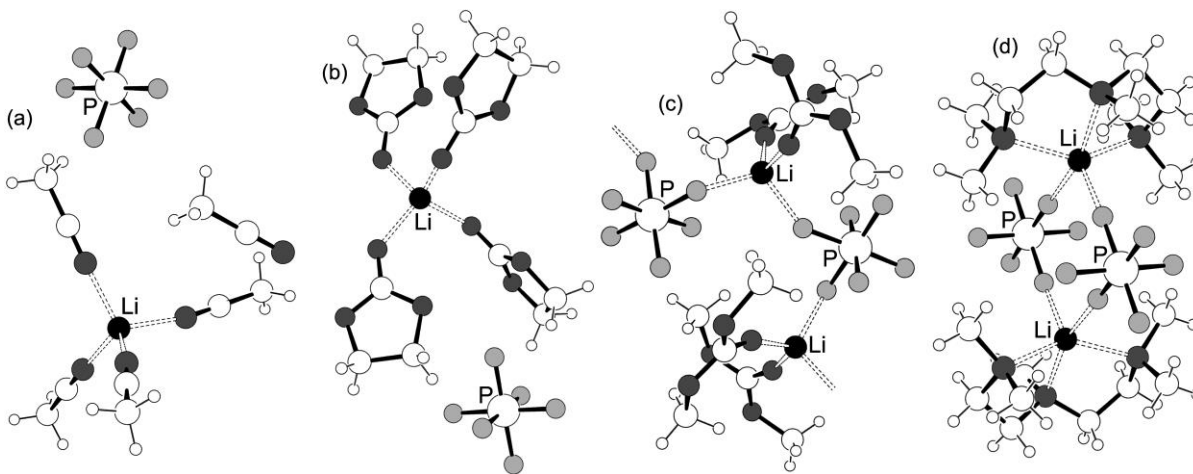


**Figure 4.12.**  $\text{PF}_6^- \dots \text{Li}^+$  cation coordination in the solvates which have been previously reported: (a) SSIP  $(\text{AN})_5:\text{LiPF}_6$ ,<sup>25</sup> (b) SSIP  $(\text{EC})_4:\text{LiPF}_6$ ,<sup>75</sup> (c) AGG-Ia  $(\text{DMC})_2:\text{LiPF}_6$ ,<sup>26</sup> and (d) AGG-Ia  $(\text{PMDETA})_1:\text{LiPF}_6$ .<sup>77,42</sup>

$\text{BF}_4^-$ ,  $\text{BH}_4^-$  and  $\text{CF}_3\text{SO}_3^-$  anions<sup>82,83</sup> in which the G3 molecules coordinate two separate  $\text{Li}^+$  cations, each with two ether oxygens. Each  $\text{Li}^+$  cation has five-fold coordination by two G3 molecules and a single  $\text{PF}_6^-$  anion with one fluorine atom (i.e., CIP-I). It is noteworthy that quantum chemical calculations for an isolated  $\text{Li}^+ \dots \text{PF}_6^-$  ion pair suggest that the order of increasing stability should be  $\text{CIP-III} > \text{CIP-II} > \text{CIP-I}$ ,<sup>84,85</sup> but this is not the case for the  $(\text{G3})_1:\text{LiPF}_6$  solvate due to steric crowding from the coordinated solvent molecules.<sup>43</sup> MD simulations for  $(\text{AN})_n\text{-LiPF}_6$  mixtures also indicate that CIP-I coordination (anions coordinated to a single  $\text{Li}^+$  cation) is predominant in electrolyte solutions.<sup>39,40,79</sup>

Fig. 4.13b shows the ion and solvent coordination within the AGG-Ib  $(\text{DEC})_2:\text{LiPF}_6$  solvate.<sup>42</sup> In this solvate, the  $\text{PF}_6^-$  anions are coordinated to two  $\text{Li}^+$  cations—one via a single fluorine atom and another using two fluorine atoms. Each  $\text{Li}^+$  cation has five-fold

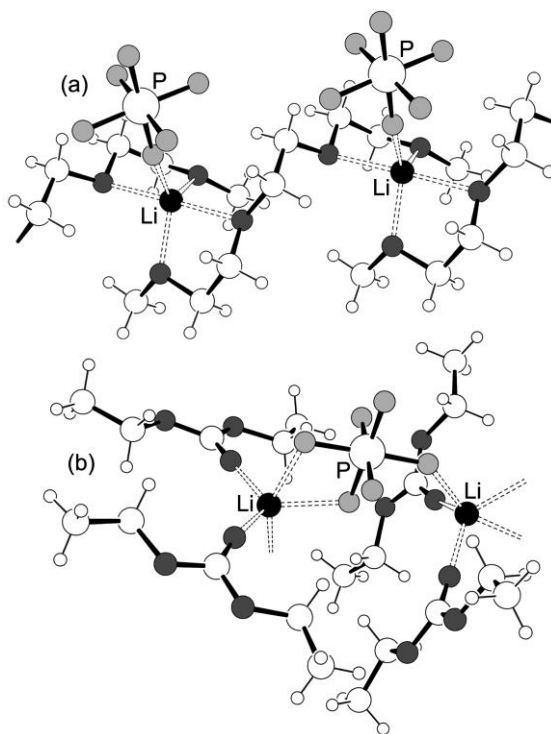


**Figure 4.13.**  $\text{PF}_6^- \dots \text{Li}^+$  cation coordination in the newly reported  $\text{LiPF}_6$  solvates: (a) CIP-I  $(\text{G3})_1:\text{LiPF}_6$  and (b) AGG-Ib  $(\text{DEC})_2:\text{LiPF}_6$ .<sup>42</sup>

coordination by two carbonyl oxygen atoms from two DEC molecules and three fluorine atoms from two  $\text{PF}_6^-$  anions. The structure of this solvate is different from the AGG-Ia  $(\text{DMC})_2:\text{LiPF}_6$  solvate structure (Fig. 4.12c) in which the  $\text{Li}^+$  cations have four-fold coordination by two carbonyl oxygen atoms from two DMC molecules and two fluorine atoms from two  $\text{PF}_6^-$  anions. The difference between the two solvates may be attributed to the differences in the overall polymeric chain structure which originates from the coordinated solvent molecules within the crystalline lattice for the two structures.<sup>42</sup>

### 4.3.2. Raman Spectroscopic Analysis of Crystalline Solvates

The uncoordinated  $\text{PF}_6^-$  anion has octahedral ( $O_h$ ) symmetry with the following vibrational modes<sup>84-86</sup>:

$$\Gamma = a_{1g} + e_g + t_{1g} + t_{2g} + 3t_{1u} + t_{2u}$$

The  $\nu_1(a_{1g})$ ,  $\nu_2(e_g)$  and  $\nu_5(t_{2g})$  modes are Raman active, and the  $\nu_3(t_{1u})$  and  $\nu_4(t_{1u})$  modes are IR active, but the  $t_{1g}$  and  $t_{2u}$  modes are inactive for both Raman and IR.<sup>84-86</sup> For the Raman spectrum of pure  $\text{LiPF}_6$ , the  $\nu_1$  vibration near  $770\text{ cm}^{-1}$  corresponding to the P–F symmetric stretching mode is the most prominent, whereas the  $\nu_2$  and  $\nu_5$  modes at  $570$  and  $473\text{ cm}^{-1}$  are relatively much weaker as shown in Fig. 4.14.<sup>42</sup>

Raman spectra were obtained for both crystalline solvates and neat  $\text{LiPF}_6$  as a function of

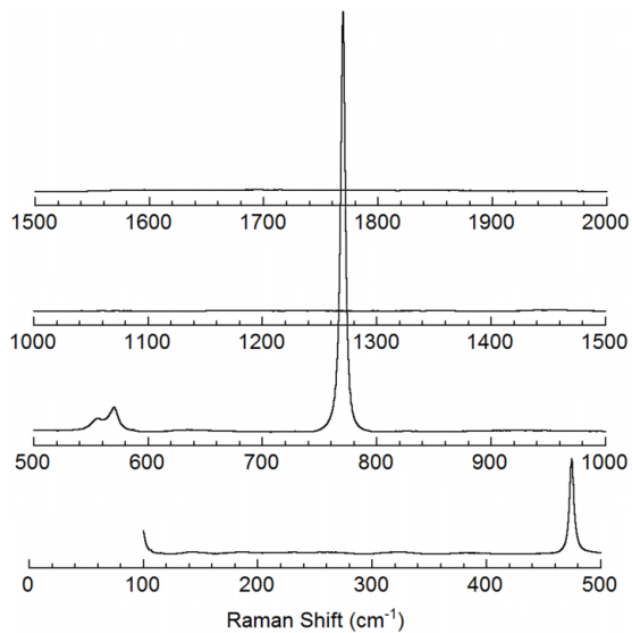
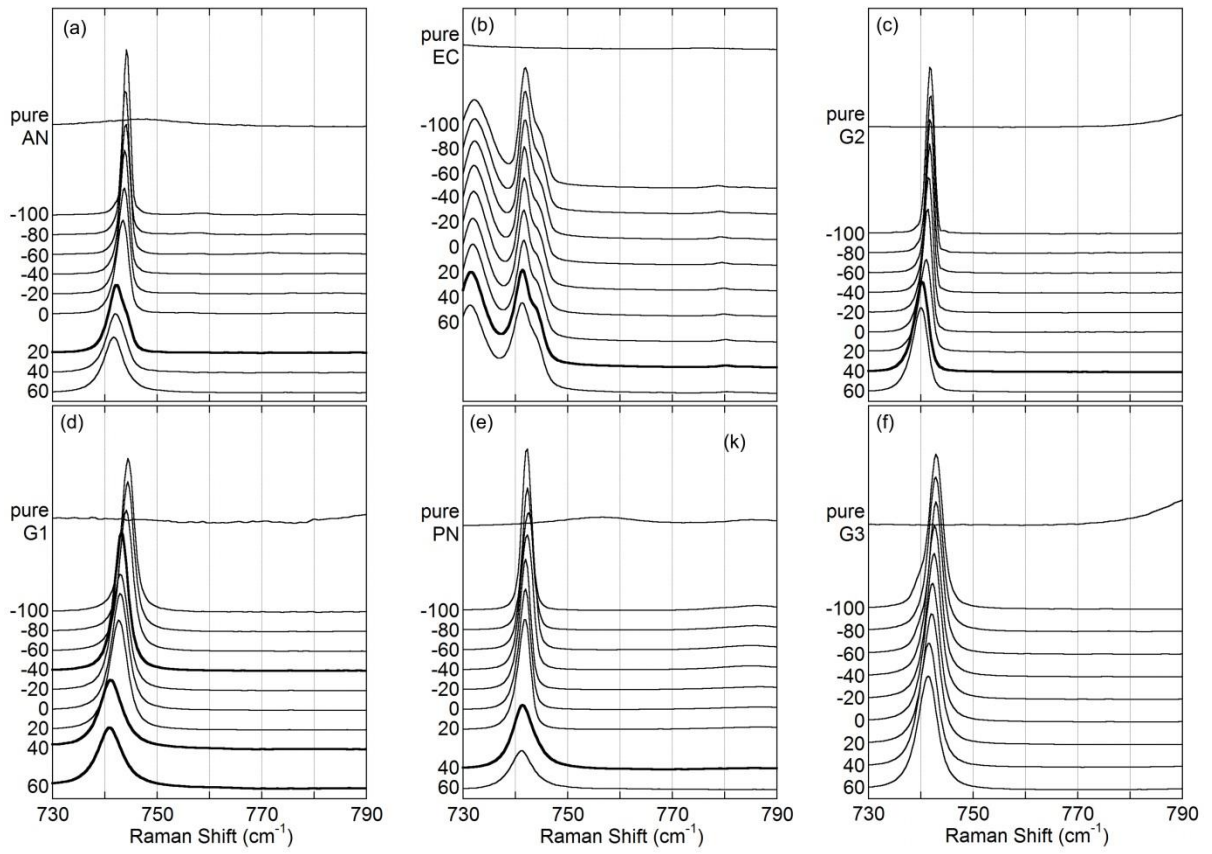


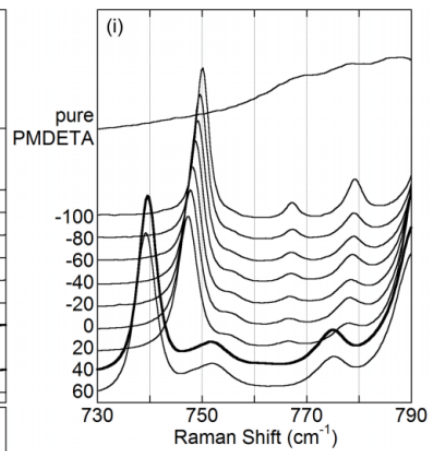
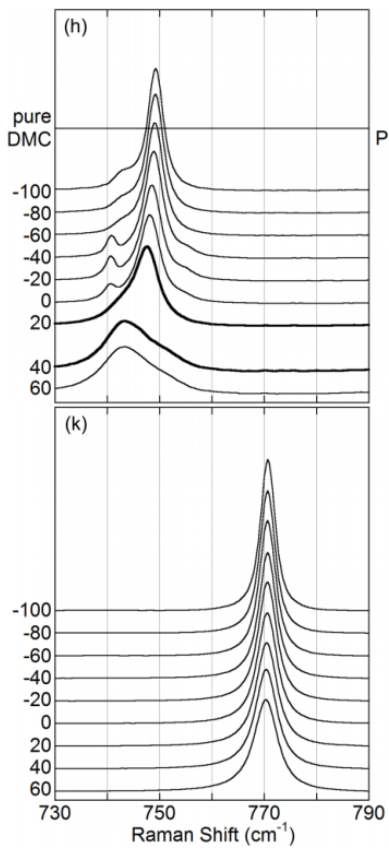
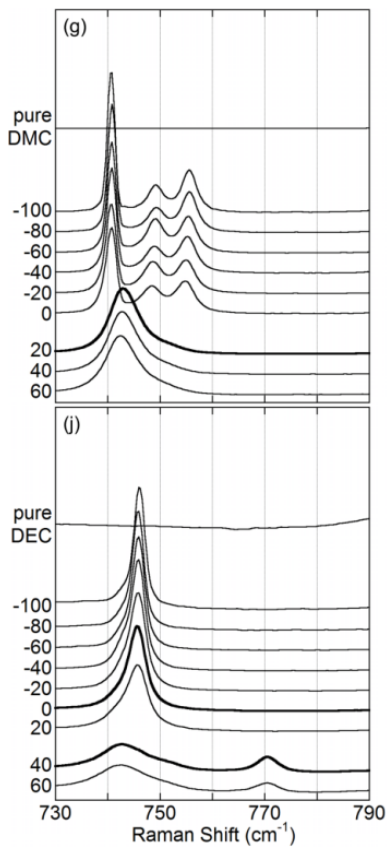
**Figure 4.14.** Raman spectrum of  $\text{LiPF}_6$  (at  $20^\circ\text{C}$ ).<sup>42</sup>

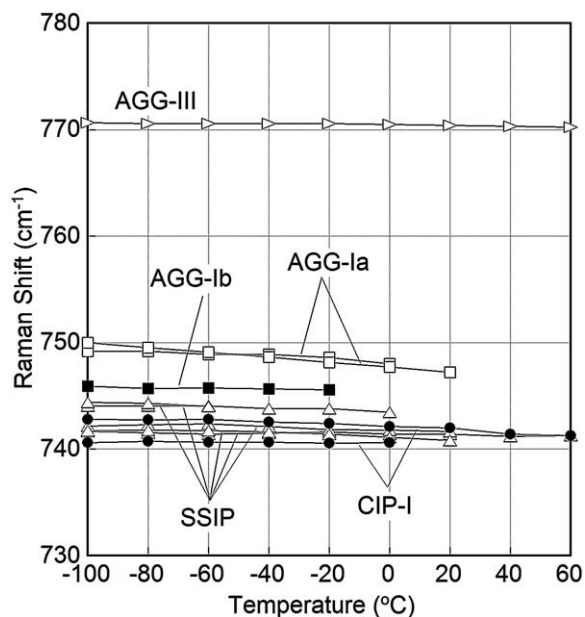
temperature to identify the variation of the anion band position for specific forms of  $\text{PF}_6^- \dots \text{Li}^+$  cation coordination. Fig. 4.15 shows the Raman data for the  $\nu_1$  vibration.<sup>42</sup> In addition to the known solvates, data were also collected for the solvates with reasonably predictable structures, such as the  $(\text{PN})_4:\text{LiPF}_6$ ,  $(\text{G2})_2:\text{LiPF}_6$ ,  $(\text{G1})_3:\text{LiPF}_6$  and  $(\text{DMC})_3:\text{LiPF}_6$  solvates. The  $(\text{PN})_4:\text{LiPF}_6$  solvate may have SSIP coordination with the four solvent nitrile groups fully coordinating the  $\text{Li}^+$  cations, similar to the crystal structures of  $(\text{AN})_4:\text{LiClO}_4$ ,<sup>87</sup>  $(\text{AN})_5:\text{LiPF}_6$ <sup>80</sup> and  $(\text{AN})_6:\text{LiPF}_6$  solvates.<sup>79</sup> Both the  $(\text{G2})_2:\text{LiPF}_6$  and  $(\text{G1})_3:\text{LiPF}_6$  crystalline solvates are also assumed to have SSIP coordination (fully solvated  $\text{Li}^+$  cations and uncoordinated anions) as is found for a large number of known  $(\text{G2})_2:\text{LiX}$  and  $(\text{G1})_3:\text{LiX}$  crystalline solvate structures.<sup>79,88</sup> The known  $(\text{DMC})_2:\text{LiPF}_6$  solvate has AGG-Ia coordination, in which the anions are coordinated to two  $\text{Li}^+$  cations.<sup>81</sup> In the case of the  $(\text{DMC})_3:\text{LiPF}_6$  solvate, if the  $\text{Li}^+$  cations have 4-fold coordination as is found for most of the known solvates with monodentate coordinating solvents,<sup>79</sup> CIP-I anion coordination is most probable in which the  $\text{Li}^+$  cations are coordinated to the three solvent carbonyl oxygen atoms and a single  $\text{PF}_6^-$  anion.<sup>42</sup>

Fig. 4.16 shows the summary of the anion  $\nu_1$  Raman band positions for the varying  $\text{PF}_6^- \dots \text{Li}^+$  cation coordination modes as a function of temperature.<sup>42</sup> There are two noteworthy points drawn from this summary. First, the  $\text{PF}_6^-$  Raman band found near  $747 \text{ cm}^{-1}$  at  $20 \text{ }^\circ\text{C}$  (empty square symbol) does not correspond to CIP solvates. Instead, this band is attributed to AGG-Ia anion coordination in which the anions are coordinated to two  $\text{Li}^+$  cations via two anion fluorine atoms (with the AGG-Ib coordination resulting in a band at

**Figure 4.15.** Raman spectra vs. temperature ( $^{\circ}\text{C}$  - shown on the left) of the  $\text{PF}_6^-$  anion vibrational bands for the crystalline solvates: (a) SSIP  $(\text{AN})_5:\text{LiPF}_6$ , (b) SSIP  $(\text{EC})_4:\text{LiPF}_6$ , (c) (speculative SSIP)  $(\text{G2})_2:\text{LiPF}_6$ , (d) (speculative SSIP)  $(\text{G1})_3:\text{LiPF}_6$ , (e) (speculative SSIP)  $(\text{PN})_4:\text{LiPF}_6$ , (f) CIP-I  $(\text{G3})_1:\text{LiPF}_6$ , (g) (speculative CIP-I)  $(\text{DMC})_3:\text{LiPF}_6$ , (h) AGG-Ia  $(\text{DMC})_2:\text{LiPF}_6$ , (i) AGG-Ia  $(\text{PMDETA})_1:\text{LiPF}_6$ , (j) AGG-Ib  $(\text{DEC})_2:\text{LiPF}_6$  and (k) AGG-III  $\text{LiPF}_6$  (the dark lines indicate that a phase transition has occurred—e.g., melting).<sup>42</sup>







**Figure 4.16.** Summary of the  $\text{PF}_6^-$  anion Raman band peak positions for the different crystalline solvates (each line is for a separate solvate).<sup>42</sup>

even lower wavenumber—black square symbols). Second, the band corresponding to CIP-I coordination—black circle symbols (i.e., anion coordinated to a single  $\text{Li}^+$  cation via a single fluorine atom) overlaps with those corresponding to SSIP coordination—empty circle symbols (i.e., uncoordinated anions). It is challenging, therefore, to distinguish between the SSIP and CIP-I forms of  $\text{PF}_6^- \dots \text{Li}^+$  cation coordination using Raman spectroscopic analysis. This can provide the explanation, in part, for the limited and misunderstood Raman spectroscopic studies for  $\text{LiPF}_6$ -based electrolytes—i.e., no peak splitting for the anion band was observed, so it has generally been assumed that the  $\text{Li}^+$  cations and  $\text{PF}_6^-$  anions are fully dissociated, which is not the case found for the MD simulation results of  $(\text{AN})_n\text{-LiPF}_6$  mixtures<sup>40</sup> and FTIR spectroscopic data indicated that some ion pairing occurs in  $\text{LiPF}_6$ -

based electrolytes.<sup>89</sup> The results shown in Fig. 4.16, therefore, may be used as a tool for the ionic association characterization of electrolytes with  $\text{LiPF}_6$ , but it is noteworthy that there are limitations to the information regarding the ionic association interactions within an electrolyte directly obtained from the Raman spectroscopic analysis.<sup>42</sup>

#### 4.4. Conclusions

Numerous crystal structures of known and newly determined  $\text{LiDFOB}$  or  $\text{LiPF}_6$  crystalline solvates are reported to provide significant insight into the manner in which the  $\text{DFOB}^-$  or  $\text{PF}_6^-$  anions coordinate  $\text{Li}^+$  cations. Utilizing Raman spectroscopic analyses, these solvates have been extensively characterized to provide unambiguous assignments for the anion Raman bands associated with specific  $\text{DFOB}^-$  or  $\text{PF}_6^- \dots \text{Li}^+$  cation coordination modes. DFT calculations complement this work by identifying the origin (vibrational modes) of the  $\text{DFOB}^-$  anion vibrational bands. This information serves as one of the important tools necessary for evaluating the ionic association interactions within electrolytes containing aprotic solvents and the  $\text{LiDFOB}$  or  $\text{LiPF}_6$  salts, which are further characterized in the next several chapters.

## 4.5. References

1. H. Zhou, F. Liu, and J. Li, *Appl. Mech. Mater.*, **152-154**, 1106 (2012).
2. C. Yang, Y. Ren, B. Wu, and F. Wu, *Adv. Mater. Res.*, **455-456**, 258 (2012).
3. V. Aravindan and P. Vickaman, *Ind. J. Phys.*, **86**, 341 (2012).
4. M. Hu, J. Wei, L. Xing, and Z. Zhou, *J. Appl. Electrochem.*, **42**, 291 (2012).
5. S. Dalavi, P. Guduru, and B. L. Lucht, *J. Electrochem. Soc.*, **159**, A642 (2012).
6. X. Wu, Z. Wang, X. Li, H. Guo, Y. Zhang, and W. Xiao, *J. Power Sources*, **204**, 133 (2012).
7. V. Aravindan, J. Gnanaraj, S. Madhavi, and H.-K. Liu, *Chem. Eur. J.*, **17**, 14326 (2011).
8. S. Li, X. Xu, X. Shi, and X. Cui, *Adv. Mater. Res.*, **197-198**, 1121 (2011).
9. J. L. Allen, S.-D. Han, P. D. Boyle, and W. A. Henderson, *J. Power Sources*, **196**, 9737 (2011).
10. S. Zugmann, M. Fleischmann, M. Amereller, R. M. Gschwind, M. Winter, and H. J. Gores, *J. Chem. Eng. Data*, **56**, 4786 (2011).
11. S. Zugmann, M. Fleischmann, M. Amereller, R. M. Gschwind, H. D. Wiemhöfer, and H. J. Gores, *Electrochim. Acta*, **56**, 3926 (2011).
12. L. Zhou, W. Li, M. Xu, and B. Lucht, *Electrochem. Solid-State Lett.*, **14**, A161 (2011).
13. S. Zugmann, D. Moosbauer, M. Amereller, C. Schreiner, F. Wudy, R. Schmitz, R. Schmitz, P. Isken, C. Dippel, R. Müller, M. Kunze, A. Lex-Balducci, M. Winter, and H. J. Gores, *J. Power Sources*, **196**, 1417 (2011).

14. J. L. Allen, P. D. Boyle, and W. A. Henderson, *Acta Crystallogr.*, **E67**, m533 (2011).
15. K. Amine, Z. Chen, Z. Zhang, J. Liu, W. Lu, Y. Qin, J. Lu, L. Curtis, and Y.-K. Sun, *J. Mater. Chem.*, **21**, 17754 (2011).
16. M. Xu, L. Zhou, L. Hao, L. Xing, W. Li, and B. L. Lucht, *J. Power Sources*, **196**, 6794 (2011).
17. L. Yang, T. Markmaitree, and B. L. Lucht, *J. Power Sources*, **196**, 2251 (2011).
18. E. Zygadło-Monikowska, Z. Florjańczyk, P. Kubisa, T. Biedroń, A. Tomaszewska, J. Ostrowska, and N. Langwald, *J. Power Sources*, **195**, 6202 (2010).
19. Z. Zhang, X. Chen, F. Li, Y. Lai, J. Li, J. Liu, and X. Wang, *J. Power Sources*, **195**, 7397 (2010).
20. M. H. Fu, K. L. Huang, S. Q. Liu, J. S. Liu, and Y. K. Li, *J. Power Sources*, **195**, 862 (2010).
21. J. Li, K. Xie, Y. Lai, Z. Zhang, F. Li, X. Hao, X. Chen, and Y. Liu, *J. Power Sources*, **195**, 5344 (2010).
22. D. Moosbauer, S. Zugmann, M. Amereller, and H. J. Gores, *J. Chem. Eng. Data*, **55**, 1794 (2010).
23. J. Huang, L.-Z. Fan, B. Yu, T. Xing, and W. Qiu, *Ionics*, **16**, 509 (2010).
24. V. Aravindan, P. Vickraman, and K. Krishnaraj, *Curr. Appl Phys.*, **9**, 1474 (2009).
25. M. Amereller, M. Multerer, C. Schreiner, J. Lodermeier, A. Schmid, J. Barthel, and H. J. Gores, *J. Chem. Eng. Data*, **54**, 468 (2009).

26. A. Xiao, L. Yang, B. L. Lucht, S.-H. Kang, and D. P. Abraham, *J. Electrochem. Soc.*, **156**, A318 (2009).
27. Z. Chen, Y. Qin, J. Liu, and K. Amine, *Electrochem. Solid-State Lett.*, **12**, A69 (2009).
28. H.-Q. Gao, Z.-A. Zhang, Y.-Q. Lai, J. Li, and Y.-X. Liu, *J. Cent. South Univ. Technol.*, **15**, 830 (2008).
29. V. Aravindan, P. Vickraman, and K. Krishnaraj, *Polym. Int.*, **57**, 932 (2008).
30. S.-H. Kang, D. P. Abraham, A. Xiao, and B. L. Lucht, *J. Power Sources*, **175**, 526 (2008).
31. D. P. Abraham, M. M. Furczon, S.-H. Kang, D. W. Dees, and A. N. Jansen, *J. Power Sources*, **180**, 612 (2008).
32. Z. Chen, J. Liu, and K. Amine, *Electrochem. Solid-State Lett.*, **10**, A45 (2007).
33. S. S. Zhang, *J. Power Sources*, **163**, 713 (2007).
34. V. Aravindan and P. Vickraman, *Solid State Sci.*, **9**, 1069 (2007).
35. J. Liu, Z. Chen, S. Busking, and K. Amine, *Electrochem. Commun.*, **9**, 475 (2007).
36. J. Liu, Z. Chen, S. Busking, I. Belharouak, and K. Amine, *J. Power Sources*, **174**, 852 (2007).
37. S. S. Zhang, *J. Power Sources*, **162**, 1379 (2006).
38. D. M. Seo, O. Borodin, S.-D. Han, Q. Ly, P. D. Boyle, and W. A. Henderson, *J. Electrochem. Soc.*, **159**, A553 (2012).
39. D. M. Seo, O. Borodin, S.-D. Han, P. D. Boyle, and W. A. Henderson, *J. Electrochem. Soc.*, **159**, A1489 (2012).

40. D. M. Seo, O. Borodin, D. Balogh, M. O'Connell, Q. Ly, S.-D. Han, S. Passerini, and W. A. Henderson, *J. Electrochem. Soc.*, **160**, A1061 (2013).
41. S.-D. Han, O. Borodin, J. L. Allen, D. M. Seo, D. W. McOwen, and W. A. Henderson, *J. Electrochem. Soc.*, in-press (2013).
42. S.-D. Han, S.-H. Yun, D. M. Seo, O. Borodin, R. D. Sommer, V. G. Young Jr., and W. A. Henderson, In-prepartaion (2013).
43. S.-D. Han, J. L. Allen, E. Jónsson, P. Johansson, D. W. McOwen, P. D. Boyle, and W. A. Henderson, *J. Phys. Chem. C*, **117**, 5521 (2013).
44. W. Huang, R. Frech, and R. A. Wheeler, *J. Phys. Chem.*, **98**, 100 (1994).
45. S. P. Gejji, C. H. Suresh, K. Babu, and S. R. Gadre, *J. Phys. Chem. A*, **103**, 7474 (1999).
46. R. Holomb, W. Xu, H. Markusson, P. Johansson, and P. Jacobsson, *J. Phys. Chem. C*, **110**, 11467 (2006).
47. J. Scheers, L. Niedzicki, G. Z. Zukowska, P. Johansson, W. Wieczorek, and P. Jacobsson, *Phys. Chem. Chem. Phys.*, **13**, 11136 (2011).
48. P. Johansson, S. Béranger, M. Armand, H. Nilsson, and P. Jacobsson, *Solid State Ionics*, **156**, 129 (2003).
49. J. Grondin, D. Talaga, J.-C. Lassègues, and W. A. Henderson, *Phys. Chem. Chem. Phys.*, **6**, 938 (2004).
50. J. Grondin, J.-C. Lassègues, M. Chami, L. Servant, D. Talaga, and W. A. Henderson, *Phys. Chem. Chem. Phys.*, **6**, 4260 (2004).

51. W. A. Henderson and N. R. Brooks, *Inorg. Chem.*, **42**, 4522 (2003).
52. W. A. Henderson, N. R. Brooks, W. W. Brennessel, and V. G. Young Jr., *J. Phys. Chem. A*, **108**, 225 (2004).
53. W. A. Henderson, N. R. Brooks, W. W. Brennessel, and V. G. Young Jr., *Chem. Mater.*, **15**, 4679 (2003).
54. W. A. Henderson, N. R. Brooks, and V. G. Young Jr., *Chem. Mater.*, **15**, 4685 (2003).
55. D. M. Seo, P. D. Boyle, J. L. Allen, S.-D. Han, E. Jónsson, P. Johansson, and W. A. Henderson, *J. Phys. Chem. C.*, in-press (2013).
56. Y. G. Andreev, V. Seneviratne, M. Khan, W. A. Henderson, R. E. Frech, and P. G. Bruce, *Chem. Mater.*, **17**, 767 (2005).
57. R. E. A. Dillon, C. L. Stern, and D. F. Shriver, *Solid State Ionics*, **133**, 247 (2000).
58. R. A. Lewis, G. Wu, and T. W. Hayton, *Inorg. Chem.*, **50**, 4660 (2011).
59. H. Hope, M. M. Olmstead, P. P. Power, and X. Xu, *J. Am. Chem. Soc.*, **106**, 819 (1984).
60. J. C. Gallucci, M. R. Sivik, L. A. Paquette, F. Zaegel, P. Meunier, and B. Gautheron, *Acta Crystallogr.*, **C52**, 1673 (1996).
61. S. T. Liddle and W. Clegg, *Polyhedron*, **22**, 3507 (2003).
62. M. W. Esterhuysen and H. G. Raubenheimer, *Eur. J. Inorg. Chem.*, **2003**, 3861 (2003).
63. J. Pauls, E. Iravani, P. Köhl, and B. Neumüller, *Z. Anorg. Allg. Chem.*, **630**, 876 (2004).
64. V. Seneviratne, R. Frech, J. E. Furneaux, and M. Khan, *J. Phys. Chem. B*, **108**, 8124 (2004).

65. W. Palitzsch, U. Böhme, C. Beyer, and G. Roewer, *Organometallics*, **17**, 2965 (1998).
66. R. Schwesinger, K. Piontek, W. Littke, and H. Prinzbach, *Tetrahedron Lett.*, **26**, 1201 (1985).
67. E. C. Constable, L.-Y. Chung, J. Lewis, and P. R. Raithby, *J. Chem. Soc., Chem. Commun.*, **1986**, 1719 (1986).
68. E. C. Constable, M. J. Doyle, J. Healy, and P. R. Raithby, *J. Chem. Soc., Chem. Commun.*, **1988**, 1262 (1988).
69. C. G. Choo, S. D. Rychnovsky, and M. C. Etter, *Chem. Mater.*, **6**, 1200 (1994).
70. Z. Gadjourova, D. M. Marero, K. H. Andersen, Y. G. Andreev, and P. G. Bruce, *Chem. Mater.*, **13**, 1282 (2001).
71. F. A. Cotton, C. A. Murillo, and H.-C. Zhou, *Inorg. Chem.*, **39**, 1039 (2000).
72. G. L. Abbati, A. Cornia, A. C. Fabretti, W. Malavasi, L. Schenetti, A. Caneschi, and D. Gatteschi, *Inorg. Chem.*, **36**, 6443 (1997).
73. P. G. Bekiarian, M. Doyle, W. B. Farnham, A. E. Feiring, P. A. Morken, M. G. Roelofs, and W. J. Marshall, *J. Fluor. Chem.*, **125**, 1187 (2004).
74. R. R. Buchholz, M. E. Etienne, A. Dorgelo, R. E. Mirams, S. J. Smith, S. Y. Chow, L. R. Hanton, G. B. Jameson, G. Schenk, and L. R. Gahan, *Dalton Trans.*, **43**, 6045 (2008).
75. P. Y. Zavalij, S. Yang, and M. S. Whittingham, *Acta Crystallogr.*, **B60**, 716 (2004).
76. P. S. Whitfield, A. Abouimrane, and I. J. Davidson, *Proc. 55th Int. Conf. Appl. X-ray Anal.* (2007).

77. D. R. Armstrong, A. H. Khandelwal, L. C. Kerr, S. Peasey, P. R. Raithby, G. P. Shields, R. Snaith, and D. S. Wright, *Chem. Commun.*, **1998**, 1011 (1998).
78. C. Röhr and R. Kniep, *Z. Naturforsch.*, **49b**, 650 (1994).
79. D. M. Seo, P. D. Boyle, O. Borodin, and W. A. Henderson, *RSC Adv.*, **2**, 8014 (2012).
80. D. M. Seo, P. D. Boyle, and W. A. Henderson, *Acta Crystallogr.*, **E67**, m1148 (2011).
81. Cambridge Crystallographic Data Centre: CCDC 875137 (GBL)<sub>4</sub>:LiPF<sub>6</sub> and 875817 (DMC)<sub>2</sub>:LiPF<sub>6</sub>.
82. W. A. Henderson, N. R. Brooks, W. W. Brennessel, and V. G. Young Jr., *Chem. Mater.*, **15**, 4679 (2003).
83. H.-H. Giese, H. Nöth, H. Schwenk, and S. Thomas, *Eur. J. Inorg. Chem.*, **1998**, 941 (1998).
84. R. Aroca, M. Nazri, G. A. Nazri, A. J. Camargo, and M. Trsic, *J. Soln. Chem.*, **29**, 1047 (2000).
85. X. Xuan, J. Wang, and H. Wang, *Electrochim. Acta*, **50**, 4196 (2005).
86. L. D. Kock, M. D. S. Lekgoathi, P. L. Crouse, and B. M. Vilakazi, *J. Mol. Struct.*, **1026**, 145 (2012).
87. Y. Yokota, V. G. Young Jr., and J. G. Verkade, *Acta Crystallogr.*, **C55**, 196 (1999).
88. W. A. Henderson, *J. Phys. Chem. B*, **110**, 13177 (2006).
89. C. M. Burba and R. Frech, *J. Phys. Chem. B*, **109**, 15161 (2005).

## Electrolyte Solvation and Ionic Association I. Acetonitrile-Lithium Salt Mixtures

---

Solution structure is the critical factor to influence electrolyte properties, but little is known about the ion solvate structures present in liquids. This topic is scrutinized here in detail utilizing acetonitrile (AN) as a model solvent. Using a combination of methods including thermal phase diagrams (from DSC data), XRD solvate structure determination (single crystal x-ray diffraction) and Raman vibrational spectroscopic analysis, the degree of solvation and ionic association have been determined for a wide variety of electrolyte mixtures with acetonitrile (AN) and conventional lithium salts ( $\text{LiPF}_6$ ,  $\text{LiTFSI}$ ,  $\text{LiClO}_4$ ,  $\text{LiBF}_4$ ,  $\text{LiCF}_3\text{SO}_3$  and  $\text{LiCF}_3\text{CO}_2$ ). Once the solution structure was well understood, the transport properties (viscosity and ionic conductivity) of the electrolyte mixtures were correlated with the structural information to obtain insight into the origin of the transport property variations for the different electrolytes. MD simulations for the  $(\text{AN})_n\text{-LiX}$  mixtures have been performed to obtain additional the insight into the solution structure and to explore the limitations of the experimental work and simulations for electrolyte characterization.

## 5.1. Introduction

For electrolyte development for Li-ion batteries, it is critical to understand how solvation is influenced by ion/solvent structure, temperature and salt concentration and how this, in turn, governs electrolyte physicochemical/transport properties and electrochemical device performance. Various types of solvated ionic species may exist in an electrolyte, which determine not only the bulk behavior (e.g., ionic conductivity, viscosity, volatility, etc.) of the electrolyte mixtures, but also the interfacial interactions of the electrolyte with electrodes. However, significant challenges still exist in the study of the structure of liquid phases. Through the combination of phase diagrams, crystalline solvate structures, solvation/ionic association information obtained from spectroscopic characterization and molecular dynamic simulations, much may be learned about solution structure, as demonstrated here. In a previous study for (glyme)<sub>n</sub>-lithium salt mixtures, the phase behavior and crystalline solvates that formed in relatively dilute mixtures suggested the following order for increasing ionic association (ionic interactions between the anions and Li<sup>+</sup> cations) with various anions<sup>1</sup>:



In the glyme mixtures, the lithium salts were therefore classified as follows: LiTFSI and LiAsF<sub>6</sub> are highly dissociated; LiClO<sub>4</sub>, LiI and LiBF<sub>4</sub> are intermediately associated; and LiCF<sub>3</sub>SO<sub>3</sub>, LiNO<sub>3</sub>, LiBr and LiCF<sub>3</sub>CO<sub>2</sub> are associated or highly associated. In solution, various types of solvate species form: solvent-separated ion pairs (SSIPs), contact ion pairs (CIPs) and aggregates (AGGs) in which the anions are coordinated to zero, one and two or more Li<sup>+</sup> cations, respectively. Thus, in dilute solutions, LiAsF<sub>6</sub> and LiTFSI tend to form

SSIP solvates, whereas  $\text{LiCF}_3\text{CO}_2$  tends to form AGG solvates. This previous studies has been extended here to examine the behavior of lithium salts in acetonitrile (AN) to determine if this classification can be broadly applied to other solvent mixtures to explain their solution behavior and properties. In aprotic solvents, the anion has only weak interactions with the solvent, which results in a competition between the solvent and anions for coordination to the  $\text{Li}^+$  cations. Therefore, the degree of coordination to the  $\text{Li}^+$  cations is strongly dependent upon the structure of the solvent/anions, salt concentration and temperature. AN was selected due to its relatively straightforward solvation interactions (the solvent has only a single electron lone-pair and thus is either coordinated or uncoordinated to a single  $\text{Li}^+$  cation) and its usefulness as a model for other nitrile or dinitrile solvents suggested as electrolyte materials such as butyronitrile, adiponitrile and glutaronitrile.<sup>2-4</sup> The phase behavior and solvation interactions of  $(\text{AN})_n\text{-LiX}$  mixtures with  $\text{LiPF}_6$ ,  $\text{LiTFSI}$ ,  $\text{LiClO}_4$ ,  $\text{LiBF}_4$ ,  $\text{LiCF}_3\text{SO}_3$  and  $\text{LiCF}_3\text{CO}_2$  are reported here. Information about the electrolyte solution structures obtained from this work can then be linked to the transport properties of the AN-lithium salt mixtures.

## **5.2. Solvent-Lithium Salt Phase Behavior**

### **5.2.1. Pure Acetonitrile (AN)**

AN undergoes a solid-solid phase transition at  $-56\text{ }^\circ\text{C}$  prior to the  $T_m$  at  $-46\text{ }^\circ\text{C}$  (Fig. 5.1).<sup>5-12</sup> The AN molecules are ordered in both the low ( $\beta$  or II) and high ( $\alpha$  or I) temperature phases, but oriented in a different manner.<sup>9</sup>

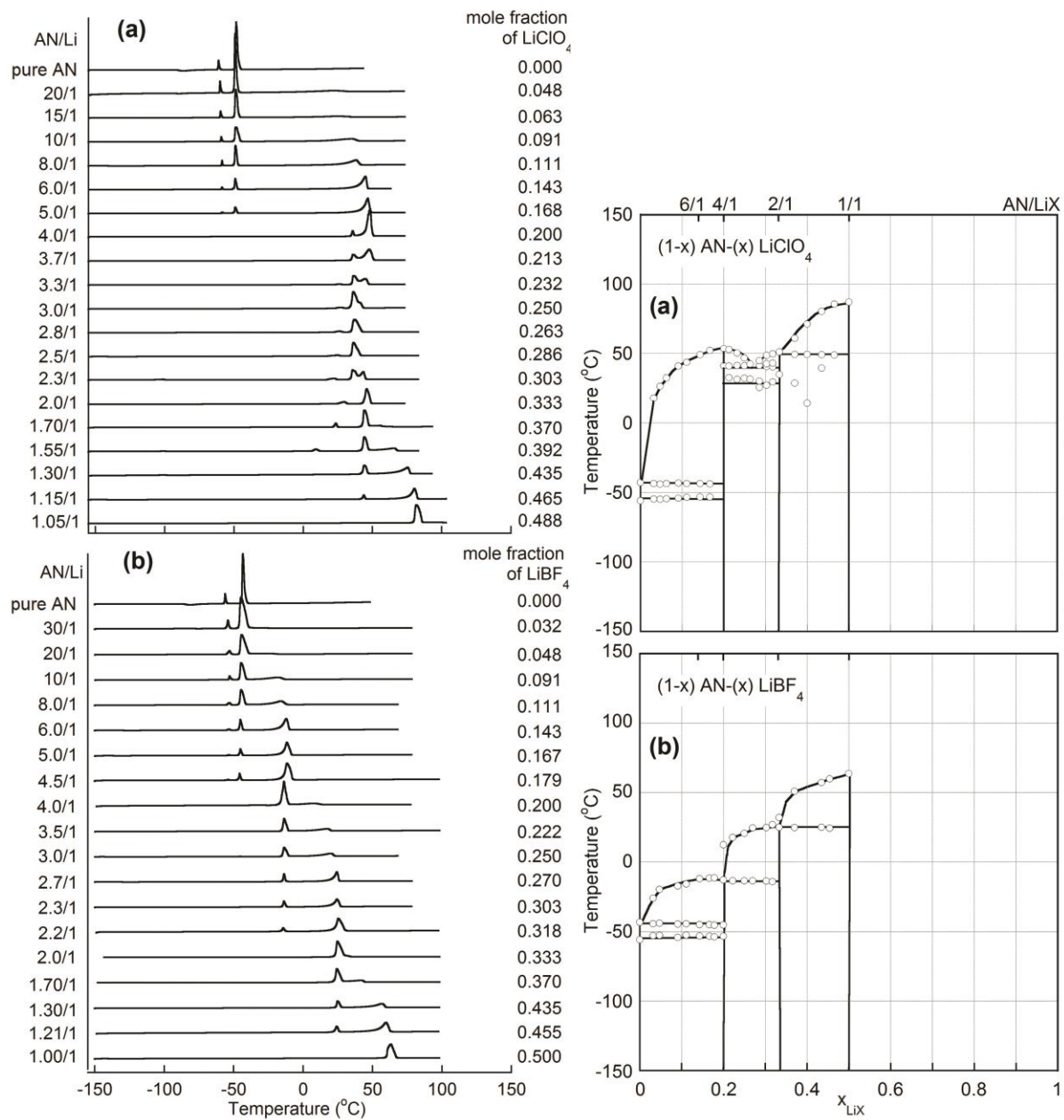


**Figure 5.1.** DSC heating traces ( $5\text{ }^{\circ}\text{C min}^{-1}$ ) and the corresponding phase diagrams for (a)  $(1-x)\text{ AN}-(x)\text{ LiClO}_4$  and (b)  $(1-x)\text{ AN}-(x)\text{ LiBF}_4$  mixtures.<sup>13</sup>

### 5.2.2. (AN)<sub>n</sub>-Lithium Salt Mixtures: Intermediate and Associated Salts

The use of differential scanning calorimetry permits the determination of the equilibrium solid-liquid thermal phase behavior for binary solvent-salt mixtures. Each individual sample is fully crystallized (if possible) by repeated cooling/heating cycles and or annealing at appropriate temperatures (the exact procedure varies for each sample). The data associated with the crystallization of the samples are not shown in Fig. 5.1. Only the final heating traces after crystallization are shown for clarity. From these data, the phase diagram is prepared by plotting the peak temperatures for thermal events such as solid-solid phase transitions and the melt transition, as well as the glass transition temperature for amorphous or partially amorphous samples when it was not possible to fully crystallize the samples. The integrated area for the DSC peaks reflects the enthalpy associated with the transitions (i.e., the energy absorbed normalized by the sample mass). The phases which form (denoted by vertical lines on the phase diagram) correspond to crystalline solvates for solvent-lithium salt mixtures. In some cases, it has been possible to crystallize single crystals for these solvates and thus obtain the crystal structures using single crystal x-ray diffraction, thereby providing direct insight into the molecular-level interactions between the solvent and ions in the solid state.

*AN-LiClO<sub>4</sub>*.—(AN)<sub>n</sub>-LiClO<sub>4</sub> mixtures form three crystalline solvates phases with 4/1, 2/1 and 1/1 (AN/Li) composition, respectively (Fig. 5.1).<sup>13</sup> The data agree well with and expand upon a partial phase diagram previously reported for (AN)<sub>n</sub>-LiClO<sub>4</sub> mixtures.<sup>14</sup> The SSIP 4/1 solvate structure (i.e., (AN)<sub>4</sub>:LiClO<sub>4</sub>) has been previously reported.<sup>13,15</sup> The Li<sup>+</sup> cations are coordinated by four AN molecules with uncoordinated ClO<sub>4</sub><sup>-</sup> anions located between the

solvated cations (Appendix C). The SSIP (AN)<sub>4</sub>:LiI solvate has the same solvate structure.<sup>16</sup> The structure of the 2/1 crystalline solvate is not known, but may resemble the AGG (AN)<sub>2</sub>:LiBr solvate in which each Li<sup>+</sup> cation has four-fold coordination by two AN molecules and two anions.<sup>16</sup> Each Br<sup>-</sup> anion is coordinated to two Li<sup>+</sup> cations forming a dimer structure. Alternatively, this may resemble the AGG (AN)<sub>2</sub>:LiBF<sub>4</sub> phase (see below). Between the 4/1 and 2/1 phases a eutectic is present and the 2/1 phase has a low energy solid-solid phase transition at around 30 °C. The 1/1 solvate structure is also not known, but may resemble the AGG (AN)<sub>1</sub>:LiBF<sub>4</sub> and (AN)<sub>1</sub>:LiCF<sub>3</sub>SO<sub>3</sub> solvates in which each Li<sup>+</sup> cation is coordinated by one AN molecule and three anions (Appendix C).<sup>13,17,18</sup>

*AN-LiBF<sub>4</sub>*.—(AN)<sub>n</sub>-LiBF<sub>4</sub> mixtures show similar phase behavior to those of LiClO<sub>4</sub> (Fig. 5.1)<sup>13</sup> with the formation of 4/1, 2/1 and 1/1 crystalline solvate phases. The structure of the 4/1 solvate is not yet known, but may resemble the 4/1 crystalline solvates with LiClO<sub>4</sub> and LiI. It is noteworthy that similar SSIP 4/1 solvates form with AgClO<sub>4</sub>, AgBF<sub>4</sub>, CuClO<sub>4</sub> and CuBF<sub>4</sub>,<sup>19-23</sup> as the Ag(I)<sup>+</sup> and Cu(I)<sup>+</sup> cations are nearly the same size as Li<sup>+</sup> cations.<sup>24</sup> The (AN)<sub>2</sub>:LiBF<sub>4</sub> solvate structure was determined as part of the present study (Appendix C).<sup>70</sup> In this structure, the Li<sup>+</sup> cations are coordinated by two AN molecules and two BF<sub>4</sub><sup>-</sup> anions. Each anion is, in turn, coordinated to two Li<sup>+</sup> cations forming linear polymeric chains. The (AN)<sub>1</sub>:LiBF<sub>4</sub> solvate structure was also determined as part of the present study (Appendix C).<sup>13,17</sup> This solvate structure consists of Li<sup>+</sup> cations coordinated by three fluorine atoms (one each from three different anions) and a single AN molecule. Each BF<sub>4</sub><sup>-</sup> anion is coordinated to three Li<sup>+</sup> cations through three anion fluorine atoms.

*AN-LiCF<sub>3</sub>SO<sub>3</sub>*.—Although LiCF<sub>3</sub>SO<sub>3</sub> dissolved in AN upon heating and stirring, it was not possible to prepare a phase diagram for the (AN)<sub>n</sub>-LiCF<sub>3</sub>SO<sub>3</sub> mixtures. All of the prepared mixtures (n = 2-10) rapidly formed a high melting (AN)<sub>1</sub>:LiCF<sub>3</sub>SO<sub>3</sub> crystalline solvate at room temperature (Appendix C). Because the boiling point (*T<sub>b</sub>*) of the excess AN (*T<sub>b</sub>* = 82 °C) is much lower than the *T<sub>m</sub>* of the crystalline solvate (*T<sub>m</sub>* = 157 °C—Fig. 5.2), homogeneous solutions cannot be prepared by heating the crystallized samples (to prepare the DSC pans for analysis). The AGG (AN)<sub>1</sub>:LiCF<sub>3</sub>SO<sub>3</sub> solvate (Fig. 5.2) has been previously reported.<sup>13,18</sup> The anions in the solvate structure are coordinated through the three oxygen atoms to three Li<sup>+</sup> cations. Each Li<sup>+</sup> cation is coordinated by three oxygen atoms from the anions (one each from three different anions) and a single AN molecule. Although the anion coordination for the (AN)<sub>1</sub>:LiBF<sub>4</sub> and (AN)<sub>1</sub>:LiCF<sub>3</sub>SO<sub>3</sub> solvates is similar, the ion packing in the crystal structures is different. The (AN)<sub>1</sub>:LiBF<sub>4</sub> phase consists of planar sheets of ions, whereas the (AN)<sub>1</sub>:LiCF<sub>3</sub>SO<sub>3</sub> phase consists of ions arranged in a linear polymeric form of packing.<sup>13</sup>

*AN-LiCF<sub>3</sub>CO<sub>2</sub>*.—LiCF<sub>3</sub>CO<sub>2</sub> readily forms highly concentrated solutions with AN without the formation of any AN-LiCF<sub>3</sub>CO<sub>2</sub> crystalline solvates in the mixtures. Thus, the phase diagram for these mixtures consists of the excess (uncoordinated) AN crystallizing in the dilute mixtures leaving a concentrated amorphous AN-LiCF<sub>3</sub>CO<sub>2</sub> phase. The DSC thermograms (Fig. 5.3)<sup>13</sup> indicate that the composition for the amorphous phase is (AN)<sub>n</sub>-LiCF<sub>3</sub>CO<sub>2</sub> (n < 2). The amorphous phase may consist of both coordinated and uncoordinated AN molecules, the latter weakly interacting with the solvated ions and thus not crystallizing

as bulk solvent.

Although both the  $(\text{AN})_n\text{-LiClO}_4$  and  $\text{-LiBF}_4$  mixtures shows similar thermal phase behaviors, differences do exist in the  $T_m$  for the solvates formed. In particular, it is noteworthy that the SSIP  $(\text{AN})_4\text{:LiClO}_4$  crystalline solvate has a significantly higher  $T_m$  than

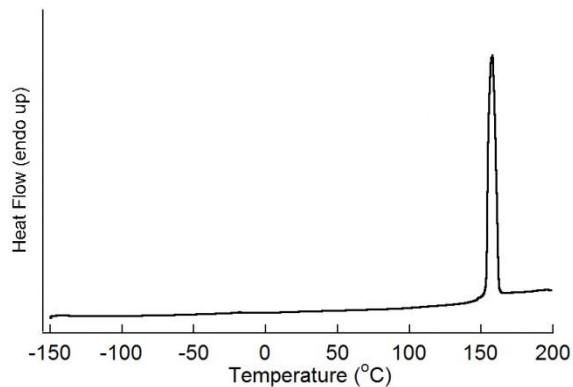


**Figure 5.2.** DSC heating trace ( $5\text{ °C min}^{-1}$ ) of the  $(\text{AN})_1\text{:LiCF}_3\text{SO}_3$  crystalline solvate.<sup>13</sup>

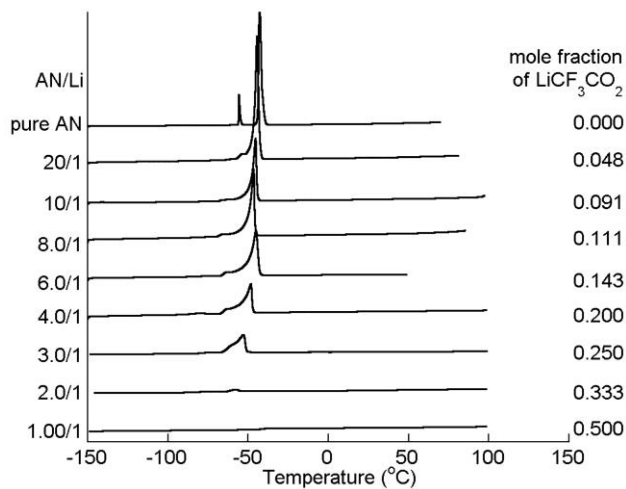


**Figure 5.3.** DSC heating traces ( $5\text{ °C min}^{-1}$ ) of  $(1-x)\text{ AN}-(x)\text{ LiCF}_3\text{CO}_2$  mixtures.<sup>13</sup>

that of the SSIP (AN)<sub>4</sub>:LiBF<sub>4</sub> crystalline solvate (Fig. 5.1) despite the fact that both anions are tetrahedral and nearly the same size.<sup>25-31</sup> This can be explained by the difference in the ionic association tendency of the two salts and the mechanisms for melting.<sup>1</sup> The highly associated salts, LiCF<sub>3</sub>SO<sub>3</sub> and LiCF<sub>3</sub>CO<sub>2</sub>, have different phase behavior from LiClO<sub>4</sub> and LiBF<sub>4</sub>, but also from one another. Both of the LiCF<sub>3</sub>SO<sub>3</sub> and LiCF<sub>3</sub>CO<sub>2</sub> salts dissolve readily in AN, but AGGs solvates primarily are formed, even in dilute mixtures. The AGG solvates with LiCF<sub>3</sub>SO<sub>3</sub> may have similar ionic coordination that found in the (AN)<sub>1</sub>:LiCF<sub>3</sub>SO<sub>3</sub> crystalline solvate thus facilitating the rapid nucleation and growth of this solid phase from dilute solutions (in addition to the high  $T_m$  for this solvate). In the case of the (AN)<sub>n</sub>-LiCF<sub>3</sub>CO<sub>2</sub> mixtures, similar AGG solvates may exist, but it may not be possible to pack the ions into an ordered crystalline phase (due to differences in the -SO<sub>3</sub> and -CO<sub>2</sub> coordinating ends)—thus highly concentrated (AN)<sub>n</sub>-LiCF<sub>3</sub>CO<sub>2</sub> mixtures do not solidify.

### 5.2.3. (AN)<sub>n</sub>-Lithium Salt Mixtures: Dissociated Salts

*AN-LiTFSI*.—DSC thermograms and the corresponding phase diagram for (AN)<sub>n</sub>-LiTFSI mixtures (Fig. 5.4)<sup>33</sup> agree well with a previously reported partial phase diagram.<sup>34</sup> Three different 6/1, 4/1 and 1/1 AN/LiTFSI crystalline solvate phases are formed. The structures of the 6/1 and 4/1 solvates are not yet known. The 6/1 solvate may have octahedral coordination in which the Li<sup>+</sup> cations are fully solvated by six AN molecules, but several previous studies have suggested that more than four AN molecules coordination to a Li<sup>+</sup> cation is not energetically favorable (in the gas phase).<sup>35-39</sup> The Raman spectroscopic data (see 5.4.2)

verifies that this is a SSIP phase with uncoordinated TFSI<sup>-</sup> anions, as expected. The 4/1 solvate is also a SSIP phase which may have tetrahedral coordination similar to those of the SSIP (AN)<sub>4</sub>:LiClO<sub>4</sub><sup>13,15</sup> and (AN)<sub>4</sub>:LiI<sup>16</sup> phases in which the Li<sup>+</sup> cations are fully solvated by four AN molecules with uncoordinated anions. For compositions between the 4/1 and 1/1 phases, a “crystallinity gap”—it was not possible to fully crystallize the samples despite subjecting the samples to extensive heating-cooling cycles at subambient temperature—occurs due to either the slow nucleation of crystalline solvates (beyond the time frame of the crystallization procedure utilized) or the inhibition of ordered crystalline solvate formation due to unfavorable packing. The structure of (AN)<sub>1</sub>:LiTFSI crystalline solvate was determined (Appendix C).<sup>33,40</sup> In this 1/1 crystalline phase, there are two different Li<sup>+</sup> cations. One Li<sup>+</sup> cation has six-fold coordinated by six oxygen atoms from four TFSI<sup>-</sup> anions, while another Li<sup>+</sup> cation has four-fold coordination by two oxygen atoms from two TFSI<sup>-</sup> anions and two nitrogen atoms from two AN solvent molecules. In this AGG solvate, each TFSI<sup>-</sup> anion is coordinated to three Li<sup>+</sup> cations.

*AN-LiPF<sub>6</sub>*.—(AN)<sub>n</sub>-LiPF<sub>6</sub> mixtures form two crystalline solvates consisting of 6/1 and 5/1 phases. In dilute mixture ( $n \geq 10$ ), the 6/1 SSIP solvate crystallizes with a  $T_m$  at 18 °C (Fig. 5.4).<sup>33</sup> It is difficult to analyze the thermal phase behavior for more concentrated mixtures (i.e.,  $10 > n \geq 6$ ) due to both the 6/1 and 5/1 phases formation. In each different composition, some of the sample crystallized into the 5/1 phase upon cooling or even rapid cooling from the melt, while the remainder of the sample then crystallized at low temperature into the 6/1 phase resulting in the complicated thermal behavior as shown in Fig. 5.4. The structure of the

(AN)<sub>6</sub>:LiPF<sub>6</sub> crystalline solvate has been determined (Appendix C).<sup>41</sup> The Li<sup>+</sup> cations are coordinated by four AN molecules with uncoordinated PF<sub>6</sub><sup>-</sup> anions and uncoordinated AN molecules (two per Li<sup>+</sup> cation) located between the solvated cations. The crystal structure of the (AN)<sub>5</sub>:LiPF<sub>6</sub> solvate phase has also been reported (Appendix C).<sup>42</sup> The structure is similar to the 6/1 structure in which Li<sup>+</sup> cations coordinated by four AN molecules with uncoordinated PF<sub>6</sub><sup>-</sup> anions and uncoordinated AN molecules (one per Li<sup>+</sup> cation) located between the solvated cations.<sup>33</sup> The same features can be found in the (AN)<sub>5</sub>:CuPF<sub>6</sub> crystalline solvate structure.<sup>43,44</sup> The (AN)<sub>5</sub>:LiPF<sub>6</sub> solvate has a solid-solid phase transition at 38 °C prior to a *T<sub>m</sub>* at 67 °C. It is noteworthy that both CuClO<sub>4</sub> and CuBF<sub>4</sub> form 4/1 phases<sup>22,23,45-48</sup> instead of a 5/1 phase, as is also found for LiClO<sub>4</sub> and LiBF<sub>4</sub> given that the Li<sup>+</sup> and Cu(I)<sup>+</sup> cations are nearly identical in size.<sup>41,49</sup> Between the 5/1 solvate and a more aggregated solvate (composition unknown) a eutectic point is observed.

Although the phase diagrams for (AN)<sub>n</sub>-LiPF<sub>6</sub> and -LiTFSI mixtures indicate that both salts are highly dissociated (i.e., both are able to form a SSIP 6/1 phase), significant differences exist between them. In particular, LiPF<sub>6</sub> forms crystalline phases with a relatively high *T<sub>m</sub>*, whereas LiTFSI forms crystalline phases which melt at low temperature. Therefore, the (AN)<sub>n</sub>-LiTFSI mixtures are liquid state at -30 °C over a large concentration range, while all of the (AN)<sub>n</sub>-LiPF<sub>6</sub> mixtures (except for the most dilute) crystallize readily at room temperature. The differences in size, shape and flexibility of the anions can explain these differences: the PF<sub>6</sub><sup>-</sup> anions are essentially spherical and easily pack together symmetrically with the solvated Li<sup>+</sup> cations, whereas the TFSI<sup>-</sup> anions are a non-spherical shape which

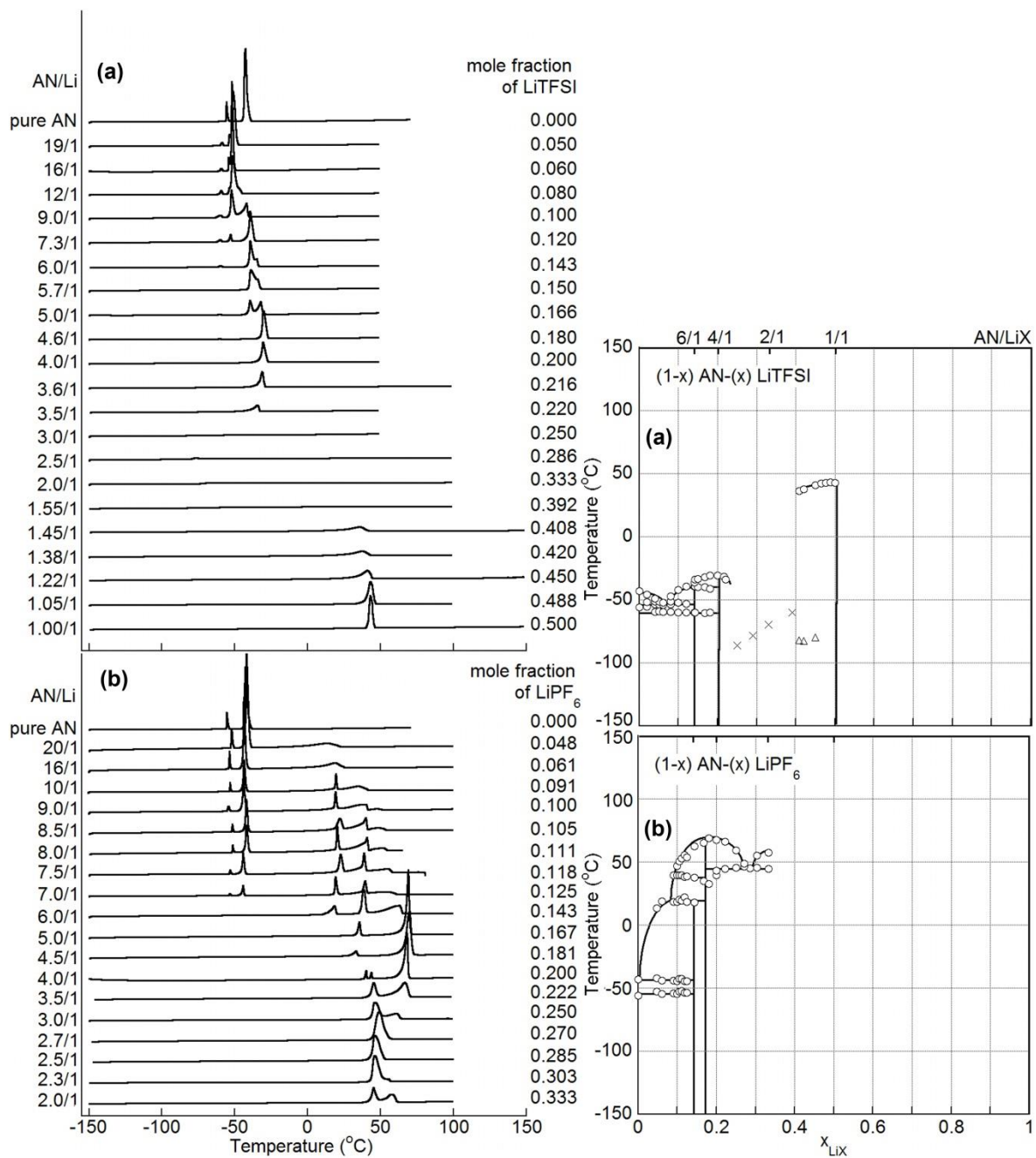


**Figure 5.4.** DSC heating traces ( $5\text{ }^{\circ}\text{C min}^{-1}$ ) and the corresponding phase diagrams of (a)  $(1-x)$  AN- $(x)$  LiTFSI and (b)  $(1-x)$  AN- $(x)$  LiPF<sub>6</sub> mixtures.<sup>33</sup>

results in a less symmetrical packing of the solvated  $\text{Li}^+$  cations amongst the uncoordinated anions. The solid-solid phase transition for the 5/1  $\text{LiPF}_6$  crystalline solvate may also result in the uncoordinated anions becoming disordered by spinning about one axis or tumbling at elevated temperature. The long-range order, however, is retained. In contrast, the  $\text{TFSI}^-$  anions are flexible<sup>50,51</sup> and may become conformationally disordered at elevated temperature thus disrupting the long-range packing of the solvate structure leading to melting instead of a disordered solid crystalline (plastic crystalline) phase.<sup>33</sup>

### 5.3. Raman Characterization of AN- $\text{Li}^+$ Cation Solvation

Uncoordinated AN has a  $\nu_4$  band at  $918\text{ cm}^{-1}$  for the C–C stretching vibration and a  $\nu_2$  Raman band at  $2254\text{ cm}^{-1}$  for the  $\text{C}\equiv\text{N}$  stretching vibration (Figs. 5.5 and 5.6),<sup>13,33</sup> with the  $922$  and  $2251\text{ cm}^{-1}$  shoulders attributed to hot bands.<sup>52,53</sup> When the electron lone-pair on the nitrogen of AN is coordinated to a  $\text{Li}^+$  cation, these bands shift to  $930$  and  $2277\text{ cm}^{-1}$ , respectively (Figs. 5.5 and 5.6).<sup>34,37,54,55</sup> In the case of  $(\text{AN})_n\text{-LiClO}_4$  mixtures, only the  $\nu_2$  AN band was analyzed because the  $\nu_4$  C–C stretching vibrational band overlaps with the Cl–O stretching vibrational mode of the  $\text{ClO}_4^-$  anion.<sup>56-58</sup> The average solvation number ( $N$ ), the fraction of solvent molecules coordinated to  $\text{Li}^+$  cations, can be determined from the following relation:

$$\frac{A_{\text{AN-C}}}{A_{\text{AN-C}} + A_{\text{AN-UC}}} = N \frac{c_{\text{LiX}}}{c_{\text{AN}}} \quad [1]$$

where  $A_{\text{AN-C}}$  and  $A_{\text{AN-UC}}$  are the integrated area intensities of the bands for the coordinated

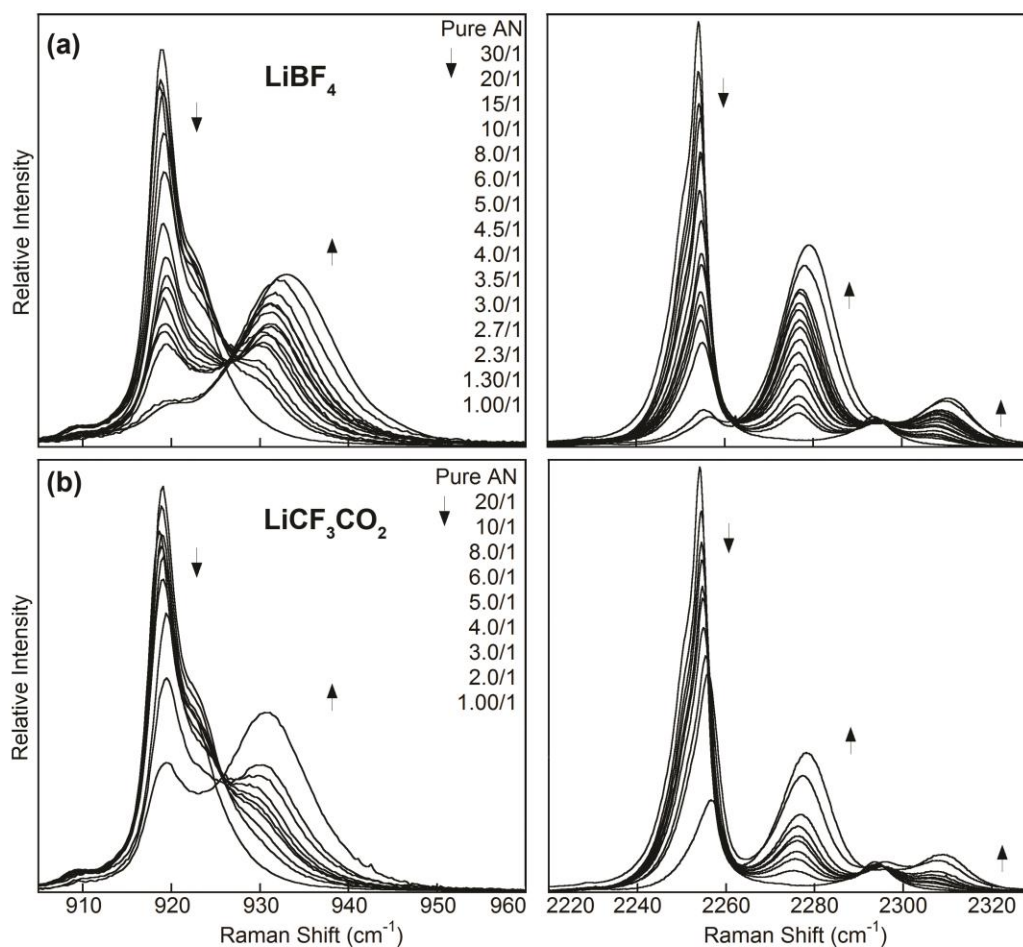


**Figure 5.5.** Raman spectra at 60°C of the AN C–C stretching mode (918 cm<sup>-1</sup>) and C≡N stretching mode (2254 cm<sup>-1</sup>) bands for (a) (AN)<sub>n</sub>-LiBF<sub>4</sub> and (b) (AN)<sub>n</sub>-LiCF<sub>3</sub>CO<sub>2</sub> mixtures (AN/LiX ratio indicated).<sup>13</sup>

and uncoordinated AN, respectively,  $c_{LiX}$  and  $c_{AN}$  are the concentrations of the salt and AN, respectively.<sup>59,60</sup> Based upon the data shown in Figs. 5.5 and 5.6, plots of the peak area for the coordinated and uncoordinated AN (normalized relative to the total peak area) were prepared (Fig. 5.7)<sup>13,33</sup> which gives an indication of the fraction of solvent molecules

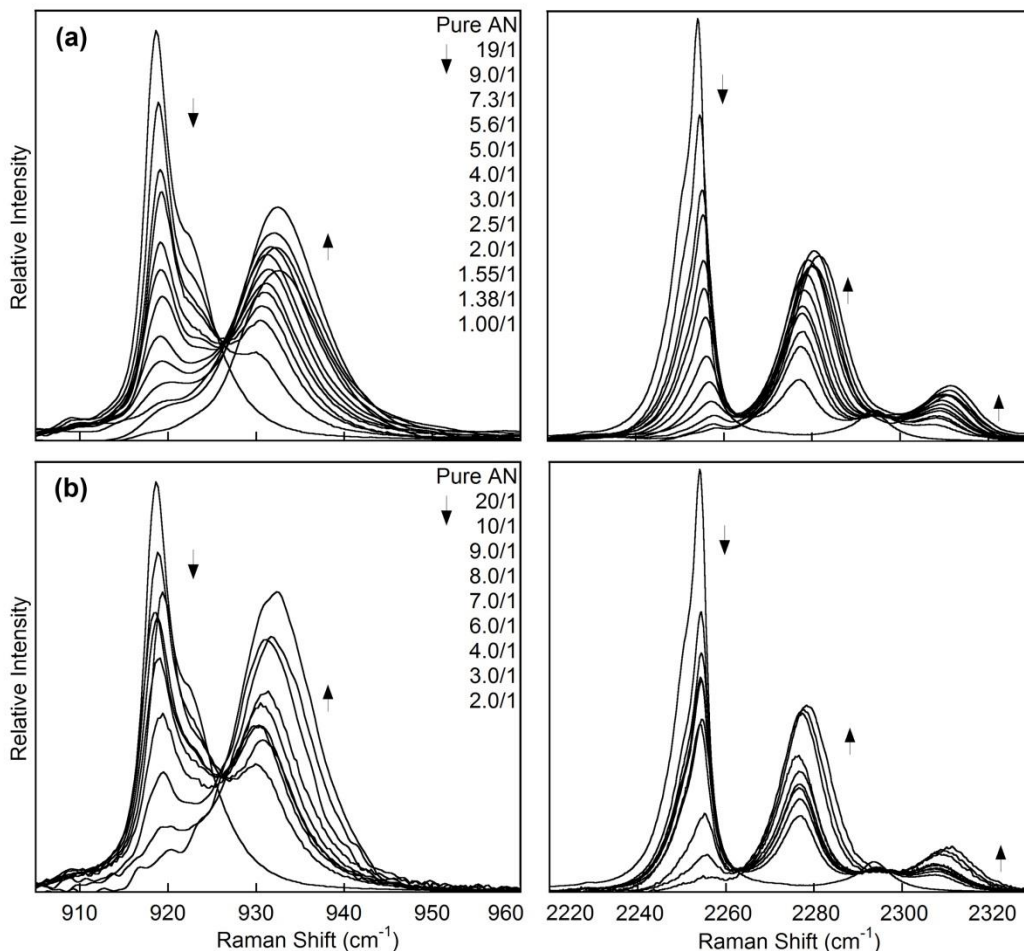


**Figure 5.6.** Raman spectra at 60 °C of AN C–C stretching mode (920  $\text{cm}^{-1}$ ) and C $\equiv$ N stretching mode (2250  $\text{cm}^{-1}$ ) bands for (a)  $(\text{AN})_n\text{-LiTFSI}$  and (b)  $(\text{AN})_n\text{-LiPF}_6$  mixtures (AN/LiX ratio indicated).<sup>33</sup>

coordinated to  $\text{Li}^+$  cations. Combining this information and the molar ratio of AN to LiX (i.e.,  $c_{\text{AN}}/c_{\text{LiX}}$ ), the  $N$  value variation with salt concentration and different LiX salts was determined (Fig. 5.7). For the most dilute solutions, analytical errors will be greatest, so  $N$  values for data with  $x < 0.10$  or thereabout are considered to be unreliable. The integrated

intensity  $A_0$  of a band is given by<sup>61</sup>:

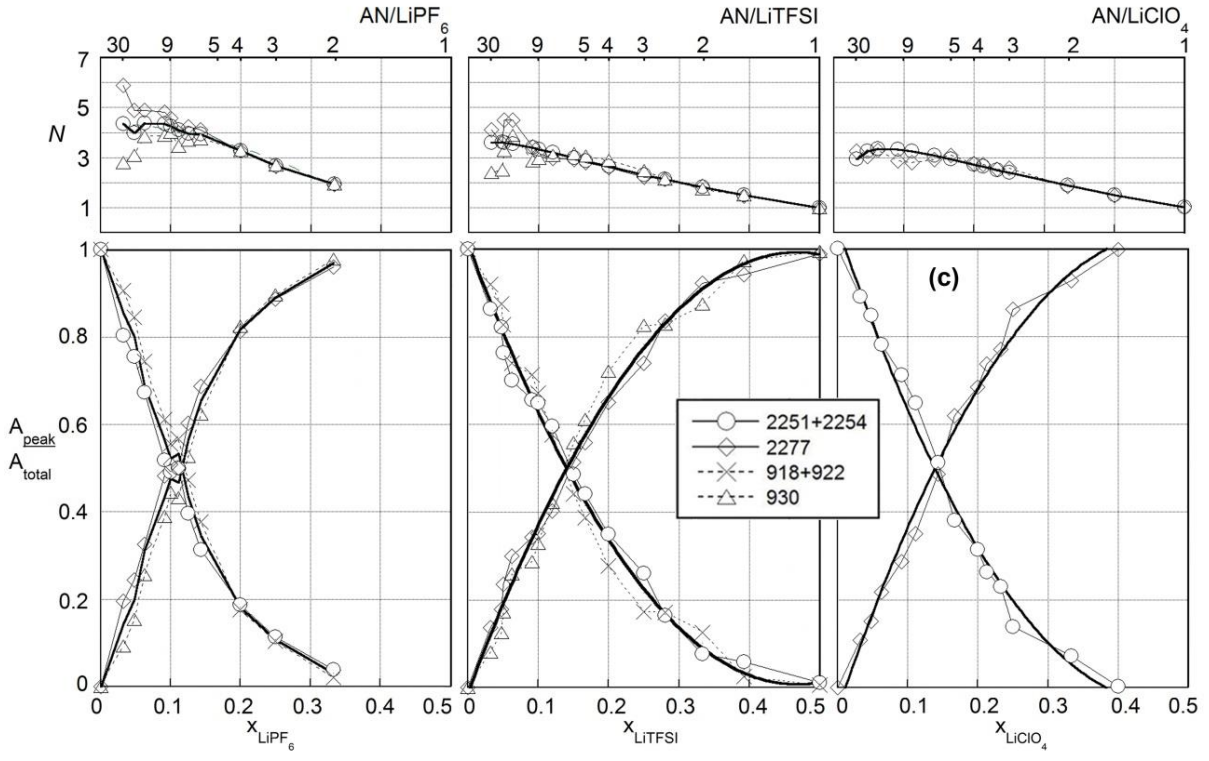
$$A_0 = KC_0 \quad [2]$$

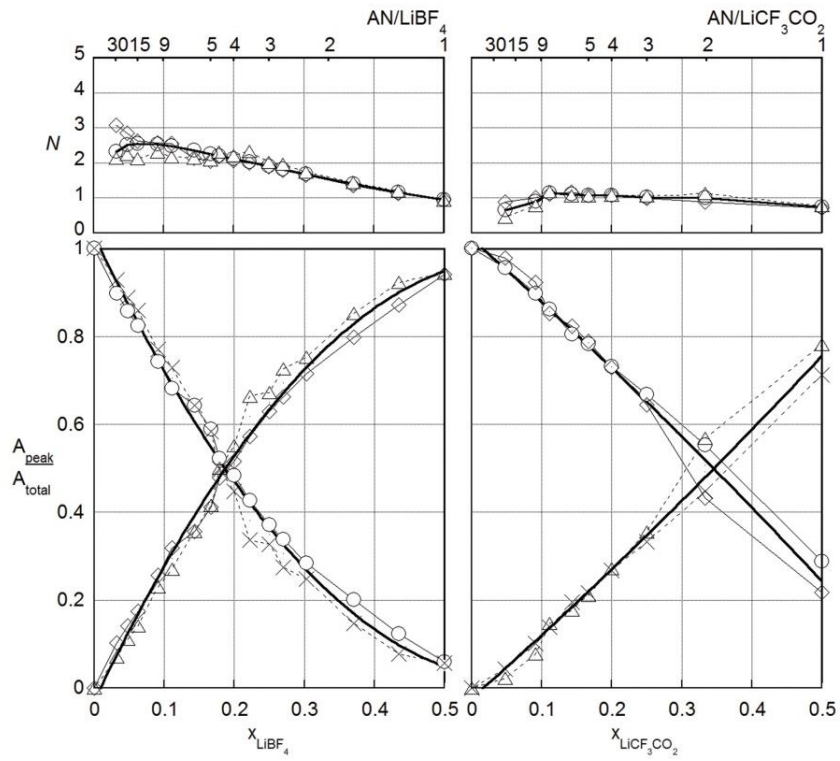
where  $K$  is a proportionality factor which includes the Raman activity of the vibration and  $C_0$  is the concentration of the species generating the band. Note the assumption that the bands associated with the uncoordinated and coordinated AN have equivalent Raman activity (no scaling is required)<sup>59,60</sup> for the analysis in Fig. 5.7. If this is not the case, the  $N$  values noted in the top of Fig. 5.7 would need to be corrected with appropriate scaling factors. Data for the  $(\text{AN})_n\text{-LiPF}_6$ ,  $\text{-LiTFSI}$ ,  $\text{-LiClO}_4$ ,  $\text{-LiBF}_4$  and  $\text{-LiCF}_3\text{CO}_2$  mixtures were collected at 60 °C to ensure that the mixtures were homogeneous solutions over a wide composition range (Figs. 5.1, 5.3 and 5.4). Selecting a particular composition,  $x = 0.20$  (i.e., 4 AN molecules per  $\text{Li}^+$  cation), the average solvation numbers are approximately 3.2 for  $\text{LiPF}_6$ , 2.8 for  $\text{LiTFSI}$ , 2.7 for  $\text{LiClO}_4$ , 2.1 for  $\text{LiBF}_4$  and 1.0 for  $\text{LiCF}_3\text{CO}_2$ . The  $N$  values do not match with the total amount of solvent present except for the most concentrated mixtures because a variety of solvates are actually present along with uncoordinated solvent in the liquid phase. This comparison suggests the following order for increasing  $\text{Li}^+$  cation solvation (decreasing ionic association) in the liquid phase:



in accord with the ionic association order reported previously.<sup>1</sup> The more associated anions, such as  $\text{LiCF}_3\text{CO}_2$ , have more coordination with the  $\text{Li}^+$  cations, which decreases the number of  $\text{AN}\dots\text{Li}^+$  cation coordination bonds. Considering the previous studies which proposed the  $\text{TFSI}^-$  anion to be a highly dissociated anion,<sup>1</sup> the results for  $\text{LiTFSI}$  are surprising. A

**Figure 5.7.** Raman spectroscopic analysis at 60 °C of solvent bands for uncoordinated AN and Li<sup>+</sup> cation coordinated AN in (a) (AN)<sub>n</sub>-LiPF<sub>6</sub>, (b) (AN)<sub>n</sub>-LiTFSI, (c) (AN)<sub>n</sub>-LiClO<sub>4</sub>, (d) (AN)<sub>n</sub>-LiBF<sub>4</sub> and (e) (AN)<sub>n</sub>-LiCF<sub>3</sub>CO<sub>2</sub> mixtures. The calculated Li<sup>+</sup> cation average solvation number (*N*) is shown at the top. The dark solid line corresponds to the average of the two sets of data from Figs. 5.5 and 5.6 (no scaling factor was applied).<sup>13,33</sup>





comparison of the crystalline phases formation for the  $(\text{AN})_n\text{-LiTFSI}$ ,  $\text{-LiPF}_6$  and  $\text{-LiClO}_4$  mixtures suggests that the  $\text{TFSI}^-$  anions are as dissociated as the  $\text{PF}_6^-$  anions. But in the liquid phase, the  $\text{TFSI}^-$  anions may have an ionic association tendency closer to  $\text{ClO}_4^-$  (see below). There is one possible explanation for the lower than expected  $N$  values noted for the  $\text{TFSI}^-$  anion—the  $\text{TFSI}^-$  anion tends to form bidentate coordination to a single  $\text{Li}^+$  cation to a much greater extent than for anions such as  $\text{PF}_6^-$ ,  $\text{ClO}_4^-$  and  $\text{BF}_4^-$ , which is evident from the MD simulation results (see below) and the known crystal structures of numerous  $\text{LiTFSI}$  solvates.<sup>34,40,62-65</sup> Therefore, when a  $\text{TFSI}^-$  anion forms bidentate coordination bonds (two rather than one donor oxygens) to the cation, this may displace an additional AN molecule which results in a lowering of the value of  $N$  to some extent from what would otherwise be predicted. For the  $(\text{AN})_n\text{-LiCF}_3\text{CO}_2$  mixtures, the  $N$  values do not change significantly ( $\sim 1$ ) with changing salt concentration (Fig. 5.7) because  $\text{LiCF}_3\text{CO}_2$  is a highly associated lithium salt and thus tends to form a stable amorphous 1/1 AGG solvate with some excess AN which is unable to crystallize (Fig. 5.3) due to its interactions with the solvates in solution.

## 5.4. Raman Characterization of Ionic Association

### 5.4.1. $(\text{AN})_n\text{-Lithium Salt Mixtures: Intermediate and Associated Salts}$

For the  $(\text{AN})_n\text{-LiClO}_4$  mixtures, Fig. 5.8 shows the  $\text{ClO}_4^-$  anion band variation with concentration at  $-80\text{ }^\circ\text{C}$ .<sup>13</sup> At this temperature, all of the samples are crystalline solids. Raman bands for both AN and the  $\text{ClO}_4^-$  anions overlapped in this region ( $\sim 930\text{ cm}^{-1}$ ). Four bands are observed for the more dilute samples ( $n > 4$ ): uncoordinated and coordinated AN at 920

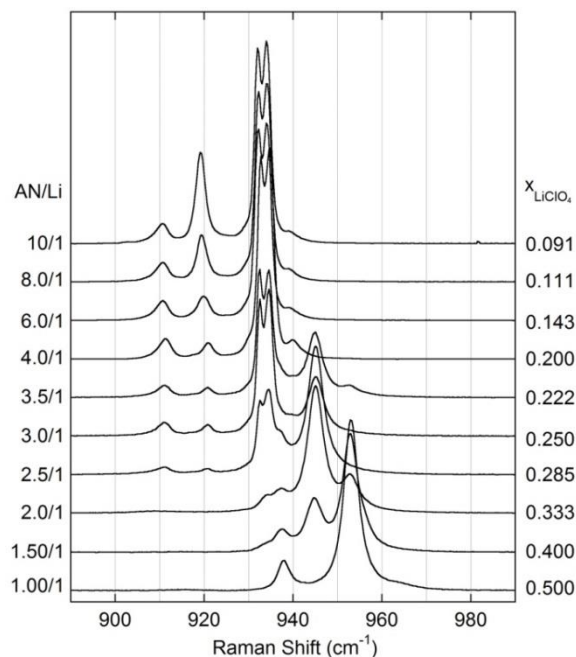


**Figure 5.8.**  $\text{ClO}_4^-$  anion band variation with concentration in the  $(\text{AN})_n\text{-LiClO}_4$  mixtures at  $-80\text{ }^\circ\text{C}$ .<sup>13</sup>

and  $931\text{ cm}^{-1}$  (the band positions have a slight temperature dependence and thus differ from the data in Fig. 5.5) and bands at  $910$  and  $933\text{ cm}^{-1}$  from the Fermi resonance overtone of the uncoordinated  $\text{ClO}_4^-$  anion and the anion  $\text{Cl-O}$  stretching vibrational mode, respectively.<sup>66</sup> A comparison with the phase diagram (Fig. 5.1) indicates that the Raman band at  $933\text{ cm}^{-1}$  corresponds to the SSIP  $(\text{AN})_4\text{:LiClO}_4$  phase in which the anions remain uncoordinated.<sup>67,68</sup> For the more concentrated mixtures ( $n < 4$ ), a new band at  $945\text{ cm}^{-1}$  corresponds to the AGG-I  $(\text{AN})_2\text{:LiClO}_4$  crystalline solvate in which the anions may be coordinated to two  $\text{Li}^+$  cations through two oxygen atoms. For the most concentrated samples ( $n \leq 2$ ), another band appears at  $953\text{ cm}^{-1}$  corresponding to the  $(\text{AN})_1\text{:LiClO}_4$  phase, which likely consists of AGG-II

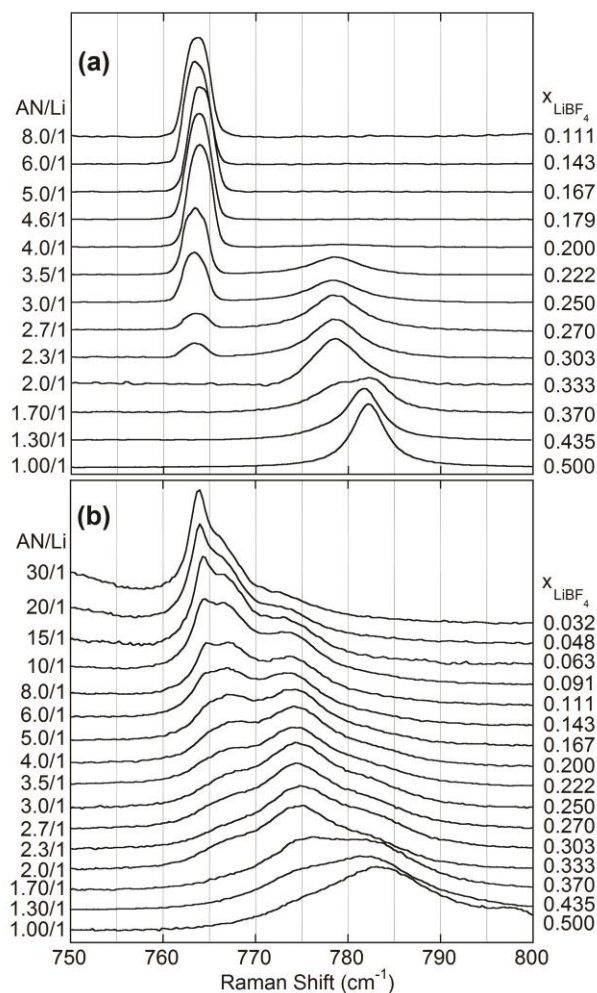


**Figure 5.9.**  $\text{BF}_4^-$  anion band variation with concentration in the  $(\text{AN})_n\text{-LiBF}_4$  mixtures at (a)  $-80\text{ }^\circ\text{C}$  and (b)  $60\text{ }^\circ\text{C}$ .<sup>13</sup>

anions coordinated to three  $\text{Li}^+$  cations through three oxygen atoms. The Raman band at about  $938\text{ cm}^{-1}$  may correspond to coordinated AN based upon the characterization of single crystals of the solvates in which the position of the coordinated AN differs in the solid-state from that noted in solutions (Fig. 5.5), perhaps due to lattice packing effects.

Fig. 5.9a shows the  $\text{BF}_4^-$  anion band variation with concentration for  $(\text{AN})_n\text{-LiBF}_4$  mixtures at  $-80\text{ }^\circ\text{C}$ .<sup>13</sup> At this temperature, all of the samples are crystalline solids. The Raman band from the anion B–F stretching vibrational mode is observed at  $760\text{-}783\text{ cm}^{-1}$ .<sup>37,69</sup> In a current spectroscopic characterization study for crystalline  $(\text{solvent})_n\text{:LiBF}_4$  solvate structures with various solvents,<sup>70</sup> the peak positions at  $-80\text{ }^\circ\text{C}/60\text{ }^\circ\text{C}$  are for SSIP ( $765\text{-}767/764\text{-}766\text{ cm}^{-1}$  – uncoordinated  $\text{BF}_4^-$  anions), CIP-I ( $766\text{-}769/765\text{-}766\text{ cm}^{-1}$  –  $\text{BF}_4^-$  anion coordinated to a single  $\text{Li}^+$  cation through one fluorine atom), AGG-I ( $777\text{-}778/775\text{-}776\text{ cm}^{-1}$  –  $\text{BF}_4^-$  anion coordinated to two  $\text{Li}^+$  cations through two fluorine atoms) and AGG-II ( $782\text{-}787/783\text{-}785\text{ cm}^{-1}$  –  $\text{BF}_4^-$  anion coordinated to three  $\text{Li}^+$  cations through three fluorine atoms) solvates. It is noteworthy that the vibrational bands shift and broaden with increasing temperature. For the more dilute samples, only a single band at  $764\text{ cm}^{-1}$  is observed. Based upon the phase diagram in Fig. 5.1b, the Raman band at  $764\text{ cm}^{-1}$  corresponds to the SSIP  $(\text{AN})_4\text{:LiBF}_4$  crystalline solvate in which the anions are uncoordinated (in agreement with the same solvate for  $\text{LiClO}_4$ ). When the concentration of  $\text{LiBF}_4$  is increased, a new band appears at  $778\text{-}779\text{ cm}^{-1}$  corresponding to an AGG-I  $(\text{AN})_2\text{:LiBF}_4$  phase in which the anions are likely coordinated to two  $\text{Li}^+$  cations through two fluorine atoms. When the concentration of  $\text{LiBF}_4$  is increased further, another band appears at  $782\text{ cm}^{-1}$  corresponding to the AGG-II  $(\text{AN})_1\text{:LiBF}_4$  phase<sup>13</sup> which consists of anions coordinated to three  $\text{Li}^+$  cations through three fluorine atoms.

At  $60\text{ }^\circ\text{C}$  the  $(\text{AN})_n\text{-LiBF}_4$  liquid mixtures (Fig. 5.9b)<sup>13</sup> have Raman bands at approximately  $764, 767, 774\text{-}775, 783\text{-}784$  and  $798\text{ cm}^{-1}$  which are attributed to SSIP, CIP-I,

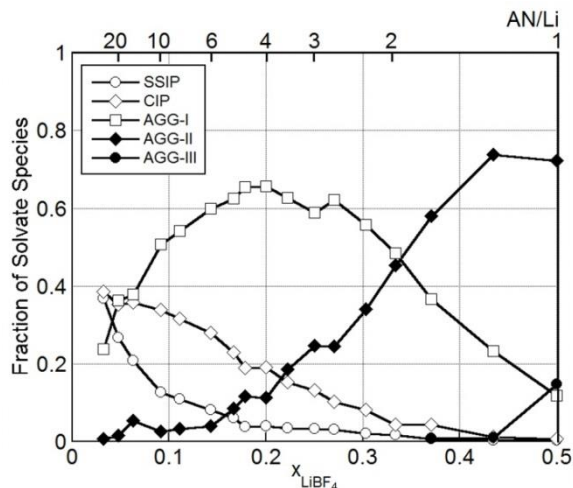


**Figure 5.10.** Solvate species distribution in the  $(AN)_n$ - $LiBF_4$  mixtures at 60 °C.<sup>13</sup>

AGG-I, AGG-II and AGG-III ( $BF_4^-$  anions coordinated to more than three  $Li^+$  cations through all four fluorine atoms) solvates, respectively. The AGG-III anion coordination may correspond to anion in large aggregated ion clusters which may resemble crystalline  $LiBF_4$ .<sup>30</sup> It is interesting that CIP solvates appear to be a prominent species present in dilute  $(AN)_n$ - $LiBF_4$  solutions even though none of the crystalline phases consist of CIP solvates. Therefore, the displacement of one (for CIP-I) or more AN molecules in the  $Li^+$  cation coordination shell for many/most of the  $Li^+$  cations is caused by (or induces) the melting of SSIP crystalline solvate.

The estimated fraction of each type of solvate present in the solutions at 60 °C (Fig. 5.10)<sup>13</sup> can be provided by the deconvolution of the Raman bands of the  $BF_4^-$  anion (Fig. 5.9b).<sup>13</sup> The assumption made in this determination is that the relative activities of the  $BF_4^-$  bands

associated with different cation coordination have an equivalent Raman activity. Based upon the information from Figs. 5.7 and 5.10, the solution SSIP, CIP-I, AGG-I, AGG-II and AGG-III solvates largely correspond to  $\text{Li}^+$  cations coordinated by four, three, two, one and zero (or near zero) AN molecules, respectively (the AN molecules are sequentially replaced with fluorine atoms from anions).

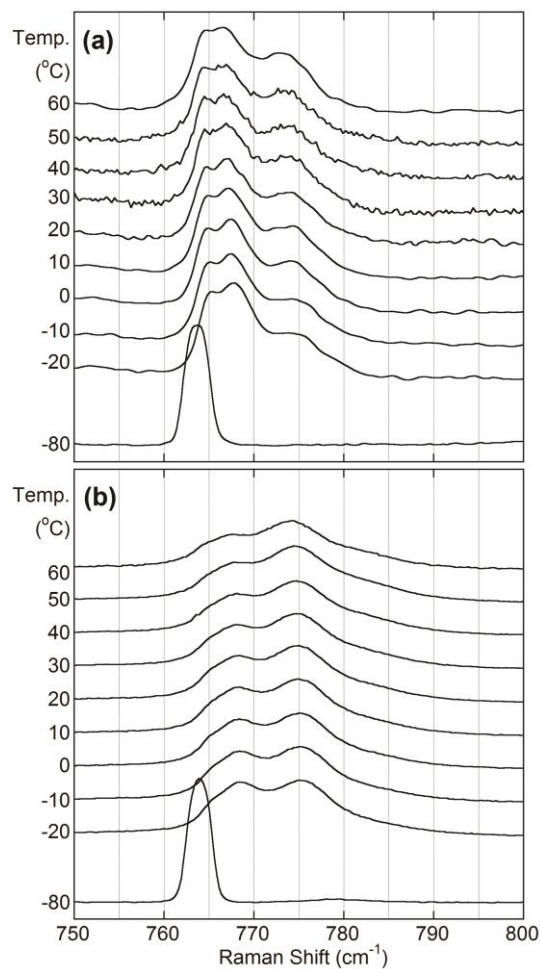


**Figure 5.11.** Temperature dependence of the  $\text{BF}_4^-$  anion bands in the  $(\text{AN})_n\text{-LiBF}_4$  mixtures for (a)  $n = 8$  and (b)  $n = 4$ .<sup>13</sup>

The identity of the solvate species present in solution is also a function of temperature. Fig. 5.11 shows the temperature dependence of the  $\text{BF}_4^-$  anion bands in the  $(\text{AN})_n\text{-LiBF}_4$  ( $n = 8$  and  $4$ ) mixtures.<sup>13</sup> When both mixtures are crystalline at  $-80\text{ }^\circ\text{C}$ , only a single band is observed corresponding to the SSIP  $(\text{AN})_4\text{:LiBF}_4$  solvate. However, after the solid to liquid phase transition occurs, the Raman vibrational band of the  $\text{BF}_4^-$  anion shifts and splits significantly. For the  $n = 8$  mixture, it is evident that Raman bands at  $764\text{-}765$ ,  $767$  and  $774\text{-}775\text{ cm}^{-1}$  corresponds to SSIP, CIP-I and AGG-I anion coordination, respectively. Deconvolution of the Raman bands indicates that the SSIP and CIP-I coordination increase, while the AGG-I coordination decrease somewhat with decreasing temperature. For the  $n = 4$  mixture, the same trend is observed at a given temperature, except that the fraction of the AGG-I anion coordination is increased at the expense of the SSIP and CIP-I coordination. The solvent competes more effectively with the anion for  $\text{Li}^+$  cation coordination at lower temperature, while the ionic association tends to increase with increasing temperature. The MD simulations also show the same temperature-dependent trends for the solvates.<sup>13</sup>

Utilizing the information obtained from the average solvation number ( $N$ ) and anion coordination at a given composition and temperature through the Raman spectroscopic characterization, it is possible to glean insight into the structure of the solvates in the liquid phase. However, it is noteworthy that in reality the solvates in solution are quite heterogeneous, so the assume that solution solvates have a similar structure to those found in the crystalline phases should be tempered. In the known crystalline solvates, it is evident that the structures constitute the optimization of  $\text{Li}^+$  cation coordination, steric packing and

minimization of repulsive interactions (i.e., electron lone-pair...lone-pair, lone pair...anion, etc.). However, the molecular motion of the solvent molecules and ions in solution is more significant with greater free volume and energy available at higher temperature. Therefore, the solvent molecules (and ions) occupy a greater effective volume and this may influence how the solvent and ions can pack around and coordinate the  $\text{Li}^+$  cations.<sup>13</sup>

#### 5.4.2. $(\text{AN})_n$ -Lithium Salt Mixtures: Dissociated Salts

Fig. 5.12 shows the  $\text{TFSI}^-$  anion band variation with changing concentration for  $(\text{AN})_n$ - $\text{LiTFSI}$  mixtures at both  $-80$  and  $60$  °C.<sup>33,71,72</sup> At  $-80$  °C, all of the samples are crystalline solids, except for those in the crystallinity gap which either remain liquid or are amorphous solids, depending upon the sample  $T_g$  (Fig. 5.4). For the dilute mixtures ( $n \geq 3.6$ ), two bands are observed which do not vary in position with varying concentration. As shown in Fig. 5.4 two different crystalline solvates (6/1 and 4/1 phases) are present for this concentration range ( $n \geq 4$ ), but the anion coordination to the  $\text{Li}^+$  cations does not change because bothSSIP phases have uncoordinated anions. The  $\text{TFSI}^-$  anion is known to have two different low-energy conformational states: a *cisoid* form ( $C_1$ ) with the  $\text{CF}_3$  groups on the same side of the S–N–S plane and a *transoid* form ( $C_2$ ) with the  $\text{CF}_3$  groups on opposite sides of the plane.<sup>72</sup> The difference in the band positions may originate from these different conformations of the anions in the solvate crystal structures. Therefore, the data in Fig. 5.12a indicate that the 6/1 phase consists of uncoordinated  $\text{TFSI}^-$  anions with the  $C_1$  conformation, whereas the 4/1 phase consists of uncoordinated  $\text{TFSI}^-$  anions with both the  $C_1$  and  $C_2$  conformations. To

verify this, the 250-450  $\text{cm}^{-1}$  region of the Raman spectra for  $(\text{AN})_n\text{-LiTFSI}$  mixtures ( $n = 6$  and 4) was examined as the  $\text{TFSI}^-$  anion vibrational bands in this region provide a fingerprint for the uncoordinated anion conformations (Fig. 5.13).<sup>33,72</sup> The band position, however,

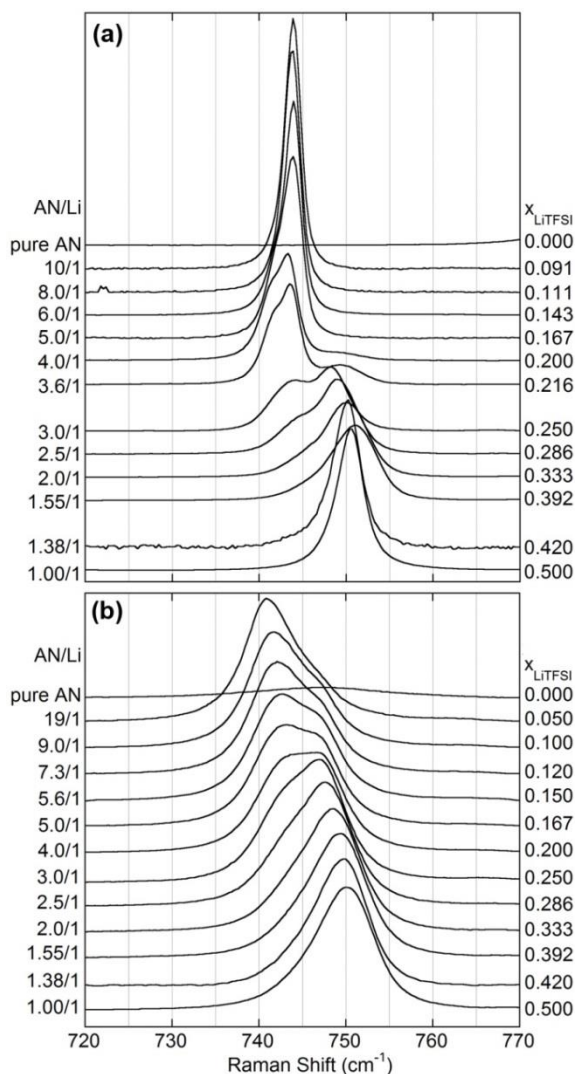


**Figure 5.12.** TFSI<sup>-</sup> anion band variation with concentration in  $(\text{AN})_n\text{-LiTFSI}$  mixtures at (a)  $-80\text{ }^\circ\text{C}$  and (b)  $60\text{ }^\circ\text{C}$ . The mixtures with  $n = 3.0, 2.5, 2.0$  and  $1.55$  are in the crystallinity gap and remain either fully amorphous liquids or glassy solids at  $-80\text{ }^\circ\text{C}$ .<sup>33</sup>

indicate that both phases consist only of anions with the  $C_2$  conformation. However, it is evident that there are new bands at  $382\text{ cm}^{-1}$  (Fig. 5.13a) for the  $n = 6$  sample and at  $315\text{ cm}^{-1}$  for the  $n = 4$  sample (Fig. 5.13b) which do not correspond to the bands typically noted for either the  $C_1$  or  $C_2$  conformations. Thus, it may be that one or more different low energy

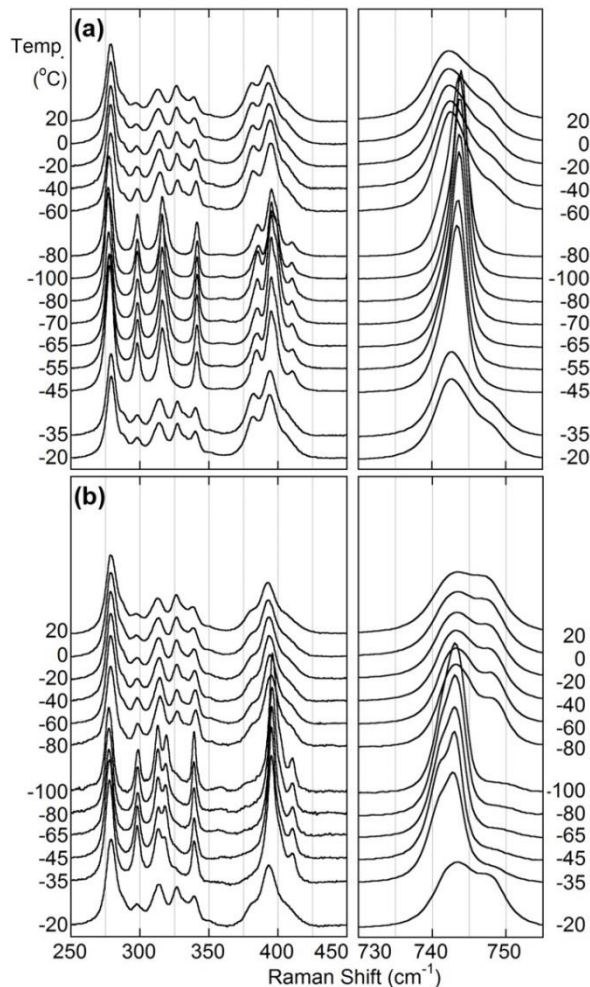


**Figure 5.13.** TFSI<sup>-</sup> anion band variation with temperature in (AN)<sub>n</sub>-LiTFSI mixtures with (a)  $n = 6.0$  (crystalline in the  $-80$  to  $-45\text{ }^{\circ}\text{C}$  range) and (b)  $n = 4.0$  (crystalline in the  $-100$  to  $-35\text{ }^{\circ}\text{C}$  range).<sup>33</sup>

conformation(s) for the TFSI<sup>-</sup> anion, which have been reported,<sup>73</sup> are present which would also account for the band at 741 cm<sup>-1</sup>. In the crystallinity gap (1.38 < n < 3.6), the samples are liquid or amorphous solids even at -80 °C and broad bands appear in the Raman spectra. With increasing concentration of LiTFSI, the Raman band variation indicates that more aggregated anion coordination (CIP and AGG) is present at the expense of the SSIP (uncoordinated) anion coordination. As the composition approaches n = 1, one sharp Raman band at 751 cm<sup>-1</sup> is observed corresponding to the AGG-IIb (AN)<sub>1</sub>:LiTFSI crystalline solvate (with the TFSI<sup>-</sup> anion coordinated to three Li<sup>+</sup> cations through four oxygens).

Fig. 5.12b shows the shift of the TFSI<sup>-</sup> anion Raman bands for the liquid mixtures at 60 °C with changing concentration. Unlike the data for the solid phases in Fig. 5.12a, the bands shift smoothly with changing concentration. Due to the different conformations from the structural flexibility of the TFSI<sup>-</sup> anion, each of the TFSI<sup>-</sup> anions may be coordinated in varying ways to one or more Li<sup>+</sup> cation(s) resulting in many different types of solvates in the liquid mixtures. Thus, it is challenging to deconvolute conclusively the overlapping bands from these numerous types of solvates to identify specific forms of anion coordination to the Li<sup>+</sup> cations. This has been done, however, using assignments from a current spectroscopic characterization study for crystalline (solvent)<sub>n</sub>:LiTFSI solvate structures with various solvents.<sup>74</sup> From the spectroscopic analysis, the solvate bands at -80 °C/60 °C are C<sub>2</sub>-SSIP (741/740 cm<sup>-1</sup> – uncoordinated TFSI<sup>-</sup> anions), C<sub>2</sub>-CIP-II (747/746 cm<sup>-1</sup> – TFSI<sup>-</sup> anion coordinated to a single Li<sup>+</sup> cation through two oxygen atoms), C<sub>2</sub>-AGG-Ib (749/748 cm<sup>-1</sup> – TFSI<sup>-</sup> anion coordinated to two Li<sup>+</sup> cations through three oxygen atoms) and C<sub>1</sub>-AGG-IIb

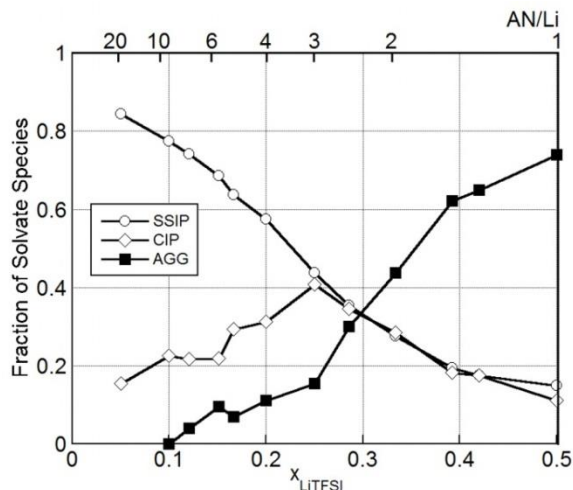


**Figure 5.14.** Solvate species distribution in  $(\text{AN})_n\text{-LiTFSI}$  mixtures at  $60\text{ }^\circ\text{C}$ .<sup>33</sup>

( $750\text{-}752/749\text{-}750\text{ cm}^{-1}$  –  $\text{TFSI}^-$  anion coordinated to three  $\text{Li}^+$  cations through four oxygen atoms). It is noteworthy that these bands may shift somewhat due to variability in the anion conformations and coordination bond lengths to the  $\text{Li}^+$  cations in the liquid phase. Fig. 5.14 shows the  $\text{TFSI}^-$  anion coordination distribution in liquid  $(\text{AN})_n\text{-LiTFSI}$  mixtures at  $60\text{ }^\circ\text{C}$  from the deconvolution of the peaks in Fig. 5.12b in terms of uncoordinated  $\text{TFSI}^-$  anions (SSIP), anions coordinated to a single  $\text{Li}^+$  cation (CIP) and those coordinated to more than one  $\text{Li}^+$  cation (AGG).<sup>33</sup> In dilute mixtures, SSIP coordination exists for more than 80% of the anions with the remainder having CIP coordination. With increasing salt concentration, the fraction of both CIP and AGG coordination increases at the expense of the SSIP coordination, but the CIP coordination starts to then decrease for more concentrated mixtures ( $n < 3$ ). Note that both the SSIP and CIP coordination persist even in the very concentrated

mixtures. Unlike for the  $\text{BF}_4^- \dots \text{Li}^+$  cation coordination, the close proximity of the bands for the  $\text{TFSI}^- \dots \text{Li}^+$  cation coordination obtained from the AGG crystalline  $(\text{solvent})_n \cdot \text{LiTFSI}$  solvates suggests that it is fruitless to attempt the identification of the different forms of the AGG  $\text{TFSI}^- \dots \text{Li}^+$  cation coordination in solution.

To study the reason for the crystallinity gap occurrence in the  $(\text{AN})_n \cdot \text{LiTFSI}$  mixtures, variable-temperature Raman measurements have been conducted for different compositions around the crystallinity gap (Fig. 5.15).<sup>33</sup> For the  $n = 4.0$  mixture, as the temperature decreases, the bands at 741 and 743  $\text{cm}^{-1}$  (corresponds to SSIP coordination) increase, while the band at 747-749  $\text{cm}^{-1}$  (attributed to CIP and AGG-I anion coordination) decreases. This indicates that the amount of SSIP solvates increases at lower temperature resulting in the nucleation and growth of the SSIP 4/1 crystalline phase. For the  $n = 3.0$  sample, however, as the temperature decreases, the SSIP bands at 741-743  $\text{cm}^{-1}$  increase, but there remains a sizeable amount of coordinated anions (corresponds to the Raman band on 748  $\text{cm}^{-1}$ ) thus hindering/preventing the formation of the 4/1 crystalline phase. Similarly, although the  $n = 2.0$  sample has a dominant peak at 750  $\text{cm}^{-1}$  (corresponding to AGG-II anion coordination as found in the 1/1 phase), a significant fraction of the anions still persist with SSIP, CIP and perhaps AGG-I coordination which hinder/prevent the nucleation and growth of the 1/1 crystalline phase. In contrast, for the  $n = 1.0$  sample, as the temperature decreases, most of the anions have AGG-II (or perhaps even higher) coordination, thus facilitating the nucleation of the 1/1 crystalline phase. Note that in the phase diagram for the  $(\text{AN})_n \cdot \text{LiTFSI}$  mixtures in Fig. 5.4, the “×” symbols indicate the  $T_g$  of the fully amorphous samples,

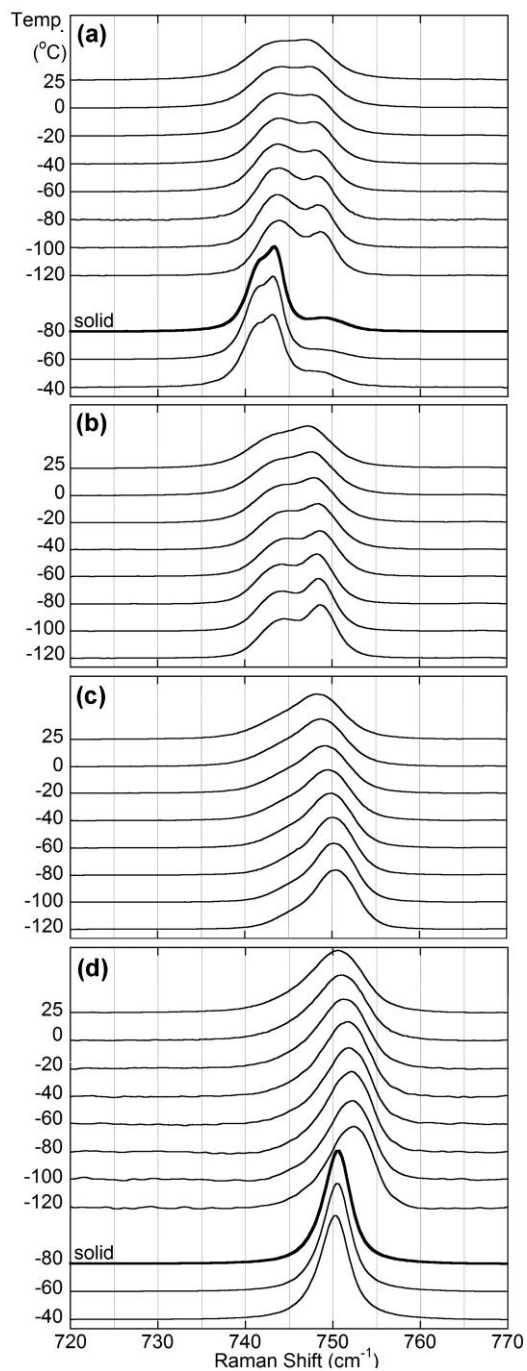


**Figure 5.15.** Variable-temperature TFSI<sup>-</sup> anion band variation with concentration in (AN)<sub>n</sub>-LiTFSI mixtures with (a)  $n = 4.0$ , (b)  $n = 3.0$ , (c)  $n = 2.0$  and (d)  $n = 1.0$ .<sup>33</sup>

whereas the “triangles” are the  $T_g$  for the amorphous phase which remains after some portion of a sample has crystallized as the 1/1 phase (partial crystallization). The composition of the latter amorphous phase will thus be more dilute than the composition of the sample itself. These samples have nearly the same  $T_g$  value of  $-82\text{ }^\circ\text{C}$  and this value can be used to estimate the composition of the stabilized amorphous phase (i.e.,  $x \sim 0.25$ ). This value corresponds to an average of 3 AN molecules per  $\text{Li}^+$  cation.<sup>33</sup>

Fig. 5.16a shows the band variation of the  $\text{PF}_6^-$  anion with varying concentration at  $-80$  and  $60\text{ }^\circ\text{C}$ .<sup>33</sup> Based upon octahedral ( $O_h$ ) symmetry from the uncoordinated  $\text{PF}_6^-$  anion, the band assignments have been determined.<sup>66,75-79</sup> As noted in Fig. 4.14, the most intense Raman band for the  $\text{PF}_6^-$  anion is observed at  $740\text{-}750\text{ cm}^{-1}$ . All of the mixtures are crystalline solids at  $-80^\circ\text{C}$ , as shown in Fig. 5.4b. For dilute mixtures ( $n \geq 5$ ), only a single band is evident at  $744\text{ cm}^{-1}$ . Based upon the previous chapter (Ch. 4.3) examining the crystalline  $(\text{solvent})_n\text{-LiPF}_6$  solvate structures with various solvents, it has been determined that the anions with SSIP (the uncoordinated  $\text{PF}_6^-$  anions) and CIP-I (the coordinated  $\text{PF}_6^-$  anions to a single  $\text{Li}^+$  cation via one fluorine atom) coordination have essentially the same Raman band position (wavenumber) for the P-F symmetrical stretch vibration of the anion (Fig. 4.16). It is therefore not possible to deconvolute the SSIP and CIP-I  $\text{PF}_6^-$  anion coordination bands, and the  $744\text{ cm}^{-1}$  band corresponds to SSIP or CIP solvates in which the  $\text{PF}_6^-$  anion is uncoordinated or coordinated to a single  $\text{Li}^+$  cation. There is a slight shift to higher wavenumber between the 6/1 and 5/1 samples which may be attributed to the differences in structure (i.e., lattice packing) between the  $(\text{AN})_6\text{:LiPF}_6$  and  $(\text{AN})_5\text{:LiPF}_6$

crystalline solvates. As the concentration increases ( $n \leq 5$ ), a new band appears at  $748 \text{ cm}^{-1}$  which corresponds to more aggregated phase (i.e., AGG-Ia, perhaps an  $(\text{AN})_1:\text{LiPF}_6$  phase) as shown in Fig. 4.16.

Fig. 5.16b shows that the  $\text{PF}_6^-$  anion Raman band for the liquid mixtures (at  $60 \text{ }^\circ\text{C}$ ) shifts to higher wavenumber and broadens as noted for other  $(\text{AN})_n\text{-LiX}$  mixtures.<sup>33</sup> In dilute

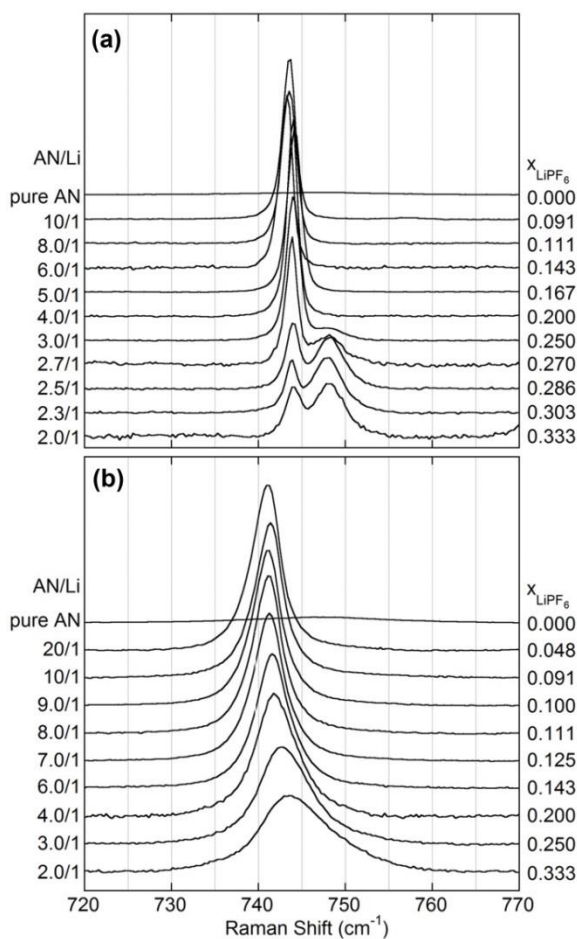


**Figure 5.16.**  $\text{PF}_6^-$  anion band variation with concentration in  $(\text{AN})_n\text{-LiPF}_6$  mixtures at (a)  $-80 \text{ }^\circ\text{C}$  and (b)  $60 \text{ }^\circ\text{C}$ .<sup>33</sup>

mixtures, one Raman band is observed at  $741\text{ cm}^{-1}$  which corresponds to SSIP and/or CIP solvates. As the concentration increases, an asymmetric shoulder at higher wavenumbers grows which is attributed to AGG anion coordination. It is clear that the SSIP and/or CIP solvates are dominant in dilute mixtures and these are also evident even in the concentrated mixtures. This confirms that  $\text{LiPF}_6$  is a highly dissociated salt.

## **5.5. MD Simulations of $(\text{AN})_n$ -Lithium Salt Mixtures**

One of the key challenges for utilizing MD simulations is associated with how the simulation results are to be analyzed and interpreted—assuming that the results are an accurate representation of real materials. To aid in this, the experimental work noted above has been directly correlated, where possible, with the simulations. MD simulations were performed by Dr. Oleg Borodin at the U.S. Army Research Laboratory (ARL).

### **5.5.1. $(\text{AN})_n$ -Lithium Salt Mixtures: Intermediate and Associated Salts**

Table 5.1 shows the fraction of the uncoordinated (fully solvated)  $\text{Li}^+$  cations, uncoordinated (free)  $\text{ClO}_4^-$  or  $\text{BF}_4^-$  anions and the composition of the  $\text{Li}^+$  cation solvation shell as determined by MD simulations.<sup>13</sup> Raman spectroscopic characterization, as shown above, focuses on the anion interactions, and thus only indirectly provides information about the  $\text{Li}^+$  cation interactions. To obtain a more comprehensive understanding of the solution structure, an MD simulation analysis was conducted by examining the proximity of the  $\text{Li}^+$

**Table 5.1.** Composition of the ion coordination shell from MD simulations of (AN)<sub>n</sub>-LiClO<sub>4</sub> and (AN)<sub>n</sub>-LiBF<sub>4</sub> mixtures at 60 °C (Note: some of the percentages do not sum to 100% due to the rounding off of the values). Experimental density values in parentheses were extrapolated from experimental data.<sup>13</sup>

<b>LiClO<sub>4</sub></b>						
Property	(AN:Li ratio):	30	20	10	5	2
No. solvent in MD box		480	640	640	640	512
No. LiClO <sub>4</sub> in MD box		16	32	64	128	256
Concentration (M)		0.59	0.88	1.73	3.26	6.66
Molality (mol kg <sup>-1</sup> )		0.75	1.09	1.95	3.24	5.40
Simulation box length (Å)		35.59	39.21	39.48	40.27	39.96
MD density (g cm <sup>-3</sup> )		0.788	0.817	0.893	101.9	1.255
Expt density (g cm <sup>-3</sup> )		0.788	0.818	0.899		
fraction of free Li ( $r_{\text{Li-Cl}} > 3.73$ Å) (SSIP)		0.44	0.39	0.30	0.17	0.05
fraction of free Cl ( $r_{\text{Li-Cl}} > 3.73$ Å) (SSIP)		0.42	0.36	0.24	0.12	0.01
<b>Li<sup>+</sup> coordination numbers</b>						
# N (within 2.40 Å of Li <sup>+</sup> )		3.13	3.05	2.80	2.44	1.67
# O (within 2.40 Å of Li <sup>+</sup> )		0.68	0.77	1.04	1.42	2.25
# Cl (within 3.73 Å of Li <sup>+</sup> )		0.69	0.77	1.04	1.41	2.27
<b>probability of finding the following number of Li<sup>+</sup> cations within the given distance from the Cl of ClO<sub>4</sub><sup>-</sup></b>						
0 Li <sup>+</sup> within 3.50/3.73 Å of Cl (SSIP)		0.46/0.40	0.42/0.35	0.29/0.22	0.17/0.10	0.03/0.01
1 Li <sup>+</sup> within 3.50/3.73 Å of Cl (CIP)		0.47/0.51	0.50/0.53	0.53/0.54	0.50/0.45	0.27/0.15
2 Li <sup>+</sup> within 3.50/3.73 Å of Cl (AGG-I)		0.06/0.09	0.09/0.12	0.16/0.22	0.29/0.37	0.47/0.45
3 Li <sup>+</sup> within 3.50/3.73 Å of Cl (AGG-II)		0.00/0.00	0.00/0.01	0.01/0.02	0.04/0.07	0.21/0.34
4 Li <sup>+</sup> within 3.50/3.73 Å of Cl (AGG-III)		0.00/0.00	0.00/0.00	0.00/0.00	0.00/0.00	0.02/0.05

**Table 5.1.** Continued

<b>LiBF<sub>4</sub></b>						
Property	(AN:Li ratio):	30	20	10	5	2
No. solvent in MD box		480	640	640	640	512
No. LiBF <sub>4</sub> in MD box		16	32	64	128	256
Concentration (M)		0.58	0.87	1.70	3.20	6.63
Molality (mol kg <sup>-1</sup> )		0.75	1.09	1.98	3.34	5.69
Simulation box length (Å)		35.78	39.42	39.71	40.51	40.02
MD density (g cm <sup>-3</sup> )		0.769	0.793	0.856	0.956	1.166
Expt density (g cm <sup>-3</sup> )		0.781	0.804	0.859	(0.961)	
fraction of free Li ( $r_{\text{Li-B}} > 3.60 \text{ \AA}$ ) (SSIP)		0.16	0.13	0.09	0.05	0.02
fraction of free B ( $r_{\text{Li-B}} > 3.60 \text{ \AA}$ ) (SSIP)		0.11	0.08	0.04	0.01	0.00
<b>Li<sup>+</sup> coordination numbers</b>						
# N (within 2.40 Å of Li <sup>+</sup> )		2.31	2.16	1.94	1.67	1.29
# F (within 2.40 Å of Li <sup>+</sup> )		1.58	1.75	2.00	2.29	2.72
# B (within 3.60 Å of Li <sup>+</sup> )		1.52	1.70	1.95	2.25	2.68
<b>probability of finding the following number of Li<sup>+</sup> cations within the given distance from the B of BF<sub>4</sub><sup>-</sup></b>						
0 Li <sup>+</sup> within 3.33/3.60 Å of B (SSIP)		0.15/0.11	0.12/0.08	0.07/0.04	0.03/0.01	0.01/0.00
1 Li <sup>+</sup> within 3.33/3.60 Å of B (CIP)		0.45/0.40	0.40/0.34	0.34/0.25	0.26/0.16	0.15/0.05
2 Li <sup>+</sup> within 3.33/3.60 Å of B (AGG-I)		0.32/0.37	0.37/0.41	0.44/0.46	0.46/0.44	0.45/0.34
3 Li <sup>+</sup> within 3.33/3.60 Å of B (AGG-II)		0.08/0.12	0.11/0.17	0.15/0.23	0.22/0.34	0.34/0.48
4 Li <sup>+</sup> within 3.33/3.60 Å of B (AGG-III)		0.00/0.00	0.00/0.00	0.01/0.02	0.02/0.05	0.05/0.13

cations to the chloride/boron atom of the ClO<sub>4</sub><sup>-</sup>/BF<sub>4</sub><sup>-</sup> anions. The method and reason for choosing the distances of 2.40 Å, 3.60 Å and 3.33 Å for LiBF<sub>4</sub> (2.40 Å, 3.50 Å and 3.73 Å for LiClO<sub>4</sub>) in Table 5.1 are explained in a previous study.<sup>13</sup> Comparing the results in Table 5.1 for LiBF<sub>4</sub> and LiClO<sub>4</sub>, LiClO<sub>4</sub> is more dissociated than LiBF<sub>4</sub>, in agreement with the experimental results.

In Table 5.1, the number of nitrogen atoms from AN coordinated to the Li<sup>+</sup> cations (average solvation number *N*) is in reasonable agreement with the experimental data shown in Fig. 5.7 for the dilute mixtures (for which there may be considerable error in the

experimental results). With increasing concentration ( $\text{AN}:\text{Li} \leq 10$ ), however, there is a large discrepancy between the values with the MD simulation having lower values. The larger fraction of AGG-II and AGG-III anion coordination, as determined from the simulations (for  $\text{LiBF}_4$ ), may partially influence this discrepancy.

Upon increasing the salt concentration in the simulation box, the  $\text{BF}_4^-$  anions replaces AN molecules in the  $\text{Li}^+$  cation coordination shells in such a way that the average number of coordinated nitrogen (from AN) and fluorine atoms within 2.40 Å of the  $\text{Li}^+$  cations remains approximately constant (between 3.89 and 4.01) over the entire range of simulated salt concentrations (Table 5.1). It is noteworthy that the number of fluorine atoms coordinated to the  $\text{Li}^+$  cations is only slightly larger than those of boron atoms indicating that the reported most energetically favorable complexes of  $\text{Li}^+/\text{BF}_4^-$  with C2V and C3V symmetry with two (CIP-II) and three (CIP-III) fluorine atoms coordinating a single  $\text{Li}^+$  cation, respectively,<sup>80,81</sup> are not favorable in the liquid phase at higher temperature (60 °C).<sup>13</sup> This result indicates that the  $\text{BF}_4^-$  anions predominantly coordinate each  $\text{Li}^+$  cation with a single fluorine atom (for CIP solvates). Similarly, the previous simulation analysis for EC:DMC/ $\text{LiPF}_6$  indicates that the coordination of  $\text{PF}_6^-$  anions to  $\text{Li}^+$  cations via one fluorine atom.<sup>82</sup> Table 5.1 shows the analogous simulation results for the  $(\text{AN})_n\text{-LiClO}_4$  mixtures, as well.

At this time, it is not completely clear why discrepancies exist between the experimental results and simulations. Many challenges remain for accurately simulating systems with charged species. However, the simulations still provide key information about plausible

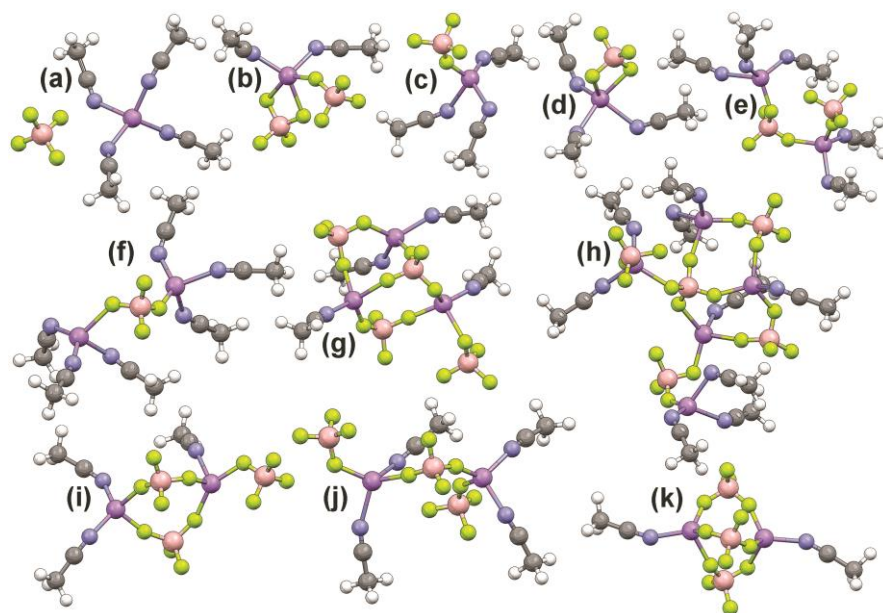


**Figure 5.17.** Representative  $\text{Li}^+$  cation solvate species (i.e., coordination shells) extracted from the MD simulations for the  $(\text{AN})_n\text{-LiBF}_4$  mixtures ( $n = 30, 20$  and  $10$ ) at  $60\text{ }^\circ\text{C}$ : (a) SSIP, (b) CIP-I, CIP-II, (c) CIP-I, (d) CIP-II, (e) CIP-I, AGG-I, (f) AGG-I, (g) CIP-I, AGG-I ( $\times 3$ ), (h) CIP-I, AGG-I ( $\times 3$ ), AGG-III, (i) CIP-I, AGG-I ( $\times 2$ ), (j) CIP-I ( $\times 2$ ), AGG-I and (k) AGG-I ( $\times 3$ ). Solvent and  $\text{BF}_4^-$  anions within  $3.33\text{ \AA}$  of a  $\text{Li}^+$  cation are shown (Li-purple, N-blue, B-tan, F-light green).<sup>13</sup>

solvate structures in solution which is unavailable directly from the experimental techniques used. For example, an examination of the solvate snapshots from the simulations (Fig. 5.17)<sup>13</sup> shows that the solvate distribution noted in Fig. 5.10 from the Raman spectroscopic data for the anion interactions is too simplistic. As shown in Figs. 5.17e, 5.17g, 5.17h, 5.17i and 5.17j, aggregate clusters contain end  $\text{BF}_4^-$  anions coordinated to a single  $\text{Li}^+$  cation through a single fluorine atom. The Raman spectroscopic data for these anions would recognize them as CIP-I solvates, even though these are actually part of larger AGG solvates. Another anion

(Figs. 5.17e) is coordinated to two  $\text{Li}^+$  cations, but with one of these  $\text{Li}^+$  cations only coordinated to the single anion thus differing from the dimeric or polymeric crystalline solvates, in which the  $\text{Li}^+$  cations are coordinated by two anions, that might be expected for AGG-I solvates. Thus, the evaluation of the experimental spectroscopic data requires some caution to avoid misconstruing the solution structure for a given electrolyte. Despite the discrepancies between the experimental and computational results, a much improved picture of the solvate structures in solution emerges when both results are examined in conjunction with one another.<sup>13</sup>

### 5.5.2. $(\text{AN})_n$ -Lithium Salt Mixtures: Dissociated Salts

Utilizing MD simulations, the calculated solvate structures in solution were examined and the ionic association tendency of the salts  $\text{LiPF}_6$  and  $\text{LiTFSI}$  in AN was explored. The MD simulations was performed to determine the fraction of the uncoordinated (fully solvated)  $\text{Li}^+$  cations and anions ( $\text{PF}_6^-$  or  $\text{TFSI}^-$ ) and the coordination of the anions, as shown in Tables 5.2 and 5.3.<sup>33</sup> The  $\text{Li}^+$  cation coordination to the  $\text{TFSI}^-$  or  $\text{PF}_6^-$  anions was defined as  $\text{Li}^+$  cations within 4.74 or 3.70 Å from the N or P atoms of the anions, respectively.<sup>33</sup>

For the  $(\text{AN})_n$ - $\text{LiPF}_6$  mixtures, reasonable agreement is noted between the MD simulations (Table 5.2) and experimental data (Fig. 5.16). For the dilute mixtures,SSIP solvates—uncoordinated anions and fully solvated  $\text{Li}^+$  cations—are dominant. Fig. 5.18 shows examples of the solvate complexes found in the simulation for the dilute mixtures ( $n =$

**Table 5.2.** Composition of the ion coordination shell from MD simulations of (AN)<sub>n</sub>-LiPF<sub>6</sub> mixtures at 60 °C (Note: some of the percentages do not sum to 100% due to the rounding off of the values).<sup>33</sup>

<b>LiPF<sub>6</sub></b>						
Property	(AN:Li ratio):	30	20	10	5	2
No. solvent in MD box		480	640	640	640	512
No. LiPF <sub>6</sub> in MD box		16	32	64	128	256
Concentration (M)		0.58	0.87	1.67	3.06	5.89
Molality (mol kg <sup>-1</sup> )		0.72	1.03	1.78	2.80	4.27
Simulation run length <sup>a</sup> (ns)		12.0 (4)	11.0 (4)	7.7 (2)	18.0 (4)	14.0 (4)
Simulation box length (Å)		35.78	39.42	39.71	40.51	40.02
MD density (g cm <sup>-3</sup> )		0.802	0.844	0.938	1.091	1.379
Expt density (g cm <sup>-3</sup> )		0.814	0.842	0.936		
Fraction of free Li ( $r_{\text{Li-P}} > 3.70 \text{ \AA}$ ) (SSIP)		0.66	0.61	0.47	0.30	0.06
Fraction of free P ( $r_{\text{Li-P}} > 3.70 \text{ \AA}$ ) (SSIP)		0.66	0.60	0.44	0.24	0.02
<b>Li<sup>+</sup> coordination numbers</b>						
# N (within 2.40 Å of Li <sup>+</sup> )		3.42	3.37	3.15	2.84	1.81
# F (within 2.40 Å of Li <sup>+</sup> )		0.38	0.44	0.68	1.02	2.13
# P (within 3.70 Å of Li <sup>+</sup> )		0.36	0.42	0.62	0.96	2.00
<b>Probability of finding the following number of Li<sup>+</sup> cations within the given distance from the P of PF<sub>6</sub><sup>-</sup></b>						
0 Li <sup>+</sup> within 3.50/3.70 Å of P (SSIP)		0.70/0.66	0.65/0.60	0.50/0.44	0.31/0.24	0.11/0.02
1 Li <sup>+</sup> within 3.50/3.70 Å of P (CIP)		0.29/0.33	0.34/0.38	0.46/0.50	0.56/0.58	0.34/0.24
2 Li <sup>+</sup> within 3.50/3.70 Å of P (AGG-I)		0.01/0.01	0.01/0.02	0.04/0.06	0.12/0.18	0.36/0.50
3 Li <sup>+</sup> within 3.50/3.70 Å of P (AGG-II)		0.00/0.00	0.00/0.00	0.00/0.00	0.00/0.01	0.16/0.22
4 Li <sup>+</sup> within 3.50/3.70 Å of P (AGG-III)		0.00/0.00	0.00/0.00	0.00/0.00	0.00/0.00	0.02/0.02

<sup>a</sup> equilibration run lengths are given in parentheses, <sup>b</sup> experimental density value in parentheses was extrapolated from experimental data

30, 20 and 10).<sup>33</sup> Note that bidentate coordination of the PF<sub>6</sub><sup>-</sup> anion to a Li<sup>+</sup> cation (i.e., Fig. 5.18f) is only rarely observed, as reflected by the similarity of the values for the number of fluorine and phosphorus atoms in close proximity (within 2.40 and 3.70 Å, respectively) to a Li<sup>+</sup> cation (Table 5.2).<sup>33</sup> For the most concentrated mixtures, the average solvation numbers (*N*) from the MD simulations (Table 5.2) and experiments (Fig. 5.7) reasonably agreed with

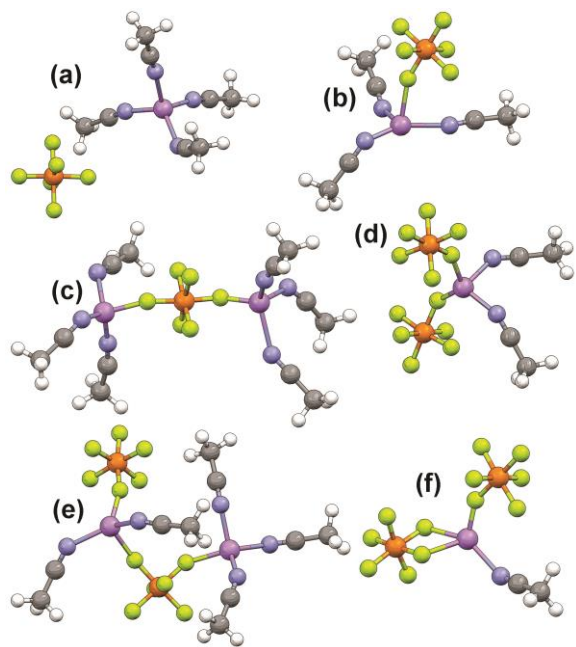


**Figure 5.18.** Representative  $\text{Li}^+$  cation solvate species (i.e., coordination shells) extracted from the MD simulations for the  $(\text{AN})_n\text{-LiPF}_6$  mixtures ( $n = 30, 20$  and  $10$ ) at  $60\text{ }^\circ\text{C}$ : (a) SSIP, (b) CIP-I, (c) AGG-I, (d) CIP-I ( $\times 2$ ), (e) CIP-I, AGG-I and (f) CIP-I, CIP-II (Li-purple, N-blue, P-orange, F-light green).<sup>33</sup>

each other, but there is a difference in the values for the  $n = 10$  composition ( $N = 3.15$  from the MD simulation, but  $\sim 4$  from the experimental results). It is not possible to distinguish between SSIP and CIP anion coordination in the experimental data for the  $n = 10$  mixture at  $60\text{ }^\circ\text{C}$  (Fig. 16b), but it may be that the simulation (i.e., force fields) overpredicts the degree of ionic association of the electrolyte mixture, as was also true for the mixtures with  $\text{LiBF}_4$  and perhaps  $\text{LiClO}_4$ .

For the highly concentrated  $(\text{AN})_n\text{-LiTFSI}$  mixtures, a comparison of the MD simulation results (Table 5.3) with the experimental data (Fig. 5.12) shows reasonable agreement. For

**Table 5.3.** Composition of the ion coordination shell from MD simulations of (AN)<sub>n</sub>-LiTFSI mixtures at 60 °C (Note: some of the percentages do not sum to 100% due to the rounding off of the values).<sup>33</sup>

<b>LiTFSI</b>						
Property	(AN:Li ratio):	30	20	10	5	2
No. solvent in MD box		480	640	640	640	512
No. LiTFSI in MD box		16	32	64	128	256
Concentration (M)		0.56	0.81	1.46	2.43	3.98
Molality (mol kg <sup>-1</sup> )		0.72	1.03	1.78	2.80	4.27
Simulation run length <sup>a</sup> (ns)		17.3 (6)	12.2 (4)	7.0 (9)	15.3 (16)	15.0 (16)
Simulation box length (Å)		36.30	40.35	41.74	44.38	43.11
MD density (g cm <sup>-3</sup> )		0.844	0.896	1.019	1.197	1.469
Expt density (g cm <sup>-3</sup> )		0.861	0.887	1.005	1.176	(1.385) <sup>b</sup>
Fraction of free Li ( $r_{\text{Li-N}} > 4.74 \text{ \AA}$ ) (SSIP)		0.37	0.31	0.20	0.10	0.02
Fraction of free N* ( $r_{\text{Li-N}} > 4.74 \text{ \AA}$ ) (SSIP)		0.36	0.27	0.16	0.06	0.01
<b>Li<sup>+</sup> coordination numbers</b>						
# N** (within 2.40 Å of Li <sup>+</sup> )		3.00	2.88	2.63	2.23	1.45
# O (within 2.40 Å of Li <sup>+</sup> )		0.83	0.97	1.24	1.67	2.49
# N* (within 4.74 Å of Li <sup>+</sup> )		0.75	0.89	1.14	1.57	2.42
<b>Probability of finding the following number of Li<sup>+</sup> cations within the given distance from the N of TFSI<sup>-</sup></b>						
0 Li <sup>+</sup> within 4.56/4.74 Å of N (SSIP)		0.41/0.36	0.32/0.27	0.25/0.16	0.10/0.06	0.02/0.01
1 Li <sup>+</sup> within 4.56/4.74 Å of N (CIP)		0.52/0.55	0.57/0.58	0.50/0.56	0.47/0.41	0.20/0.12
2 Li <sup>+</sup> within 4.56/4.74 Å of N (AGG-I)		0.07/0.10	0.11/0.14	0.22/0.25	0.36/0.42	0.45/0.41
3 Li <sup>+</sup> within 4.56/4.74 Å of N (AGG-II)		0.00/0.00	0.01/0.01	0.03/0.03	0.07/0.10	0.28/0.37
4 Li <sup>+</sup> within 4.56/4.74 Å of N (AGG-III)		0.00/0.00	0.00/0.00	0.00/0.00	0.00/0.01	0.05/0.09

\* N from TFSI, \*\* N from AN

<sup>a</sup> equilibration run lengths are given in parentheses, <sup>b</sup> experimental density value in parentheses was extrapolated from experimental data

the (AN)<sub>n</sub>-LiTFSI (n = 5) mixture, simulations predict that the Li<sup>+</sup> cations have (on average) 0.6 less AN coordination as compared to the (AN)<sub>n</sub>-LiPF<sub>6</sub> (n = 5) mixture, in reasonable agreement with the experimental data for n = 4 (i.e., x = 0.20) where coordination of the Li<sup>+</sup> cations in the (AN)<sub>n</sub>-LiTFSI mixture contains 0.4 less AN (on average) than in the (AN)<sub>n</sub>-

LiPF<sub>6</sub> mixture (Fig. 5.7). However, there is poor agreement between the MD simulations (Table 5.3) and experimental data (Fig. 5.14) for the dilute mixtures. The experimental data from the phase behavior (Fig. 5.4) and the anion spectroscopy (Figs. 5.12 and 5.14) analysis indicates that the LiTFSI salt is highly dissociated, although to a lesser extent than LiPF<sub>6</sub>. The MD simulations results, however, suggest that the majority of the TFSI<sup>-</sup> anions are coordinated to the Li<sup>+</sup> cations as CIP solvates and the solvation number of LiTFSI (Table 5.3) is lower than that of LiClO<sub>4</sub>. No experimental evidence supports the MD simulation conclusion that LiTFSI is more associated than LiClO<sub>4</sub>. For the estimated experimental solvate distribution (Fig. 5.14), there is one potential source of error in the use of a band at 747 cm<sup>-1</sup> to estimate the fraction of CIP solvates during the band deconvolution. The QC calculation results<sup>33</sup> suggest that this may only account for the CIP-II (bidentate) coordination, while the CIP-I (monodentate) coordination may be included with the SSIP fraction due to band overlap. Thus, a new band would need to be introduced during the deconvolution (for CIP-I solvates) which would change both the SSIP and CIP (i.e., CIP-II) band areas resulting in an increase in the fraction of SSIP coordination and decrease in the fraction of CIP coordination, respectively. Even so, it is still evident that the MD simulations predict for the dilute mixtures increased ionic association (fraction of CIP and AGG solvates) relative to the experimental data—this is true for all of the salts studied thus far (i.e., LiPF<sub>6</sub>, LiTFSI, LiClO<sub>4</sub> and LiBF<sub>4</sub>).

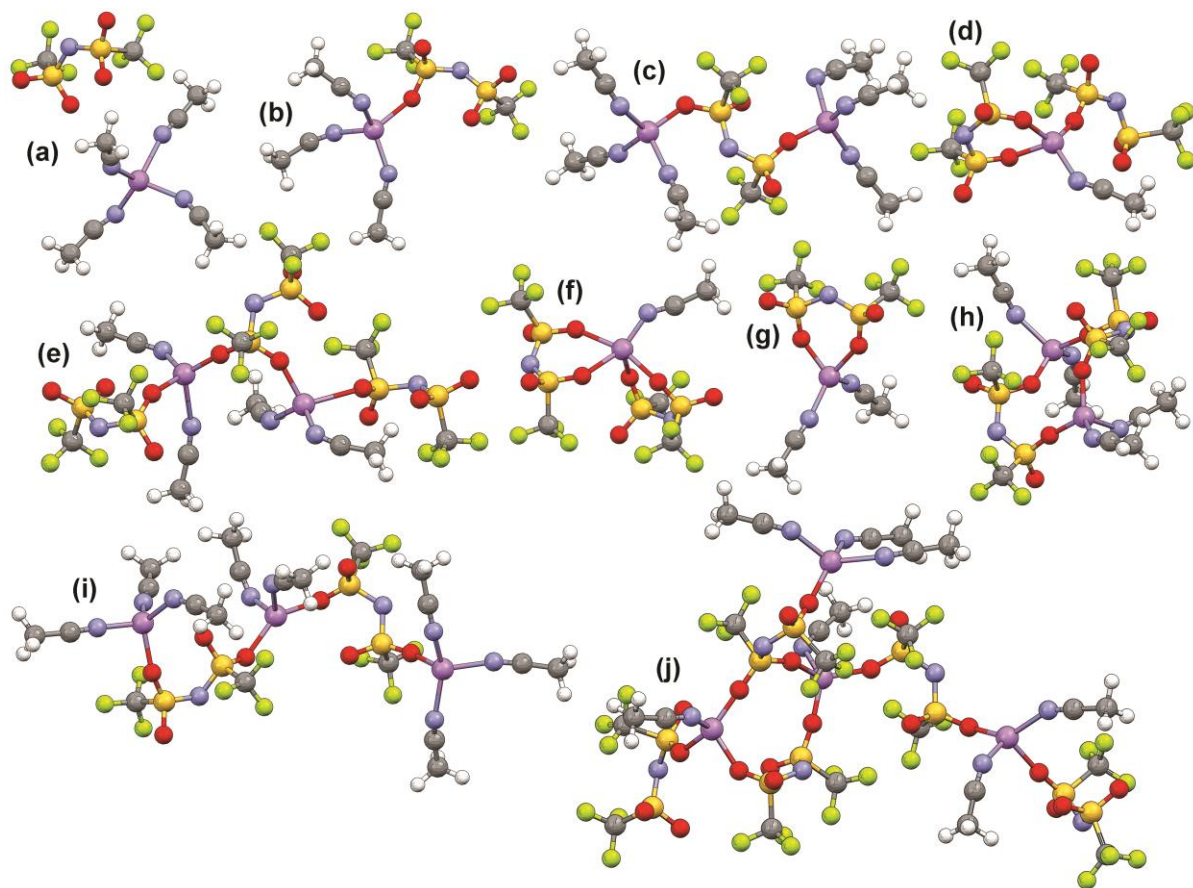


**Figure 5.19.** Representative  $\text{Li}^+$  cation solvate species (i.e., coordination shells) extracted from the MD simulations for the  $(\text{AN})_n\text{-LiTFSI}$  mixtures ( $n = 30, 20$  and  $10$ ) at  $60\text{ }^\circ\text{C}$ : (a)  $C_1\text{-SSIP}$ , (b)  $C_1\text{-CIP-I}$ , (c)  $C_2\text{-AGG-I}$ , (d)  $C_2\text{-CIP-I}$ ,  $C_1\text{-CIP-II}$  (e)  $C_2\text{-CIP-I}$  ( $\times 2$ ),  $C_1\text{-AGG-I}$ , (f)  $C_2\text{-CIP-II}$  ( $\times 2$ ), (g)  $C_1\text{-CIP-II}$ , (h)  $C_1\text{-AGG-I}$  ( $\times 2$ ), (i)  $C_1\text{-AGG-I}$ ,  $C_2\text{-AGG-I}$  and (j)  $C_1\text{-CIP-I}$  ( $\times 2$ ),  $C_1\text{-AGG-I}$ ,  $C_2\text{-AGG-I}$ ,  $C_2\text{-AGG-II}$  (Li-purple, N-blue, O, red, S-yellow, F-light green).<sup>33</sup>

Although there are discrepancies between the simulation and experimental results, it is quite informative to explore the coordination manner of the  $\text{TFSI}^-$  anions and the  $\text{Li}^+$  cations in the solvates from the MD simulations, as shown in Fig. 5.19.<sup>33</sup> Compared to the semi-

spherical anions (i.e.,  $\text{PF}_6^-$ ,  $\text{ClO}_4^-$  and  $\text{BF}_4^-$ ), bidentate coordination of the  $\text{TFSI}^-$  anion is more common in the MD simulations (Fig. 5.19d, 5.19f and 5.19g). For instance, for the  $n = 10$  concentration, 12% of the  $\text{TFSI}^-$  anions have two oxygen atoms from the same anion coordinated to the same  $\text{Li}^+$  cation, which is similar to the observations from previous simulations of  $(\text{EC})_n\text{-LiTFSI}^{83}$  and  $(\text{ionic liquid})_n\text{-LiTFSI}^{84}$  mixtures. As noted above, this can be one possible explanation for the lower than expected experimental average solvation numbers for  $\text{LiTFSI}$  (as comparable to  $\text{LiClO}_4$ ) despite the additional experimental evidence (i.e., phase diagram and Raman spectroscopy of the  $\text{TFSI}^-$  anion coordination) which suggest that  $\text{LiTFSI}$  is more dissociated than  $\text{LiClO}_4$  in AN. Thus, the designation of the  $\text{TFSI}^-$  anion as “highly dissociated” may be questionable and it may be more appropriate to categorize this anion instead as “dissociated” with the  $\text{PF}_6^-$  anion retaining the “highly dissociated” appellation.<sup>33</sup>

## 5.6. Transport Properties of $(\text{AN})_n\text{-Lithium Salt Mixtures}$

A systematic approach for electrolyte study has been employed to explore how solution structure dictates electrolyte properties.<sup>85</sup> In particular, the transport properties (viscosity and ionic conductivity) of  $(\text{AN})_n\text{-LiX}$  mixtures with  $\text{LiPF}_6$ ,  $\text{LiTFSI}$ ,  $\text{LiClO}_4$ ,  $\text{LiBF}_4$  and  $\text{LiCF}_3\text{CO}_2$  are reported here. Widely varying ion solvation/ionic association behavior of these salts is directly reflected in the transport properties of the AN solutions. Utilizing the solution structure in concert with molecular dynamic (MD) simulations, mechanistic explanations for

the variability noted in the transport properties of the electrolyte mixtures are provided.

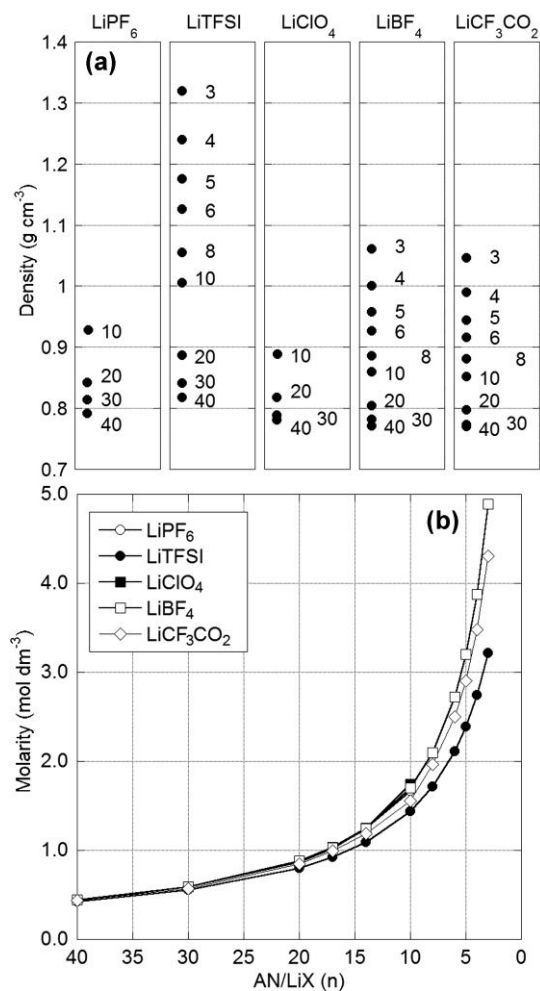
### 5.6.1. Concentration and Density of (AN)<sub>n</sub>-LiX Mixtures

The formula weights ( $\text{g mol}^{-1}$ ) of the lithium salts are:  $\text{LiPF}_6$  (151.91),  $\text{LiTFSI}$  (287.09),  $\text{LiClO}_4$  (106.39),  $\text{LiBF}_4$  (93.75) and  $\text{LiCF}_3\text{CO}_2$  (119.96). Density data for the (AN)<sub>n</sub>-LiX mixtures with varying temperature and salt concentration are reported in Appendix C.<sup>85</sup> The isothermal density data (60 °C) of the (AN)<sub>n</sub>-LiX mixtures are provided in Fig. 5.20a.<sup>85</sup> It is helpful to relate the properties to the ratio of solvent molecules per  $\text{Li}^+$  cation (i.e.,  $n$  or literature is given in terms of molarity or molality. Therefore, Fig. 5.20b shows the link between the concentration ( $n$ ) vs. molarity (M or  $\text{mol-salt dm}^{-3}$ -solution).<sup>85</sup> For the concentrated mixtures ( $n < 20$ ), the different salts result in differing molarity values for a fixed  $n$  concentration. As a reference point, a 1.0 M solution corresponds to a concentration of  $n \sim 15$ -18 (for the AN solutions) (Fig. 5.20b).

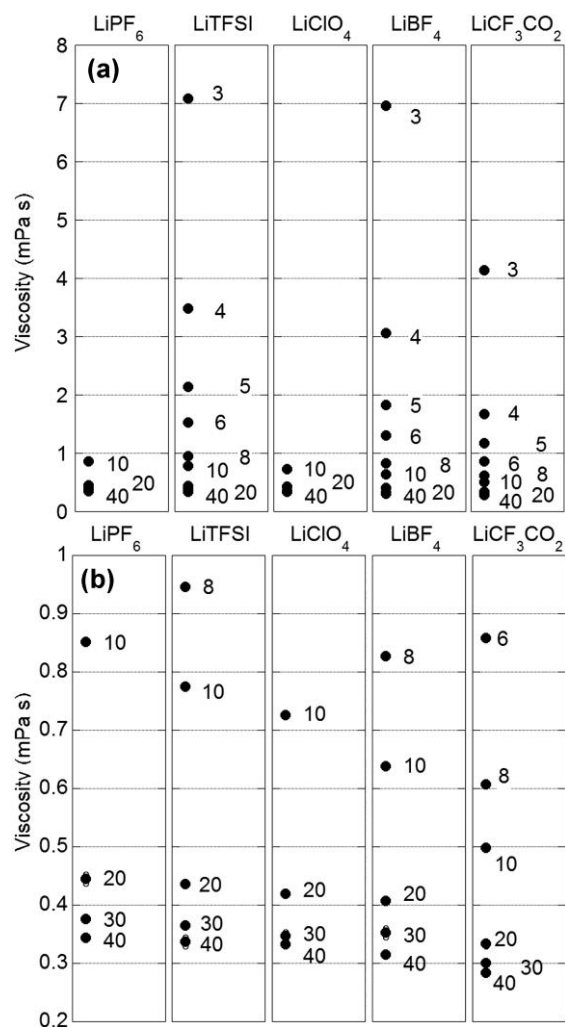
### 5.6.2. Viscosity of (AN)<sub>n</sub>-LiX Mixtures

Fig. 5.21 shows the isothermal viscosity values (60 °C) of the (AN)<sub>n</sub>-LiX mixtures.<sup>85</sup> Viscosity data for the (AN)<sub>n</sub>-LiX mixtures with varying temperature and salt concentration are reported in Appendix C. Viscosity is a measure of a fluid's resistance to deformation (internal resistance to flow) by shear (or tensile) stress.<sup>85</sup> From the MD simulations, the electrolytes studied (except for the most concentrated electrolytes) are composed principally

of mixtures of isolated (rather than polymeric) solvates, anions and uncoordinated solvent molecules.<sup>13,33,85</sup> For mixtures with different concentrations and anions, the identity of these solvates and their distribution differ significantly. The previous MD simulation studies show that the most dissociated salts have a greater amount of solvent coordinated to the  $\text{Li}^+$  cations



**Figure 5.20.** (a) Density of  $(\text{AN})_n\text{-LiX}$  mixtures at 60 °C ( $\text{AN}/\text{LiX}$  ( $n$ ) noted in plots) and (b) relationship between molarity vs.  $\text{AN}/\text{LiX}$  ( $n$ ) for  $(\text{AN})_n\text{-LiX}$  mixtures.<sup>85</sup>



**Figure 5.21.** (a) Viscosity of (AN)<sub>n</sub>-LiX mixtures at 60 °C (AN/LiX (n) noted in plots) and (b) the same data for the dilute mixtures alone. Data for concentrated mixtures with LiPF<sub>6</sub> and LiClO<sub>4</sub> was not gathered as these samples crystallize during the measurements.<sup>85</sup>

and thus less uncoordinated solvent.<sup>13,33,85</sup> In contrast, the more associated salts have more uncoordinated solvent which may serve as a lubricant for the solvates thus (in part) contributing to the reduction in the solution viscosity. In addition, the more dissociated salts

will result in more charged species dispersed in solution which will also impact the viscosity as these species will have greater long-range electrostatic interactions with one another (i.e., effectively creating a charged network rather than isolated clusters of charged entities). The order of increasing ionic association in the (AN)<sub>n</sub>-LiX mixtures is:<sup>13,33</sup>



The observed differences in viscosity for the most dilute mixtures (i.e.,  $n \geq 8$ ) agree well with this order (Fig. 5.21b). For the most concentrated mixtures (i.e.,  $n \leq 5$ ), the viscosity values for the LiTFSI and LiBF<sub>4</sub> mixtures are close, but those for the LiCF<sub>3</sub>CO<sub>2</sub> mixtures are notably lower (Fig. 5.21a). The highly concentrated mixtures begin to resemble clusters of SSIP, CIP and AGG solvates all closely packed together (with different distributions for different anions), so there is little to no uncoordinated solvent separating the solvates. Thus, the anions surround the fully or partially solvated cations to which they are either in close proximity or directly coordinated. The reduction in the shielding and separation of the charged ions results in stronger electrostatic interactions between the ions which strongly dictate both the mobility and positioning of the neighboring ions (i.e., influence the manner in which the ions realign relative to one another). This, in turn, greatly increases the viscosity. In the case of the LiCF<sub>3</sub>CO<sub>2</sub> mixtures, the salt forms concentrated AGG solvates (approximately one AN molecule per Li<sup>+</sup> cation) in solution, even in very dilute mixtures. Therefore, even for the highly concentrated mixtures, there are still a sizeable amount of uncoordinated solvent molecules present resulting in a much lower solution viscosity than for the other salt mixtures.

### 5.6.3. Conductivity of (AN)<sub>n</sub>-LiX Mixtures

Fig. 5.22 shows the variation with temperature and concentration of the ionic conductivity of the (AN)<sub>n</sub>-LiX mixtures.<sup>85</sup> Based upon the previously reported phase behavior for (AN)<sub>n</sub>-LiPF<sub>6</sub>, -LiClO<sub>4</sub>, -LiBF<sub>4</sub> mixtures (Figs. 5.1 and 5.4), the rapid drops in the conductivity plots (Figs. 5.22a, 5.22c and 5.22d) are due to the crystallization of solvates in these mixtures. It is difficult to ascribe particular meaning to the data in these figures as they are quite convoluted, but an examination of Fig. 5.22 indicates two trends. First, the more dilute solutions have (more) Arrhenius-like (linear) behavior, while the concentrated solutions have Vogel–Tammann–Fulcher (VTF)-like (curved) behavior, in particular, at low temperature.<sup>85</sup> The ionic association information mentioned above (i.e., increasing association with increasing concentration for these salts) suggests that increasing the ionic interactions corresponds to a transition from Arrhenius to VTF behavior. However, the data for the most associated salts (i.e., LiBF<sub>4</sub> and LiCF<sub>3</sub>CO<sub>2</sub>) have less curvature than those for more dissociated salts (i.e., LiTFSI) contradicting this interpretation. Note that an alternative to the VTF description of conductivity has also recently been proposed using a compensated Arrhenius explanation where the non-Arrhenius portion of the data is attributed to the temperature dependence of the dielectric constant contained in an exponential prefactor.<sup>86</sup> In practice, however, the fitted parameters from these forms of analysis provide only limited insight into conductivity mechanisms within electrolytes, so the detailed solution structure information provides an alternative for obtaining the necessary additional insight to aid in interpreting the conductivity data.

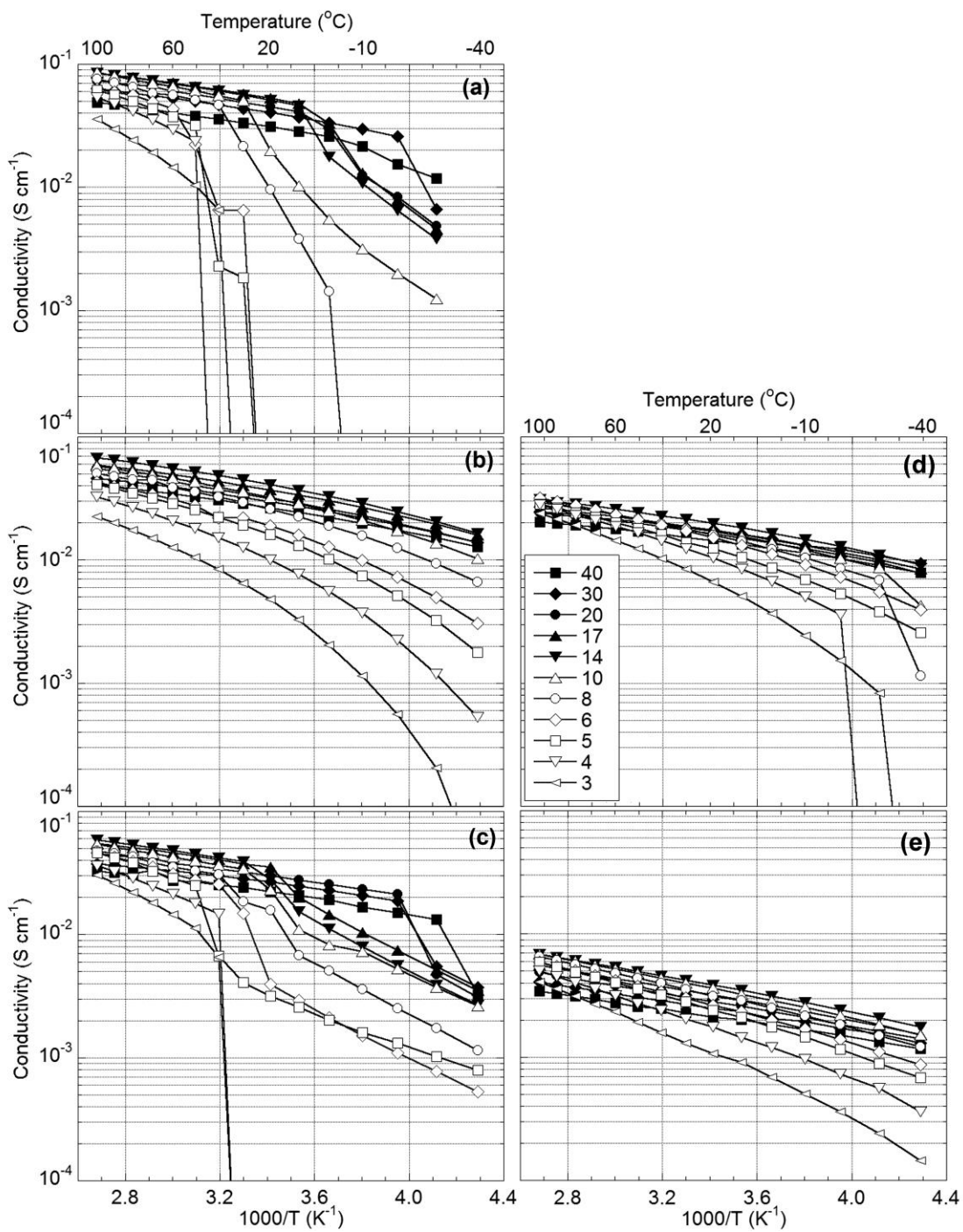


**Figure 5.22.** Ionic conductivity of  $(AN)_n\text{-LiX}$  mixtures: (a)  $\text{LiPF}_6$ , (b)  $\text{LiTFSI}$ , (c)  $\text{LiClO}_4$ , (d)  $\text{LiBF}_4$  and (e)  $\text{LiCF}_3\text{CO}_2$  ( $AN/LiX$  ( $n$ ) noted in plot).<sup>85</sup>

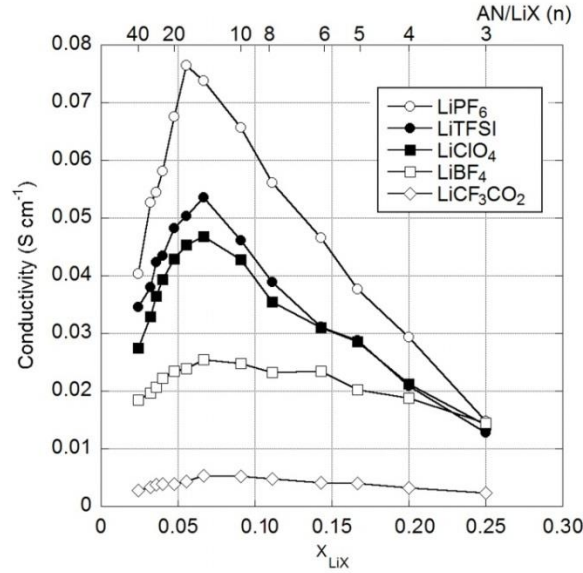


**Figure 5.23.** Ionic conductivity of  $(AN)_n$ -LiX mixtures at 60 °C (AN/LiX (n) noted at the top of the plot).<sup>85</sup>

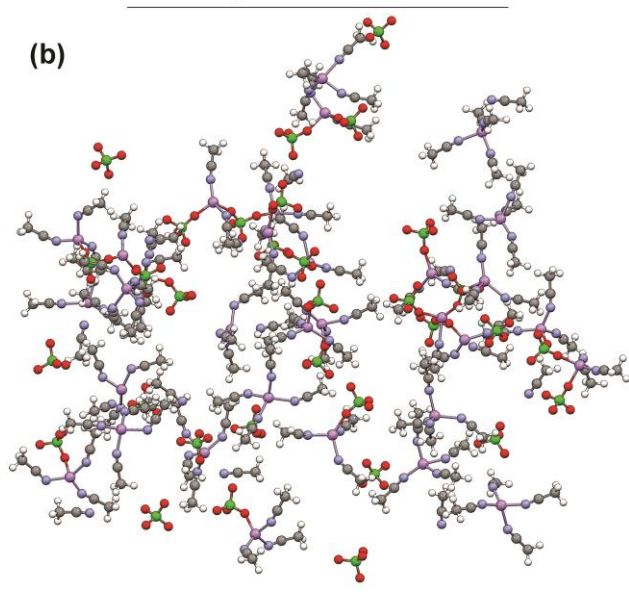
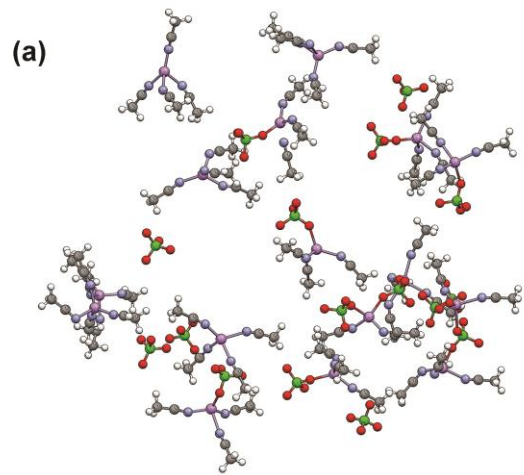
Fig. 5.23 shows the isothermal (60 °C) conductivity data for the electrolyte mixtures.<sup>85</sup> The conductivity peaks near a concentration of 1 M (or 1 m) as is observed as for most other electrolyte mixtures with aprotic solvents (Figs. 5.20 and 5.23).<sup>87</sup> For strong electrolytes (with fully dissociated monovalent cations (+) and anions (-)), the conductivity of an electrolyte is given by:

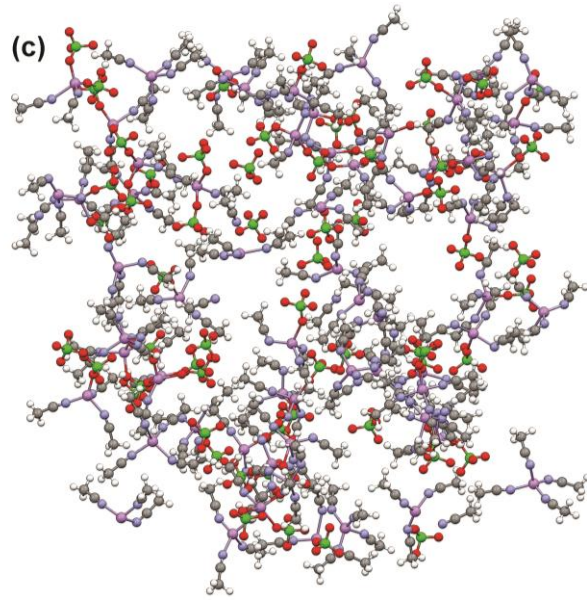
$$\kappa = F|z_+|u_+C_+ + F|z_-|u_-C_- \quad [3]$$

Therefore, the conductivity is a function of the charge of the charge carriers, the number of charge carriers (individual ions and/or solvates) which migrate in an electric field and their mobility. Note that when ionic association into CIP and AGG solvates occurs, this is complicated by the diversity of the solvates present.

In Fig. 5.23, the lower conductivity values for the dilute mixtures ( $n > 20$ ), as compared to more concentrated mixtures ( $10 \leq n \leq 20$ ), is frequently attributed to the limited number of charge carriers in dilute mixtures. As the salt concentration becomes greater and approaches the value for the peak conductivity, the number of charge carriers increases without overly reducing the mobility of the charge carriers. A further increase in concentration, however, may lead to the formation of CIP solvates and larger AGG species which both reduces the number of charge carriers and their mobility. Utilizing the results from the MD simulations and spectroscopic characterization for the mixtures, these arguments may be scrutinized. The snapshots taken from the simulations for the  $(AN)_n\text{-LiClO}_4$  ( $n = 30, 20$  and  $10$ ) mixtures are shown in Fig. 5.24.<sup>85</sup> Each snapshot suggests that there are only minor differences in the SSIP and CIP solvate distribution (with very few AGG solvates) between the  $n = 30$  and  $20$  mixtures, whereas the distribution changes significantly between the  $n = 20$  and  $10$  mixtures (with a significant reduction in the SSIP solvates and increase in the AGG solvates). Along with the changes of the solvate distribution, the separation of the solvates is largely eliminated for the  $n = 10$  mixture relative to that for the  $n = 20$  mixture (Fig. 5.24). For the  $n = 10$  mixture, the anions and solvates are in close proximity to one another resulting in an increase in the attractive/repulsive electrostatic interactions between them, which supports the postulation noted above (the conductivity for these mixtures increases until about  $n = 14$  and then steadily declines with a further increase in salt concentration). All of the salts studied show a similar trend (Fig. 5.23), so the variation in the conductivity with concentration can be attributed to both the concentration of charge carriers and their mobility,

**Figure 5.24.** Molecular simulation snapshots of  $(\text{AN})_n\text{-LiBF}_4$  mixtures with (a)  $n = 30$ , (b)  $n = 20$  and (c)  $n = 10$  (Li-purple, N-blue, B-tan, F-light green). Uncoordinated AN has been removed to aid in discerning the solvates present.<sup>85</sup>





as expected.

For a given  $(AN)_n$ -LiX concentration, the variations in the magnitude of the conductivity is in accord with the solution structure (ion solvation, ionic association) characterization (Fig. 5.23). The solutions with the most dissociated salt (i.e.,  $LiPF_6$ ) have the highest conductivity (consisting principally of SSIP and CIP solvates), whereas the mixtures with the most associated salts (i.e.,  $LiCF_3CO_2$ ) have the lowest conductivity (consisting principally of AGG solvates). For the most concentrated mixtures ( $n = 3$ ), the conductivity of all of the salt solutions converges (except for the solution with the highly aggregated  $LiCF_3CO_2$  salt), even though the MD simulations results indicate that the mixtures with  $n = 2$  still have significant differences in the solvate distribution between them. If the simulations accurately depict the interactions of such concentrated mixtures, restricted mobility (due to strong electrostatic interactions and clustering of the solvates) may dominate the conductivity for such concentrations rather than the identity of the charge carriers.

Fig. 5.25a shows the molar conductivity data for varying salt concentration.<sup>85</sup> There is no evident peak, but reasonably smooth curves are found for the most dilute mixtures which have the highest molar conductivity values (up to  $n = 40$ ). If the ions are fully dissociated (i.e., strong electrolyte), then the molar conductivity is, in effect, the conductivity normalized in terms of the number of available charge carriers. But since the ions are not fully dissociated, this is not the case. The same trends with regard to the conductivity and anions are found with the most dissociated salts having the highest molar conductivity. For the highly concentrated mixtures ( $n \leq 5$ ), the molar conductivity values also converge, except for

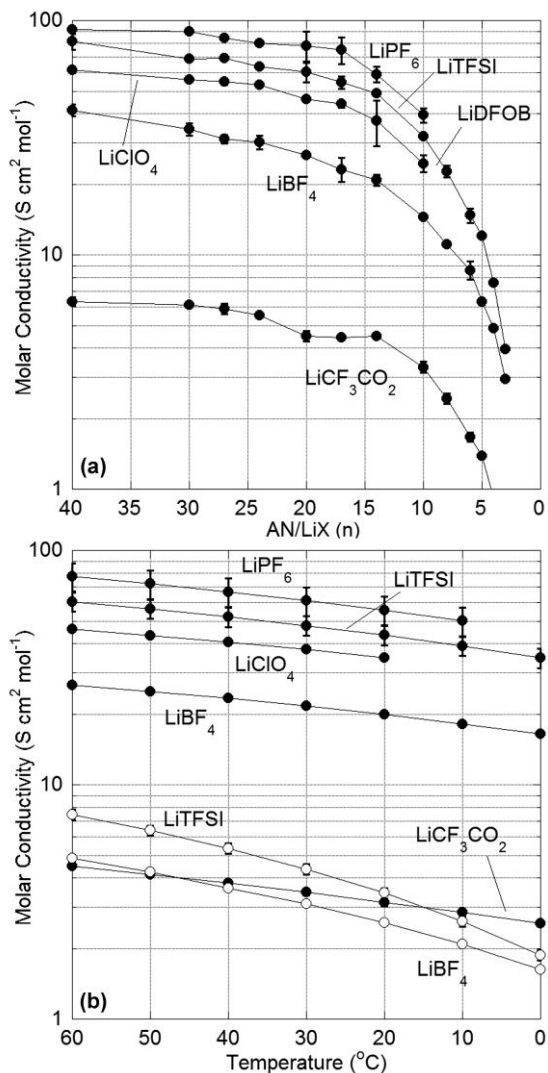


**Figure 5.25.** Molar conductivity of (a)  $(AN)_n$ -LiX mixtures (60 °C) for varying AN/LiX (n) and (b)  $(AN)_n$ -LiX mixtures (n = 20 - filled circles are average values, individual measurements shown as small open circles and n = 4 - larger open circles) with varying temperature.<sup>85</sup>

the mixtures with  $LiCF_3CO_2$ . Fig. 5.25b suggests that the conductivity for the  $(AN)_n$ - $LiCF_3CO_2$  (n = 20) mixture is comparable to that for the  $(AN)_n$ -LiTFSI or  $-BF_4$  (n = 4)

mixtures (although a different temperature dependence is found) indicating how crucial the aggregation of the  $\text{LiCF}_3\text{CO}_2$  mixtures is for lowering the solution conductivity.<sup>85</sup>

#### 5.6.4. Dynamics of Solvate Formation

The dynamics of solvate formation can be provided by the MD simulations, which are unavailable from the experimental work performed. In the present work, simulations have been used as a complementary tool to support and verify the experimentally-derived information regarding the solution structure of  $(\text{AN})_n\text{-LiX}$  electrolytes.

As noted for the conduction mechanisms in polymer electrolytes and water,<sup>99,100</sup> the MD simulations for the  $(\text{AN})_n\text{-LiX}$  mixtures suggest that a dynamic shuffling transpires in which frequent exchanges of solvent and anions occur in a  $\text{Li}^+$  cation's coordination shell.<sup>85</sup> Thus, a given  $\text{Li}^+$  cation continuously transforms from one form of solvate to another. Fig. 5.26 demonstrates this for one of the  $\text{Li}^+$  cations in the MD simulation from the  $(\text{AN})_n\text{-LiBF}_4$  ( $n = 30$ ) mixture.<sup>85</sup> The bottom of the figure represents the different AN molecules coordinated to the specified  $\text{Li}^+$  cation and the length of time that they remain coordinated. A dot is shown if a particular solvent molecule remains coordinated or in close proximity to the specified cation (i.e.,  $r_{\text{Li-N}}(\text{AN}) \leq 2.80 \text{ \AA}$ ) for at least 4 ps during the 10 ps intervals. However, the dot does not necessarily indicate that the solvent is still coordinated to the cation at the end of the 10 ps interval. Similarly, the “Anions” indicate that a particular  $\text{BF}_4^-$  anion is coordinated to the specified  $\text{Li}^+$  cation (i.e.,  $r_{\text{Li-B}}(\text{BF}_4^-) \leq 3.60 \text{ \AA}$ ) for at least 4 ps during the 10 ps interval. Finally, to determine if the specified  $\text{Li}^+$  cation is part of a larger AGG solvate, the “Other

$\text{Li}^{+\text{other}}$  indicates other  $\text{Li}^+$  cations which are in close proximity to the specified  $\text{Li}^+$  cation (i.e.,  $r_{\text{Li-Li}} \leq 4.8 \text{ \AA}$ ) for at least 4 ps during the 10 ps interval (this does not indicate, however, the

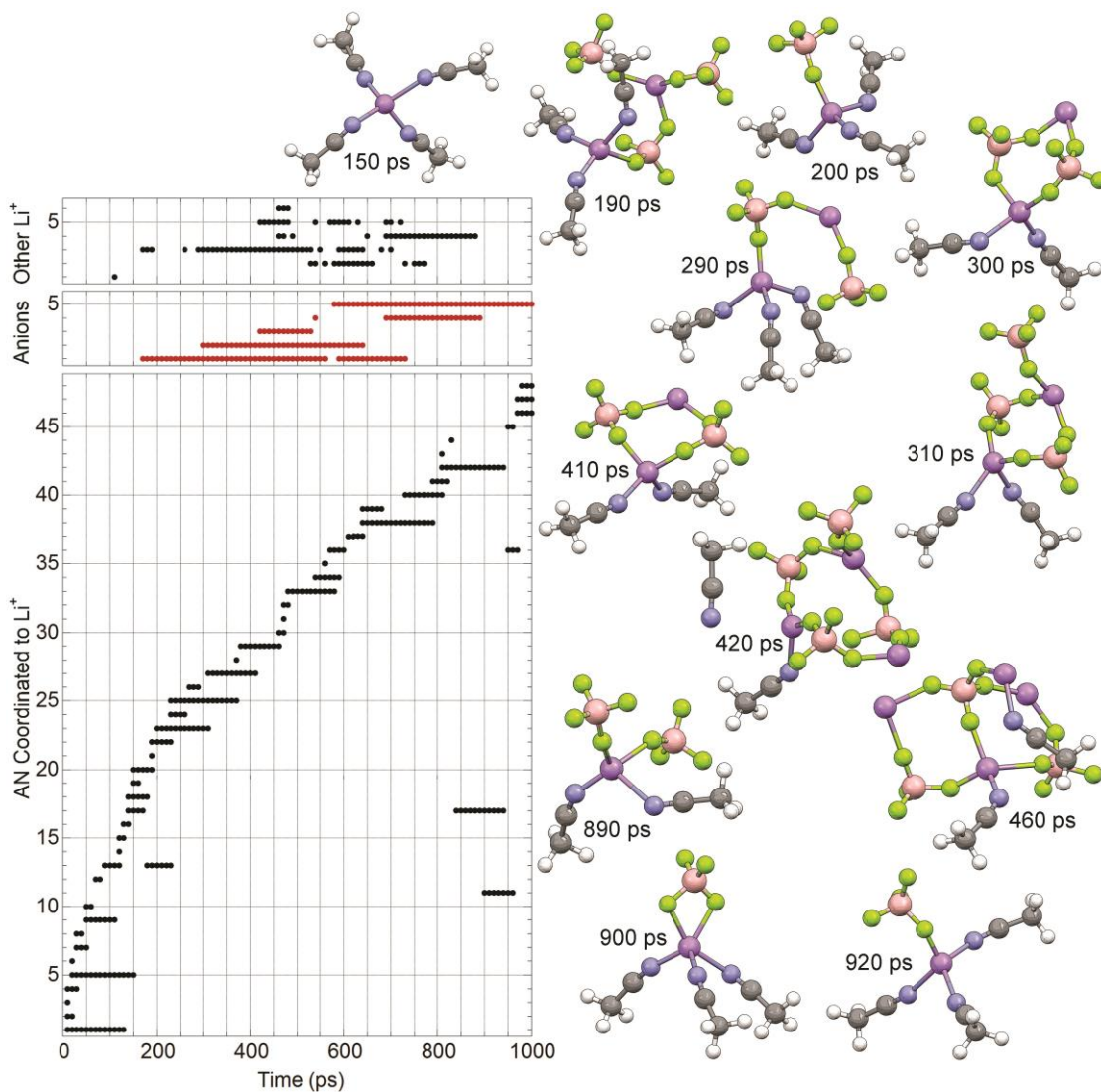
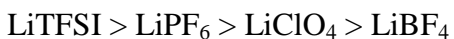


**Figure 5.26.** Dynamics of solvate formation for a  $\text{Li}^+$  cation (No. 2973) in the MD simulation of the  $(\text{AN})_n\text{-LiBF}_4$  ( $n = 30$ ) mixture at  $60 \text{ }^\circ\text{C}$ . Full coordination for the "other  $\text{Li}^+$ " cations not shown (i.e., full solvate structure).<sup>85</sup>

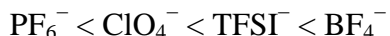
overall size of the AGG solvate). Initially, the  $\text{Li}^+$  cation is fully solvated by four AN molecules (i.e., aSSIP solvate), then the cation's solvation shell rapidly exchanges numerous AN molecules. After approximately 170 ps, one of the coordinating solvent molecules is exchanged with a  $\text{BF}_4^-$  anion which is also coordinated to another  $\text{Li}^+$  cation, thus forming an AGG solvate for approximately 30 ps, prior to forming a CIP solvate for approximately 80-90 ps. The  $\text{Li}^+$  cation then becomes part of an AGG solvate which transforms over time to a larger aggregated cluster of ions. At about 900 ps, however, the AGG solvate once again becomes a CIP solvate for 100 ps or more. Throughout this evolution of the solvate species in which the  $\text{Li}^+$  cation participates, it continuously exchanges coordinating AN solvent molecules (48 different solvent molecules with several reentering the  $\text{Li}^+$  cation coordination shell). The anions are exchanged to a much lesser extent. The previously mentioned data regarding the ionic association state of the  $(\text{AN})_n\text{-LiX}$  mixtures therefore represents the equilibrium distribution of the solvates (or rather the anion coordination and fraction of coordinated solvent) for a particular lithium salt, concentration and temperature, but the solvates themselves continuously metamorphose into various solvate species. For a given  $\text{Li}^+$  cation in the simulations, its local environment over the 1000 ps time periods can differ significantly from another  $\text{Li}^+$  cation in the same simulation mixture. Examples of the dynamic plots for different cations with the different salts and concentrations are provided in the previous study.<sup>85</sup>

Fig. 5.27 shows a summary of the anions and AN residence times ( $\tau_{\text{res}}$ ) in the  $\text{Li}^+$  cation coordination shell from the MD simulations.<sup>85</sup> For the dilute mixtures, the  $\text{AN}\dots\text{Li}^+$  cation

residence times are quite similar, but as the salt concentration increases (i.e.,  $n \leq 5$ ) they become remarkably different. The order of increasing AN residence times with different lithium salts for the highly concentrated mixtures are (open symbols in Fig. 5.27a):



Thus, for the mixtures with the most dissociated anions, the solvent tends to remain coordinated to the  $\text{Li}^+$  cations for a longer period of time (with the exception of the  $\text{TFSI}^-$  anion). As shown in Figs. 5.26 and 5.27, the concentration dependence of the anion... $\text{Li}^+$  cation residence times is quite different from that of the AN... $\text{Li}^+$  cation residence times as the anions remain coordinated to a given  $\text{Li}^+$  cation much longer than the AN solvent molecules. From the MD simulations, the order of increasing anion residence times is as follows (filled symbols in Fig. 5.27a):



This order indicates that as the ionic association tendency of the anions increases, the length of time that the anions remain coordinated to the  $\text{Li}^+$  cations increases as well (except for the  $\text{TFSI}^-$  anion). In Fig. 5.27a, the residence times refer to the time in which the anion center (i.e., P, Cl, N or B atoms) remain in close proximity to the  $\text{Li}^+$  cations. Relative to the anion center... $\text{Li}^+$  cation times (filled symbols in Fig. 5.27a), noticeably smaller (by a factor of 5 to 15) donor atom (F or O)... $\text{Li}^+$  cation residence times (filled symbols in Fig. 5.27b) suggest that the coordinated anions rotate multiple times (i.e., multiple donor atoms from an anion coordinated to a given  $\text{Li}^+$  cation) before the anion becomes dissociated. The differences between the  $\text{TFSI}^-$  anion and the other anions can be explained by the greater extent of

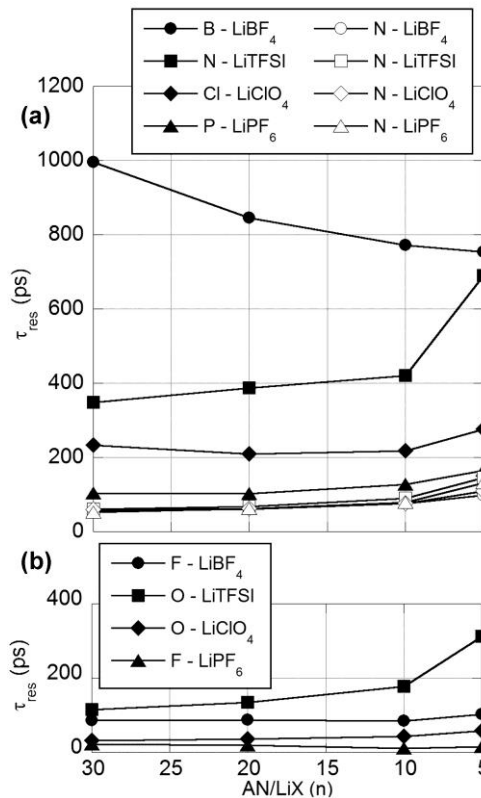


**Figure 5.27.** Anion...Li<sup>+</sup> and AN...Li<sup>+</sup> cation residence times in the (AN)<sub>n</sub>-LiX mixtures from the MD simulations: (a) filled symbols are anions, open symbols are AN and (b) filled symbols are anions.<sup>85</sup>

bidentate coordination (coordinate to the Li<sup>+</sup> cations with two donor atoms rather than one) of the TFSI<sup>-</sup> anions relative to the other anions, as well as the significant difference in densities (Fig. 5.20a) and thus separation between the Li<sup>+</sup> cations.

## 5.7. Conclusions

Phase diagrams for (AN)<sub>n</sub>-LiClO<sub>4</sub>, -LiBF<sub>4</sub>, -LiTFSI and -LiPF<sub>6</sub> mixtures were determined

and the phase behavior of  $(\text{AN})_n\text{-LiCF}_3\text{SO}_3$  and  $\text{-LiCF}_3\text{CO}_2$  mixtures was studied for comparison. Both the solvent and anion interactions with  $\text{Li}^+$  cations were examined using Raman spectroscopy. Based upon the spectroscopic analysis for the solvent (AN) vibrational bands, an average  $\text{Li}^+$  cation solvation number ( $N$ ) in AN was determined as a function of salt concentration. There are significant differences in the  $N$  values with varying anions ( $\text{PF}_6^-$ ,  $\text{TFSI}^-$ ,  $\text{ClO}_4^-$ ,  $\text{BF}_4^-$  and  $\text{CF}_3\text{CO}_2^-$ ) for the relatively dilute mixtures. The experimental vibrational band analysis and MD simulations results for each anion suggest that there are a diverse range of different types of solvates (i.e., SSIPs, CIPs and AGGs) in a solution. The combination of phase diagrams with crystalline solvate structures, Raman spectroscopic characterization and computational simulations greatly aids in identifying these solvates. The simulation results support the experimental data which indicates that  $\text{LiClO}_4$  is significantly more dissociated than  $\text{LiBF}_4$  in AN despite the similarity in the anion sizes and shapes.  $\text{LiPF}_6$  and  $\text{LiTFSI}$  are found to be highly dissociated and dissociated, respectively, in dilute mixtures. The demonstrated results show that both the experimental and computational analyzes contain some measure of error. Together, however, they provide significant insight into the solution structure present in the electrolytes.

The solution structure (ion solvation and ionic association) of the  $(\text{AN})_n\text{-LiX}$  mixtures can be directly link to the transport properties (viscosity and ion conductivity) of the mixtures. The viscosity variations for the mixtures with different lithium salts can be explained using both the ionic association behavior and the corresponding amount of uncoordinated solvent present. However, the ion conductivity variations and mechanisms for  $(\text{AN})_n\text{-LiX}$  mixtures

are determined not just by the identity of the solvates and their distribution, but also by the dynamics for the solvent molecules and anions in the  $\text{Li}^+$  cation coordination shells (i.e., the continuous transformation of the solvate species), as noted by the MD simulations. In contrast to the general expectations, the mixtures with the highest conductivity are found to also have the highest viscosity. These properties are thus demonstrated to not be directly correlated with one another (as is commonly supposed), but rather are indirectly linked through the solution structure. Thus, the solution structure information utilizing the combination of phase behavior, solvates structures, ion solvation/ionic association analysis and MD simulations can be a highly effective tool to understand and predict the transport properties of the electrolytes.

## 5.8. References

1. W. A. Henderson, *J. Phys. Chem. B*, **110**, 13177 (2006).
2. Y. Abu-Lebdeh and I. Davidson, *J. Electrochem. Soc.*, **156**, A60 (2009).
3. M. Nagahama, N. Hasegawa, and S. Okada, *J. Electrochem. Soc.*, **157**, A748 (2010).
4. Y. Abu-Lebdeh and I. Davidson, *J. Power Sources*, **189**, 576 (2009).
5. M. J. Barrow, *Acta Crystallogr.*, **B37**, 2239 (1981).
6. O. K. Antson, K. J. Tilli, and N. H. Andersen, *Acta Crystallogr.*, **B43**, 296 (1987).
7. B. H. Torrie and B. M. Powell, *Mol. Phys.*, **75**, 613 (1992).
8. H. Abramczyk and K. Paradowska-Moszkowska, *Chem. Phys.*, **265**, 177 (2001).
9. R. Enjalbert and J. Galy, *Acta Crystallogr.*, **B58**, 1005 (2002).
10. Y. Suzuki, M. Sato, K. Takanohashi, T. Ida, and M. J. Mizuno, *Phys. Chem. A*, **112**, 13481 (2008).
11. A. Olejniczak and A. Katrusiak, *J. Phys. Chem. B*, **112**, 7183 (2008).
12. S. Hore, R. Dinnebier, W. Wen, J. Hanson, and J. Maier, *Z. Anorg. Allg. Chem.*, **635**, 88 (2009).
13. D. M. Seo, O. Borodin, S.-D. Han, Q. Ly, P. D. Boyle, and W. A. Henderson. *J. Electrochem. Soc.*, **159**, A553 (2012).
14. G. Perron, L. Couture, D. Lambert, and J. E. Desnoyers, *J. Electroanal. Chem.*, **355**, 277 (1993).
15. Y. Yokota, V. G. Young Jr., and J. G. Verkade, *Acta Crystallogr.*, **C55**, 196 (1999).
16. C. L. Raston, C. R. Whitaker, and A. H. White, *Aust. J. Chem.*, **42**, 201 (1989).

17. D. M. Seo, P. D. Boyle, and W. A. Henderson, *Acta Crystallogr.*, **E67**, m547 (2011).
18. N. R. Brooks, W. A. Henderson, and W. H. Smyrl, *Acta Crystallogr.*, **E58**, m176 (2002).
19. K. Nilsson and Å. Oskarsson, *Acta Chem. Scand. A*, **38**, 79 (1984).
20. P. G. Jones and E. Bembenek, *Z. Kristallogr.*, **208**, 213 (1993).
21. A. A. M. Aly, B. Walfort, and H. Lang, *Z. Kristallogr.*, **219**, 489 (2004).
22. I. Csöreg, P. Kierkegaard, and K. Norrestam, *Acta Crystallogr.*, **B31**, 314 (1975).
23. P. G. Jones and O. Crespo, *Acta Crystallogr.*, **C54**, 18 (1998).
24. R. D. Shannon, *Acta Crystallogr.*, **A32**, 751 (1976).
25. M. Ue, *J. Electrochem. Soc.*, **141**, 3336 (1994).
26. D. J. J. Van Rensburg and J. C. A. Boeyens, *J. Solid State Chem.*, **5**, 79 (1972).
27. H. J. Prask, C. S. Choi, N. J. Chesser, and G. J. Rosasco, *J. Chem. Phys.*, **88**, 5106 (1988).
28. E. Palacios, J. J. Melero, R. Burriel, and P. Ferloni, *Phys. Rev. B*, **54**, 9099 (1996).
29. E. Palacios, R. Burriel, and P. Ferloni, *Acta Crystallogr.*, **B59**, 625 (2003).
30. K. Matsumoto, R. Hagiwara, Z. Mazej, E. Goreshnik, and B. Žemva, *J. Phys. Chem. B*, **110**, 2138 (2006).
31. J. Kivikoski, J. A. K. Howard, P. Kelly, and D. Parker, *Acta Crystallogr.*, **C51**, 535 (1995).
32. X. Wu, F. R. Fronczek, and L. G. Butler, *Inorg. Chem.*, **33**, 1363 (1994).

33. D. M. Seo, O. Borodin, S.-D. Han, P. D. Boyle, and W. A. Henderson. *J. Electrochem. Soc.*, **159**, A1489 (2012).
34. D. Brouillette, D. E. Irish, N. J. Taylor, G. Perron, M. Odziemkowski, and J. E. Desnoyers, *Phys. Chem. Chem. Phys.*, **4**, 6063 (2002).
35. W. Kunz, J. Barthel, L. Klein, T. Cartailier, P. Turq, and B. Reindl, *J. Soln. Chem.*, **20**, 875 (1991).
36. E. M. Cabaleiro-Lago and M. A. R ós, *Chem. Phys.*, **254**, 11 (2000).
37. X. P. Xuan, H. C. Zhang, J. J. Wang, and H. Q. Qang, *J. Phys. Chem. A*, **108**, 7513 (2004).
38. D. Sp ångberg and K. Hermansson, *Chem. Phys.*, **300**, 165 (2004).
39. E. Pasgreta, R. Puchta, A. Zahl, and R. van Eldik, *Eur. J. Inorg. Chem.*, 1815 (2007).
40. D. M. Seo, P. D. Boyle, and W. A. Henderson, *Acta Crystallogr. E*, **67**, m534 (2011).
41. D. M. Seo, P. D. Boyle, O. Borodin, and W. A. Henderson, *RSC Adv.*, **2**, 8014 (2012).
42. D. M. Seo, P. D. Boyle, and W. A. Henderson, *Acta Crystallogr. E*, **67**, m1148 (2011).
43. J. R. Black, W. Levason, and M. Webster. *Acta Crystallogr. C*, **51**, 623 (1995).
44. L. A. Dakin, P. C. Ong, J. S. Panek, R. J. Staples, and P. Stavrosoulos, *Organometallics*, **19**, 2896 (2000).
45. G. A. Bowmaker, D. S. Gill, B. W. Skelton, N. Somers, and A. H. White, *Z. Naturforsch.*, **B59**, 1307 (2004).
46. E. K. Beloglazkina, A. V. Shimorsky, A. G. Mazhuga, O. V. Shilova, V. A. Tafeenko, and N. V. Zyk, *Russ. J. Gen. Chem.*, **79**, 1504 (2009).

47. H.-G. Hao, X.-D. Zheng, and T.-B. Lu, *Angew. Chem. Int. Ed.*, **49**, 8148 (2010).
48. J. W. Bats, T. Kretz, and H.-W. Lerner, *Acta Crystallogr. C*, **65**, m94 (2009).
49. R. D. Shannon, *Acta Crystallogr. A*, **32**, 751 (1976).
50. P. Johansson, S. P. Gejji, J. Tegenfeldt, and J. Lindgren, *Electrochim. Acta*, **43**, 1375 (1998).
51. M. Herstedt, W. A. Henderson, M. Smirnov, L. Ducasse, L. Servant, D. Talaga, and J.-C. Lassègues, *J. Mol. Struct.*, **783**, 145 (2006).
52. P. Neelakantan, *P. Indian Acad. Sci. A*, **60**, 422 (1964).
53. G. Fini and P. Mirone, *Spectrochim. Acta*, **32A**, 439 (1976).
54. J. Barthel, R. Buchner, and E. Wismeth, *J. Soln. Chem.*, **29**, 937 (2004).
55. J. M. Alia, H. G. M. Edwards, and J. Moore, *Spectrochim. Acta*, **51A**, 2039 (1995).
56. D. W. James and R. E. Mayes, *Aust. J. Chem.*, **35**, 1775 (1982).
57. D. W. James and R. E. Mayes, *Aust. J. Chem.*, **35**, 1785 (1982).
58. D. W. James and R. E. Mayes, *J. Phys. Chem.*, **88**, 637 (1984).
59. J.-S. Seo, B.-S. Cheong, and H.-G. Cho, *Spectrochim. Acta A*, **58**, 1747 (2002).
60. B. G. Oliver and G. J. Jantz, *J. Phys. Chem.*, **74**, 3819 (1970).
61. S. Dulard, J. Grondin, J.-L. Bruneel, I. Pianet, A. Gréard, G. Campet, M.-H. Delville, and J.-C. Lassègues, *J. Raman Spectrosc.*, **39**, 627 (2008).
62. M. G. Davidson, P. R. Raithby, A. L. Johnson, and P. D. Bolton, *Eur. J. Inorg. Chem.*, **18**, 3445 (2003).

63. Q. Zhou, P. D. Boyle, L. Malpezzi, A. Mele, J.-H. Shin, S. Passerini, and W. A. Henderson, *Chem. Mater.*, **23**, 4331 (2011).
64. Q. Zhou, K. Fitzgerald, P. D. Boyle, and W. A. Henderson, *Chem. Mater.*, **22**, 1203 (2010).
65. W. A. Henderson, F. McKenna, M. A. Khan, N. R. Brooks, V. G. Young Jr., and R. Frech, *Chem. Mater.*, **17**, 2284 (2005).
66. J. Grondin, L. Ducasse, J.-L. Bruneel, L. Servant, and J.-C. Lassègues, *Solid State Ionics*, **166**, 441 (2004).
67. J. Grondin, D. Talaga, J.-C. Lassègues, and W. A. Henderson, *Phys. Chem. Chem. Phys.*, **6**, 938 (2004).
68. J. Grondin, J.-C. Lassègues, M. Chami, L. Servant, D. Talaga, and W. A. Henderson, *Phys. Chem. Chem. Phys.*, **6**, 4260 (2004).
69. A. S. Quist, J. B. Bates, and G. E. Boyd, *J. Chem. Phys.*, **54**, 4896 (1971).
70. D. M. Seo, P. D. Boyle, J. L. Allen, S.-D. Han, E. Jónsson, P. Johansson, and W. A. Henderson. *J. Phys. Chem. C* (2013) in-press.
71. I. Rey, P. Johansson, J. C. Lassègues, J. Grondin, and L. Servant, *J. Phys. Chem. A*, **102**, 3249 (1998).
72. M. Herstedt, M. Smirnov, P. Johansson, M. Chami, and J. Grondin, *J. Raman Spectrosc.*, **36**, 762 (2005).
73. L. Xue, C. W. Padgett, D. D. DesMarteau, and W. T. Pennington, *Solid State Sci.*, **4**, 1535 (2002).

74. D. M. Seo, P. D. Boyle, R. D. Sommer, J. S. Daubert, O. Borodin, and W. A. Henderson. *J. Phys. Chem. C* (2013) submitted.
75. A. M. Heyns and D. de Waal, *J. Chem. Phys.*, **97**, 8086 (1992).
76. X. Xuan, J. Wang, and H. Wang, *Electrochim. Acta*, **50**, 4196 (2005).
77. R. Aroca, M. Nazri, G. A. Nazri, A. J. Camargo, and M. Trsic, *J. Soln. Struct.*, **29**, 1047 (2000).
78. A. M. Heyns, *Spectrochim. Acta A*, **33**, 315 (1977).
79. C. M. Burba and R. Frech, *J. Phys. Chem. B*, **109**, 15161 (2005).
80. J. S. Francisco and I. H. Williams, *J. Phys. Chem.*, **94**, 8522 (1990).
81. O. Borodin, G. D. Smith, and R. Douglas, *J. Phys. Chem. B*, **107**, 6824 (2003).
82. O. Borodin, *J. Phys. Chem. B*, **113**, 11463 (2009).
83. O. Borodin and G. D. Smith, *J. Phys. Chem. B*, **110**, 4971 (2006).
84. O. Borodin, G. D. Smith, and W. Henderson, *J. Phys. Chem. B*, **110**, 16879 (2006).
85. D. M. Seo, O. Borodin, D. Balogh, M. O'Connell, Q. Ly, S.-D. Han, S. Passerini, and W. A. Henderson. *J. Electrochem. Soc.*, **160**, A1061 (2013).
86. M. Petrowsky and R. Frech, *J. Phys. Chem. B*, **113**, 5996 (2009).
87. M. S. Ding, *J. Electrochem. Soc.*, **151**, A40 (2004).
88. O. Borodin and G. D. Smith, *J. Phys. Chem. B*, **104**, 8017 (2000).
89. O. Borodin and G. D. Smith, *J. Solution. Chem.*, **36**, 803 (2007).
90. O. Borodin and G. D. Smith, *J. Phys. Chem. B*, **110**, 6279 (2006).
91. O. Borodin and G. D. Smith, *J. Phys. Chem. B*, **110**, 6293 (2006).

92. O. Borodin and G. D. Smith, *J. Phys. Chem. B*, **113**, 1763 (2009).
93. M. D. Bhatt, M. Cho, and K. Cho, *Model. Simul. Mater. Sci. Eng.*, **20**, 065004 (2012).
94. J. Newman, K. E. Thomas, H. Hafezi, and D. R. Wheeler, *J. Power Sources*, **119**, 838 (2003).
95. M. Masia, M. Probst, and R. Rey, *J. Phys. Chem. B*, **108**, 2016 (2004).
96. J. C. Soetens, C. Millot, and B. Maigret, *J. Phys. Chem. A*, **102**, 1055 (1998).
97. P. Ganesh, D.-e. Jiang, and P. R. C. Kent, *J. Phys. Chem. B*, **115**, 3085 (2011).
98. J. K. Hyun, H. T. Dong, C. P. Rhodes, R. Frech, and R. A. Wheeler, *J. Phys. Chem. B*, **105**, 3329 (2001).
99. C. J. T. de Grotthuss, *Ann. Chim.*, **58**, 54 (1806).
100. K.-D. Kreuer, A. Rabenau, and W. Weppner, *Angew. Chem. Int. Ed.*, **21**, 208 (1982).

## Electrolyte Solvation and Ionic Association II. Acetonitrile-Lithium Difluoro(oxalato)borate (LiDFOB) Mixtures

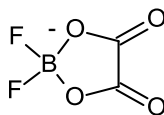
---

The previous methodology is applied for the evaluation of the bulk electrolyte characteristics of the LiDFOB salt and for the comparison of LiDFOB to the other lithium salts studied. AN has been used as a model solvent. Utilizing information from a combination of methods—i.e., the determination of the (AN)<sub>n</sub>-LiDFOB thermal phase behavior (phase diagram and the corresponding solvate crystal structures), a Raman spectroscopic evaluation of the solvation/ionic association interactions and molecular dynamics (MD) simulations—detailed insight into the coordination interactions of the DFOB<sup>-</sup> anion has been obtained and explanations are readily available for the solution behavior and variability in the transport properties (viscosity and ionic conductivity) of AN solutions with this salt relative to other lithium salts.

### 6.1. Introduction

Lithium difluoro(oxalato)borate (LiDFOB), also known as lithium oxalyldifluoroborate (LiODFB), is a relatively new salt developed for lithium battery electrolytes. The DFOB<sup>-</sup>

anion:



was first reported in a patent application filed in 1999 by Metallgesellschaft AG<sup>1</sup> and then later in a publication in 2006 by the U.S. Army Research Laboratory (ARL).<sup>2</sup> A number of publications have now been reported<sup>3-46</sup> which indicate that this salt shows many useful properties, relative to the state-of-the-art electrolyte salt LiPF<sub>6</sub>, when used in mixed carbonate solvents. Most of the reported work thus far has focused on demonstrations of enhanced battery performance—including the improved cyclability/stabilization of electrode materials, such as LiFePO<sub>4</sub> and Li<sub>4</sub>Ti<sub>5</sub>O<sub>12</sub>, at elevated temperature (60 °C) and of high-voltage cathode materials when cycled up to 5 V—often with LiDFOB used as an additive. Much remains unknown, however, about the behavior of this salt in bulk electrolyte solutions. The present study therefore continues previous work which has examined the link between the solution structure (i.e., Li<sup>+</sup> cation solvation and ionic association interactions) and the transport properties of electrolytes in depth.<sup>47-50</sup>

## 6.2. Solvent-Lithium Salt Phase Behavior of (AN)<sub>n</sub>-LiDFOB Mixtures

(AN)<sub>n</sub>-LiDFOB mixtures form two phases consisting of 3/1 and 1/1 (AN/Li) crystalline solvates, respectively (Fig. 6.1a).<sup>51</sup> Both crystalline solvates are aggregate (AGG) structures, which were determined using single crystal x-ray diffraction. The structure of the 3/1 solvate

(i.e., AGG-Ia (AN)<sub>3</sub>:LiDFOB) was determined as part of the present work.<sup>6</sup> Each Li<sup>+</sup> cation has four-fold coordination by two AN molecules and two anions (Fig. 6.1b).<sup>51</sup> The DFOB<sup>-</sup> anions are coordinated to two Li<sup>+</sup> cations through the two anion carbonyl oxygen atoms

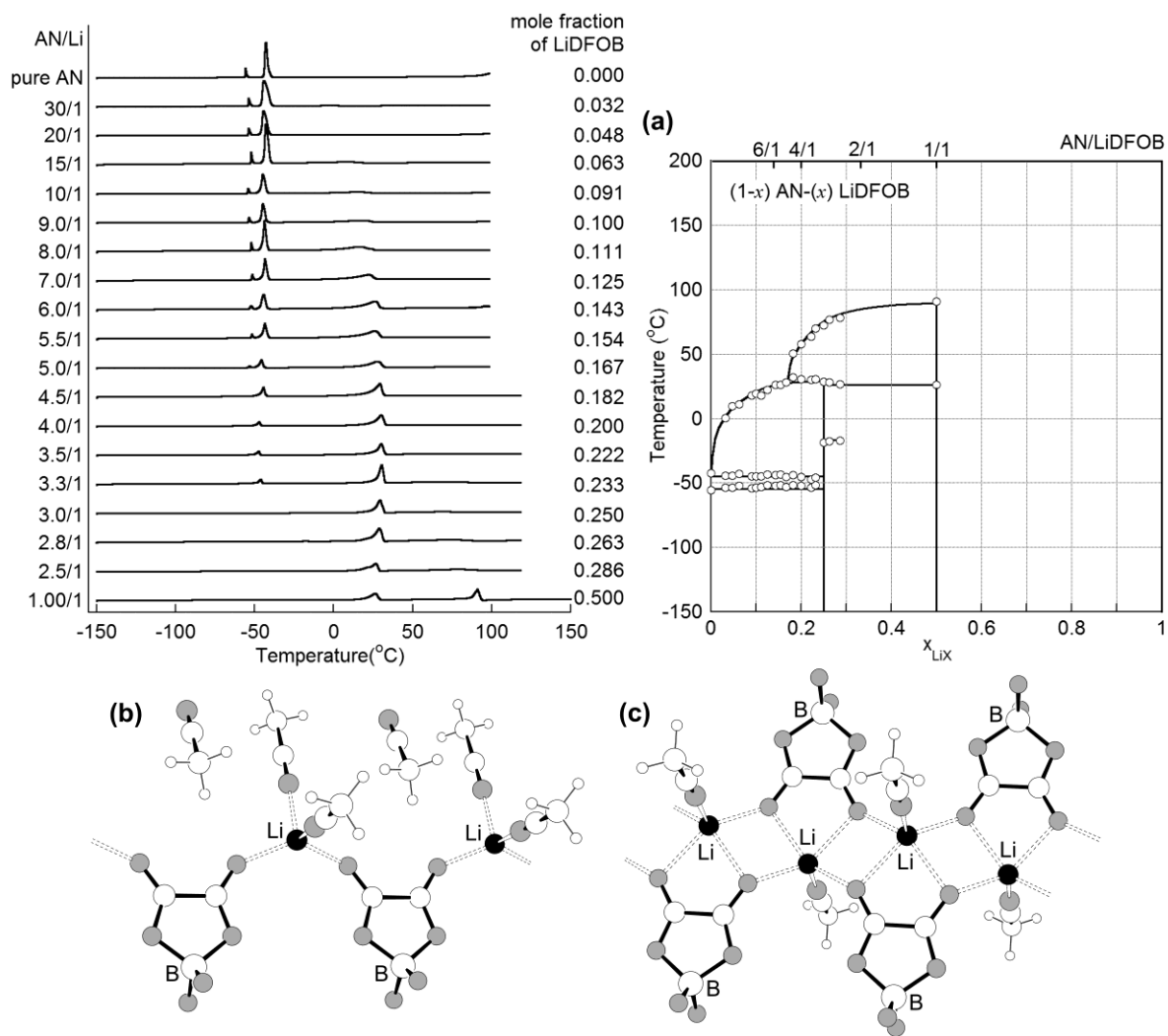


**Figure 6.1.** (a) DSC heating traces ( $5\text{ }^{\circ}\text{C min}^{-1}$ ) and the corresponding phase diagram for  $(1-x)$  AN- $(x)$  LiDFOB mixtures and  $\text{DFOB}^{-}\dots\text{Li}^{+}$  cation coordination in the crystalline solvates: (b) AGG-Ia (AN)<sub>3</sub>:LiDFOB<sup>6</sup> and (c) AGG-IIa (AN)<sub>1</sub>:LiDFOB.<sup>6,51</sup>

resulting in linear polymeric ion chains. The anion fluorine atoms remain uncoordinated. One uncoordinated AN molecule is also present per  $\text{Li}^+$  cation. The structure of the AGG 1/1 crystalline solvate (i.e., AGG-IIa  $(\text{AN})_1:\text{LiDFOB}$ ) was also determined as part of the present work.<sup>6</sup> Each  $\text{Li}^+$  cation in this solvate structure has five-fold coordination by one AN molecule and three anions (Fig. 6.1c).<sup>51</sup> Each anion is coordinated to three  $\text{Li}^+$  cations through the carbonyl oxygen atoms, with one of the  $\text{Li}^+$  cations coordinated by both carbonyl oxygen atoms (divalent coordination), again resulting in polymeric ion chains.

The 3/1 solvate may have a very low-energy solid-solid phase transition at  $-19\text{ }^\circ\text{C}$  prior to the  $T_m$  at  $29\text{ }^\circ\text{C}$ , while the 1/1 solvate has a  $T_m$  at  $91\text{ }^\circ\text{C}$  (Fig. 6.1a). Incongruent melting is observed for the  $(\text{AN})_n\text{-LiDFOB}$  mixtures ( $5.0 > n \geq 3.0$ ) with 1/1 solvate formation after the 3/1 solvate melts. Note that although the salt has a solubility limit of about  $n = 2.5$ , at room temperature, single crystals of the 1/1 solvate phase grew in the concentrated mixtures. These crystals were isolated from the solution and analyzed separately. The resulting thermogram has a peak which appear to correspond to the  $T_m$  for the 3/1 solvate (Fig. 6.1a). It was confirmed that this was not due to contamination from the solution. One explanation for this may be that this peak actually corresponds to a solid-solid phase transition (at  $26\text{ }^\circ\text{C}$ ) for the 1/1 solvate which overlaps with the  $T_m$  for the 3/1 solvate. If this is the case, then the  $(\text{AN})_n\text{-LiDFOB}$  mixtures ( $3.0 > n \geq 2.5$ ) may have two solid-solid phase transitions for the 3/1 and 1/1 solvates at  $-19\text{ }^\circ\text{C}$  and  $26\text{ }^\circ\text{C}$ , respectively.

The solid-liquid thermal phase behavior leads to the expectation that the  $(\text{AN})_n\text{-LiDFOB}$  mixtures are more associated than those with  $\text{LiBF}_4$ , as the first crystalline solvate to form

from dilute  $(\text{AN})_n\text{-LiBF}_4$  solutions is a 4/1 SSIP phase (albeit with a low  $T_m$ ) with uncoordinated anions.<sup>47</sup> In contrast, the dilute mixtures with LiDFOB instead form the aggregated 3/1 crystalline solvate phase. This assumption about the ionic association tendency of the ions in dilute solution and its link to the solid-liquid phase behavior of the mixtures, based upon the conclusions from a previous study of the phase behavior of glyme solvents with various lithium salts,<sup>52</sup> will be demonstrated to be incorrect in the following solution characterization. This indicates that the solvate formation from dilute solutions is a function of more than the ionic association tendency of the anions (although this factor does often largely govern the phase behavior).

### 6.3. Raman Characterization of AN-Li<sup>+</sup> Cation Solvation

Based upon the previous studies,<sup>47,48</sup> Raman data were collected for mixtures with LiDFOB at 60 °C to ensure that the mixtures were homogeneous solutions (or melts) over a wide composition range (Fig. 6.1a). Note that the mixtures with  $n \leq 3$  remain supercooled liquids at this temperature after melting the 1/1 solvate phase at a higher temperature. From the Raman spectra of the AN C–C and C≡N bands, plots of the peak area for the coordinated and uncoordinated AN (normalized relative to the total peak area) were prepared (Fig. 6.2).<sup>51</sup> Data obtained from the integration of the peaks can then be used to determine the fraction of solvent molecules coordinated to Li<sup>+</sup> cations (Fig. 6.2), as has been discussed in detail and done in the previous manuscripts in this series.<sup>47,48</sup> The AN solvent Raman band at 930 cm<sup>-1</sup>, however, overlaps with that of a DFOB<sup>-</sup> anion Raman band.<sup>51</sup> It is not possible to deconvolute

these bands. This explains the erratic data noted for the analysis based upon the 918, 922 and 930  $\text{cm}^{-1}$  bands (Fig. 6.2). Thus, only the data for the 2251, 2254 and 2277  $\text{cm}^{-1}$  bands was used to determine the average solvation numbers in the present study (Fig. 6.2).

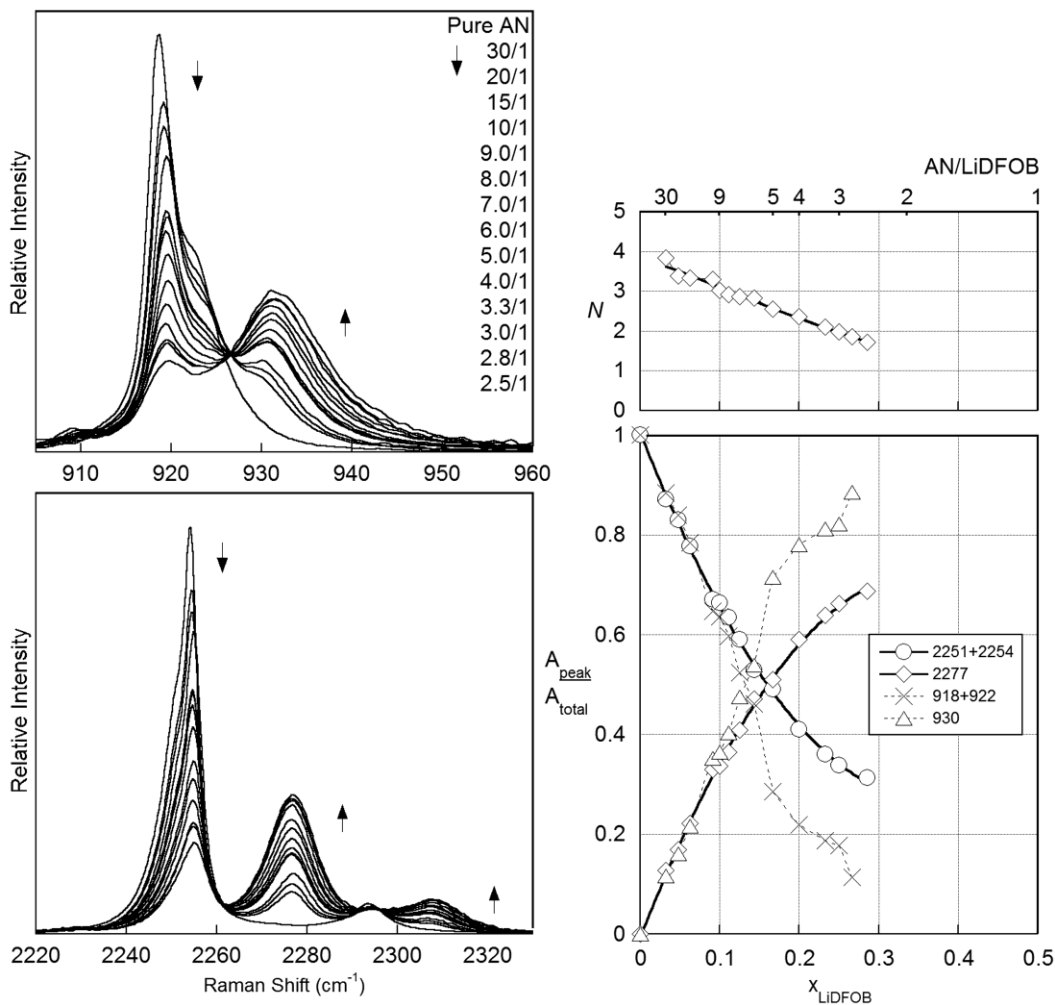


**Figure 6.2.** Raman spectra at 60°C of the AN C–C stretching mode (918  $\text{cm}^{-1}$ ) and C≡N stretching mode (2254  $\text{cm}^{-1}$ ) bands for (AN)<sub>n</sub>-LiDFOB mixture (AN/LiX ratio indicated) and Raman spectroscopic analysis at 60 °C of the solvent bands for uncoordinated AN and Li<sup>+</sup> cation coordinated AN in the (AN)<sub>n</sub>-LiDFOB mixtures. The calculated Li<sup>+</sup> cation average solvation number (*N*) is shown at the top.<sup>51</sup>

Based upon this information and the molar ratio of AN to LiX ( $n$ ), the average solvation number ( $N$ ) variation with salt concentration for the  $(AN)_n$ -LiDFOB mixtures was determined (Fig. 6.2). A comparison with the solvation numbers obtained for other  $(AN)_n$ -LiX mixtures is then possible. Selecting a particular composition, for the  $n = 4$  samples (four AN molecules per  $Li^+$  cation) at 60 °C, the solvation number are approximately 3.2 for  $LiPF_6$ , 2.8 for  $LiTFSI$ , 2.7 for  $LiClO_4$ , 2.3 for  $LiDFOB$ , 2.1 for  $LiBF_4$  and 1.0 for  $LiCF_3CO_2$ .<sup>47,48</sup> This comparison indicates the following order for increasing  $Li^+$  cation solvation in the liquid phase:



The increasing association tendency for the anions (i.e., anion... $Li^+$  cation coordination) results in decreasing solvation for a fixed  $Li^+$  cation coordination number. This is readily understandable if one notes that solvate crystal structures and MD simulations for the  $(AN)_n$ -LiX mixtures indicate that four-fold coordination of the  $Li^+$  cations by the AN molecules and/or anions predominates.<sup>47-50</sup>

These solvation number values are the first indication that the assumption from the phase behavior that  $LiDFOB$  is more associated than  $LiBF_4$  is incorrect. For more dilute mixtures, in fact, the solvation numbers for the  $LiDFOB$  mixtures approach those for mixtures with  $LiClO_4$  (i.e., the slope of the  $N$  vs.  $x_{LiX}$  variation is greater for  $LiDFOB$  than for the other salts). Thus, for  $n = 8$ , the solvation numbers are approximately 3.2-3.3 for  $LiClO_4$ , 3.0 for  $LiDFOB$  and 2.5 for  $LiBF_4$ .<sup>47</sup> The solvation interactions thus change with concentration more significantly for the  $LiDFOB$  mixtures than for  $LiClO_4$  and  $LiBF_4$ .

## 6.4. Raman Characterization of Ionic Association

A detailed study which links the  $\text{DFOB}^-$  anion Raman band positions to various forms of  $\text{DFOB}^- \dots \text{Li}^+$  cation coordination was conducted as part of the present work (Chapter 4).<sup>6</sup> A Raman band attributed with the anion ring breathing vibrational mode, observed at 700-730

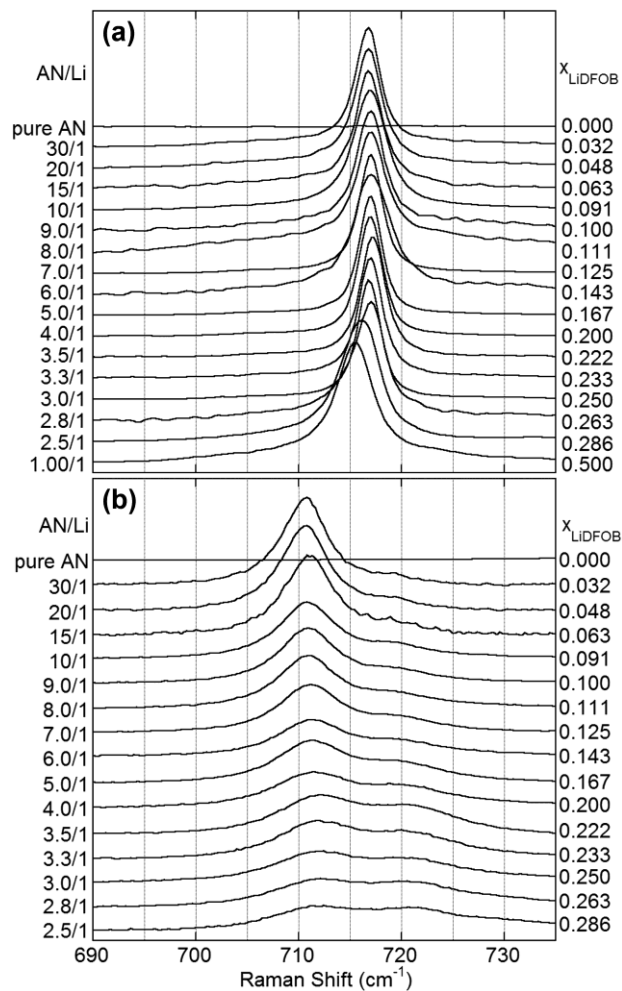


**Figure 6.3.**  $\text{DFOB}^-$  anion band variation with concentration for the  $(\text{AN})_n\text{-LiDFOB}$  mixtures at (a)  $-80\text{ }^\circ\text{C}$  and (b)  $60\text{ }^\circ\text{C}$ .<sup>51</sup>

$\text{cm}^{-1}$ , provides significant insight into the anion coordination. Fig. 6.3a shows the  $\text{DFOB}^-$  anion band variation for this mode for  $(\text{AN})_n\text{-LiDFOB}$  mixtures with varying concentration at  $-80\text{ }^\circ\text{C}$ .<sup>51</sup> At this temperature, all of the samples are crystalline solids. For the dilute mixtures ( $n \geq 3.0$ ), only a single band at  $717\text{ cm}^{-1}$  is observed. A comparison of this plot with the phase diagram in Fig. 6.1a indicates that the  $717\text{ cm}^{-1}$  band corresponds to the AGG phase of the crystalline  $(\text{AN})_3\text{:LiDFOB}$  solvate (Fig. 6.1b) in which the anions are coordinated to two  $\text{Li}^+$  cations (i.e., AGG-Ia).<sup>6</sup> The new band which appears at  $715\text{ cm}^{-1}$  as the concentration is increased further corresponding to a phase consisting of the AGG  $(\text{AN})_1\text{:LiDFOB}$  solvate (Fig. 6.1c) in which the anions are coordinated to three  $\text{Li}^+$  cations through the two carbonyl oxygen atoms (i.e., AGG-IIa).<sup>6</sup> Interestingly, the anion vibrational band moves to lower (rather than higher, as is typical with other anions)<sup>47,48</sup> wavenumber with increasing aggregation.

In the case of the liquid  $(\text{AN})_n\text{-LiDFOB}$  mixtures at  $60\text{ }^\circ\text{C}$  (Fig. 6.3b),<sup>51</sup> broad  $\text{DFOB}^-$  anion bands appear centered at approximately  $711\text{ cm}^{-1}$  and  $720\text{-}725\text{ cm}^{-1}$ , respectively. The former peak is attributed to both SSIP and CIP solvates with anions which are uncoordinated or coordinated to a single  $\text{Li}^+$  cation, respectively.<sup>6</sup> The very broad peak centered near  $720\text{-}725\text{ cm}^{-1}$  is attributed to a range of AGG solvates which can form with this anion.<sup>6</sup> These data indicate that the ions in the dilute  $(\text{AN})_n\text{-LiDFOB}$  mixtures are reasonably dissociated (with SSIP and/or CIPs anion coordination). This is again contrary to the expectations from the phase diagram (Fig. 2a) which indicated that the solid-state solvates are highly associated (and thus one might expect the ions in the liquid to also be highly associated). From the

Raman spectroscopic data, the more concentrated mixtures appear to contain a wide variety of AGG solvates (from the Raman data).<sup>6</sup> Unfortunately, the overlap in the SSIP and CIP Raman bands and the diverse range of AGG solvates that can form make it difficult to deconvolute the spectra (Fig. 6.3b) to identify specific distributions of anion coordination. The previous analysis of the Raman spectra of the DFOB<sup>-</sup> anion bands for crystalline solvates<sup>6</sup> also did not include any CIP solvates in which one of the anion fluorine atoms is coordinated to a Li<sup>+</sup> cation. Thus, it is unknown how such CIP solvates would contribute to the Raman spectra for the liquid electrolytes (Fig. 6.3b). Nevertheless, it is clear that even the most concentrated liquid samples retain some SSIP and/or CIP anion coordination. Such CIP anion coordination, however, may actually correspond to anions in AGG solvates (see below).

The identity of the solvate species present in solution is also a function of temperature. Fig. 6.4 shows the DFOB<sup>-</sup> anion band variation with increasing temperature for the (AN)<sub>n</sub>-LiDFOB (n = 7 and 4) mixtures.<sup>51</sup> When these mixtures are crystalline at -80 °C, only a single band centered at 717 cm<sup>-1</sup> is observed corresponding to the AGG-Ia (AN)<sub>3</sub>:LiDFOB solvate. The Raman vibrational band of the DFOB<sup>-</sup> anion shifts significantly, however, after the solid-to-liquid (melting) phase transition occurs. For the n = 7 mixture, a band centered at 711-712 cm<sup>-1</sup>, corresponding to more dissociated solvates with SSIP and/or CIP anion coordination, is evident for the melt (liquid), as is a shoulder band centered at about 720 cm<sup>-1</sup>. This suggests that upon melting the crystalline solvate, some of the uncoordinated AN solvent available displaces the coordinated anions and coordinates the Li<sup>+</sup> cations instead. An

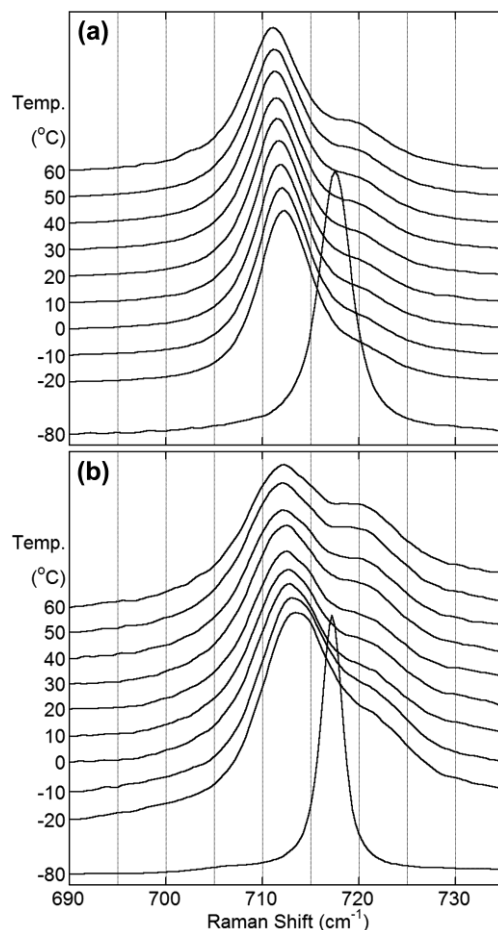


**Figure 6.4.** Temperature dependence of the DFOB<sup>-</sup> anion bands for the (AN)<sub>n</sub>-LiDFOB mixtures for (a)  $n = 7$  and (b)  $n = 4$  (the measurements were obtained while cooling the samples, thus the  $n = 4$  mixture at  $-20\text{ }^{\circ}\text{C}$  is a supercooled liquid).<sup>51</sup>

examination of the Raman data indicates that with increasing temperature, the AGG anion coordination increase somewhat, while the SSIP or CIP anion coordination decreases, but this is not a strong function of temperature. For the  $n = 4$  mixture, the same trend is observed. The solvent thus competes more effectively with the anion for  $\text{Li}^+$  cation coordination at lower temperature and ionic association therefore tends to increase with increasing

temperature (in the liquid state).

## **6.5. Force Field Development and MD Simulations of (AN)<sub>n</sub>-LiDFOB Mixtures**

MD simulations were performed by Dr. Oleg Borodin at the Army Research Laboratory, through an extensive discourse which involved computational iterations to link the work closely with the experimental results, on AN doped with LiDFOB employing a recently developed, many-body polarizable APPLE&P force field for AN and AN/Li<sup>+</sup>, while the force field for the DFOB<sup>-</sup> anion and DFOB<sup>-</sup>/Li<sup>+</sup> interactions has been developed and validated in this work. The APPLE&P functional form was used for all bonded and non-bonded interactions as described elsewhere.<sup>53</sup>

DFOB<sup>-</sup> partial charges were fit to an electrostatic potential grid (89 x 98 x 112 points) around the anion calculated at the MP2/aug-cc-pvTz level with points beyond 4 Å from any atom and closer than 1.7 Å for oxygen, 2.3 Å for carbon, 2.0 Å for boron and 1.8 Å for fluorine excluded from the fit. The mean-square deviation of the electrostatic potential from the force field from MP2/aug-cc-pvTz values was 0.94 (kcal mol)<sup>2</sup>.<sup>54</sup> The in-plane polarizability of the DFOB<sup>-</sup> anion was 8.5 Å<sup>3</sup> and 8.7 Å<sup>3</sup> from the developed force field and M05-2X/aug-cc-pvTz calculations, respectively. The out-of-plane polarizability of the DFOB<sup>-</sup> anion of 5.7 Å<sup>3</sup> from the M05-2X/aug-cc-pvTz calculations was overestimated by the force field which yielded a value of 7.7 Å<sup>3</sup> because the 1-2 (bonds) and 1-3 (bends)

interactions between the induced dipoles were not included in the force field.

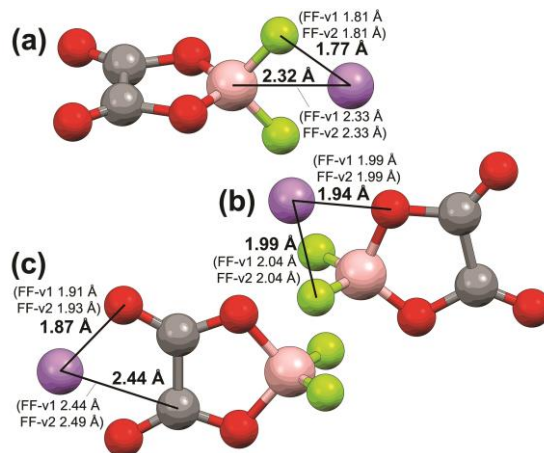
The DFOB<sup>-</sup> anion bond lengths and natural bending angles were fit to the DFOB<sup>-</sup> anion geometry optimized at the M05-2X/aug-cc-pvTz level. All of the repulsion-dispersion parameters were taken from the APPLE&P force field.<sup>53</sup> The repulsion-dispersion parameters for the DFOB<sup>-</sup>/Li<sup>+</sup> interactions were transferred from the EC/Li<sup>+</sup> and BF<sub>4</sub><sup>-</sup>/Li<sup>+</sup> force fields<sup>47,55</sup> without change.

In order to evaluate the ability of the developed force field to accurately predict the DFOB<sup>-</sup>/Li<sup>+</sup> binding energies for the three geometries shown in Fig. 6.5,<sup>51</sup> a set of quantum chemistry calculations was performed. The most accurate estimates of the DFOB<sup>-</sup>/Li<sup>+</sup> binding energies were obtained from the composite G4MP2 level and MP2/aug-cc-pvTz//M05-2X/cc-pvTz shown in Table 6.1.<sup>51</sup> There is good agreement between the binding energies obtained at these two levels thus providing fidelity in the obtained results. Li<sup>+</sup> cation binding to both of the carbonyl oxygen atoms is the most energetically favorable coordination (coord-c) (Table 6.1 and Fig. 6.5). Li<sup>+</sup> cation coordination to the BF<sub>2</sub> group (coord-a) or etheral oxygen and BF<sub>2</sub> group (coord-b) is much less favorable (Table 6.1 and Fig. 6.5). The ability of the DFT calculations to predict the DFOB<sup>-</sup>/Li<sup>+</sup> binding energies was also briefly investigated, as they are much less computationally expensive than using MP2/aug-cc-pvTz and G4MP2. The binding energies calculated using M05-2X/6-31+G\*\* and LC- $\omega$ PBE/6-31+G\*\* are in good agreement with the G4MP2 estimates (Table 6.1). Interestingly, the use of the significantly larger basis set aug-cc-pvTz resulted in worse agreement with the G4MP2 binding energies relative to the smaller 6-31+G\*\* basis set (Table 6.1). The worst results

**Table 6.1.** Binding energies of DFOB<sup>-</sup>/Li<sup>+</sup> complexes (kcal mol<sup>-1</sup>) (see Fig. 6.1).<sup>51</sup>

method	coordination		
	(a)	(b)	(c)
G4MP2	-122.3	-119.5	-134.1
MP2/aug-cc-pvTz <sup>a</sup>	-122.2	-119.4	-135.3
M06-L/aug-pvTz	-122.9	-120.6	-137.5
M05-2X/aug-cc-pvTz	-124.7	-121.9	-139.9
M05-2X/cc-pvTz	-126.2	-123.7	-142.4
M05-2X/6-31+G**	-122.6	-119.7	-136.9
LC- $\omega$ PBE/6-31+G**	-122.2	-119.6	-135.6
FF (v1)	-118.7	-117.6	-133.1
FF (v2)	-118.7	-117.6	-131.4
	BSSE corrections		
MP2/aug-cc-pvTz	0.7	0.8	0.6
LC- $\omega$ PBE/6-31+G**	0.5	0.6	0.5

<sup>a</sup> M05-2X/cc-pvTz geometry was used

**Figure 6.5.** Optimized geometries from G4MP2 calculations (bold) and the force field for the (a), (b) and (c) coordination noted in Table 6.1.<sup>51</sup>

were observed for the cc-pvTz basis set without the polarization and diffuse functions (Table 6.1) which are expected to be important for adequately describing the anions. The basis set superposition errors (BSSE) were calculated from the MP2/aug-cc-pvTz and LC- $\omega$ PBE/6-31+G\*\* methods as 0.5-0.8 kcal mol<sup>-1</sup>.

**Table 6.2.** MD simulation data for the (AN)<sub>n</sub>-LiDFOB mixtures at 60 °C.<sup>51</sup>

Property	AN:Li ratio (n)			
	30	20	10	5
No. solvent in MD box	480	640	640	640
No. LiDFOB in MD box	16	32	64	128
Concentration (M)	0.58	0.86	1.65	2.98
Molality (mol kg <sup>-1</sup> )	0.75	1.08	1.95	3.24
Simulation run length (ns)_v1	22	18	48	29
Simulation box length (Å)_v1	35.74	39.47	40.12	41.47
Simulation run length (ns)_v2	22	22	41	38
Simulation box length (Å)_v2	35.76	39.45	40.06	41.40
MD density (g cm <sup>-3</sup> )_v1	0.800	0.834	0.912	1.040
MD density (g cm <sup>-3</sup> )_v2	0.799	0.835	0.916	1.045
Expt density (g cm <sup>-3</sup> )	0.798	0.824	0.896	1.014
MD viscosity (mPa s)_v1	0.31	0.40	0.65	1.68
MD viscosity (mPa s)_v2	0.31	0.39	0.69	1.72
Expt viscosity (mPa s)	0.35	0.42	0.69	2.11
MD conductivity (mS cm <sup>-1</sup> )_v1	36.8	46.0	45.2	40.4
MD conductivity (mS cm <sup>-1</sup> )_v2	52.6	64.3	75.9	50.2
Expt conductivity (mS cm <sup>-1</sup> )	35.7	41.6	41.9	30.3
Li <sup>+</sup> coordination numbers_v1:				
# N (from AN) (within 2.40 Å of	3.14	3.03	2.74	2.37
# O (within 2.40 Å of Li <sup>+</sup> )	0.61	0.71	0.96	1.23
# F (within 2.40 Å of Li <sup>+</sup> )	0.05	0.07	0.12	0.22
Li <sup>+</sup> coordination numbers_v2:				
# N (from AN) (within 2.40 Å of	3.36	3.25	3.01	2.59
# O (within 2.40 Å of Li <sup>+</sup> )	0.38	0.47	0.67	0.97
# F (within 2.40 Å of Li <sup>+</sup> )	0.05	0.08	0.13	0.26

**Table 6.3.** Probability matrix for DFOB<sup>-</sup> anion coordination to Li<sup>+</sup> cations through the anion carbonyl oxygen and/or fluorine donor atoms.<sup>51</sup>

v1: AN:Li ratio = 30				AN:Li ratio = 20			v2: AN:Li ratio = 30				AN:Li ratio = 20		
O\F	0	1	2	0	1	2	O\F	0	1	2	0	1	2
0	0.41	0.03	0.00	0.34	0.03	0.00	0	0.60	0.04	0.00	0.51	0.05	0.00
1	0.49	0.02	0.00	0.53	0.03	0.00	1	0.34	0.02	0.00	0.39	0.03	0.00
2	0.05	0.00	0.00	0.07	0.00	0.00	2	0.01	0.00	0.00	0.03	0.00	0.00
	AN:Li ratio = 10			AN:Li ratio = 5				AN:Li ratio = 10			AN:Li ratio = 5		
0	0.18	0.03	0.00	0.08	0.02	0.00	0	0.34	0.06	0.00	0.16	0.06	0.00
1	0.54	0.07	0.00	0.44	0.12	0.01	1	0.46	0.06	0.00	0.45	0.14	0.01
2	0.16	0.02	0.00	0.27	0.06	0.00	2	0.07	0.01	0.00	0.15	0.04	0.00

Geometry optimizations were performed using the developed force field parameters resulting in the geometries shown in Fig. 6.5. These are in good agreement with the G4MP2 values. The developed force field predicts the correct order for the DFOB<sup>-</sup>/Li<sup>+</sup> binding energies for coordination modes a-c (Table 6.1), but the binding energies from the force field were systematically low by 1.9-3.8 kcal mol<sup>-1</sup>, as compared to the G4MP2 calculations. This is a similar magnitude of underestimation of the binding energies as was observed for the EC/Li<sup>+</sup> and DMC/Li<sup>+</sup> interactions in previous work.<sup>55</sup>

In addition to the MD simulations (v1) performed with the DFOB<sup>-</sup> anion force field noted above, a set of MD simulations, denoted as v2, was also performed employing a modified force field. In the modified force field, the repulsion between a Li<sup>+</sup> cation and carbonyl oxygen atoms of the DFOB<sup>-</sup> anion was increased resulting in a weaker DFOB<sup>-</sup>/Li<sup>+</sup> binding energy by 1.8 kcal mol<sup>-1</sup> for coord-c in Fig. 6.5. Notably, this difference is less than the difference between the G4MP2 calculations and DFT results summarized in Table 6.1. The

influence of this  $\text{DFOB}^-/\text{Li}^+$  binding energy reduction on the structural, thermodynamic and transport properties was then examined. Table 6.2 compares the results for the original (v1) and modified (v2) force fields.<sup>51</sup> The reduction of the  $\text{DFOB}^-/\text{Li}^+$  binding energy resulted in an increase in the number of AN molecules in the first coordination shell of the  $\text{Li}^+$  cations by  $\sim 0.2$  AN molecules for all of the studied concentrations and a corresponding decrease (by 0.2-0.3) in the number of carbonyl oxygens from the  $\text{DFOB}^-$  anions around the  $\text{Li}^+$  cations. The corresponding decreased ionic association resulted in a higher conductivity (Table 6.2) despite the somewhat lower  $\text{Li}^+$  cation diffusion rate (not shown) in the more dissociated solutions for the AN:Li = 30, 20 and 10 compositions.

Data regarding the average modes of anion coordination over the course of the simulations are provided in Table 6.3.<sup>51</sup> According to both sets of simulations, the  $\text{DFOB}^-$  anions predominantly coordinate the  $\text{Li}^+$  cations through the carbonyl oxygen atoms, but coordination to the cations via the fluorine atoms also occurs to a lesser extent. For example, for the  $n = 20$  mixture, Table 6.3 indicates that 34%/51% (v1/v2 simulations) of the anions are uncoordinated (SSIP coordination - Fig. 6.6a). 53%/39% of the anions are coordinated to a single  $\text{Li}^+$  cation by one of the carbonyl oxygen atoms (CIP coordination - Fig. 6.6c,f,g,i,j,l,m), while only 3%/5% are coordinated to a single  $\text{Li}^+$  cation by one of the fluorine atoms (CIP coordination - Fig. 6.6e,i,j,m). The remaining anions have various forms of AGG coordination—i.e., AGG-I: 7%/3% to two  $\text{Li}^+$  cations by two carbonyl oxygen atoms (Fig. 6.6f,h,i), 3%/3% to two  $\text{Li}^+$  cations by one carbonyl oxygen atom and one fluorine atom (Fig. 6.6i,j,k) and  $< 1\%/< 1\%$  to two  $\text{Li}^+$  cations by two fluorine oxygen atoms;

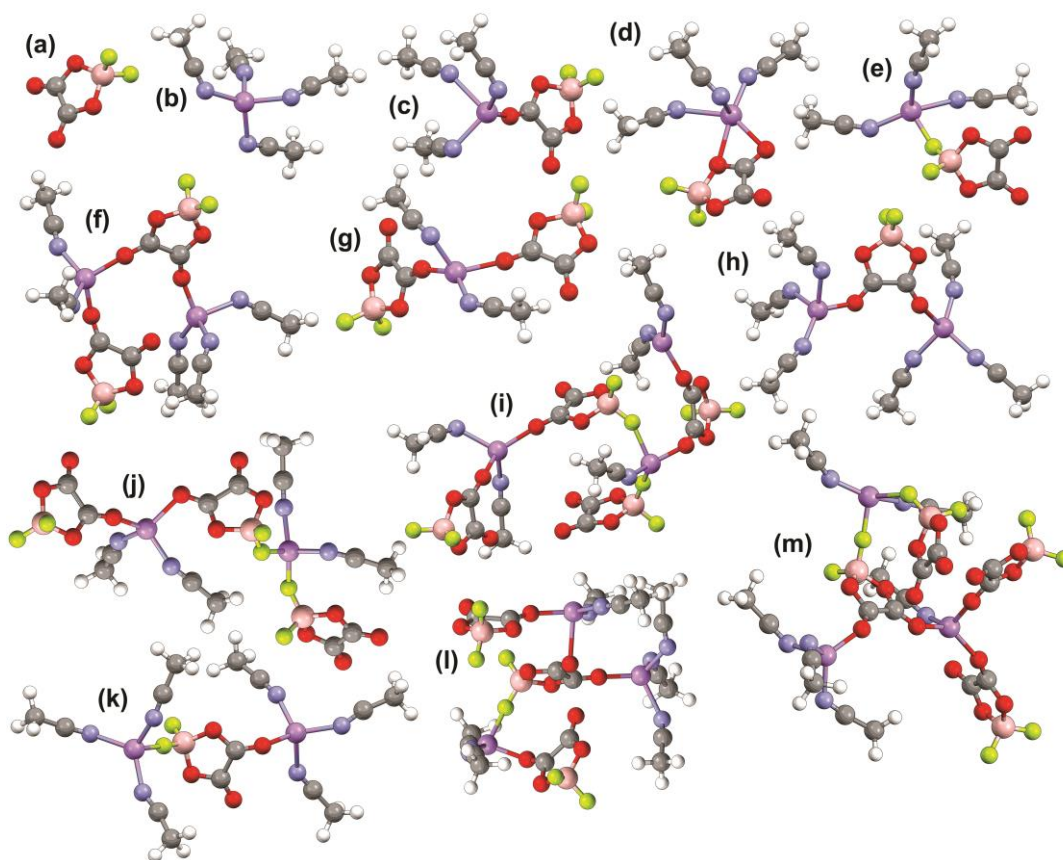


**Figure 6.6.** Representative  $\text{Li}^+$  cation solvate species extracted from the MD simulations for the  $(\text{AN})_n$ -LiDFOB mixtures ( $n = 30, 20$  and  $10$ ) at  $60^\circ\text{C}$  (Li-purple, N-blue, O-red, B-tan, F-light green).<sup>51</sup>

AGG-II:  $< 1\%/< 1\%$  to three  $\text{Li}^+$  cations by two carbonyl oxygen atoms and one fluorine atom (Fig. 6.6l,m) and  $< 1\%/< 1\%$  to three  $\text{Li}^+$  cations by one carbonyl oxygen atom and two fluorine atoms and AGG-III:  $< 1\%/< 1\%$  to four  $\text{Li}^+$  cations by two carbonyl oxygen atoms and two fluorine atoms. Note that when aggregate solvates are present, many of the anions that are coordinated to a single  $\text{Li}^+$  cation (i.e., which spectroscopically have CIP coordination) are actually part of larger aggregate solvates as the  $\text{Li}^+$  cation is coordinated by

more than one anion (Fig. 6.6f,g,i,j,l,m). An additional point of note is that AGG-I anion coordination, in which a given anion is coordinated to two  $\text{Li}^+$  cations, is highly unfavorable for two fluorine atoms (Table 6.3). Instead, this form of coordination is principally via two carbonyl oxygen atoms, but coordination by one carbonyl oxygen atom and one fluorine atom is also somewhat favorable (Table 6.3). This can perhaps be explained by both the energetic preference for carbonyl oxygen... $\text{Li}^+$  cation coordination, as well as steric/packing considerations which also make it favorable (due to a more open, less clustered solvate structure) to aggregate the ions together via coordination bonds if the bonding occurs across the anion (through one carbonyl oxygen atom and one fluorine atom) rather than the closer packing required if the coordination is on one end alone (through both carbonyl oxygen atoms) (Fig. 6.6).<sup>51</sup>

Snapshots of the MD simulations (v1 and v2) were created by modifying the simulation box results as follows—unwrapping all of the molecules/ions and applying periodic boundary conditions so as not to divide the solvate structures across the boundaries of the simulation box (thereby retaining entire solvates) and removing solvent molecules if they were  $> 2.70 \text{ \AA}$  from the  $\text{Li}^+$  cations (uncoordinated and not in close proximity) to facilitate the viewing of the solvates (Appendix C).<sup>51</sup> Fig. 6.6, and the information provided in the Appendix C, exemplify the following features:

- (1) as for the MD simulations for other  $(\text{AN})_n\text{-LiX}$  mixtures,<sup>47-50</sup> the vast majority of the  $\text{Li}^+$  cations have four-fold coordination to the AN molecules and/or anions, as noted above;

- (2) the AN mixtures with LiDFOB have a similar (or somewhat lower) fraction of uncoordinated anions as that found for the AN mixtures with LiClO<sub>4</sub>...and thus are notably more dissociated than comparable mixtures with LiBF<sub>4</sub>;<sup>47,49</sup>
- (3) the majority of the Li<sup>+</sup> cation coordination occurs via coordination bond formation with the DFOB<sup>-</sup> anion carbonyl oxygen atoms—instead of the fluorine atoms, but the fluorine atoms do serve as linkages in the AGG solvates;
- (4) only rare instances of Li<sup>+</sup> cation coordination to the non-carbonyl oxygen atoms of the DFOB<sup>-</sup> anions are observed (Fig. 6.6d); and
- (5) surprisingly, bidentate coordination of a single Li<sup>+</sup> cation by both of the carbonyl oxygen atoms of a given DFOB<sup>-</sup> anion is not evident in the simulations, despite this being a prominent feature of LiDFOB crystalline solvates<sup>6</sup>—it is not clear at this time if this is a real feature of the liquid electrolyte mixtures or if it is instead a limitation of the MD simulation force field developed for this anion.

The validity of these points is dependent upon the degree to which the force fields utilized accurately depict the interactions within actual (AN)<sub>n</sub>-LiDFOB mixtures. The experimental results do mirror the simulation conclusions well where comparisons are possible. Overall, there is generally reasonable agreement found between the experimentally measured and MD simulation calculated viscosity and conductivity values (Table 6.2), with the modified MD simulations (v2) predicting a systematically higher conductivity—this, however, is in accord with previous simulations of (AN)<sub>n</sub>-LiX mixtures with other lithium salts which also predicted conductivity values which exceeded the experimental values. An examination of

the experimental  $\text{Li}^+$  cation solvation and ionic association data for the  $(\text{AN})_n\text{-LiDFOB}$  mixtures (Figs. 6.2 and 6.3) suggests that the ions in the v1 simulations are too associated, whereas those for the v2 simulations may be too dissociated. The modest change to the  $\text{DFOB}^-/\text{Li}^+$  force field binding energy, comparable to the differences noted for the different computational methods (Table 6.1), resulted in sizeable differences in the solvation and ionic association interactions (Tables 6.2 and 6.3, Appendix C).

## 6.6. Transport Properties of $(\text{AN})_n\text{-LiDFOB}$ Mixtures

The relationship between the AN/LiDFOB ratio (i.e.,  $n$ ) and molarity is shown in Fig. 6.7.<sup>51</sup> For reference, a 1 M solution corresponds to a  $n = 17$  composition. Density data for the  $(\text{AN})_n\text{-LiDFOB}$  mixtures with varying temperature are provided in the Appendix C.

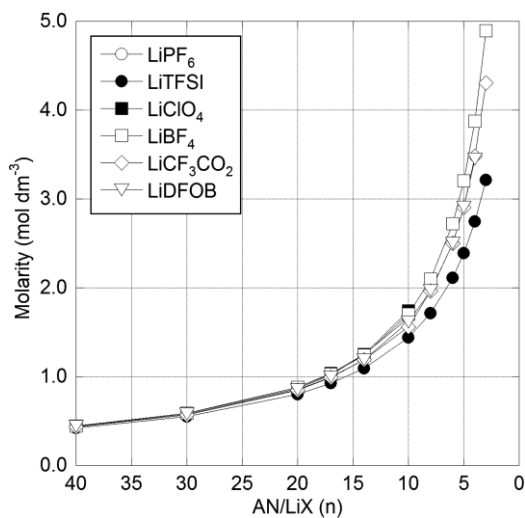


**Figure 6.7.** Relationship between molarity and AN/LiX (i.e.,  $n$ ) for  $(\text{AN})_n\text{-LiX}$  mixtures. Data for salts other than LiDFOB reported for comparison.<sup>49,51</sup>

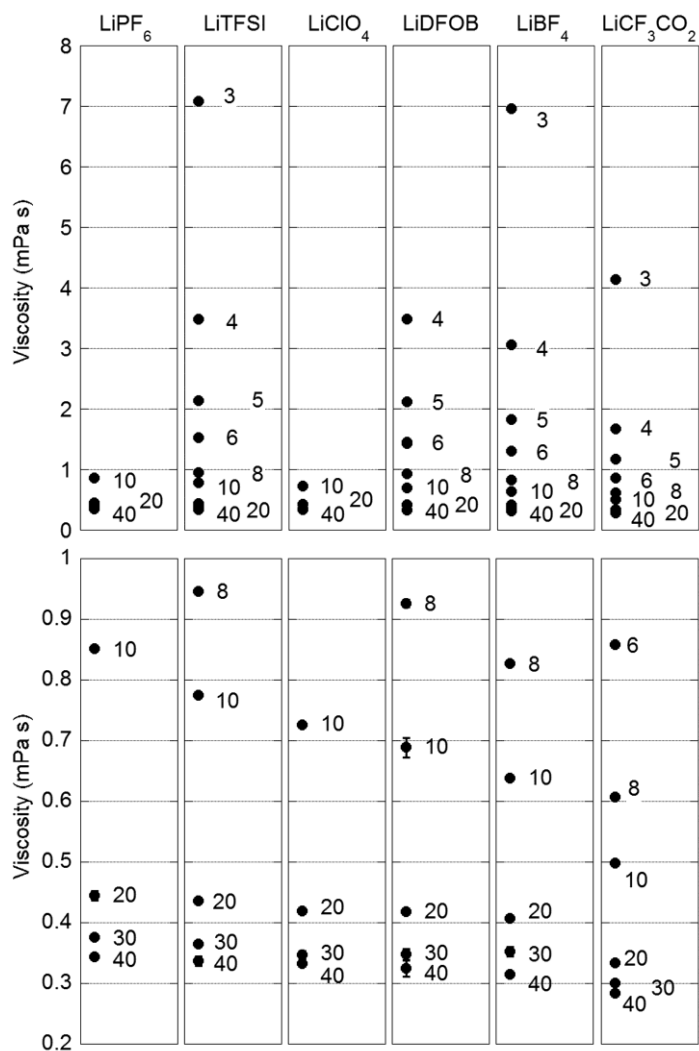


**Figure 6.8.** Viscosity of the  $(AN)_n$ -LiX mixtures at  $60\text{ }^\circ\text{C}$  (AN/LiX ratio noted in plots). Data for salts other than LiDFOB reported for comparison.<sup>49,51</sup>

Viscosity data for the  $(AN)_n$ -LiDFOB mixtures with varying temperature are also provided in the Appendix C. The isothermal viscosity values at  $60\text{ }^\circ\text{C}$  are shown in Fig. 6.8,<sup>51</sup> along with values for the corresponding mixtures with  $\text{LiPF}_6$ ,  $\text{LiTFSI}$ ,  $\text{LiClO}_4$ ,  $\text{LiBF}_4$  and

**Table 6.4.** Fraction of uncoordinated AN (i.e.,  $r_{\text{Li-N}} > 2.40 \text{ \AA}$ ) in the MD simulations. Data for other salts shown for comparison.<sup>47,48,51</sup>

Salt	AN:Li ratio (n)				
	30	20	10	5	2
LiPF <sub>6</sub>	0.89	0.83	0.43	0.43	0.10
LiTFSI	0.90	0.86	0.74	0.56	0.28
LiClO <sub>4</sub>	0.90	0.85	0.72	0.51	0.17
LiBF <sub>4</sub>	0.92	0.89	0.81	0.67	0.36
LiCF <sub>3</sub> CO <sub>2</sub>	0.95	0.93	0.87	0.75	0.44
LiDFOB_v1	0.90	0.85	0.73	0.53	-
LiDFOB_v2	0.89	0.84	0.70	0.48	-

LiCF<sub>3</sub>CO<sub>2</sub>, for comparison.<sup>49</sup> This plot indicates that the viscosity values of the LiDFOB solutions are intermediate between those for LiClO<sub>4</sub> and LiBF<sub>4</sub>. This is in accord with the evaluation results noted above which indicate that the experimental solvation numbers and ionic association interactions of LiDFOB are also intermediate between these salts. These factors are relevant as it has been suggested that the viscosity of such electrolytes is largely influenced by the amount of uncoordinated solvent present.<sup>49</sup> Table 6.4 lists the fraction of the AN molecules in the simulations which are uncoordinated to the Li<sup>+</sup> cations (averaged over the entire simulation runs).<sup>51</sup> A more complete explanation for the viscosity variation, however, also takes into account the differences in the solvates and their populations. The data in Table 6.4 for LiCF<sub>3</sub>CO<sub>2</sub> is unpublished data from an ongoing study. This work indicates that the ions for the mixtures with the LiCF<sub>3</sub>CO<sub>2</sub> salt are almost entirely aggregated into solvated ion clusters, even for the dilute mixtures. Thus, these mixtures resemble the pure solvent with a few larger solvated ion clusters present. In contrast, the dilute LiPF<sub>6</sub> and

**Table 6.5.** Comparison of experimental (from Raman spectroscopic data) and computational (from MD simulations) solvation numbers for the (AN)<sub>n</sub>-LiX mixtures at 60 °C.<sup>47,48,51</sup>

AN:Li ratio (n)	LiPF <sub>6</sub>		LiClO <sub>4</sub>		LiDFOB			LiBF <sub>4</sub>	
	Expt	MD	Expt	MD	Expt	MD_v1	MD_v2	Expt	MD
10	4.35	3.15	3.34	2.80	3.18	2.74	3.01	2.54	1.94
8	4.10	-	3.26	-	3.01	-	-	2.48	-
6	3.93	-	3.09	-	2.76	-	-	2.36	-
5	-	2.84	2.94	2.44	2.57	2.37	2.59	2.26	1.67
4	3.27	-	2.73	-	2.33	-	-	2.12	-

LiClO<sub>4</sub> mixtures consist principally of uncoordinated anions, fully solvated Li<sup>+</sup> cations and solvated contact ion pairs with the LiPF<sub>6</sub> mixtures having less ion pairs than those with LiClO<sub>4</sub>. In addition to the lower amount of uncoordinated solvent present (Tables 6.4 and 6.5),<sup>51</sup> these dispersed species electrostatically interact with one another to a greater extent than for fewer, larger and more widely separated ion clusters thus explaining the higher viscosity found for the more dissociated salts. The MD simulations indicate that the (AN)<sub>n</sub>-LiDFOB mixtures have a comparable (perhaps somewhat lower) overall number of dispersed uncoordinated anions and solvates than the LiClO<sub>4</sub> mixtures, as well as a comparable solvation number (although the experimental solvation number is lower indicating somewhat higher ionic association than for the LiClO<sub>4</sub> mixtures—Table 6.5). The similar (slightly lower) experimental viscosity of the LiDFOB mixtures, relative to the LiClO<sub>4</sub> mixtures, is therefore in accord with this explanation for the origin of the differences in the measured viscosity values.

Conductivity data for the (AN)<sub>n</sub>-LiDFOB mixtures with varying temperature is provided

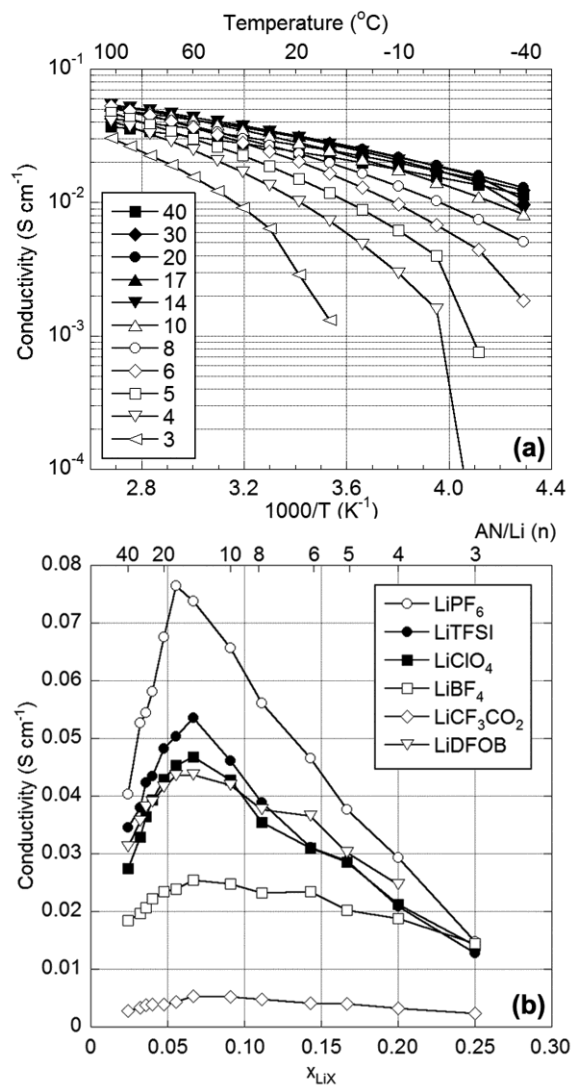


**Figure 6.9.** Ionic conductivity of the (a) (AN)<sub>n</sub>-LiDFOB mixtures (AN/LiX ratio (n) noted in plot) and the (b) (AN)<sub>n</sub>-LiX mixtures at 60 °C. Data for salts other than LiDFOB reported for comparison.<sup>49,51</sup>

in Fig. 6.9a.<sup>51</sup> An isothermal plot of the conductivity of the LiDFOB mixtures at 60 °C is also shown in Fig. 6.9b, while Fig. 6.10 reports the molar conductivity of the mixtures.<sup>51</sup> Data for other salts is included in these figures for comparison.<sup>49</sup> It is interesting to note that the

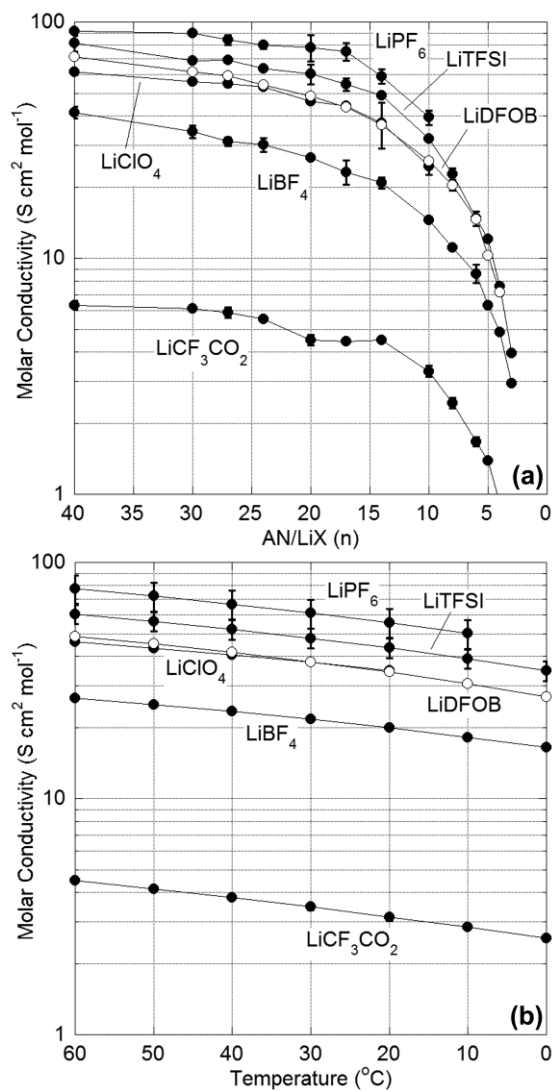


**Figure 6.10.** Molar conductivity of the (a)  $(AN)_n-LiX$  mixtures (60 °C) for varying AN/LiX (n) concentrations and (b)  $(AN)_n-LiX$  mixtures with varying temperature. Data for salts other than LiDFOB reported for comparison.<sup>49,51</sup>

conductivity of the LiDFOB mixtures is comparable to the conductivity of the  $LiClO_4$  mixtures. This is perhaps surprising given that the solvation numbers for the LiDFOB mixtures are lower than those for the  $LiClO_4$  mixtures (Table 6.5). The explanation for this

may lie with the differences, noted above from the simulation results, in the number of uncoordinated anions, fully solvated  $\text{Li}^+$  cations and CIP/AGG solvates. Although the LiDFOB mixtures have less uncoordinated anions (on average) than is found for the  $\text{LiClO}_4$  mixtures, the mixtures with LiDFOB have a greater number of fully solvated  $\text{Li}^+$  cations (Appendix C). This is due to the somewhat higher extent of AGG solvate formation found for the LiDFOB electrolytes (many of which contain more anions than  $\text{Li}^+$  cations thus resulting in negatively charged aggregates) in the MD simulations, in contrast to the  $\text{LiClO}_4$  mixtures which form more isolated CIP and smaller AGG solvates (which often are neutral with equal numbers of anions and  $\text{Li}^+$  cations). Thus, the total number of uncoordinated anions and fully solvated  $\text{Li}^+$  cations in the AN mixtures with  $\text{LiClO}_4$  and LiDFOB is approximately the same. It is reasonable to assume that these smaller charged species dominate the charged species participation in conduction. This implies that the  $(\text{AN})_n$ -LiDFOB electrolytes should have a higher  $\text{Li}^+$  transport number ( $T_{\text{Li}}$ ) than comparable  $(\text{AN})_n$ - $\text{LiClO}_4$  electrolytes. The greater fraction of charged AGG solvates, instead of neutral CIP and AGG solvates, will also contribute to increasing the LiDFOB conductivity. Solvation numbers therefore only provide indirect information about the solvate species and their relation to conduction mechanisms. This discussion about solvate types/population and the relationship to the measured ionic conductivity, however, ignores the dynamic aspects of the solvate formation. It is therefore important to emphasize that the individual solvates are not static in nature—the solvates continuously exchange solvent molecules and anions resulting in relatively rapid transformations from a given solvate species to other solvate species.<sup>49</sup> The information

obtained from the spectroscopic characterization therefore only represents the overall equilibrium distribution of the ion solvation and ionic association interactions.

## 6.7. Conclusions

The phase behavior and solution structure (solvation numbers, ionic association interactions and MD simulations) of  $(\text{AN})_n\text{-LiDFOB}$  electrolyte mixtures have been examined in detail. The salt is found to be dissociated to a similar extent as  $\text{LiClO}_4$ , although significant differences exist between the solvates present in solution and solvation interactions. The associated  $\text{DFOB}^-$  anions tend to form AGG solvates to a greater extent than the associated  $\text{ClO}_4^-$  anions (which instead largely form CIP solvates). The  $\text{LiDFOB}$  salt is considerably more dissociated than  $\text{LiBF}_4$  when dissolved in AN. The variations in the viscosity and conductivity can be directly correlated to the differences noted in the solution structure of these electrolytes. This study demonstrates how this electrolyte characterization methodology—employing several modes of experimental evaluation in concert with MD simulations—enables the rapid scrutiny of the behavior and properties of a given salt.

## 6.8. References

1. S. Tsujioka, H. Takase, M. Takahashi, H. Sugimoto, and M. Koide, US Patent 6,506,516 B1, 2003 (filed: June 7, 1999).
2. S. S. Zhang, *Electrochem. Commun.*, **8**, 1423 (2006).
3. T. Schedlbauer, S. Krueger, R. Schmitz, R. W. Schmitz, C. Schreiner, H. J. Gores, S. Passerini, and M. Winter, *Electrochim. Acta*, **92**, 102 (2013).
4. F. Wu, Q. Zhu, L. Li, R. Chen, and S. Chen, *J. Mater. Chem. A*, **1**, 3659 (2013).
5. S. Li, W. Zhao, X. Cui, Y. Zhao, B. Li, H. Zhang, Y. Li, G. Li, X. Ye, and Y. Luo, *Electrochim. Acta*, **91**, 282 (2013).
6. S.-D. Han, J. L. Allen, E. Jonsson, P. Johansson, D. W. McOwen, P. D. Boyle, and W. A. Henderson, *J. Phys. Chem. C*, **117**, 5521 (2013).
7. H. Zhou, Z. Fang, and J. Li, *J. Power Sources*, **230**, 148 (2013).
8. Y. Zhu, Y. Li, M. Bettge, and D. P. Abraham, *J. Electrochem. Soc.*, **159**, A2109 (2012).
9. S. Li, X. Xu, X. Shi, B. Li, Y. Zhao, H. Zhang, Y. Li, W. Zhao, X. Cui, and L. Mao, *J. Power Sources*, **217**, 503 (2012).
10. H. Zhou, F. Liu, and J. Li, *Appl. Mech. Mater.*, **152-154**, 1106 (2012).
11. C. Yang, Y. Ren, B. Wu, and F. Wu, *Adv. Mater. Res.*, **455-456**, 258 (2012).
12. V. Aravindan and P. Vickaman, *Ind. J. Phys.*, **86**, 341 (2012).
13. M. Hu, J. Wei, L. Xing, and Z. Zhou, *J. Appl. Electrochem.*, **42**, 291 (2012).
14. S. Dalavi, P. Guduru, and B. L. Lucht, *J. Electrochem. Soc.*, **159**, A642 (2012).

15. X. Wu, Z. Wang, X. Li, H. Guo, Y. Zhang, and W. Xiao, *J. Power Sources*, **204**, 133 (2012).
16. V. Aravindan, J. Gnanaraj, S. Madhavi, and H.-K. Liu, *Chem. Eur. J.*, **17**, 14326 (2011).
17. S. Li, X. Xu, X. Shi, and X. Cui, *Adv. Mater. Res.*, **197-198**, 1121 (2011).
18. J. L. Allen, S.-D. Han, P. D. Boyle, and W. A. Henderson, *J. Power Sources*, **196**, 9737 (2011).
19. S. Zugmann, M. Fleischmann, M. Amereller, R. M. Gschwind, M. Winter, and H. J. Gores, *J. Chem. Eng. Data*, **56**, 4786 (2011).
20. S. Zugmann, M. Fleischmann, M. Amereller, R. M. Gschwind, H. D. Wiemhöfer, and H. J. Gores, *Electrochim. Acta*, **56**, 3926 (2011).
21. L. Zhou, W. Li, M. Xu, and B. Lucht, *Electrochem. Solid-State Lett.*, **14**, A161 (2011).
22. S. Zugmann, D. Moosbauer, M. Amereller, C. Schreiner, F. Wudy, R. Schmitz, R. Schmitz, P. Isken, C. Dippel, R. Müller, M. Kunze, A. Lex-Balducci, M. Winter, and H. J. Gores, *J. Power Sources*, **196**, 1417 (2011).
23. J. L. Allen, P. D. Boyle, and W. A. Henderson, *Acta Crystallogr.*, **E67**, m533 (2011).
24. K. Amine, Z. Chen, Z. Zhang, J. Liu, W. Lu, Y. Qin, J. Lu, L. Curtis, and Y.-K. Sun, *J. Mater. Chem.*, **21**, 17754 (2011).
25. M. Xu, L. Zhou, L. Hao, L. Xing, W. Li, and B. L. Lucht, *J. Power Sources*, **196**, 6794 (2011).
26. L. Yang, T. Markmaitree, and B. L. Lucht, *J. Power Sources*, **196**, 2251 (2011).

27. E. Zygadło-Monikowska, Z. Florjańczyk, P. Kubisa, T. Biedroń, A. Tomaszewska, J. Ostrowska, and N. Langwald, *J. Power Sources*, **195**, 6202 (2010).
28. Z. Zhang, X. Chen, F. Li, Y. Lai, J. Li, P. Liu, and X. Wang, *J. Power Sources*, **195**, 7397 (2010).
29. M. H. Fu, K. L. Huang, S. Q. Liu, J. S. Liu, and Y. K. Li, *J. Power Sources*, **195**, 862 (2010).
30. J. Li, K. Xie, Y. Lai, Z. Zhang, F. Li, X. Hao, X. Chen, and Y. Liu, *J. Power Sources*, **195**, 5344 (2010).
31. D. Moosbauer, S. Zugmann, M. Amereller, and H. J. Gores, *J. Chem. Eng. Data*, **55**, 1794 (2010).
32. J. Huang, L.-Z. Fan, B. Yu, T. Xing, and W. Qiu, *Ionics*, **16**, 509 (2010).
33. V. Aravindan, P. Vickraman, and K. Krishnaraj, *Curr. Appl Phys.*, **9**, 1474 (2009).
34. M. Amereller, M. Multerer, C. Schreiner, J. Lodermeier, A. Schmid, J. Barthel, and H. J. Gores, *J. Chem. Eng. Data*, **54**, 468 (2009).
35. A. Xiao, L. Yang, B. L. Lucht, S.-H. Kang, and D. P. Abraham, *J. Electrochem. Soc.*, **156**, A318 (2009).
36. Z. Chen, Y. Qin, J. Liu, and K. Amine, *Electrochem. Solid-State Lett.*, **12**, A69 (2009).
37. H.-Q. Gao, Z.-A. Zhang, Y.-Q. Lai, J. Li, and Y.-X. Liu, *J. Cent. South Univ. Technol.*, **15**, 830 (2008).
38. V. Aravindan, P. Vickraman, and K. Krishnaraj, *Polym. Int.*, **57**, 932 (2008).

39. S.-H. Kang, D. P. Abraham, A. Xiao, and B. L. Lucht, *J. Power Sources*, **175**, 526 (2008).
40. D. P. Abraham, M. M. Furczon, S.-H. Kang, D. W. Dees, and A. N. Jansen, *J. Power Sources*, **180**, 612 (2008).
41. Z. Chen, J. Liu, and K. Amine, *Electrochem. Solid-State Lett.*, **10**, A45 (2007).
42. S. S. Zhang, *J. Power Sources*, **163**, 713 (2007).
43. V. Aravindan and P. Vickraman, *Solid State Sci.*, **9**, 1069 (2007).
44. J. Liu, Z. Chen, S. Busking, and K. Amine, *Electrochem. Commun.*, **9**, 475 (2007).
45. J. Liu, Z. Chen, S. Busking, I. Belharouak, and K. Amine, *J. Power Sources*, **174**, 852 (2007).
46. S. S. Zhang, *J. Power Sources*, **162**, 1379 (2006).
47. D. M. Seo, O. Borodin, S.-D. Han, Q. Ly, P. D. Boyle, and W. A. Henderson, *J. Electrochem. Soc.*, **159**, A553 (2012).
48. D. M. Seo, O. Borodin, S.-D. Han, P. D. Boyle, and W. A. Henderson, *J. Electrochem. Soc.*, **159**, A1489 (2012).
49. D. M. Seo, O. Borodin, D. Balogh, M. O'Connell, Q. Ly, S.-D. Han, S. Passerini, and W. A. Henderson, *J. Electrochem. Soc.*, **160**, A1061 (2013).
50. D. M. Seo, P. D. Boyle, O. Borodin, and W. A. Henderson, *RSC Adv.*, **2**, 8014 (2012).
51. S.-D. Han, O. Borodin, J. L. Allen, D. M. Seo, D. W. McOwen, and W. A. Henderson, *J. Electrochem. Soc.*, in-press (2013).
52. W. A. Henderson, *J. Phys. Chem. B*, **110**, 13177 (2006).

53. O. Borodin, *J. Phys. Chem. B*, **113**, 11463 (2009).
54. O. Borodin, G. V. Zhuang, P. N. Ross, and K. Xu, *J. Phys. Chem. C*, **117**, 7433 (2013).
55. O. Borodin and G. D. Smith, *J. Phys. Chem. B*, **113**, 1763 (2009).

---

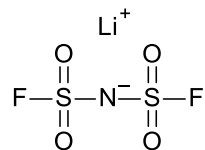
Electrolyte Solvation and Ionic Association  
III. Acetonitrile-Lithium Bis(oxlato)borate (LiFSI) Mixtures

---

Utilizing the previous combination of methods, the electrolyte characteristics of the salt lithium bis(fluorosulfonyl)imide (LiFSI) have been evaluated and compared with those for the other lithium salts previously studied. As a model solvent, acetonitrile (AN) has been used. The information from the thermal phase behavior (phase diagram and solvate crystal structures), the solvation and ionic association interactions (Raman spectroscopic analysis) and the molecular dynamics (MD) simulations of the  $(\text{AN})_n\text{-LiFSI}$  mixtures is shown to provide detailed insight into the coordination interactions of the  $\text{FSI}^-$  anion and explanations for the variability in the transport property (i.e., ionic conductivity) of the AN solutions with this salt relative to other lithium salts.

### 7.1. Introduction

Lithium bis(fluorosulfonyl)imide (LiFSI or  $\text{LiN}(\text{SO}_2\text{F})_2$ ) has drawn significant attention in recent years as a strong candidate for the replacement of  $\text{LiPF}_6$ . The LiFSI salt:



was first reported in a patent application filed in 1995 which indicated a method for its synthesis.<sup>1</sup> Its use in research studies, however, has been restricted until quite recently due to the limited availability and high cost of this salt. A number of publications have been reported about a FSI<sup>-</sup> anion,<sup>2-46</sup> but most of them discuss FSI-based ionic liquids instead of the LiFSI salt. Recent papers, however, indicate that electrolytes with LiFSI have many useful properties (i.e., relatively high thermal and hydrolytic stability, a comparable conductivity to similar electrolytes with the state-of-the-art electrolyte salt LiPF<sub>6</sub> and wide liquidus range).<sup>2-13</sup> It was reported that the use of the LiFSI salt in electrolytes results in severe corrosion of the Al current collector at high potential,<sup>10</sup> but it has recently been demonstrated that this is likely due to chloride impurities in the salt rather than the LiFSI salt itself.<sup>7</sup> To use LiFSI as an alternative lithium salt in advanced Li-ion batteries, however, it is necessary to understand the behavior of this salt in bulk electrolyte solutions. The present study, thus, is an extension of previous work which has scrutinized the relationship between the solution structure (i.e., Li<sup>+</sup> cation solvation and ionic association interactions) and the transport properties of electrolytes in detail.<sup>47-50</sup>

## 7.2. Solvent-Lithium Salt Phase Behavior of (AN)<sub>n</sub>-LiFSI Mixtures

DSC heating traces and the corresponding phase diagrams of (AN)<sub>n</sub>-LiFSI mixtures are

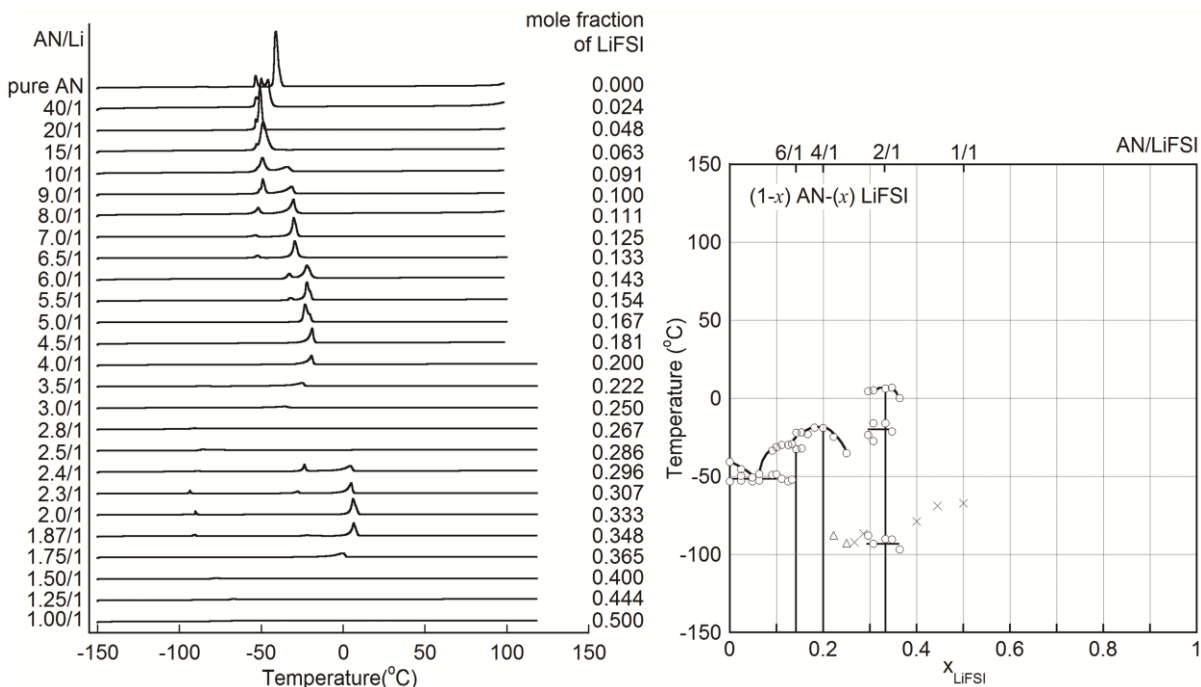


**Figure 7.1.** DSC heating traces ( $5\text{ }^{\circ}\text{C min}^{-1}$ ) and the corresponding phase diagrams for  $(1-x)$  AN- $(x)$  LiFSI mixtures.

shown in Fig. 7.1. The mixtures form three different phases consisting of 6/1, 4/1 and 2/1 (AN/Li) crystalline solvates, respectively. The structures of these solvates are not yet known. For the 6/1 solvate (i.e.,  $(\text{AN})_6\text{:LiFSI}$ ), it is possible that the  $\text{Li}^+$  cations are fully coordinated by six AN molecules (octahedral structure) with uncoordinated  $\text{FSI}^-$  anions, but several studies have suggested that it is not energetically favorable (in the gas phase) to coordinate more than four AN molecules to a  $\text{Li}^+$  cation.<sup>51-56</sup> Notably, the  $(\text{AN})_6\text{:LiPF}_6$  crystalline solvate phase consists of  $\text{Li}^+$  cations fully solvated by four AN molecules, uncoordinated  $\text{PF}_6^-$  anions and two uncoordinated AN molecules (per  $\text{Li}^+$  cation).<sup>56</sup> The 4/1 solvate is also likely to be a SSIP phase which may resemble the known structures for the SSIP  $(\text{AN})_4\text{:LiClO}_4$ <sup>57</sup>

and  $(\text{AN})_4:\text{LiI}^{58}$  solvates in which the  $\text{Li}^+$  cations are coordinated by four AN molecules with uncoordinated anions located between the solvated cations. The structure of the 2/1 solvate may consist of  $\text{Li}^+$  cations coordinated by two or more anion oxygen atoms and two AN molecules, perhaps forming an aggregate dimer. The DSC data suggest that a eutectic is present between the pure crystalline AN solvent and the 6/1 phase. For mixtures more concentrated than  $n = 3.5$ , the  $T_m$  of the 4/1 solvate decreases due to partial crystallization of the 4/1 solvate (the glass transition temperature ( $T_g$ ) is indicated with ‘ $\Delta$ ’ symbols for partially crystalline samples and ‘ $\times$ ’ for fully amorphous samples in Fig. 7.1). There is no crystallization noted for the sample concentrations  $n = 2.8-2.5$  and  $1.50-1.00$  despite the repeated cycling of the samples at various subambient temperatures: in these ‘crystallinity gaps’ (i.e., the samples remained amorphous). The crystallinity gaps can be explained by the fact that the nucleation and growth of ordered crystalline phases is slowed or inhibited altogether when the local structure in the amorphous phase does not resemble that of the crystalline state or when there is no favorable way to pack the solvated ions together for a given concentration.<sup>59</sup> Endotherms at approximately  $-92\text{ }^\circ\text{C}$  and  $-18\text{ }^\circ\text{C}$  indicate solid-solid phase transitions for the 2/1 solvate, respectively, and the endotherms at approximately  $4\text{ }^\circ\text{C}$  correspond to the  $T_m$  for this phase. Although the relatively dissociative salts LiFSI and LiTFSI have similar chemical structures, differences do exist in the phases formed. In particular, it is noteworthy that the 2/1 solvate forms in  $(\text{AN})_n\text{-LiFSI}$  mixture, while a 1/1 solvate instead forms in  $(\text{AN})_n\text{-LiTFSI}$  mixtures (Fig. 7.1).<sup>48</sup>

### 7.3. Raman Characterization of AN-Li<sup>+</sup> Cation Solvation

As mentioned in the previous chapters, uncoordinated AN has an asymmetric C–C ( $\nu_4$ ) stretching vibration band at 918 cm<sup>-1</sup> and an asymmetric C≡N ( $\nu_2$ ) stretching vibration band at 2254 cm<sup>-1</sup>, with the 922 and 2251 cm<sup>-1</sup> shoulders originating from hot bands.<sup>60,61</sup> When the electron lone-pair on the AN nitrogen atom is coordinated to a Li<sup>+</sup> cation, these Raman bands shift to 930 and 2277 cm<sup>-1</sup>, respectively (Fig. 7.2).<sup>62-64</sup> Raman measurements were performed for the mixtures with LiFSI at 60 °C in which the mixtures are homogeneous solutions (or melts) over a wide composition range (Fig. 7.1). From the Raman spectra of the AN C–C and C≡N stretching bands for the (AN)<sub>n</sub>-LiFSI mixtures, plots of the peak area for the Li<sup>+</sup> cation coordinated and uncoordinated AN (normalized relative to the total peak area) were prepared (Fig. 7.2). From this information and the molar ratio of AN to LiX (i.e.,  $c_{\text{AN}}/c_{\text{LiX}}$ ), the average solvation number ( $N$ ) variation with salt concentration for the (AN)<sub>n</sub>-LiFSI mixtures was determined (Fig. 7.2) and compared with the solvation number data for other (AN)<sub>n</sub>-LiX mixtures.<sup>47-50</sup> For comparison, for the  $n = 4$  samples which consist of mixtures with four AN molecules per Li<sup>+</sup> cation (at 60 °C), the solvation numbers are approximately 3.2 for LiPF<sub>6</sub>, 2.8 for LiFSI, 2.8 for LiTFSI, 2.7 for LiClO<sub>4</sub>, 2.3 for LiDFOB, 2.1 for LiBF<sub>4</sub> and 1.0 for LiCF<sub>3</sub>CO<sub>2</sub>.<sup>47-50</sup> This comparison indicates the following order for increasing Li<sup>+</sup> cation solvation (decreasing ionic association) in the liquid phase:



The decreasing association tendency for the anions (i.e., anion...Li<sup>+</sup> cation coordination) results in increasing solvation for a fixed Li<sup>+</sup> cation coordination number. This is readily

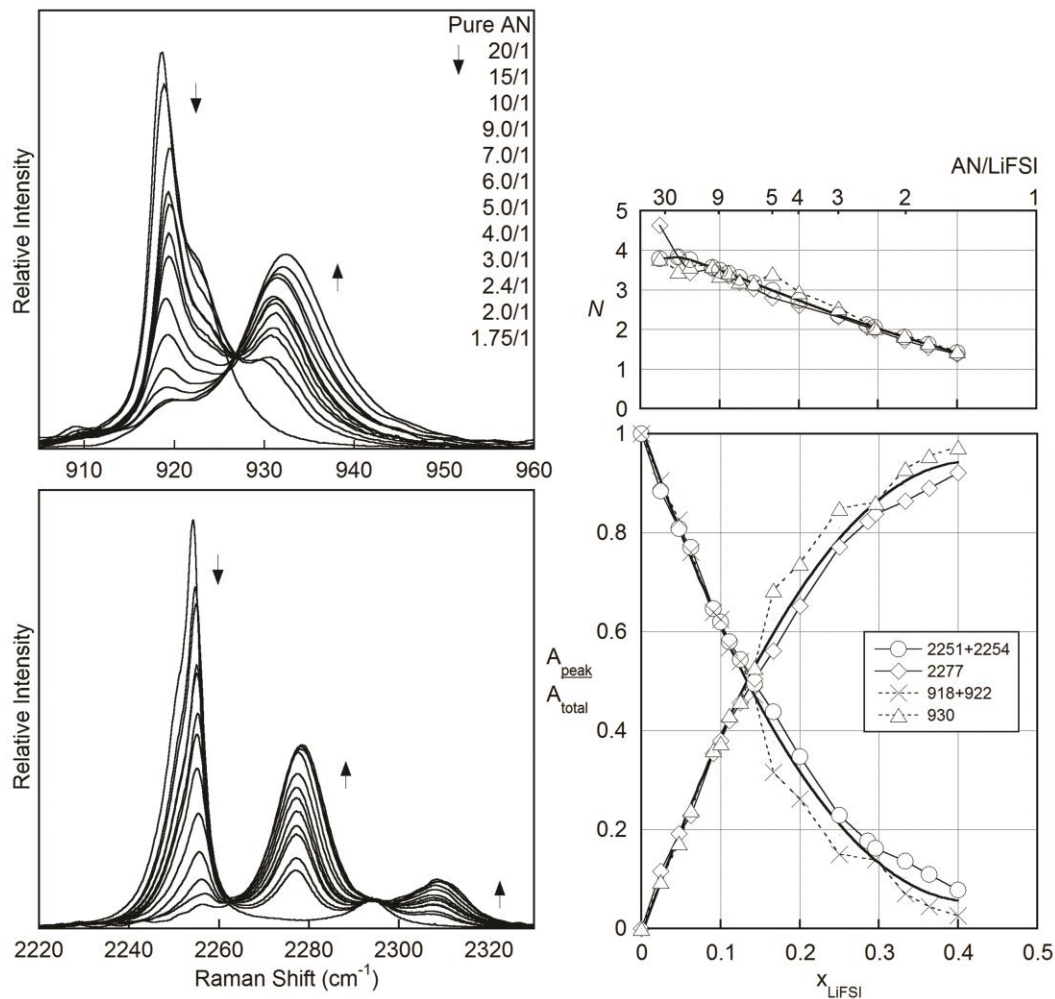


**Figure 7.2.** Raman spectra at 60 °C of the AN C–C (920  $\text{cm}^{-1}$ ) and C $\equiv$ N (2250  $\text{cm}^{-1}$ ) stretching mode bands for the  $(\text{AN})_n$ -LiFSI mixtures (AN/LiX ratio indicated) and Raman spectroscopic analysis at 60 °C of the solvent bands for the uncoordinated and coordinated (to  $\text{Li}^+$  cations) AN in the  $(\text{AN})_n$ -LiFSI mixtures. The calculated  $\text{Li}^+$  cation average solvation number ( $N$ ) is shown at the top.

understandable considering the predominant four-fold coordination of the  $\text{Li}^+$  cations by the AN molecules and/or anions as determined from the known solvate crystal structures and MD simulations studies for  $(\text{AN})_n$ -LiX mixtures.<sup>47-50,56</sup>

As for the  $(\text{AN})_n\text{-LiTFSI}$  mixtures, the  $\text{FSI}^-$  anions in the  $(\text{AN})_n\text{-LiFSI}$  mixtures are able to adopt bidentate coordination to the  $\text{Li}^+$  cations due to the flexible structure of the anions, which makes this salt appear as associated as  $\text{LiClO}_4$  from the solvation data alone. In a later section, however, the MD simulations and analysis of the transport properties for the  $(\text{AN})_n\text{-LiFSI}$  mixtures will prove that  $\text{LiFSI}$  is a more dissociated salt than  $\text{LiClO}_4$ .

#### 7.4. Raman Characterization of Ionic Association

Fig. 7.3a shows the  $\text{FSI}^-$  anion band variation with concentration for the  $(\text{AN})_n\text{-LiFSI}$  mixtures at  $-80\text{ }^\circ\text{C}$ . At this temperature, all of the samples except those in the crystallinity gaps are crystalline solids. For the dilute mixtures ( $n \geq 4.0$ ), two anion bands are observed which indicate two different solvate phases, 6/1 and 4/1, as shown in the phase diagram (Fig. 7.1), as well as a solvent band. The  $\text{FSI}^-$  anion is known to be flexible with two low-energy  $C_2$  (*trans*) and  $C_1$  (*cis*) conformers.<sup>34,40,65</sup> These two conformational states likely are the origin of the different band positions ( $726$  and  $720\text{ cm}^{-1}$ ) for the mixtures with  $n = 4.0\text{-}6.5$  and  $6.0\text{-}4.5$ , even though all of these mixtures with crystalline solvate phases are likely to contain uncoordinated anions (i.e., SSIP solvates). Both the  $n = 5$  and  $4.5$  mixtures have a Raman band at  $720\text{ cm}^{-1}$  with a shoulder at  $728\text{ cm}^{-1}$ , which may be due to the different anion conformations in the 6/1 and 4/1 crystalline phases. The  $n = 4$  mixture, however, has a Raman band at  $728\text{ cm}^{-1}$  with a shoulder at  $720\text{ cm}^{-1}$  which suggests that the amounts of the two different conformers are reversed for the  $n = 5$  and  $4.5$  mixtures. In the case of the  $n = 3$  mixture, the band at  $728\text{ cm}^{-1}$  and the new broad band at  $740\text{-}750\text{ cm}^{-1}$  indicate that there is

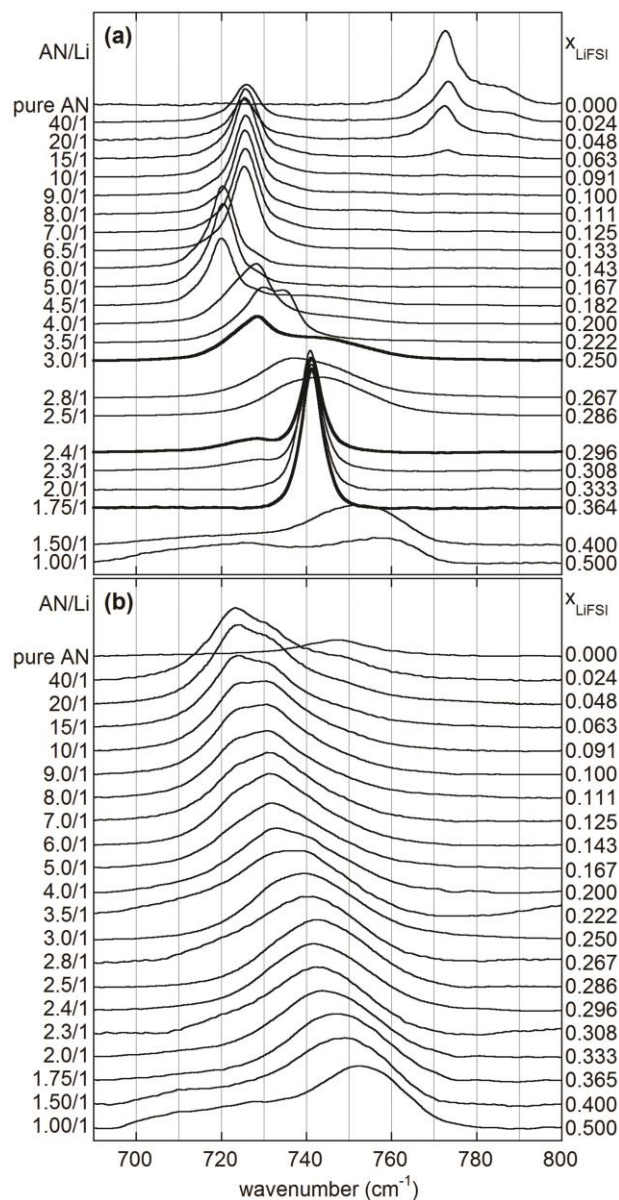


**Figure 7.3.** FSI<sup>-</sup> anion band variation with concentration in the (AN)<sub>n</sub>-LiFSI mixtures at (a) -80 °C and (b) 60 °C (The mixtures with n = 2.8, 2.5, 1.50 and 1.00 are in the crystallinity gap and remain either fully amorphous liquids or glassy solids at -80 °C).

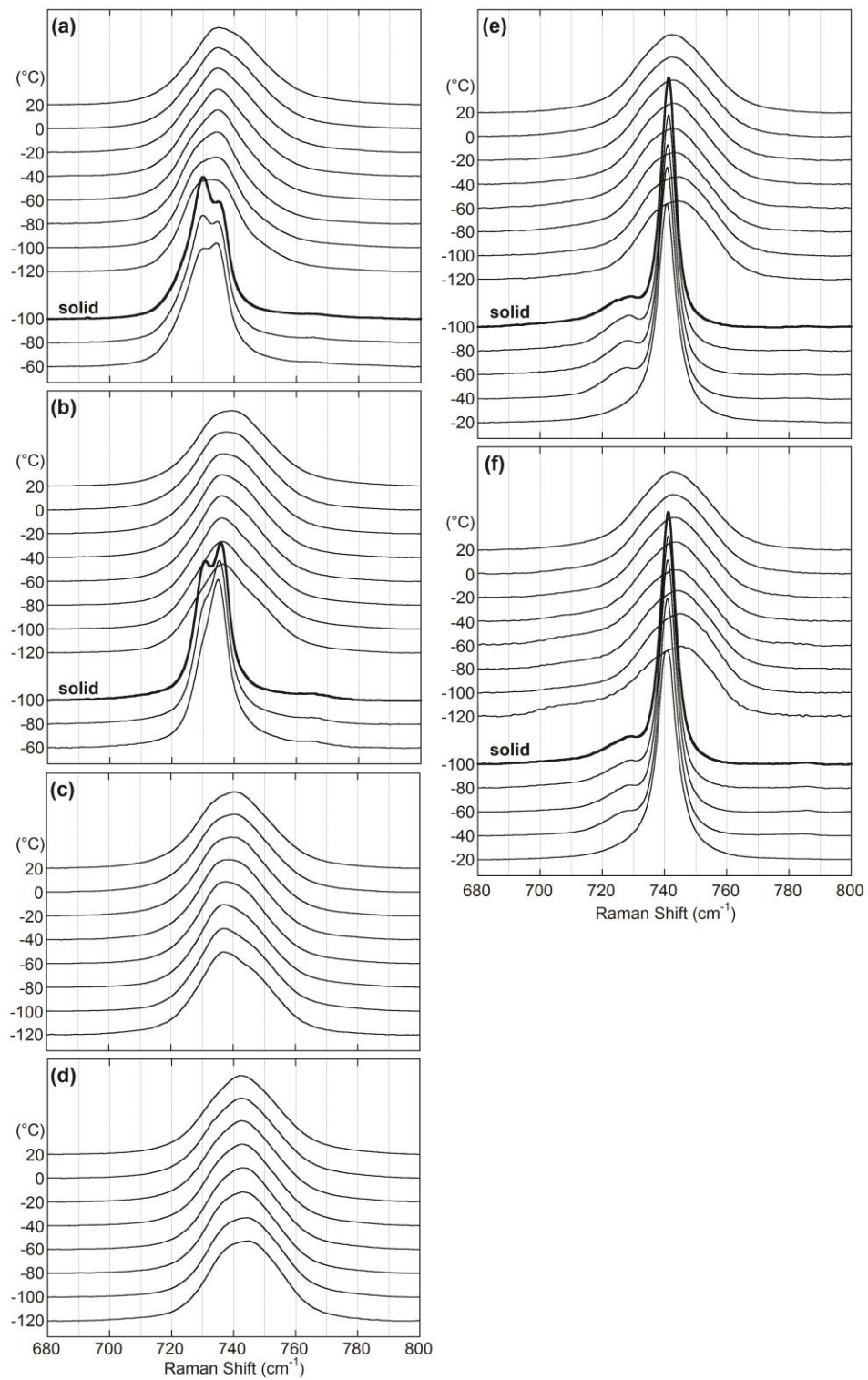
partial crystallization of the 4/1 solvate phase, as well as some amorphous phase present, as

shown in Fig. 7.1. In the first crystallinity gap ( $2.4 < n < 3.0$ ), the mixtures are liquids with broad Raman bands. With increasing concentration, the Raman bands shift to a higher band position of  $741 \text{ cm}^{-1}$  due to the crystallization of the more aggregated 2/1 solvate. For the  $n = 2.4$  mixture, two bands due to the 4/1 ( $728 \text{ cm}^{-1}$ ) and 2/1 ( $741 \text{ cm}^{-1}$ ) solvate phases are evident. For the second crystallinity gap ( $n < 1.75$ ), the mixtures show the same trends (broad bands) as for the first crystallinity gap.

In the case of the liquid phase at  $60 \text{ }^\circ\text{C}$ , the  $\text{FSI}^-$  anion bands for  $(\text{AN})_n\text{-LiFSI}$  mixtures shift consistently from  $723 \text{ cm}^{-1}$  to  $752 \text{ cm}^{-1}$  with increasing salt concentration, as shown in Fig. 7.3b. The  $\text{FSI}^-$  anion is able to coordinate  $\text{Li}^+$  cations in a variety of ways. This makes the accurate deconvolution of the anion bands for the different solvates a significant challenge. For dilute mixtures ( $n \geq 4.0$ ), the anion bands are observed at  $723 \text{ cm}^{-1}$  and  $731 \text{ cm}^{-1}$  which indicates that less aggregated solvates such as SSIP and CIP are dominant. For the concentrated mixtures ( $n < 4.0$ ), however, the anion bands shift from  $739 \text{ cm}^{-1}$  to  $752 \text{ cm}^{-1}$ , which indicates that more aggregated solvates (AGG) are dominant. Even though it is difficult to determine deconvolute the anion spectra at a specific concentration, it is clear that the degree of ionic association increases as the concentration of the salt increases.

The Raman band variation for the  $\text{FSI}^-$  anion in the crystallinity gap with changing temperature and concentration is shown in Fig. 7.4. Raman spectroscopy may be used to aid in explaining why the crystallinity gaps exist for the  $(\text{AN})_n\text{-LiFSI}$  mixtures. For the  $n = 3.5$  (Fig. 7.4a) and  $3.0$  (Fig. 7.4b) mixtures, the Raman band at  $731 \text{ cm}^{-1}$  increases as the temperature decreases, which indicated that the amount of less associated solvates, such as

**Figure 7.4.** Variable-temperature  $\text{FSI}^-$  anion band variation with concentration in the  $(\text{AN})_n\text{-LiFSI}$  mixtures with (a)  $n = 3.5$ , (b)  $n = 3.0$ , (c)  $n = 2.8$ , (d)  $n = 2.5$ , (e)  $n = 2.4$  and (f)  $n = 2.3$ .



CIPs, may dominant. In this concentration range, the mixtures are easily crystallized. However, at low temperature the Raman anion band peak for the  $n = 2.8$  (Fig. 7.4c) and 2.5 (Fig. 7.4d) mixtures, in which the nucleation and growth of ordered crystalline phases is slowed or inhibited altogether, shifts from about  $736 \text{ cm}^{-1}$  to  $744 \text{ cm}^{-1}$ . A diverse range of anion coordination in terms of both anion conformations and number of  $\text{Li}^+$  cations coordinated appears to be present for these mixtures. It may be that this medley of ionic interactions does not resemble the coordination found in the crystalline solvate phases and this hinders the nucleation and subsequent growth of the crystalline phases. At low temperature, the more concentrated  $n = 2.4$  (Fig. 7.4e) and 2.3 (Fig. 7.4f) mixtures have a substantial Raman band at  $741 \text{ cm}^{-1}$ , which corresponds to the Raman band of more aggregated solvates (AGG). This amount of aggregated anions is sufficient to induce nucleation of the aggregated crystalline phase. Thus, both of these mixtures form the AGG 2/1 solvate in this concentrated range.

Fig. 7.5 shows the temperature dependence of the  $\text{FSI}^-$  anion bands in the  $(\text{AN})_n\text{-LiFSI}$  ( $n = 8$  and 4) mixtures. When the  $n = 8$  mixture is crystalline at  $-80 \text{ }^\circ\text{C}$ , a single band is observed corresponding to the dissociated SSIP  $(\text{AN})_6\text{:LiFSI}$  solvate. When the  $n = 4$  mixture is crystallized at  $-80 \text{ }^\circ\text{C}$ , a band ( $723 \text{ cm}^{-1}$ ) with both left ( $720 \text{ cm}^{-1}$ ) and right ( $741 \text{ cm}^{-1}$ ) shoulders is observed which correspond to the SSIP  $(\text{AN})_6\text{:LiFSI}$ , SSIP  $(\text{AN})_4\text{:LiFSI}$  and AGG  $(\text{AN})_2\text{:LiFSI}$  solvates, respectively. However, a significant Raman vibrational band shift for the  $\text{FSI}^-$  anion is observed after the solid to liquid phase transition occurs. For the  $n = 8$  mixture, bands at  $725$  and  $731 \text{ cm}^{-1}$ , corresponding to dissociated solvates, such as SSIPs

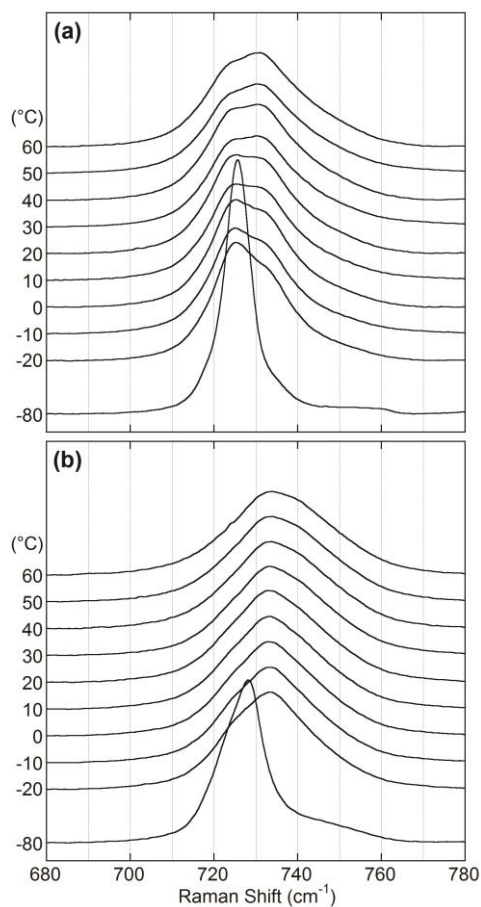


**Figure 7.5.** Temperature dependence of the FSI<sup>-</sup> anion bands in the (AN)<sub>n</sub>-LiFSI mixtures for (a) n = 8 and (b) n = 4.

or CIPs, are evident. Deconvolution of the Raman bands indicates that with decreasing temperature, the more associated anion coordination (731 cm<sup>-1</sup>) decreases somewhat, while the uncoordinated anions (725 cm<sup>-1</sup>) increase. For the n = 4 mixture, the same trend is observed, except that the concentration of associated anions (AGG, 741 cm<sup>-1</sup>) increases at the expense of the SSIP or CIP anion coordination. Again, solvation is more effective at lower temperature, while ionic association tends to increase with increasing temperature.

## 7.5. MD Simulations of (AN)<sub>n</sub>-LiFSI Mixtures

MD simulations were conducted for the liquid (AN)<sub>n</sub>-LiFSI mixtures (60 °C) with  $n = 30$ , 20, 10 and 5 by Dr. Oleg Borodin at the U.S. Army Research Laboratory (ARL). A summary of the simulation information is provided in Table 7.1. Comparing the results in Table 7.1 with other lithium salts studied previously, LiFSI is found to be more dissociated than LiClO<sub>4</sub>, but less dissociated than LiPF<sub>6</sub>, in agreement with the experimental results. For example, the average solvation numbers  $N$  (the number of nitrogen atoms from AN coordinated to the Li<sup>+</sup> cations) in Table 7.1 are somewhat lower than the experimental values (Fig. 7.2), but they are also in reasonable agreement with the ionic association strength order.

Examples of the coordination found for the FSI<sup>-</sup> anions to the Li<sup>+</sup> cations in the solvates from the MD simulations are shown in Fig. 7.6. The solvates (and uncoordinated anions) extracted from snapshots of the simulations for the (AN)<sub>n</sub>-LiFSI mixtures ( $n = 30$  and 10) are also shown in Figs. C17-C22 (in Appendix C) which are visual lists of the solvates and uncoordinated anions in the simulation snapshots. These figures provide information about both the solvate distribution (at a given time) in the different simulations, as well as the solvate structures. The information from Figs. 7.6 and C17-C22 exemplify the following features:

- (1) as mentioned above, the FSI<sup>-</sup> anion, like TFSI<sup>-</sup>, is flexible with two low-energy  $C_1$  (*cis*) and  $C_2$  (*trans*) conformers (Figs. 7.6a and 7.6b) which result in the two different anion band positions for the uncoordinated anions (Fig. 7.3);<sup>34,40,65</sup>

**Table 7.1.** MD simulations data for the (AN)<sub>n</sub>-LiFSI mixtures at 60 °

Property	AN:Li ratio			
	30	20	10	5
No. solvent in MD box	480	640	640	640
No. LiFSI in MD box	16	32	64	128
Concentration (M)	0.58	0.85	1.60	2.84
Molality (mol kg <sup>-1</sup> )	0.71	0.99	1.67	2.55
Simulation run length (ns)	23	20	16	18
Simulation box length (Å)	35.87	39.65	40.48	42.14
MD density (g cm <sup>-3</sup> )	0.816	0.859	0.957	1.114
Expt density (g cm <sup>-3</sup> )	0.818	0.853	0.947	1.096
MD conductivity (mS cm <sup>-1</sup> )	61.9	61.5	76.0	59.5
Expt conductivity (mS cm <sup>-1</sup> )	49.9	58.5	65.5	51.3
Fraction of free Li (r <sub>Li-N</sub> > 4.80 Å) (SSIP)	0.61	0.52	0.35	0.16
Fraction of free N <sup>**</sup> (r <sub>Li-N</sub> > 4.80 Å) (SSIP)	0.60	0.52	0.34	0.15
Li <sup>+</sup> coordination numbers				
# N* (within 2.40 Å of Li <sup>+</sup> )	3.40	3.32	3.09	2.69
# O (within 2.40 Å of Li <sup>+</sup> )	0.40	0.50	0.74	1.16
# N** (within 4.80 Å of Li <sup>+</sup> )	0.43	0.54	0.81	1.29
Probability of finding the following number of Li <sup>+</sup> within the given distance from the N of FSI <sup>-</sup>				
0 Li <sup>+</sup> within 4.60/4.80 Å of N (SSIP)	0.64/0.60	0.56/0.52	0.39/0.34	0.19/0.18
1 Li <sup>+</sup> within 4.60/4.80 Å of N (CIP)	0.33/0.36	0.40/0.43	0.49/0.51	0.51/0.44
2 Li <sup>+</sup> within 4.60/4.80 Å of N (AGG-I)	0.02/0.03	0.04/0.05	0.11/0.14	0.26/0.30
3 Li <sup>+</sup> within 4.60/4.80 Å of N (AGG-II)	0.00/0.00	0.00/0.00	0.01/0.01	0.04/0.08
4 Li <sup>+</sup> within 4.60/4.80 Å of N (AGG-III)	0.00/0.00	0.00/0.00	0.00/0.00	0.00/0.01

\* N from AN, \*\* N from FSI<sup>-</sup>

- (2) almost all of the Li<sup>+</sup> cations have four-fold coordination to the AN molecules and/or anions, as is found for the MD simulations results for other (AN)<sub>n</sub>-LiX mixtures;<sup>47-50</sup>
- (3) essentially all of the Li<sup>+</sup> cation coordination occurs via coordination bond formation with the FSI<sup>-</sup> anion sulfonyl oxygen atoms instead of the fluorine (or nitrogen) atoms;
- (4) in contrast with semi-spherical anions such as PF<sub>6</sub><sup>-</sup>, ClO<sub>4</sub><sup>-</sup> and BF<sub>4</sub><sup>-</sup>, bidentate coordination of the FSI<sup>-</sup> anion to a given Li<sup>+</sup> cation in the MD simulations is not

uncommon (Figs. 7.6f and 7.6k), but less bidentate coordination is found than for the (AN)<sub>n</sub>-LiTFSI mixtures;<sup>47-49</sup>

(5) the (AN)<sub>n</sub>-LiFSI mixtures have a lower fraction of uncoordinated anions than is found for the AN mixtures with LiPF<sub>6</sub>, but the fraction is much higher than that for the (AN)<sub>n</sub>-LiClO<sub>4</sub> mixtures—the (AN)<sub>n</sub>-LiFSI mixtures are therefore notably more dissociated than the (AN)<sub>n</sub>-LiClO<sub>4</sub> mixtures and comparable in dissociation to the (AN)<sub>n</sub>-LiPF<sub>6</sub> mixtures;<sup>47-49</sup> and

(6) for the most dilute mixture (n = 30), the numbers of both uncoordinated anions and solvated Li<sup>+</sup> cations for the mixtures with LiFSI are lower than those for the comparable mixtures with LiPF<sub>6</sub>, but as the concentration increased (n < 10), these numbers for the (AN)<sub>n</sub>-LiFSI mixtures are higher than those with LiPF<sub>6</sub> (Figs. C17-C22).

Note that the degree to which the MD simulation force fields utilized accurately depict the interactions within actual (AN)<sub>n</sub>-LiFSI mixtures determines the validity of these points. The MD simulation results agree well with the experimental data, but differences do exist. Similar to the mixtures with the other lithium salts studied previously (Table 6.5), the computational solvation numbers for the (AN)<sub>n</sub>-LiFSI mixtures (at 60 °C) are somewhat lower than the experimental values (Table 7.1), which suggests that the simulations tend to overpredict the extent of ionic association within the electrolytes. Considering the inherent error associated with both sets of analyses, however, the overall trends from the experimental data and MD simulation results for the conductivity shows good agreement (Table 7.1).

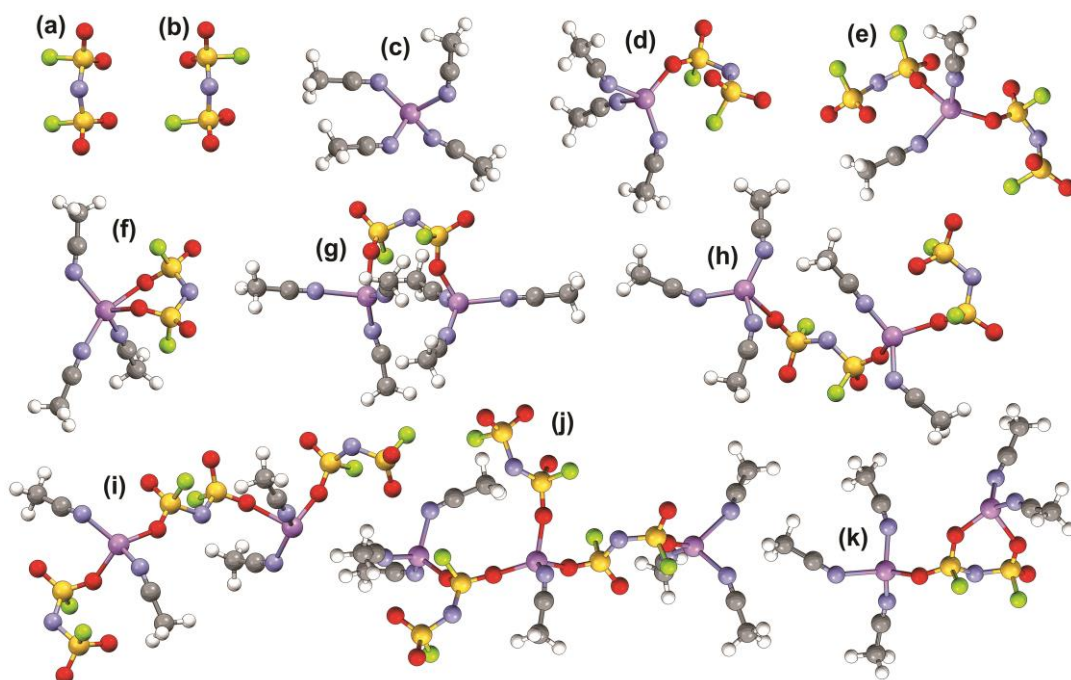
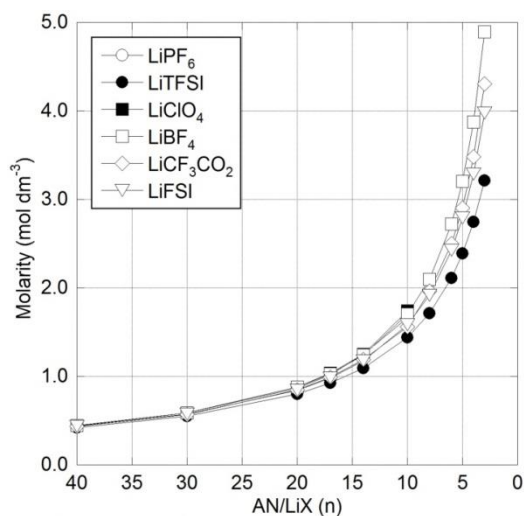


**Figure 7.6.** Representative  $\text{Li}^+$  cation solvate species extracted from the MD simulations for the  $(\text{AN})_n$ -LiFSI mixtures ( $n = 30, 20$  and  $10$ ) at  $60^\circ\text{C}$  (Li-purple, N-blue, O-red, S-yellow, F-light green).

## 7.6. Transport Properties of $(\text{AN})_n$ -LiFSI Mixtures

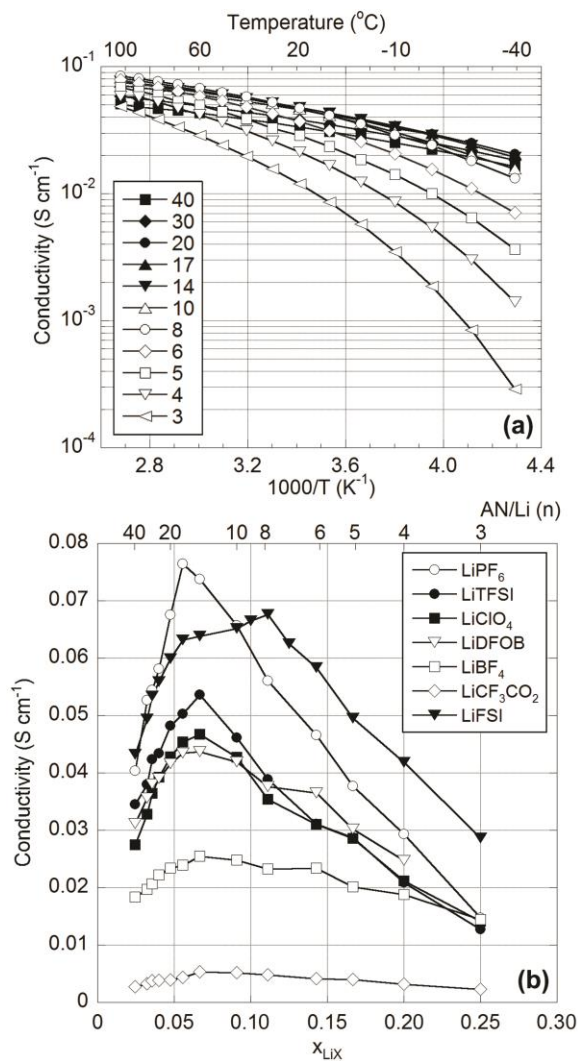
Fig. 7.7. shows the relationship between the AN/LiFSI ratio (i.e.,  $n$ ) and molarity. As a reference, a  $n = 17$  composition corresponds to a 1 M solution. Density data for the  $(\text{AN})_n$ -LiFSI mixtures with varying temperature are provided in Appendix C. The viscosity measurements for the  $(\text{AN})_n$ -LiFSI mixtures and the comparison with other  $(\text{AN})_n$ -LiX mixtures are on-going.

Fig. 7.8a shows the conductivity data for the  $(\text{AN})_n$ -LiFSI mixtures with varying temperature, while an isothermal ( $60^\circ\text{C}$ ) plot of the conductivity for the LiFSI mixtures is



**Figure 7.7.** Relationship between molarity and AN/LiX (i.e.,  $n$ ) for the (AN)-LiX mixtures. Data for salts other than LiFSI are reported for comparison.<sup>49</sup>

shown in Fig. 7.8b. The molar conductivity of the mixtures is represented in Fig. 7.9. All of the conductivity plots include data for other salts for comparison.<sup>47-50</sup> For the diluted concentrations ( $n \leq 24$ ), the conductivity of the LiFSI mixtures is comparable to the conductivity of the LiPF<sub>6</sub> mixtures. As the salt concentration increases, however, the conductivity values of the LiPF<sub>6</sub> mixtures ( $10 < n < 24$ ) are higher than those of the LiFSI mixtures. But for the more concentrated electrolytes, the LiFSI mixtures have a much higher conductivity than the LiPF<sub>6</sub> mixtures. It is interesting that the LiFSI mixtures a peak conductivity value at  $n = 8$ , which is not the case for other lithium salts. For the most concentrated mixtures ( $n = 3$ ), the conductivity of the LiFSI containing electrolyte is remarkably higher than the values for the other lithium salts including LiPF<sub>6</sub>. This is somewhat surprising given that the solvation numbers for the intermediate and concentrated



**Figure 7.8.** Ionic conductivity of the (a)  $(\text{AN})_n\text{-LiFSI}$  mixtures with varying temperature (AN/LiX ratio (n) noted in plot) and (b)  $(\text{AN})_n\text{-LiX}$  mixtures with varying concentration at  $60\text{ }^{\circ}\text{C}$ . Data for salts other than  $\text{LiFSI}$  are reported for comparison.<sup>49,50</sup>

$\text{LiFSI}$  mixtures ( $n \leq 8$ ) are lower than those for the  $\text{LiPF}_6$  mixtures and almost the same as those for the  $\text{LiTFSI}$  and  $\text{LiClO}_4$  mixtures. Similar to the  $(\text{AN})_n\text{-LiTFSI}$  mixtures, bidentate coordination of the  $\text{FSI}^-$  anion to a given  $\text{Li}^+$  cation, in part, may explain the lower than

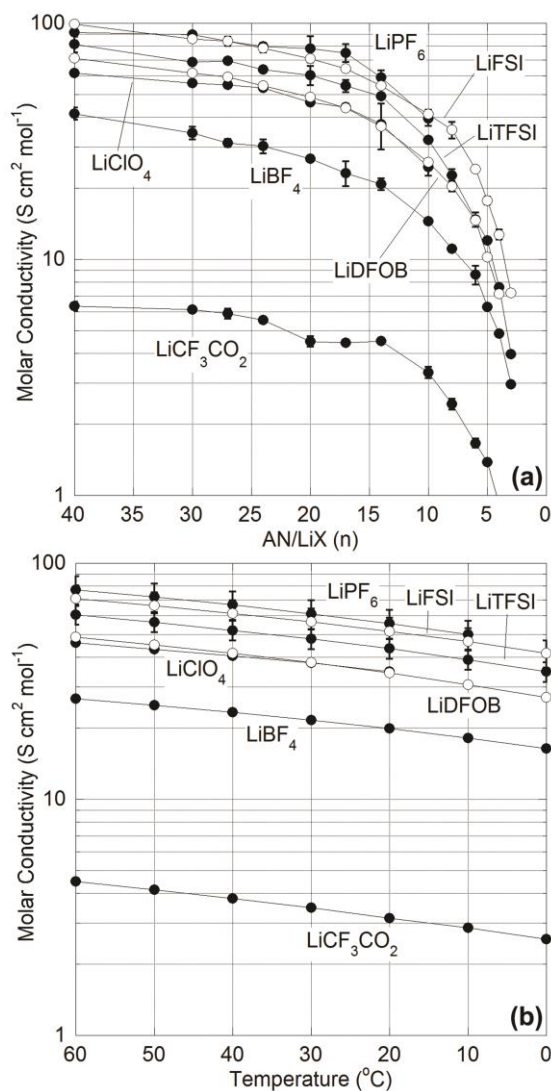


**Figure 7.9.** Molar conductivity of the (a) (AN)<sub>n</sub>-LiX mixtures (60 °C) for varying AN/LiX (n) concentrations and (b) (AN)<sub>n</sub>-LiX mixtures with varying temperature. Data for salts other than LiFSI reported for comparison.<sup>49,50</sup>

expected average solvent coordination numbers noted experimentally for LiFSI despite the additional experimental evidence (i.e., phase diagram and Raman spectroscopy of the FSI<sup>-</sup> anion coordination) which suggest that LiFSI is dissociated to a comparable extent to LiPF<sub>6</sub>

in AN. As mentioned above for the other salts mixtures studied, solvation numbers only provide indirect information about the solvate species and their relation to conduction mechanisms. It is also noteworthy that the information obtained from the spectroscopic characterization only indicates the overall equilibrium distribution of the ion solvation and ionic association interactions without considering the dynamic aspects of the solvate formation.<sup>49</sup>

## 7.7. Conclusions

The phase behavior and solution structure (average solvation numbers and ionic association interactions) of the (AN)<sub>n</sub>-LiFSI electrolyte mixtures have been scrutinized in detail. The LiFSI salt is found to be dissociated to a similar extent as LiPF<sub>6</sub>, although the average solvation numbers (*N*) for AN with LiFSI mixtures are somewhat lower than those found for AN mixtures with LiPF<sub>6</sub>, which may perhaps be due to some amount of bidentate coordination of the Li<sup>+</sup> cations by the FSI<sup>-</sup> anions. Lithium salts with both FSI<sup>-</sup> and TFSI<sup>-</sup> anions show similar phase behavior with AN in that they form SSIP solvates in diluted mixtures and AGG solvates in concentrated mixtures. Based upon the results from the spectroscopic analysis and the transport properties characterization, however, the LiFSI salt is more dissociated than LiTFSI when dissolved in AN. As demonstrated above, the differences found in the solution structure of these mixtures obtained from the MD simulations can be directly correlated to the variations in the conductivity. Note that utilizing both an experimental evaluation and a computational simulation analysis, the rapid

examination of the properties of a given salt is possible.

## 7.8. References

1. C. Michot, M. Armand, J.-Y. Sanchez, Y. Choquette, and M. Gauthier, Int. Patent WO 95/26056, 1995.
2. J. L. Allen, D. W. McOwen, S. A. Delp, E. T. Fox, J. S. Dickmann, S.-D. Han, Z.-B. Zhou, T. R. Jow, and W. A. Henderson, *J. Power Sources*, **237**, 104 (2013).
3. Y. Liu, S. Zhou, H. Han, H. Li, J. Nie, Z. Zhou, L. Chen, and X. Huang, *Electrochim. Acta*, **105**, 524 (2013).
4. G. G. Eshetu, S. Grugeon, G. Gachot, D. Mathiron, M. Armand, and S. Laruelle, *Electrochim. Acta*, **102**, 133 (2013).
5. K. Zaghbi, M. Dontigny, A. Guerfi, J. Trottier, J. Hamel-Paquet, V. Gariépy, K. Galoutov, P. Hovington, A. Mauger, H. Groult, and C. M. Julien, *J. Power. Sources*, **216**, 192 (2012).
6. J. Reiter, M. Nálhern á and R. Dominko, *J. Power. Sources*, **205**, 402 (2012).
7. H.-B. Han, S.-S. Zhou, D.-J. Zhang, S.-W. Feng, L.-F. Li, K. Liu, W.-F. Feng, J. Nie, H. Li, X.-J. Huang, M. Armand, and Z.-B. Zhou, *J. Power. Sources*, **196**, 3623 (2011).
8. L. Li, S. Zhou, H. Han, H. Li, J. Nie, M. Armand, Z. Zhou, and X. Huang, *J. Electrochem. Soc.*, **158**, A74 (2011).
9. J. Huang and A. F. Hollenkamp, *J. Phys. Chem. C*, **114**, 21840 (2010).
10. A. Abouimrane, J. Ding, and I. J. Davidson, *J. Power Sources*, **189**, 693 (2009).
11. E. Paillard, Q. Zhou, W. A. Henderson, G. B. Appetecchi, M. Montanino, and S. Passerini, *J. Electrochem. Soc.*, **156**, A891 (2009).

12. G. D. Smith, O. Borodin, S. P. Russo, R. J. Rees, and A. F. Hollenkamp, *Phys. Chem. Chem. Phys.*, **11**, 9884 (2009).
13. A. Guerfi, M. Dontigny, Y. Kobayashi, A. Vijh, and K. Zaghbi, *J. Solid State Electrochem.*, **13**, 1003 (2009).
14. M. Yamagata, N. Nishigaki, S. Nishishita, Y. Matsui, T. Sugimoto, M. Kikuta, T. Higashizaki, M. Kono, and M. Ishikawa, *Electrochim. Acta*, in-press (2013).
15. J. Reiter, E. Paillard, L. Grande, M. Winter, and S. Passerini, *Electrochim. Acta*, **91**, 101 (2013).
16. A. Basile, A. F. Hollenkamp, A. I. Bhatt, and A. P. O'Mullane, *Electrochem. Commun.*, **27**, 69 (2013).
17. H. Wang, N. Imanishi, A. Hirano, Y. Takeda, and O. Yamamoto, *J. Power. Sources*, **219**, 22 (2012).
18. G.-T. Kim, S. S. Jeong, M.-Z. Xue, A. Balducci, M. Winter, S. Passerini, F. Alessandrini, and G. B. Appetecchi, *J. Power. Sources*, **199**, 239 (2012).
19. M. Nádherná, J. Reiter, J. Moškon, and R. Dominko, *J. Power. Sources*, **196**, 7700 (2011).
20. H.-B. Han, Y.-X. Zhou, K. Liu, J. Nie, X.-J. Huang, M. Armand, and Z.-B. Zhou, *Chem. Lett.*, **39**, 472 (2010).
21. M. Berana, J. Příhoda, and J. Taraba, *Polyhedron*, **29**, 991 (2010).
22. A. I. Bhatt, A. S. Best, J. Huang, and A. F. Hollenkamp, *J. Electrochem. Soc.*, **157**, A66 (2010).

23. A. S. Best, A. I. Bhatt, and A. F. Hollenkamp, *J. Electrochem. Soc.*, **157**, A903 (2010).
24. G. H. Lane, P. M. Bayley, B. R. Clare, A. S. Best, D. R. MacFarlane, M. Forsyth, and A. F. Hollenkamp, *J. Phys. Chem. C*, **114**, 21775 (2010).
25. Q. Zhou, W. A. Henderson, G. B. Appetecchi, and S. Passerini, *J. Phys. Chem. C*, **114**, 6201 (2010).
26. A. Lewandowski and I. Acznik, *Electrochim. Acta*, **56**, 211 (2010).
27. H.-B. Han, K. Liu, S.-W. Feng, S.-S. Zhou, W.-F. Feng, J. Nie, H. Li, X.-J. Huang, H. Matsumoto, M. Armand, and Z.-B. Zhou, *Electrochim. Acta*, **55**, 7134 (2010).
28. H.-B. Han, J. Nie, K. Liu, W.-K. Li, W.-F. Feng, M. Armand, H. Matsumoto, and Z.-B. Zhou, *Electrochim. Acta*, **55**, 1221 (2010).
29. S. F. Lux, M. Schmuck, G. B. Appetecchi, S. Passerini, M. Winter, and A. Balducci, *J. Power Sources*, **192**, 606 (2009).
30. G. B. Appetecchi, M. Montanino, A. Balducci, S. F. Lux, M. Winter, and S. Passerini, *J. Power Sources*, **192**, 599 (2009).
31. T. Sugimoto, Y. Atsumi, M. Kikuta, E. Ishiko, M. Kono, and M. Ishikawa, *J. Power Sources*, **189**, 802 (2009).
32. L. J. Hardwick, J. A. Saint, I. T. Lucas, M. M. Doeff, and R. Kostecki, *J. Electrochem. Soc.*, **156**, A120 (2009).
33. J. Saint, A. S. Best, A. F. Hollenkamp, J. Kerr, J.-H. Shin, and M. M. Doeff, *J. Electrochem. Soc.*, **155**, A172 (2008).

34. J. N. C. Lopes, K. Shimizu, A. A. H. Pádua, Y. Umebayashi, S. Fukuda, K. Fujii, and S. Ishiguro, *J. Phys. Chem. B*, **112**, 9449 (2008).
35. S. Seki, Y. Kobayashi, H. Miyashiro, Y. Ohno, Y. Mita, and N. Terada, *J. Phys. Chem. C*, **112**, 16708 (2008).
36. Q. Zhou, W. A. Henderson, G. B. Appetecchi, M. Montanino, and S. Passerini, *J. Phys. Chem. B*, **112**, 13577 (2008).
37. K. Kubota, T. Nohira, T. Goto, and R. Hagiwara, *Electrochem. Commun.*, **10**, 1886 (2008).
38. T. Sugimoto, M. Kikuta, E. Ishiko, M. Kono, and M. Ishikawa, *J. Power Sources*, **183**, 436 (2008).
39. A. Guerfi, S. Duchesne, Y. Kobayashi, A. Vijh, and K. Zaghieb, *J. Power Sources*, **175**, 866 (2008).
40. K. Fujii, S. Seki, S. Fukuda, R. Kanzaki, T. Takamuku, Y. Umebayashi, and S. Ishiguro, *J. Phys. Chem. B*, **111**, 12829 (2007).
41. Y. Wang, K. Zaghieb, A. Guerfi, F. F. C. Bazito, R. M. Torresi, and J. R. Dahn, *Electrochim. Acta*, **52**, 6346 (2007).
42. M. Beran, J. Příhoda, Z. Žák, and M. Černík, *Polyhedron*, **25**, 1292 (2006).
43. M. Ishikawa, T. Sugimoto, M. Kikuta, E. Ishiko, and M. Kono, *J. Power Sources*, **162**, 658 (2006).
44. H. Matsumoto, H. Sakaebe, K. Tatsumi, M. Kikuta, E. Ishiko, and M. Kono, *J. Power Sources*, **160**, 1308 (2006).

45. K. Zaghbi, P. Charest, A. Guerfi, J. Shim, M. Perrier, and K. Striebel, *J. Power Sources*, **146**, 380 (2005).
46. K. Zaghbi, P. Charest, A. Guerfi, J. Shim, M. Perrier, and K. Striebel, *J. Power Sources*, **134**, 124 (2004).
47. D. M. Seo, O. Borodin, S.-D. Han, Q. Ly, P. D. Boyle, and W. A. Henderson, *J. Electrochem. Soc.*, **159**, A553 (2012).
48. D. M. Seo, O. Borodin, S.-D. Han, P. D. Boyle, and W. A. Henderson, *J. Electrochem. Soc.*, **159**, A1489 (2012).
49. D. M. Seo, O. Borodin, D. Balogh, M. O'Connell, Q. Ly, S.-D. Han, S. Passerini, and W. A. Henderson, *J. Electrochem. Soc.*, **160**, A1061 (2013).
50. S.-D. Han, O. Borodin, J. L. Allen, D. M. Seo, D. W. McOwen, and W. A. Henderson, *J. Electrochem. Soc.*, in-press (2013).
51. W. Kunz, J. Barthel, L. Klein, T. Cartailier, P. Turq, and B. Reindl, *J. Soln. Chem.*, **20**, 875 (1991).
52. E. M. Cabaleiro-Lago and M. A. R ós, *Chem. Phys.*, **254**, 11 (2000).
53. X. Xuan, H. Zhang, J. Wang, and H. Wang, *J. Phys. Chem. A*, **108**, 7513 (2004).
54. D. Spångberg and K. Hermansson, *Chem. Phys.*, **300**, 165 (2004).
55. E. Pasgreta, R. Puchta, A. Zahl, and R. van Eldik, *Eur. J. Inorg. Chem.*, **1815** (2007).
56. D. M. Seo, P. D. Boyle, O. Borodin, and W. A. Henderson, *RSC Adv.*, **2**, 8014 (2012).
57. Y. Yokota, V. G. Young Jr., and J. G. Verkade, *Acta Crystallogr. C*, **55**, 196 (1999).
58. C. L. Raston, C. R. Whitaker, and A. H. White, *Aust. J. Chem.*, **42**, 201 (1989).

59. W. A. Henderson, *J. Phys. Chem. C*, **110**, 13177 (2006).
60. P. Neelakantan, *P. Indian Acad. Sci. A*, **60**, 422 (1964).
61. G. Fini and P. Mirone, *Spectrochim. Acta A*, **32**, 439 (1976).
62. D. Brouillette, D. E. Irish, N. J. Taylor, G. Perron, M. Odziemkowski, and J. E. Desnoyers, *Phys. Chem. Chem. Phys.*, **4**, 6063 (2002).
63. J. Barthel, R. Buchner, and E. Wismeth, *J. Soln. Chem.*, **29**, 937 (2004).
64. J. M. Alia, H. G. M. Edwards, and J. Moore, *Spectrochim. Acta A*, **51**, 2039 (1995).
65. O. Borodin, W. Gorecki, G. D. Smith, and M. Armand, *J. Phys. Chem. B*, **114**, 6786 (2010).

## Conclusion

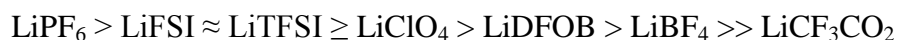
---

The goals of this research were to demonstrate new and/or improved methods for electrolyte characterization and to discover how ion and solvent structure influence the solution behavior and properties of nitrile-LiDFOB/LiFSI electrolyte mixtures. Utilizing a combination of methods including thermal phase behavior analysis with solvate structure determination, Raman vibrational spectroscopic characterization and MD simulations, detailed insight into the solvation and ionic association behavior was obtained and explanations were readily available for the solution behavior and variability in the transport properties (viscosity and ionic conductivity) of AN solutions with LiDFOB and LiFSI relative to other conventional lithium salts. MD simulations for the (AN)<sub>n</sub>-LiX mixtures provided additional insight into the solution structure and explored the limitations of both the experimental work and simulations for electrolyte characterization.

As a preliminary study, numerous crystal structures of known and newly determined LiCF<sub>3</sub>SO<sub>3</sub>, LiDFOB and LiPF<sub>6</sub> crystalline solvates were reported to provide significant insight into the manner in which the CF<sub>3</sub>SO<sub>3</sub><sup>-</sup>, DFOB<sup>-</sup> and PF<sub>6</sub><sup>-</sup> anions coordinate Li<sup>+</sup> cations. Utilizing Raman spectroscopic analyses, these solvates have been extensively

characterized to provide unambiguous assignments for the anion Raman bands associated with specific  $\text{CF}_3\text{SO}_3^-$ ,  $\text{DFOB}^-$  and  $\text{PF}_6^-$  anion... $\text{Li}^+$  cation coordination modes. This information serves as one of the important tools necessary for evaluating the ionic association interactions within electrolytes containing aprotic solvents and the  $\text{LiCF}_3\text{SO}_3$ ,  $\text{LiDFOB}$  and  $\text{LiPF}_6$  salts. In particular, the vibrational spectroscopic characterization results for various solvents with  $\text{LiCF}_3\text{SO}_3$  demonstrated that most of polarity parameters (i.e., dielectric constant, DN, AN and  $E_T(30)$ ) are, in fact, poor indicators of the effectiveness of a given solvent for  $\text{Li}^+$  cation solvation.

Phase diagrams for AN with new and conventional lithium salt mixtures were determined. Raman spectroscopic analyses were performed to examine both the solvent and anion interactions with  $\text{Li}^+$  cations. Based upon the spectroscopic analysis for the solvent (AN) vibrational bands, the average solvation number ( $N$ ) and the degree of ionic association in the liquid mixtures were determined. The mixtures with more weakly associating anions have a higher solvation number and lower degree of ionic association with the order of decreasing association being:

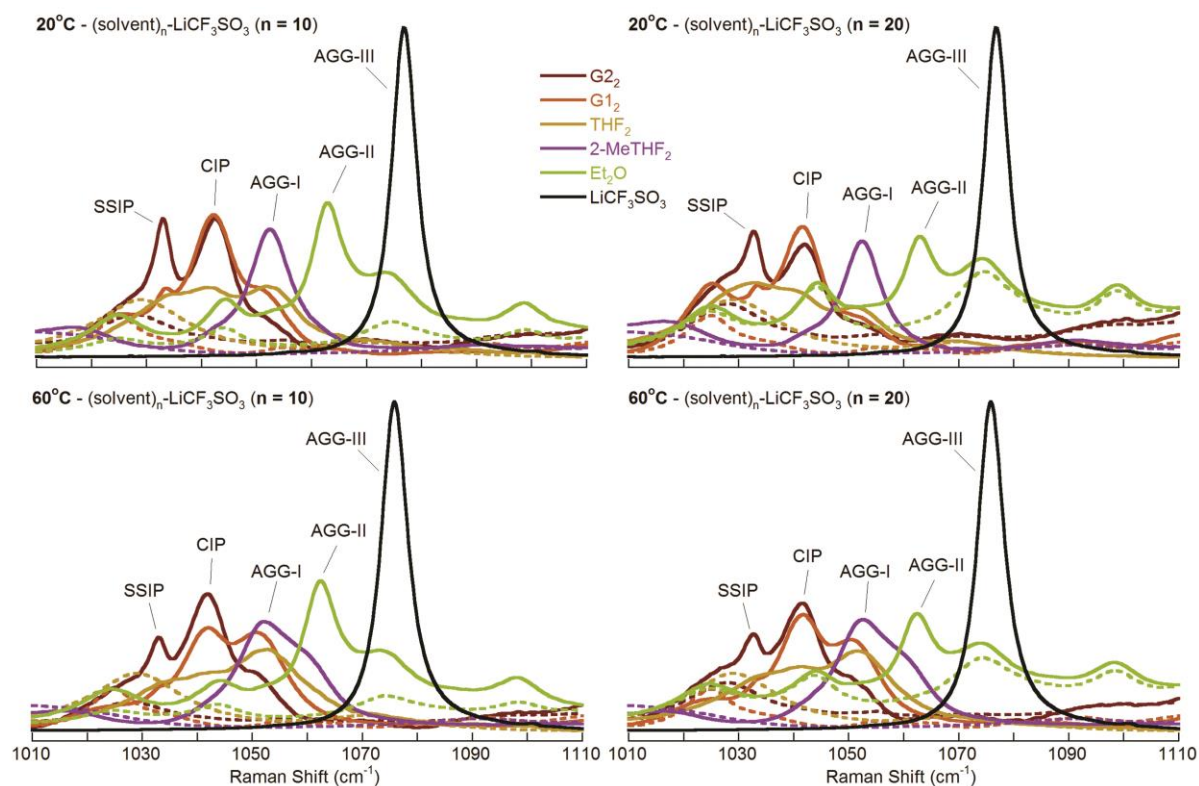


The combination of phase diagrams with crystalline solvate structures, Raman spectroscopic analysis and MD simulations greatly aids in identifying a diverse range of different types of solvates (i.e., SSIPs, CIPs and AGGs) in solution. The simulation results support the experimental data which indicates that  $\text{LiClO}_4$  is significantly more dissociated than  $\text{LiBF}_4$  in AN, despite the similarity in the anion sizes and shapes.  $\text{LiPF}_6$  and  $\text{LiTFSI}$  are found to be

highly dissociated and dissociated, respectively, in dilute mixtures. LiDFOB is dissociated to a similar extent as LiClO<sub>4</sub>, and more dissociated than LiBF<sub>4</sub> when dissolved in AN. The LiFSI salt is dissociated to a similar extent as LiPF<sub>6</sub>, while it is more dissociated than LiTFSI in AN in spite of the similar phase behavior with AN.

The solution structure of the (AN)<sub>n</sub>-LiX mixtures can be directly linked to the transport properties of the mixtures. The viscosity variations for the mixtures with different lithium salts are explained using both the ionic association behavior and the corresponding amount of uncoordinated solvent present, while the ion conductivity variations and mechanisms for (AN)<sub>n</sub>-LiX mixtures are determined not just by the identity of the solvates and their distribution, but also by the dynamics for the solvent molecules and anions in the Li<sup>+</sup> cation coordination shells, as noted by the MD simulations. In contrast to general expectations, the mixtures with the highest conductivity are found to also have the highest viscosity, which indicates that these properties are indirectly linked through the solution structure rather than directly correlated with one another (as is often assumed). Thus, the solution structure information obtained from the combination of phase behavior, solvates structures, ion solvation/ionic association analyses and MD simulations is highly effective for understanding and predicting the transport properties of the electrolytes. This study demonstrated how this electrolyte characterization methodology—employing several modes of experimental evaluation in concert with MD simulations—enables the rapid scrutiny of the behavior and properties of a given salt for electrolyte applications.

## APPENDICES

Reassessing Polarization Parameters and Li<sup>+</sup> Cation Solvation

**Figure A1.** Raman spectra of the SO<sub>3</sub><sup>-</sup> stretching mode ( $\nu_s$ SO<sub>3</sub>) for (solvent)<sub>n</sub>-LiCF<sub>3</sub>SO<sub>3</sub> mixtures with ether solvents. The spectra for the pure salt (black) and pure solvents (dashed) are shown for comparison.

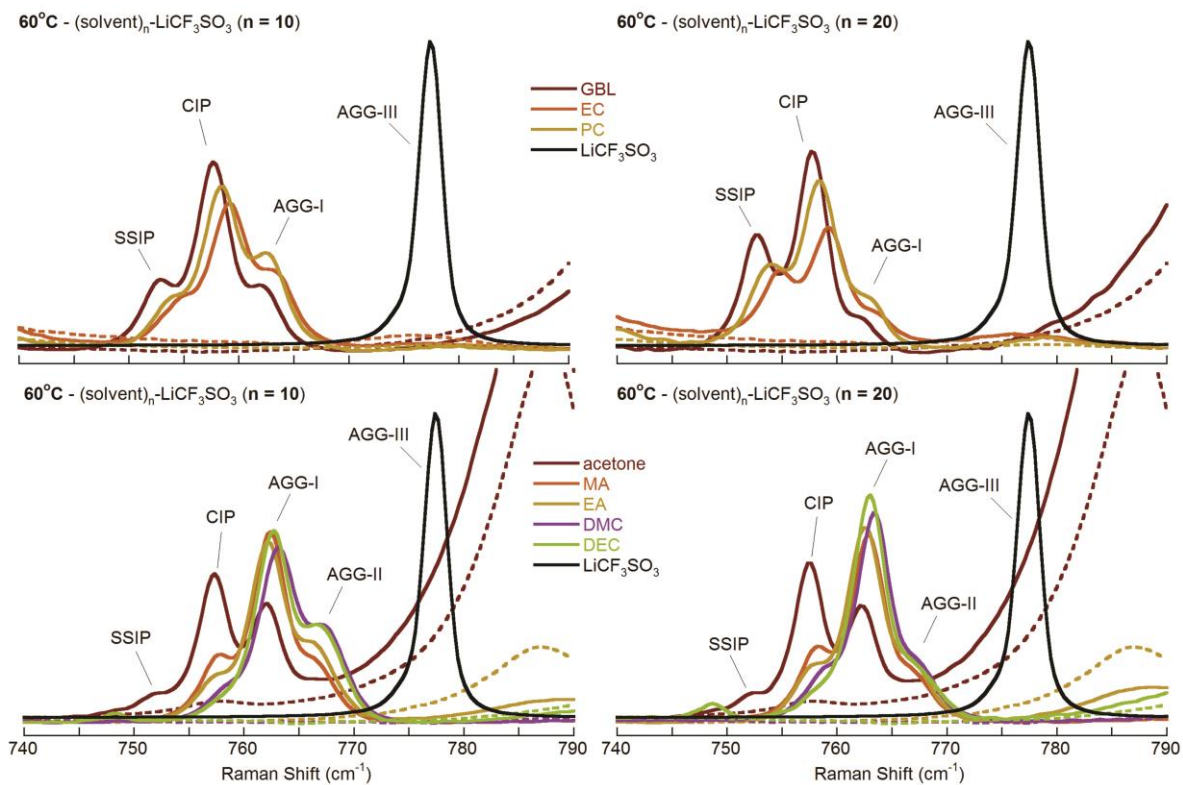


**Figure A2.** Raman spectra (at 60 °C) of the  $\text{CF}_3$  symmetric bending mode ( $\delta_s\text{CF}_3$ ) for  $(\text{solvent})_n\text{-LiCF}_3\text{SO}_3$  mixtures with cyclic and acyclic carbonate/ester solvents. The spectra for the pure salt (black) and pure solvents (dashed) are shown for comparison.

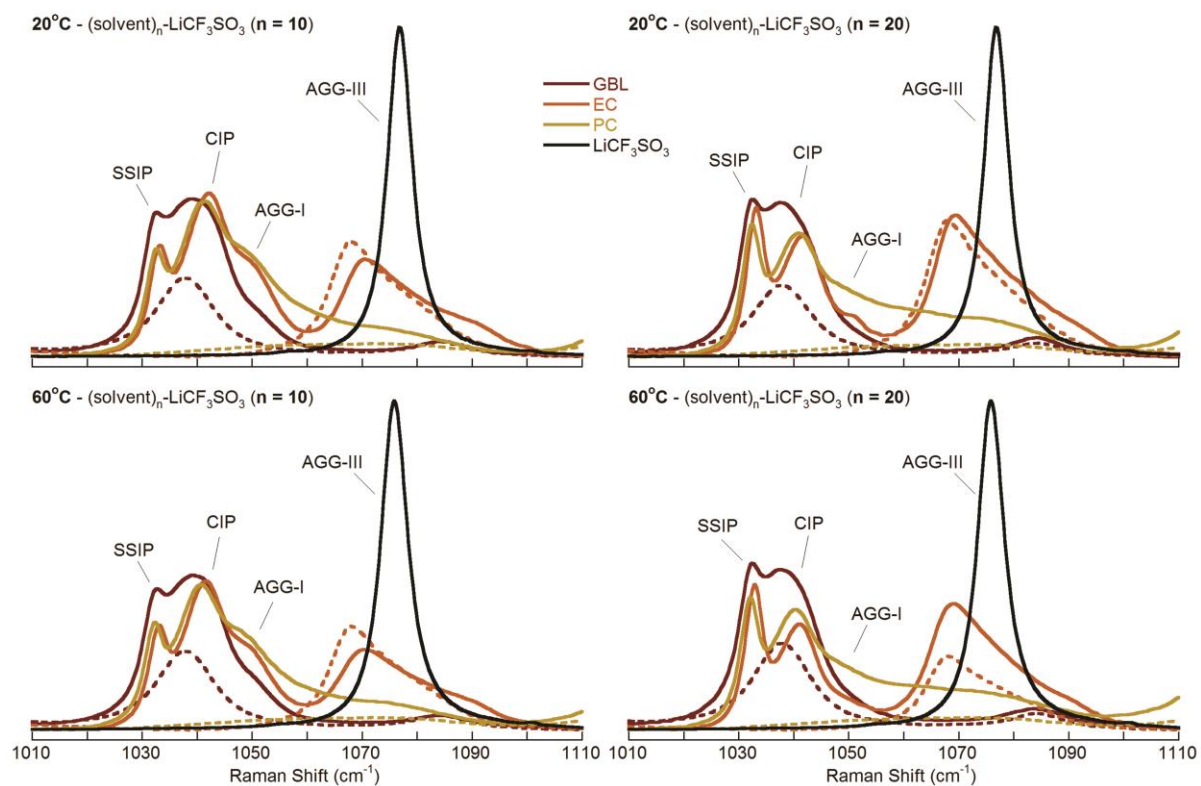


**Figure A3.** Raman spectra of the SO<sub>3</sub><sup>-</sup> stretching mode (ν<sub>3</sub>SO<sub>3</sub>) for (solvent)<sub>n</sub>-LiCF<sub>3</sub>SO<sub>3</sub> mixtures with cyclic solvents. The spectra for the pure salt (black) and pure solvents (dashed) are shown for comparison.

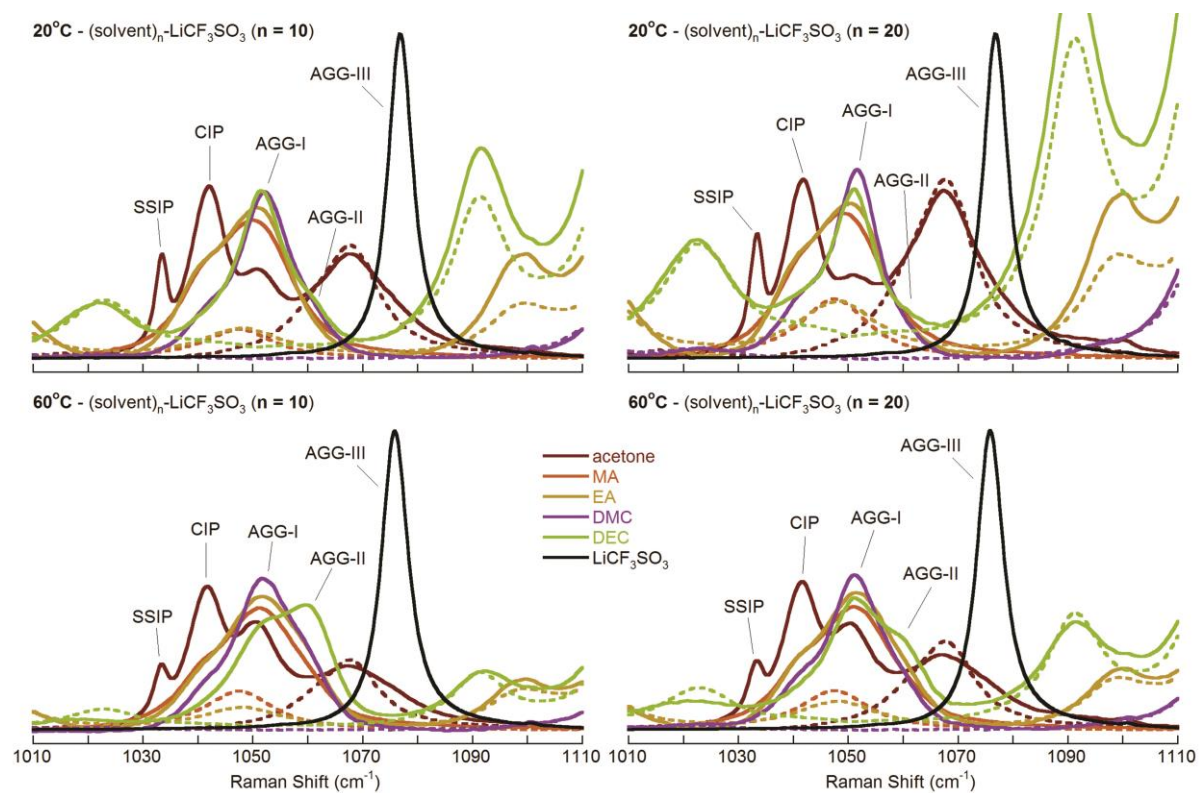


**Figure A4.** Raman spectra of the  $\text{SO}_3^-$  stretching mode ( $\nu_s\text{SO}_3$ ) for  $(\text{solvent})_n\text{-LiCF}_3\text{SO}_3$  mixtures with acyclic carbonate/ester solvents. The spectra for the pure salt (black) and pure solvents (dashed) are shown for comparison.

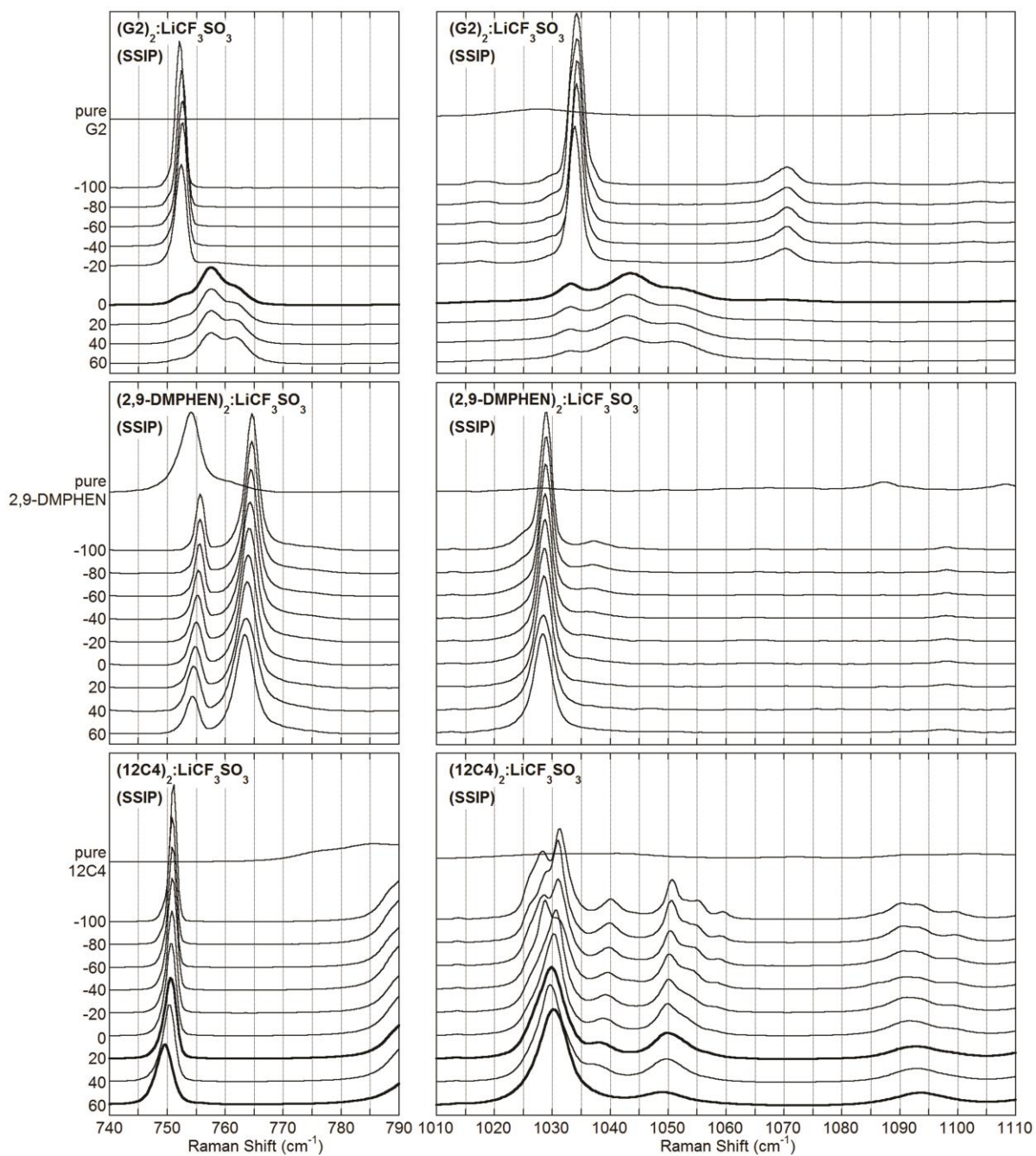


**Figure A5.** Raman spectra of the  $\text{CF}_3\text{SO}_3^-$  anion  $\nu_1$  vibrational band for the SSIP crystalline solvates: (a)  $(2,9\text{-DMPHEN})_2:\text{LiCF}_3\text{SO}_3$  and (b)  $(12\text{C4})_2:\text{LiCF}_3\text{SO}_3$  (the bold curves indicate that solid-solid phase transition has occurred at this temperature).

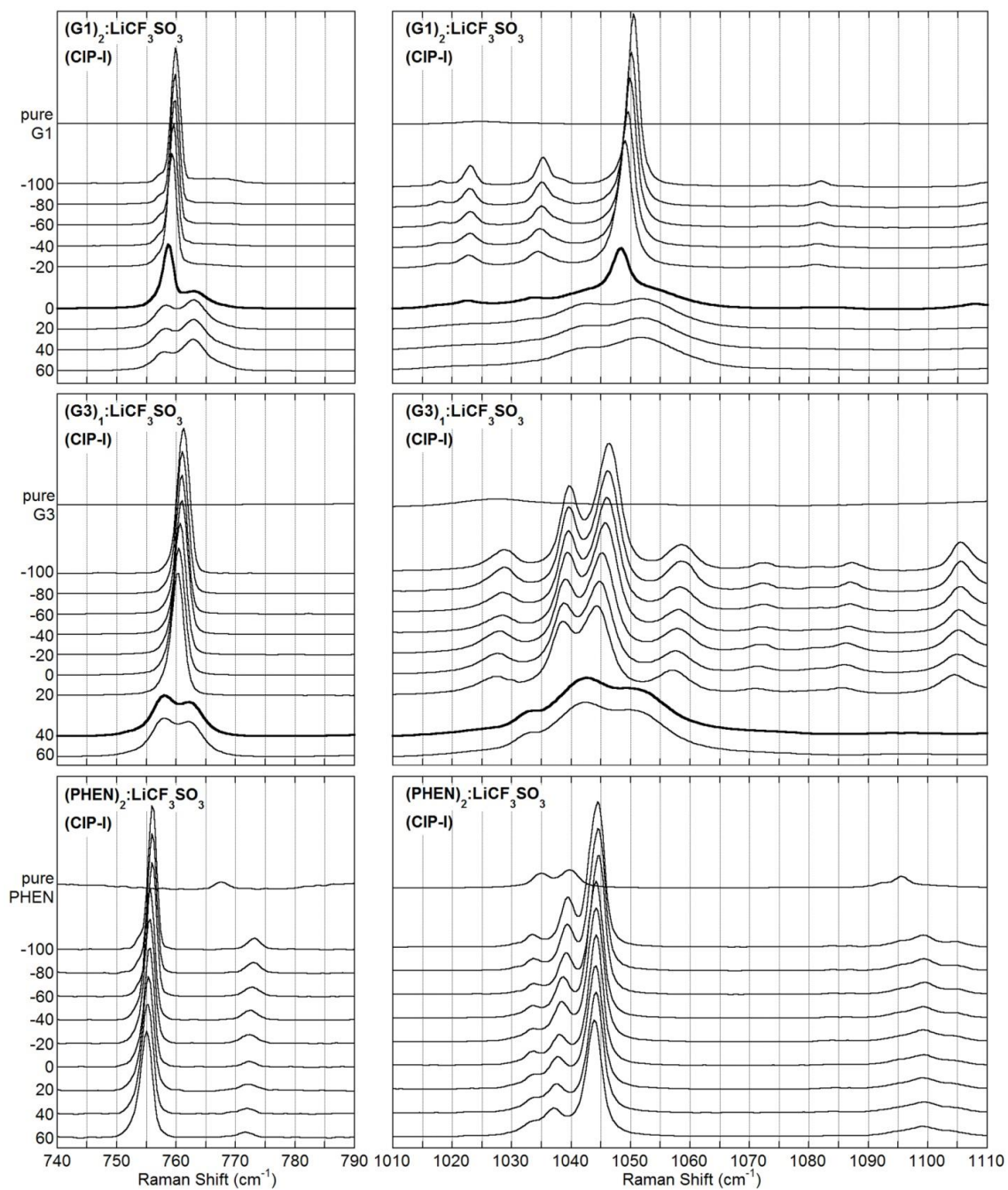


**Figure A6.** Raman spectra of the  $\text{CF}_3\text{SO}_3^-$  anion  $\nu_1$  vibrational band for the CIP-I crystalline solvates: (a)  $(\text{G3})_1:\text{LiCF}_3\text{SO}_3$  and (b)  $(\text{PHEN})_2:\text{LiCF}_3\text{SO}_3$  (the double spaced bold curve indicates that the solvate melted at the temperature).

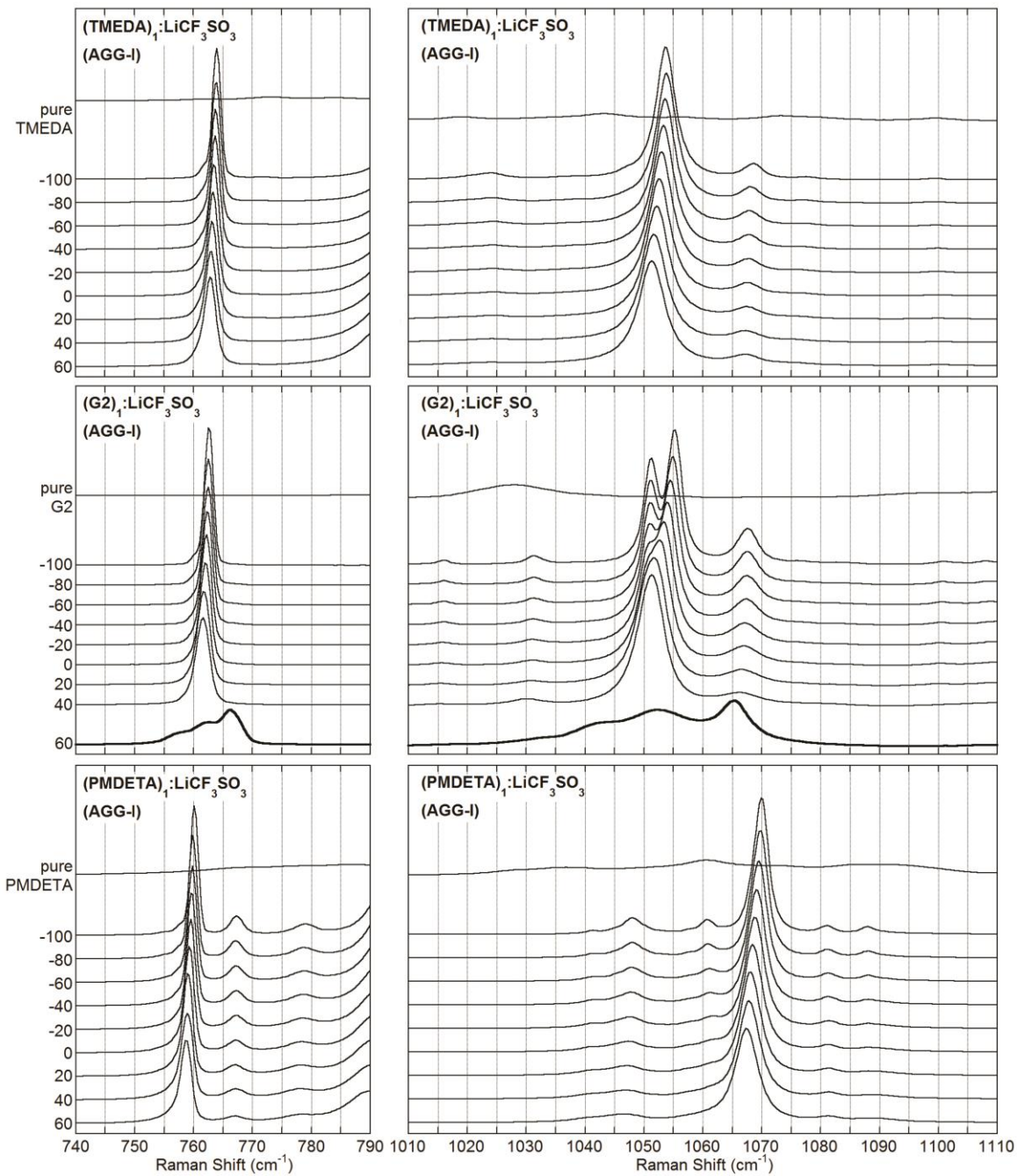


**Figure A7.** Raman spectra of the  $\text{CF}_3\text{SO}_3^-$  anion  $\nu_1$  vibrational band for the AGG-I crystalline solvates: (a)  $(\text{G2})_1:\text{LiCF}_3\text{SO}_3$  and (b)  $(\text{PMDETA})_1:\text{LiCF}_3\text{SO}_3$  (the double spaced bold curve indicates that the solvate melted at the temperature).

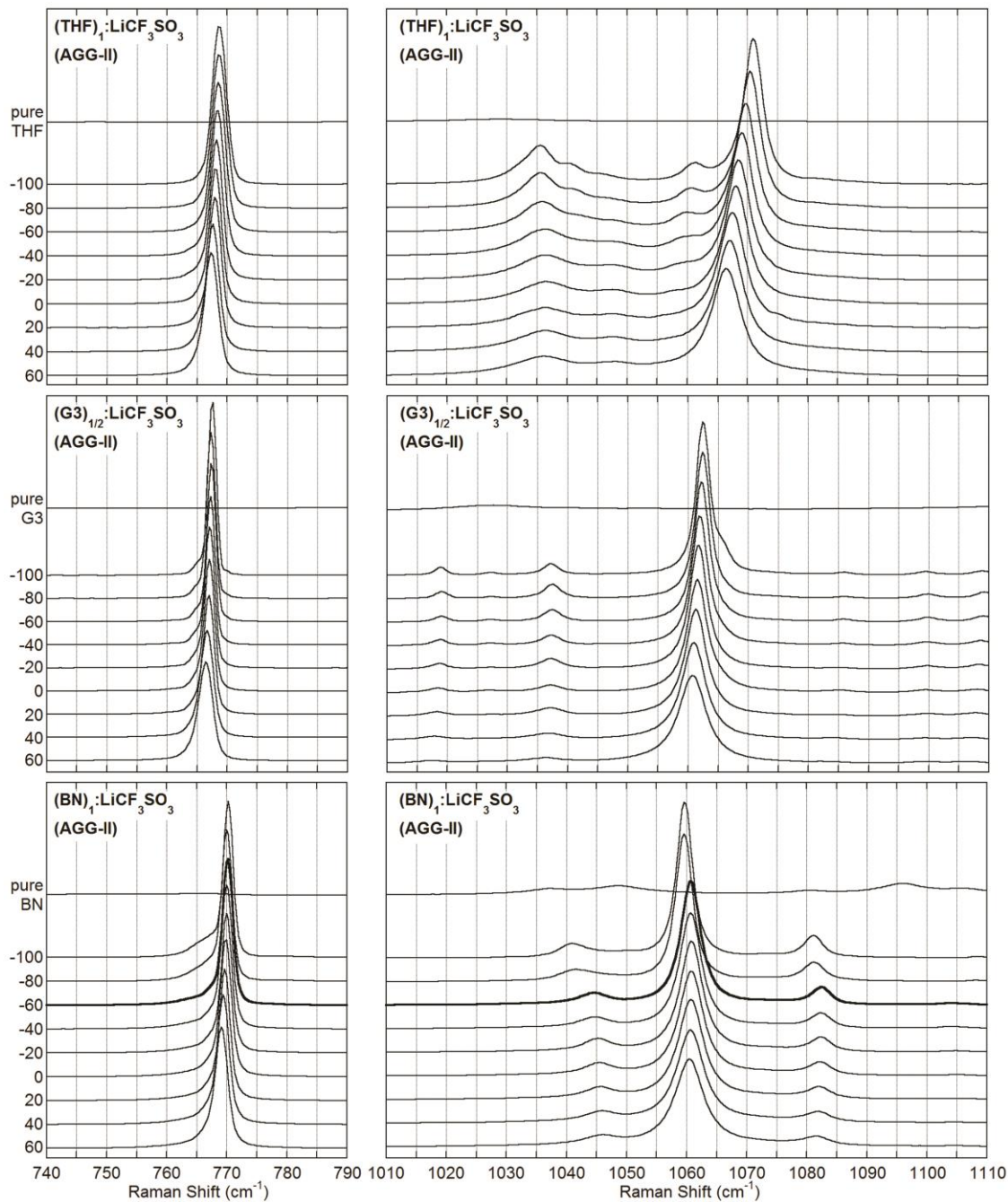


**Figure A8.** Raman spectra of the  $\text{CF}_3\text{SO}_3^-$  anion  $\nu_1$  vibrational band for the AGG-II crystalline solvates:  $(\text{G3})_{1/2}:\text{LiCF}_3\text{SO}_3$ ,  $(\text{AN})_1:\text{LiCF}_3\text{SO}_3$  and  $(\text{BN})_1:\text{LiCF}_3\text{SO}_3$  (the bold curves indicate that the solid-solid phase transition of the solvates has occurred at this temperature).

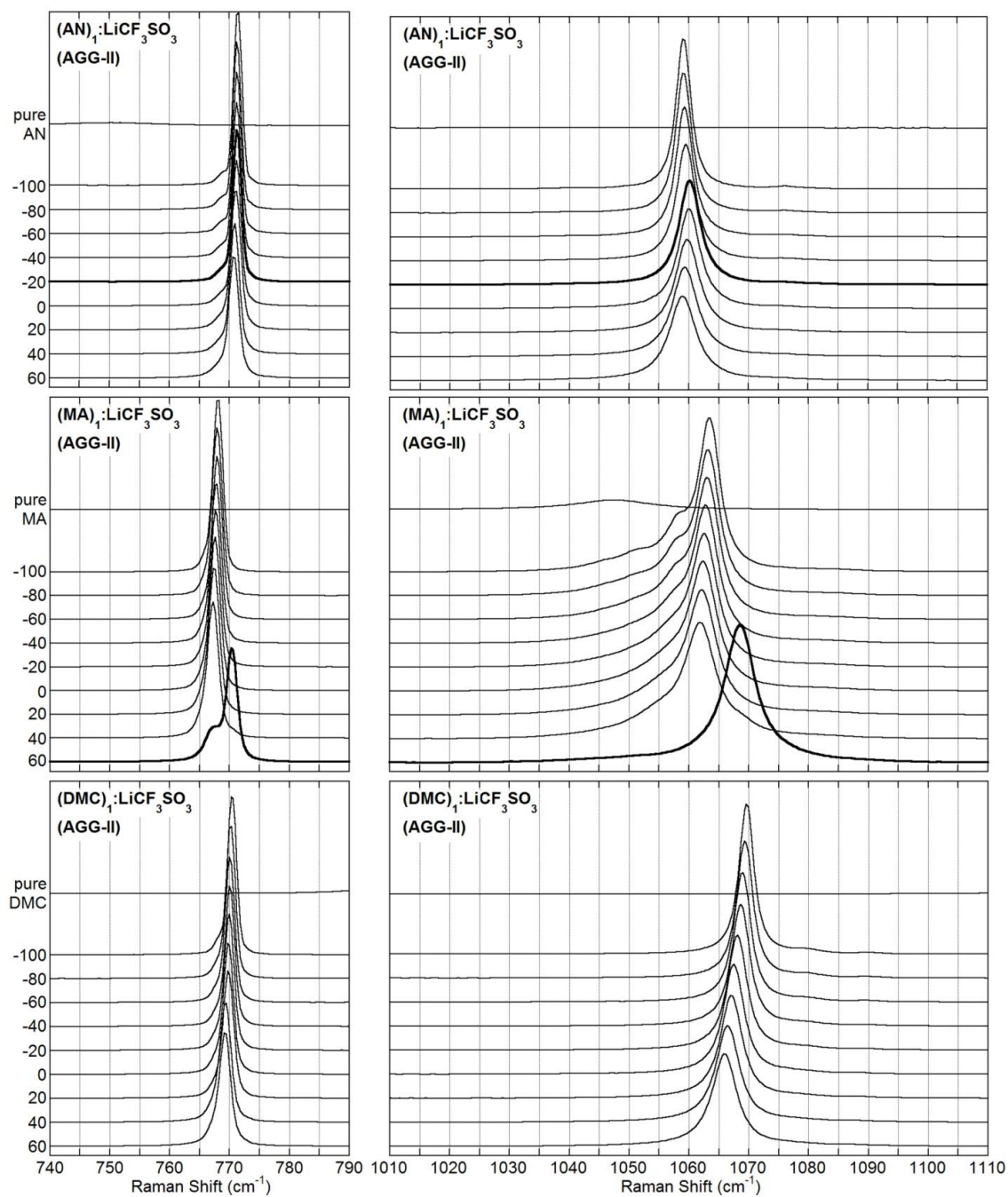


**Figure A9.** Raman spectra of the  $\text{CF}_3\text{SO}_3^-$  anion  $\nu_1$  vibrational band for the AGG-II crystalline solvates:  $(\text{MA})_1:\text{LiCF}_3\text{SO}_3$ ,  $(\text{DMC})_1:\text{LiCF}_3\text{SO}_3$  and  $(\text{DEC})_1:\text{LiCF}_3\text{SO}_3$  (the bold curve indicates that the solid-solid phase transition of the solvate has occurred at this temperature).

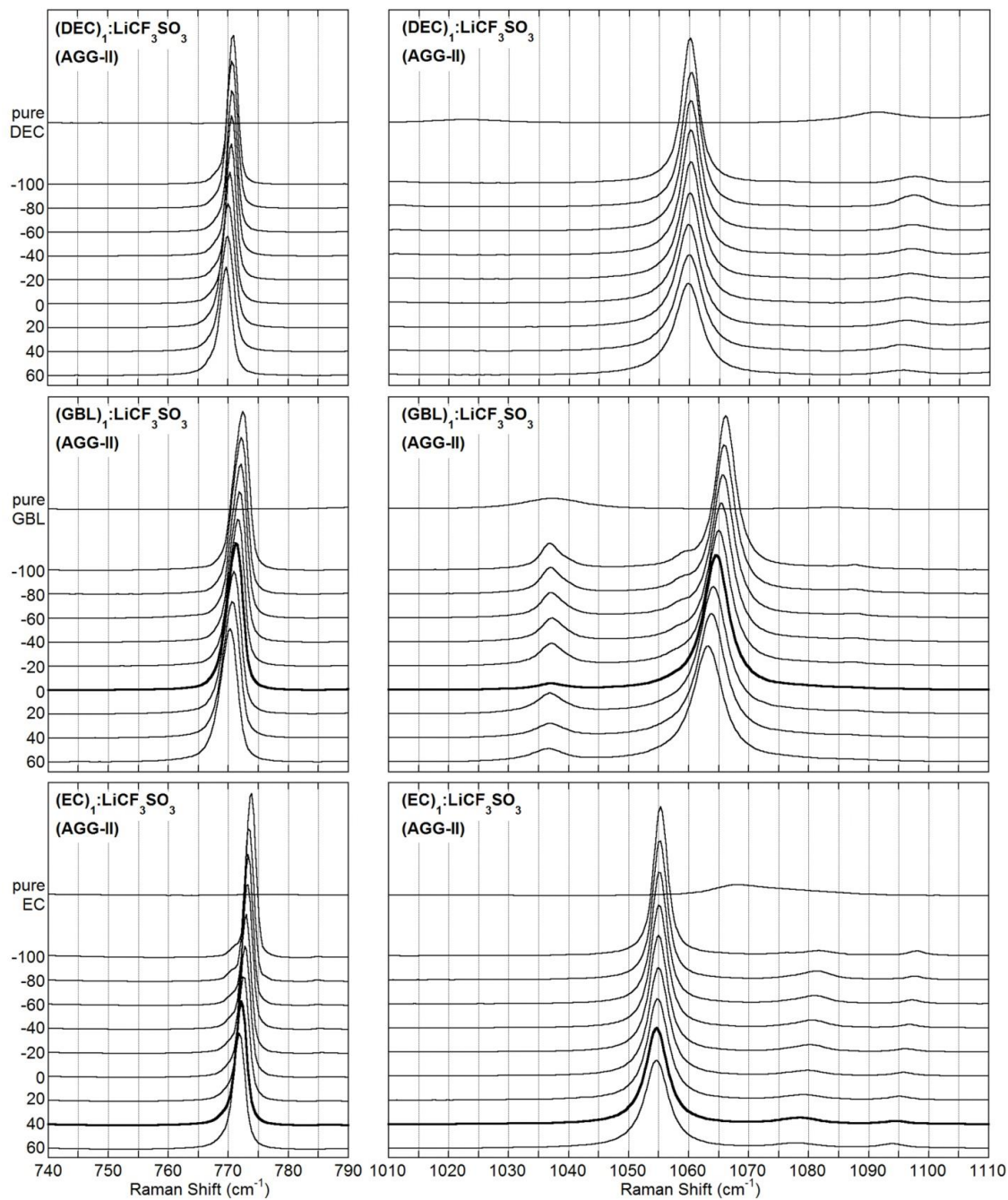


**Figure A10.** Raman spectra of the  $\text{CF}_3\text{SO}_3^-$  anion  $\nu_1$  vibrational band for the AGG-II crystalline solvates:  $(\text{GBL})_1:\text{LiCF}_3\text{SO}_3$  and  $(\text{EC})_1:\text{LiCF}_3\text{SO}_3$  (the bold curves indicate the solid-solid phase transition of the solvates has occurred at this temperature).

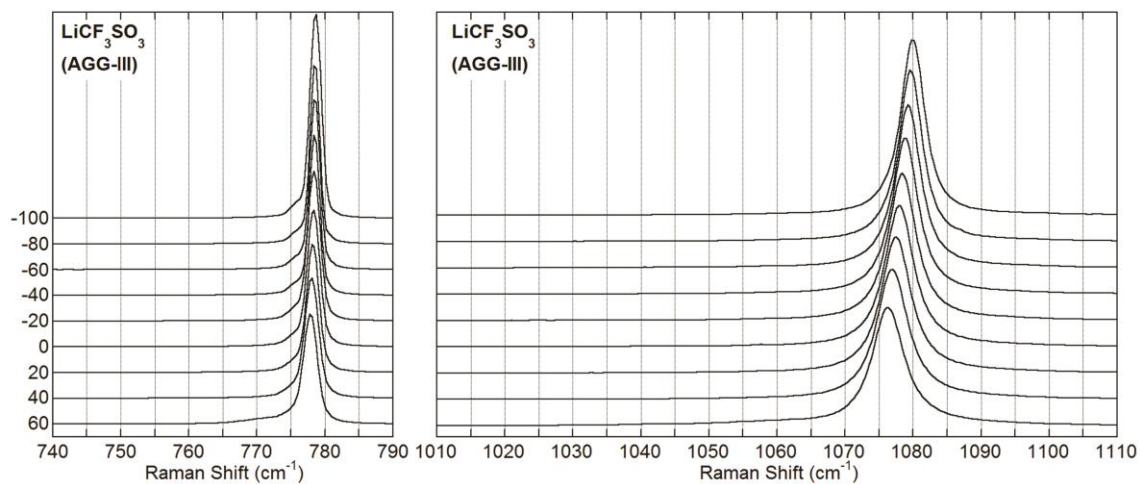


**Figure A11.** Raman spectra of the  $\text{CF}_3\text{SO}_3^-$  anion  $\nu_1$  vibrational band for the AGG-III crystalline solvates: pure  $\text{LiCF}_3\text{SO}_3$ .

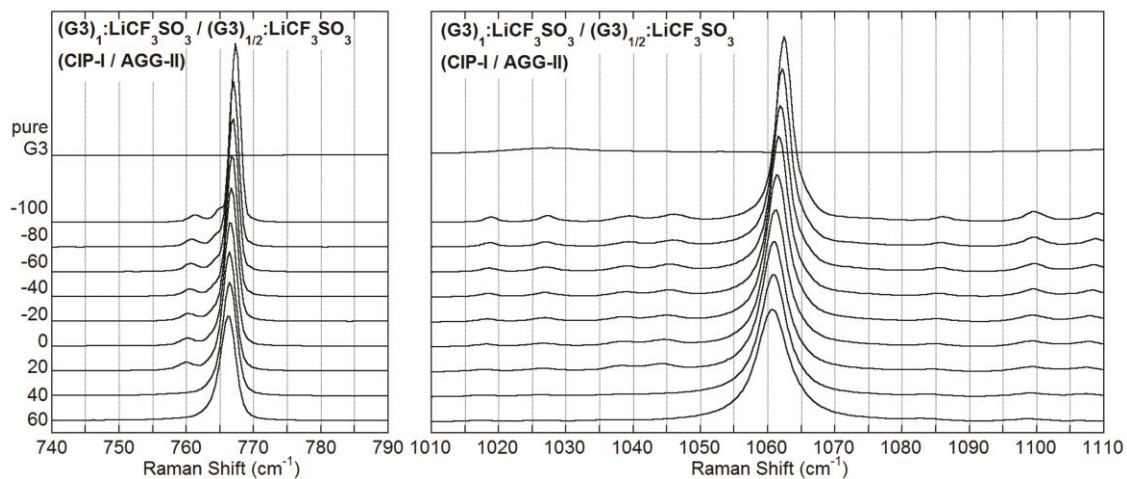


**Figure A12.** Raman spectra of the  $\text{CF}_3\text{SO}_3^-$  anion  $\nu_1$  vibrational band of the original solvate for mixture of CIP-I/AGG-II  $(\text{G3})_1:\text{LiCF}_3\text{SO}_3/(\text{G3})_{1/2}:\text{LiCF}_3\text{SO}_3$ .

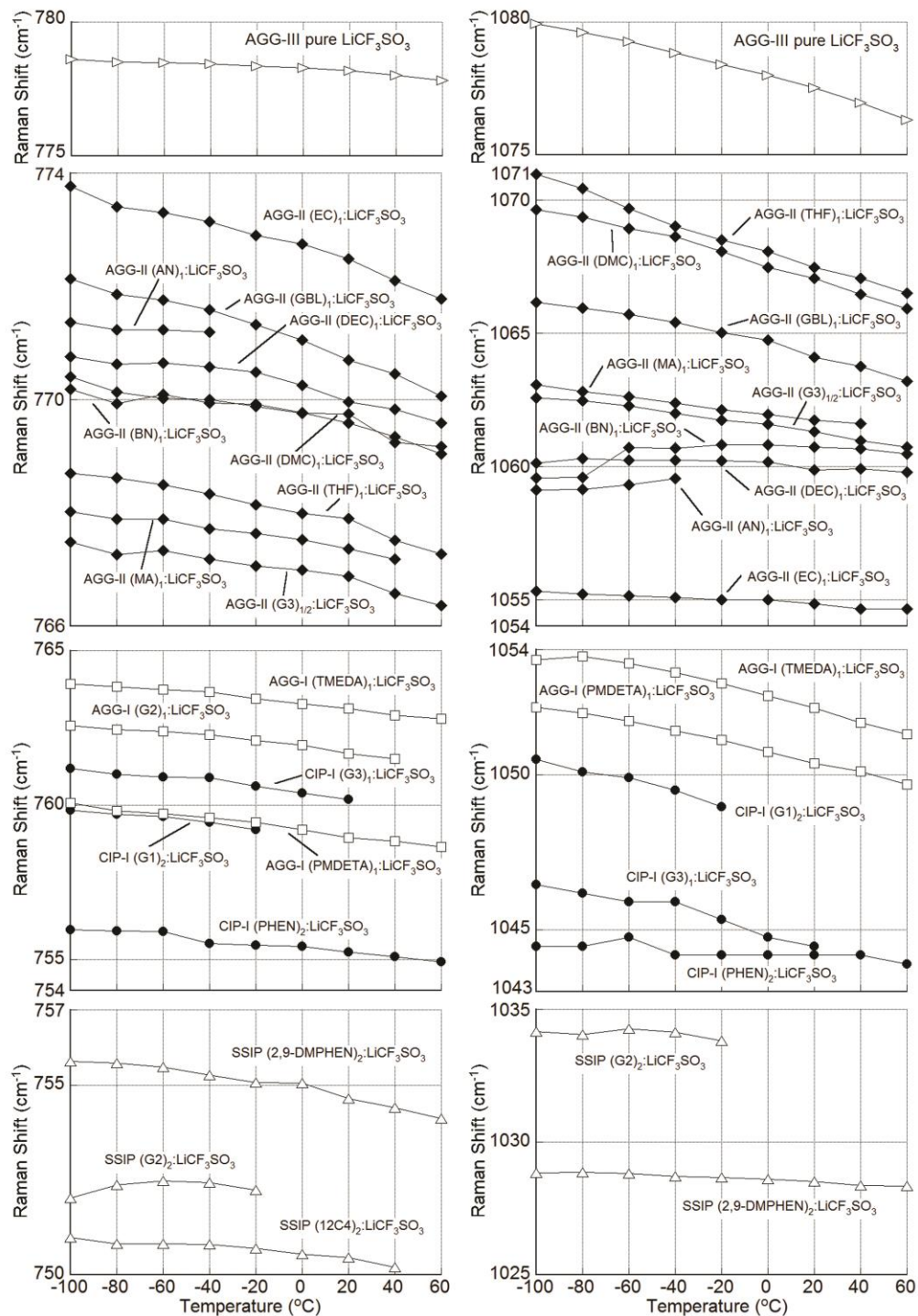


**Figure A13.** Raman band peak positions for the  $\text{CF}_3\text{SO}_3^-$  anion  $\nu_1$  vibrational band for the different crystalline solvates. The peak positions at  $1000\text{ cm}^{-1}$  region are unavailable for the  $\text{SSIP (12C4)}_2\text{:LiCF}_3\text{SO}_3$  and  $\text{AGG-I (G2)}_1\text{:LiCF}_3\text{SO}_3$  solvates.

## Crystalline Solvate Structures and Ionic Association Interactions

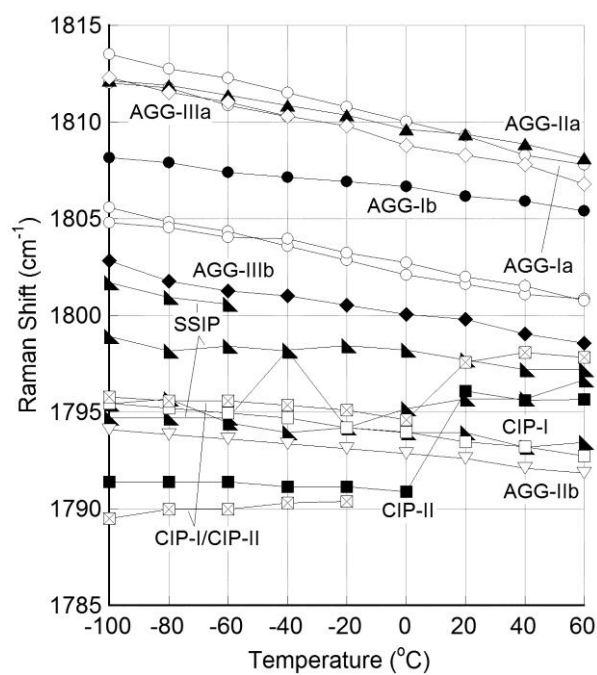


**Figure B1.** Raman band peak positions for the DFOB<sup>-</sup> anion symmetric carbonyl stretching vibrational bands for various crystalline solvates.<sup>1</sup>

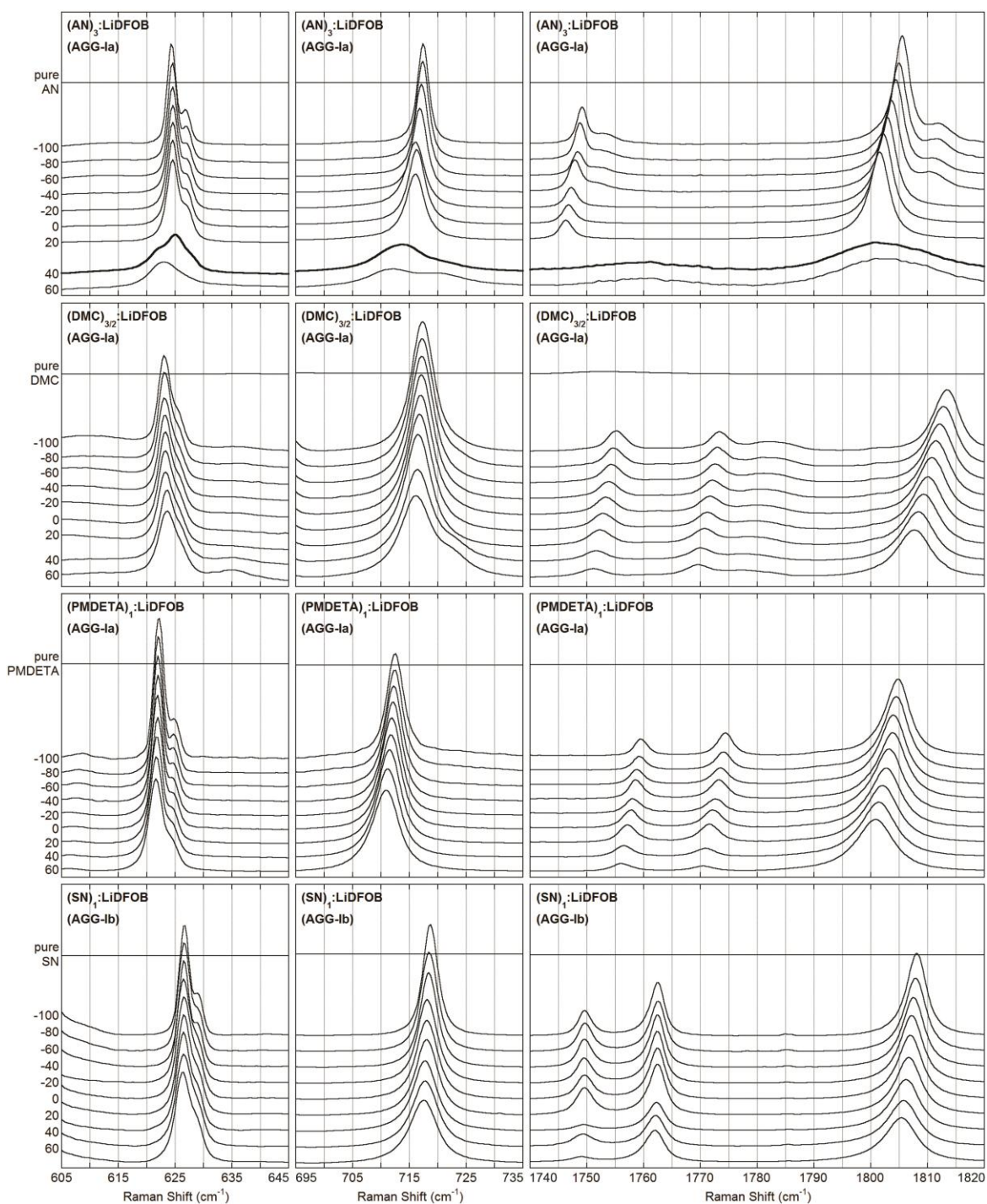


**Figure B2.** Raman spectra of the  $\text{DFOB}^-$  anion vibrational band for the AGG-I crystalline solvates: AGG-Ia  $(\text{AN})_3:\text{LiDFOB}$ , AGG-Ia  $(\text{DMC})_{3/2}:\text{LiDFOB}$ , AGG-Ia  $(\text{PMDETA})_1:\text{LiDFOB}$  and AGG-Ib  $(\text{SN})_1:\text{LiDFOB}$ .<sup>1</sup>

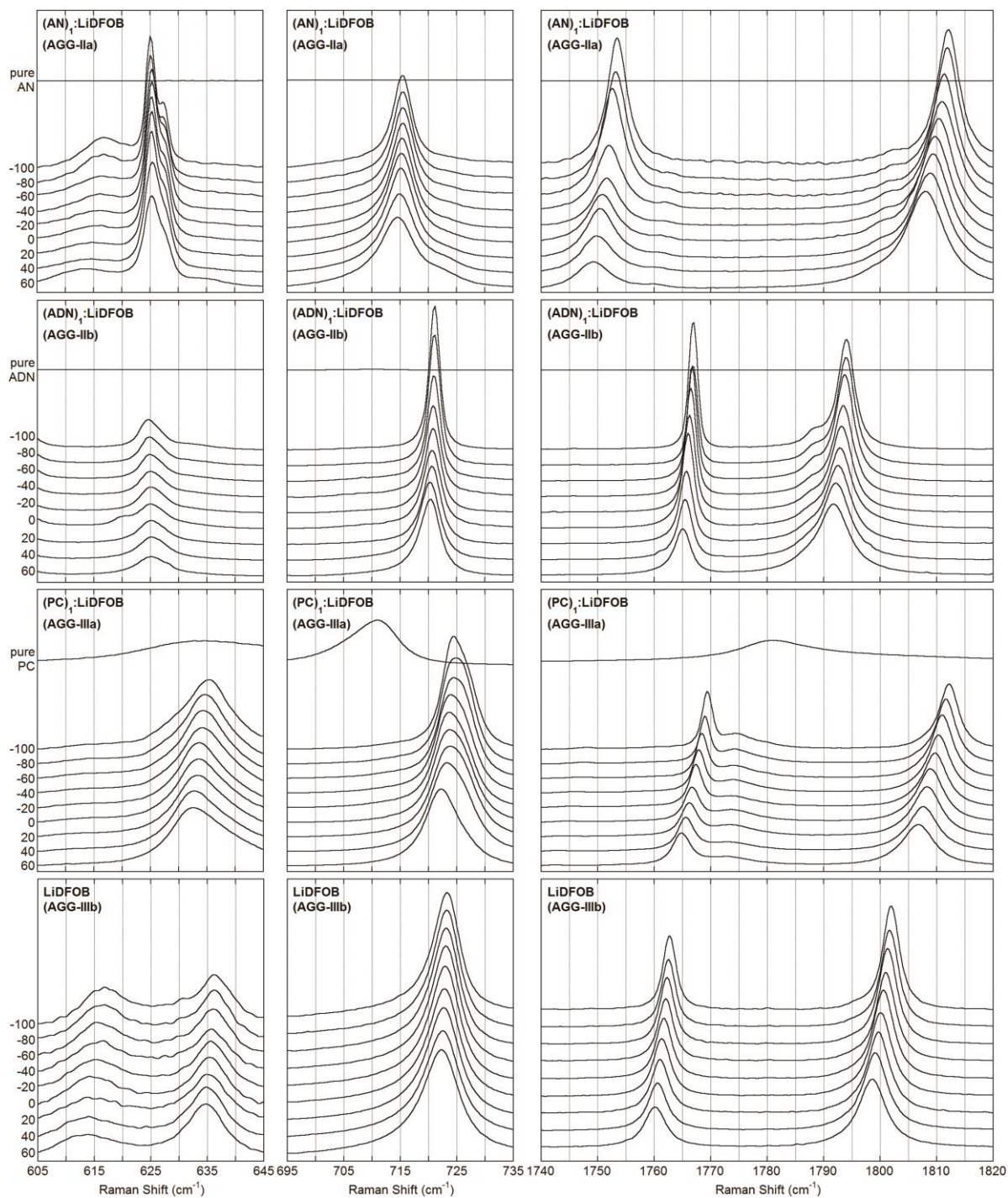


**Figure B3.** Raman spectra of the DFOB<sup>-</sup> anion vibrational band for the AGG crystalline solvates and pure LiDFOB salt: AGG-IIa (AN)<sub>1</sub>:LiDFOB, AGG-IIb (ADN)<sub>1</sub>:LiDFOB, AGG-IIIa (PC)<sub>1</sub>:LiDFOB and AGG-IIIb LiDFOB.<sup>1</sup>

## References

1. S.-D. Han, J. L. Allen, E. Jónsson, P. Johansson, D. W. McOwen, P. D. Boyle, and W. A. Henderson, *J. Phys. Chem. C*, **117**, 5521 (2013).

---

## Electrolyte Solvation and Ionic Association

---

### Crystal Structures of Solvates

Crystal structures have been reported for the following solvates:  $(\text{AN})_4:\text{LiClO}_4$ ,<sup>1</sup>  $(\text{AN})_1:\text{LiBF}_4$ ,<sup>3</sup>  $(\text{AN})_1:\text{LiCF}_3\text{SO}_3$ ,<sup>4</sup>  $(\text{AN})_1:\text{LiTFSI}$ ,<sup>5</sup>  $(\text{AN})_6:\text{LiPF}_6$ <sup>7</sup> and  $(\text{AN})_5:\text{LiPF}_6$ .<sup>8</sup> The  $\text{Li}^+$  cation coordination for these solvates are reported in Figs. C1-C5 for the reader's convenience.

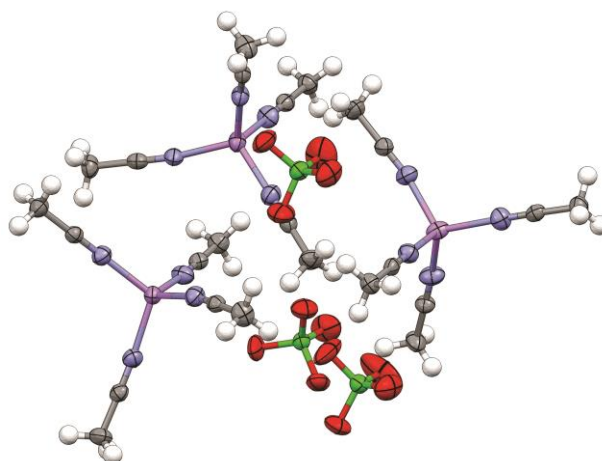


**Figure C1.**  $\text{Li}^+$  cation coordination in the  $(\text{AN})_4:\text{LiClO}_4$  solvate crystal structure (Li-purple, N-blue, Cl-dark green, O-red).<sup>1,2</sup>

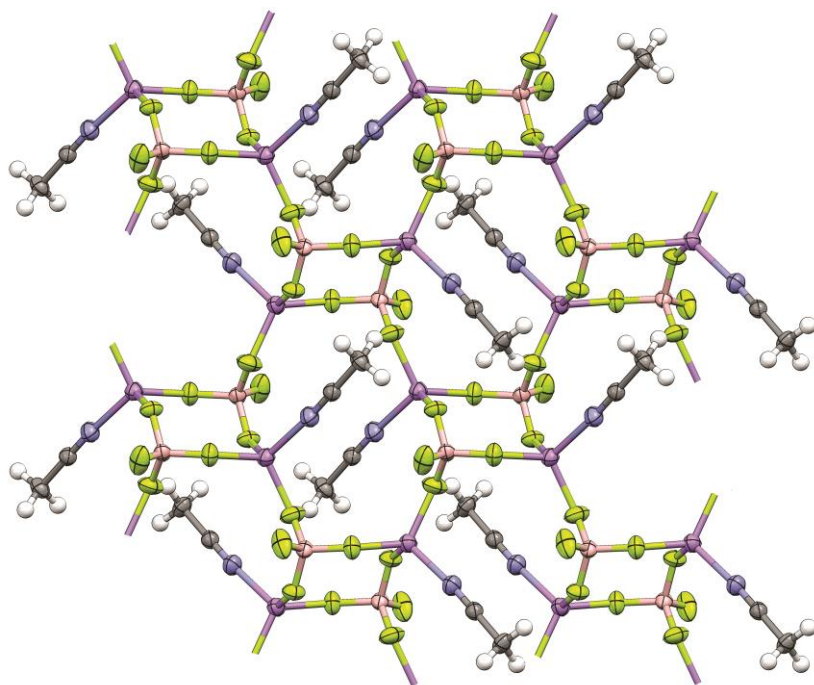


**Figure C2.**  $\text{Li}^+$  cation coordination in the  $(\text{AN})_1:\text{LiBF}_4$  solvate crystal structure (Li-purple, N-blue, B-tan, F-light green).<sup>2,3</sup>

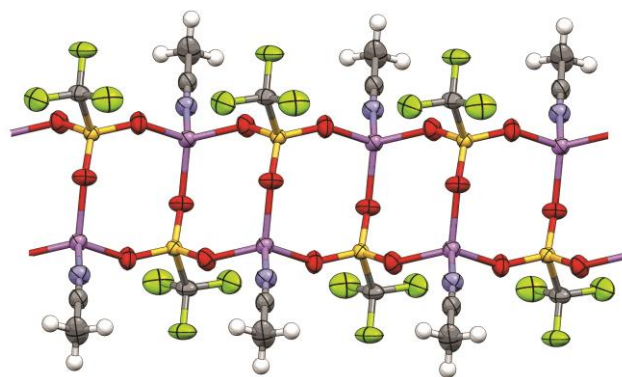


**Figure C3.**  $\text{Li}^+$  cation coordination in the  $(\text{AN})_1:\text{LiCF}_3\text{SO}_3$  solvate crystal structure (Li-purple, N-blue, S-yellow, O-red, F-light green).<sup>2,4</sup>

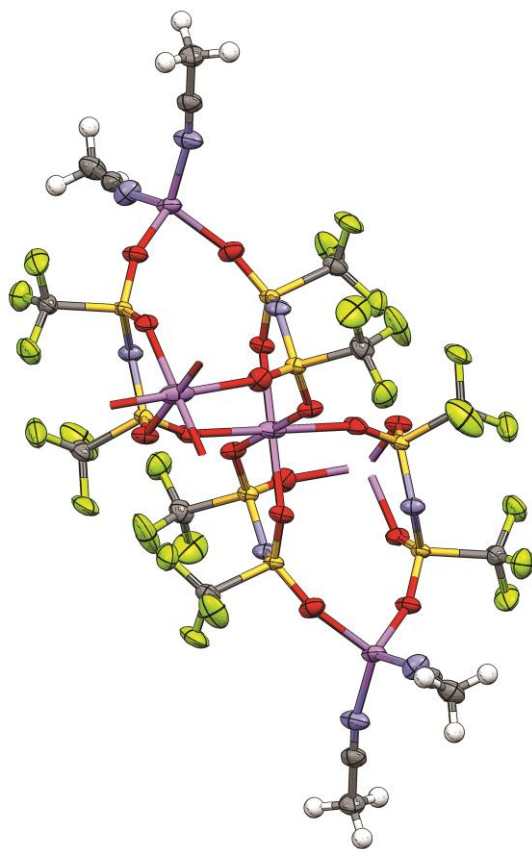


**Figure C4.** Li<sup>+</sup> cation coordination in the (AN)<sub>1</sub>:LiTFSI solvate crystal structure (Li-purple, N-blue, O-red, S-yellow, F-light green).<sup>5,6</sup>

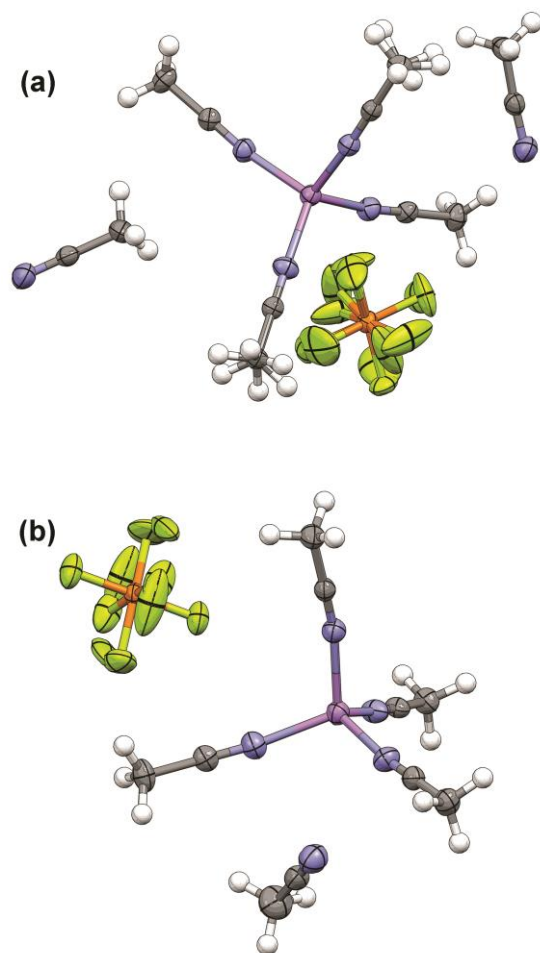


**Figure C5.** Li<sup>+</sup> cation coordination in the (a) (AN)<sub>6</sub>:LiPF<sub>6</sub> and (b) (AN)<sub>5</sub>:LiPF<sub>6</sub> solvate crystal structures (Li-purple, N-blue, P-orange, F-light green).<sup>6,7,8</sup>

## Density and Viscosity Data (Experimental):

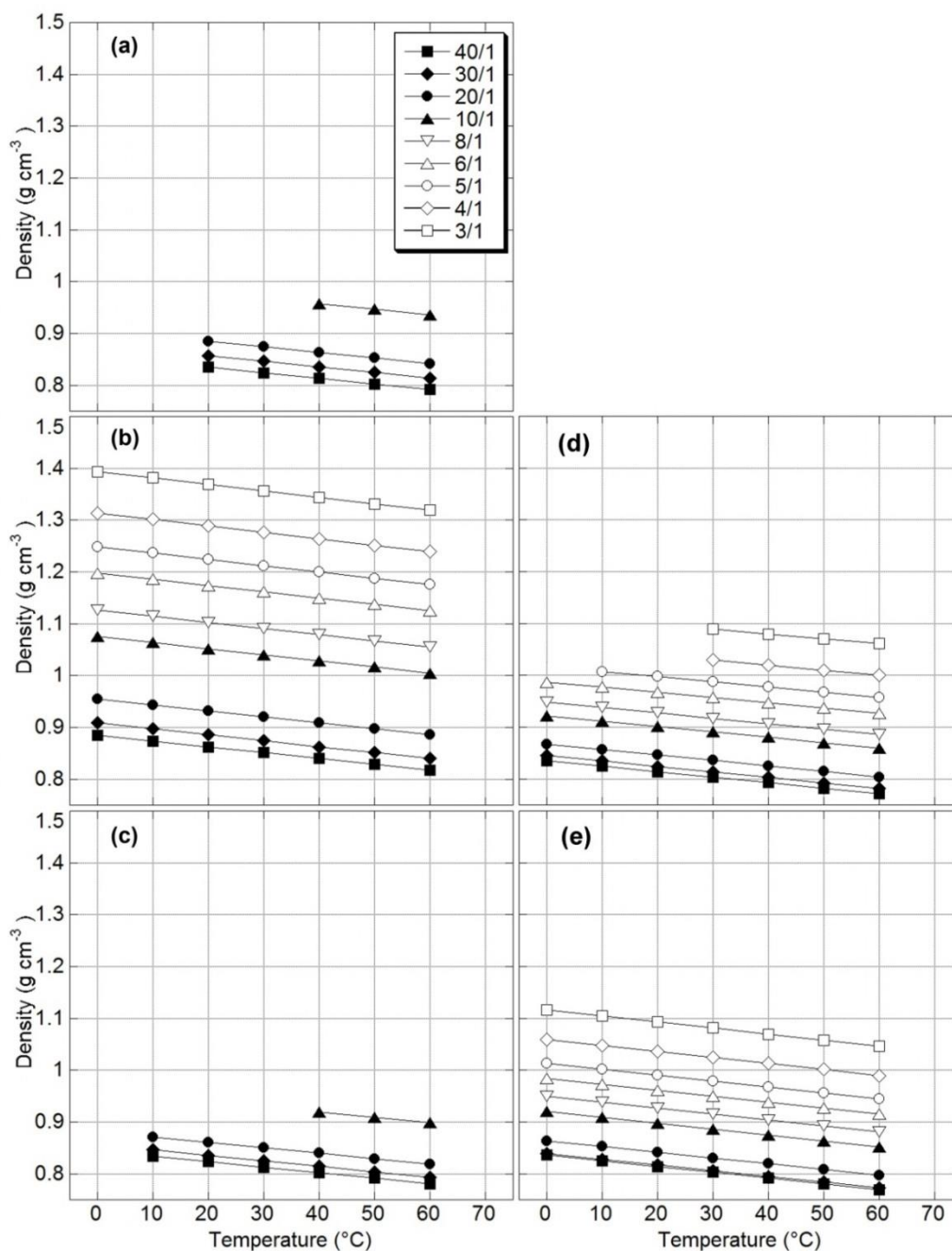


**Figure C6.** Density of (AN)<sub>n</sub>-LiX mixtures: (a) LiPF<sub>6</sub>, (b) LiTFSI, (c) LiClO<sub>4</sub>, (d) LiBF<sub>4</sub> and (e) LiCF<sub>3</sub>CO<sub>2</sub> (AN/LiX ratio noted in plot). In some cases, data is absent because the samples crystallized during the measurements.<sup>9</sup>

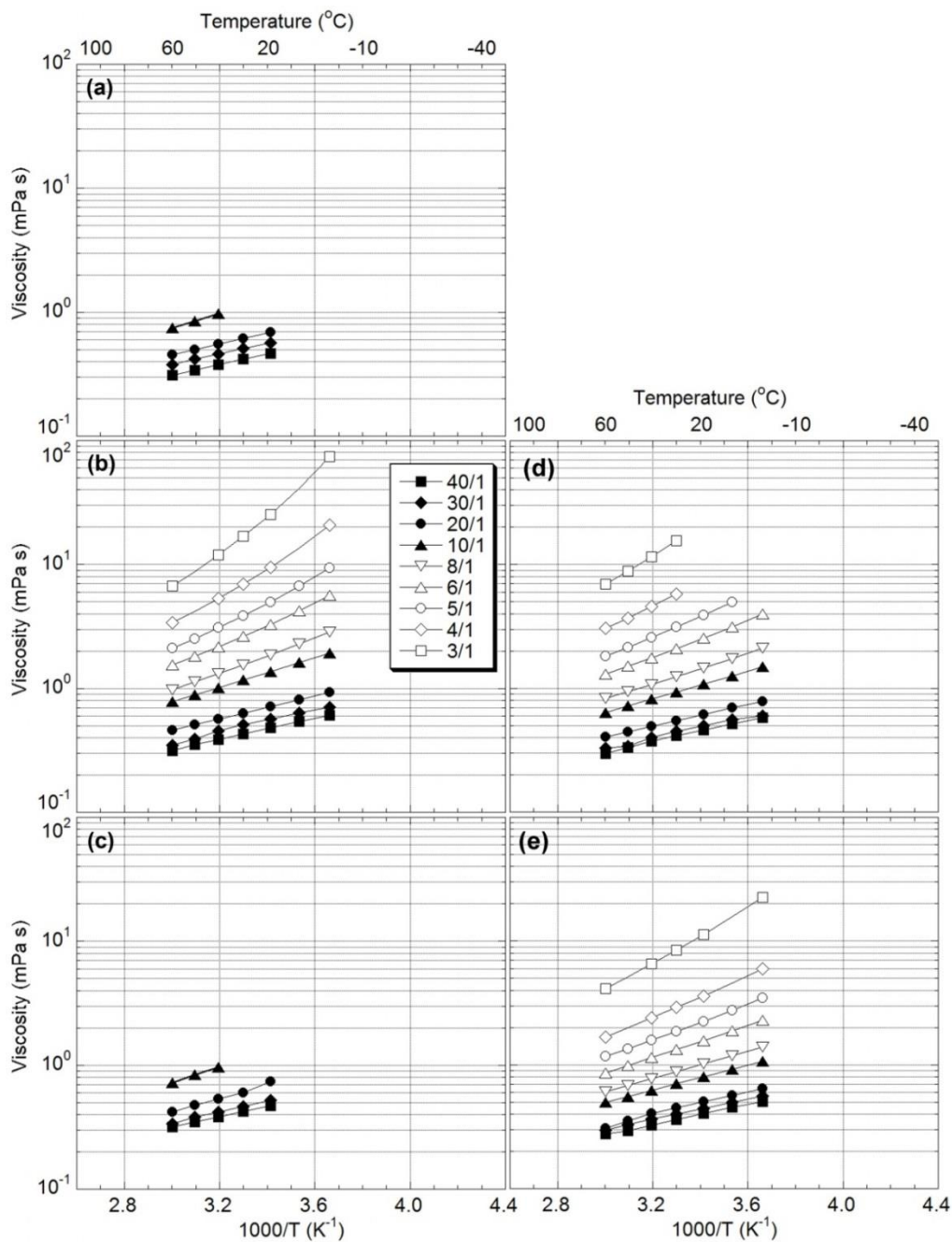


**Figure C7.** Viscosity of  $(AN)_n$ -LiX mixtures: (a)  $LiPF_6$ , (b)  $LiTFSI$ , (c)  $LiClO_4$ , (d)  $LiBF_4$  and (e)  $LiCF_3CO_2$  (AN/LiX ratio noted in plot). In some cases, data is absent because the samples crystallized during the measurements.<sup>9</sup>

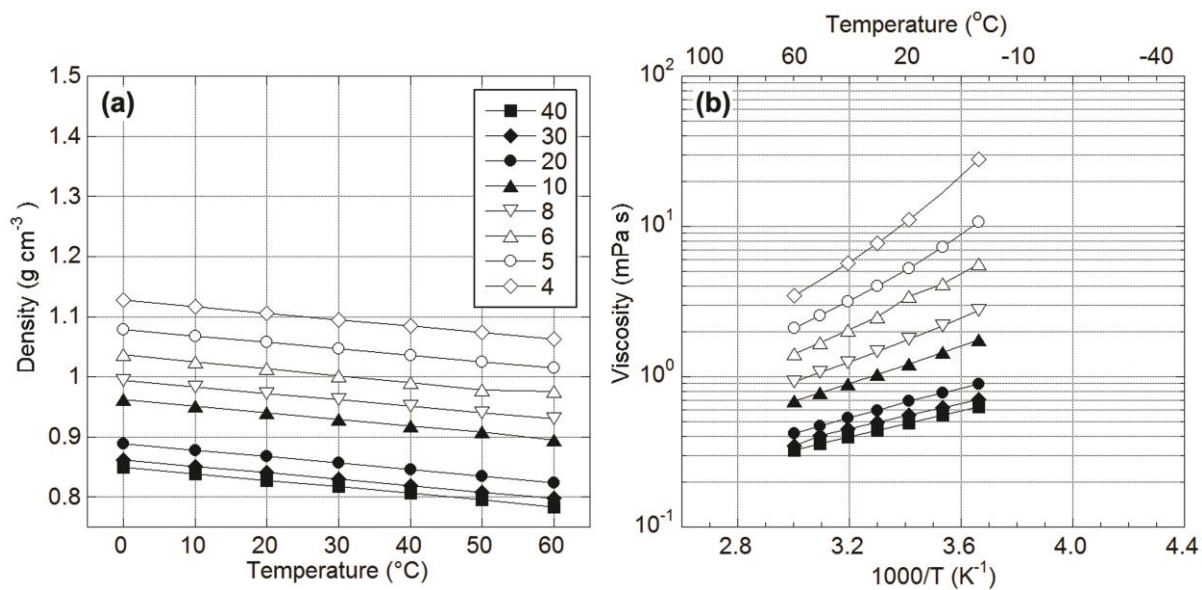


**Figure C8.** (a) Density and (b) viscosity of (AN)<sub>n</sub>-LiDFOB mixtures (AN/LiX ratio noted in plot).<sup>10</sup>

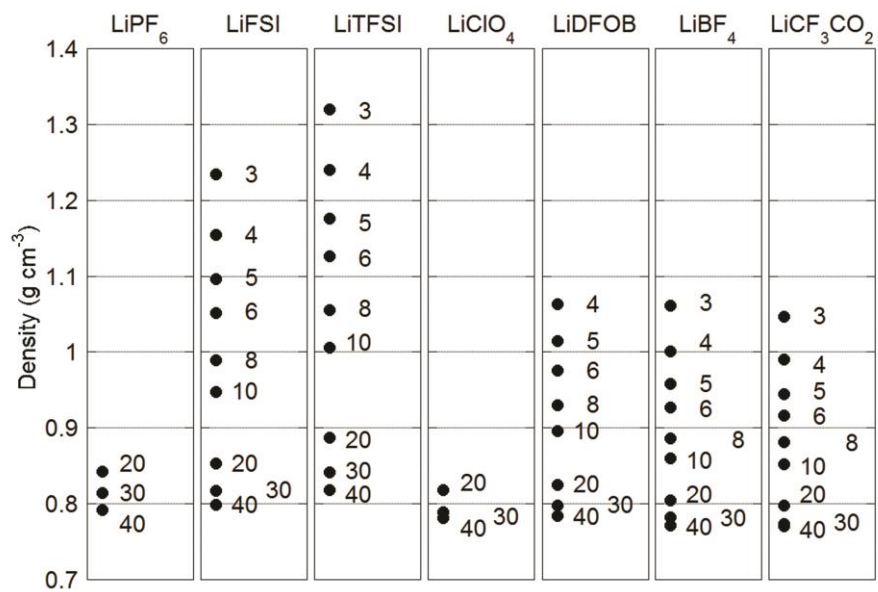


**Figure C9.** Density of (AN)<sub>n</sub>-LiX mixtures at 60 °C (AN/LiX ratio noted in plot).<sup>9,10</sup>

## Solvate Distribution and Structures (from MD Simulations):

The following figures (Figs. C10-C27) show the solvates (and uncoordinated anions) extracted from snapshots of the simulations (these are simply visual lists of the solvates and uncoordinated anions in the simulation snapshots). These figures are intended to provide the reader with information about both the solvate distribution (at a given time) in the different simulations (five are dissected in this manner for the  $n = 30$  mixtures...and one for the  $n = 10$  mixtures), as well as the solvate structures (with using the program Mercury to view the simulation snapshots in 3-D).

### (AN)<sub>n</sub>-LiDFOB—Version 1 (v1):

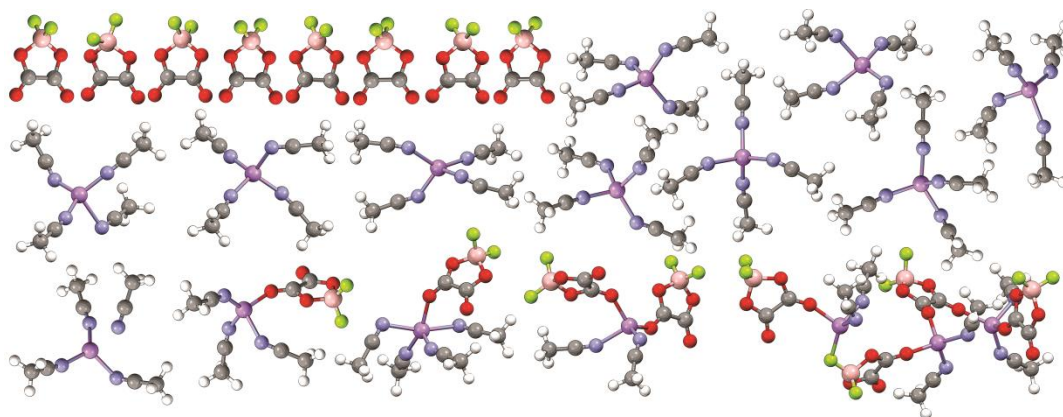


**Figure C10.** Solvates extracted from the MD simulations at 60 °C for the (AN)<sub>n</sub>-LiDFOB ( $n = 30$ ) mixture (from file: 1-v1\_AN-LiDFOB-e50-30-333K \_solvAnion.xyz) (Li-purple, N-blue, B-tan, F-light green, O-red).<sup>10</sup>

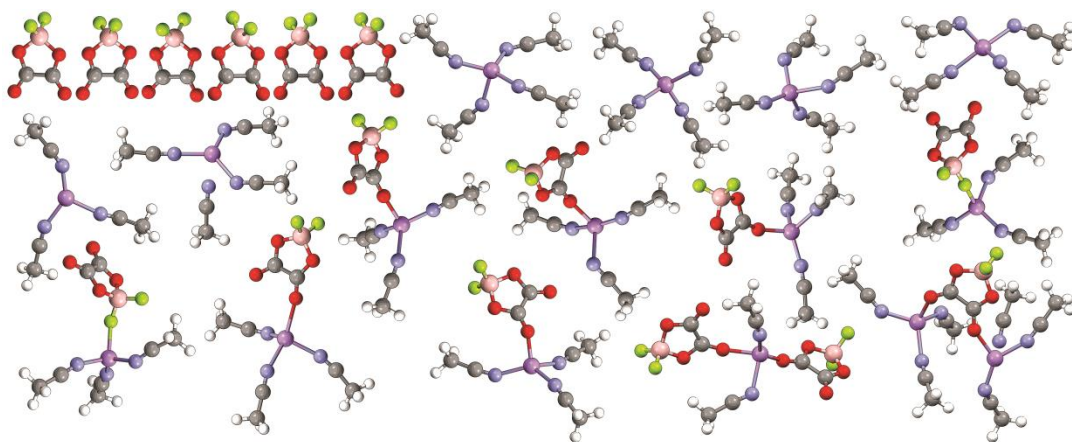


**Figure C11.** Solvates extracted from the MD simulations at 60 °C for the  $(AN)_n$ -LiDFOB ( $n = 30$ ) mixture (from file: 2-v1\_AN-LiDFOB-e50-30-333K\_solvAnion.xyz).<sup>10</sup>

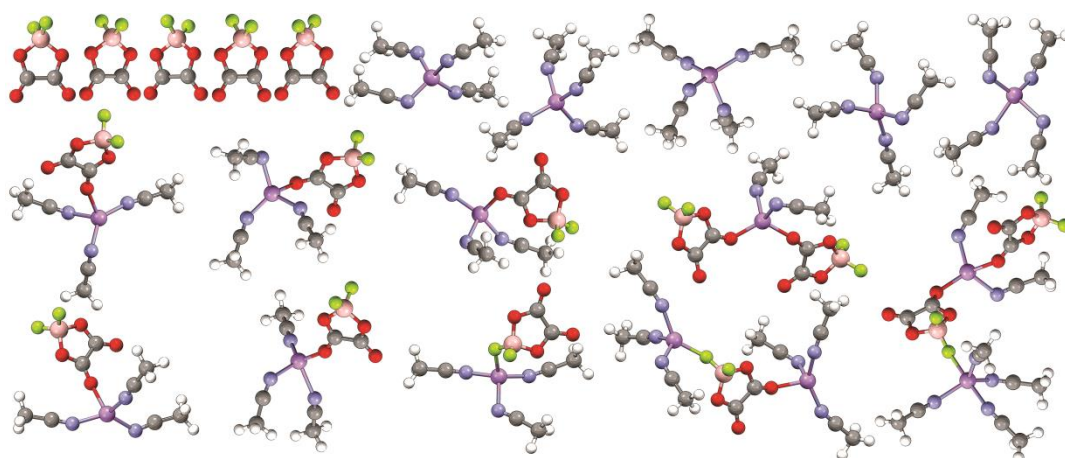


**Figure C12.** Solvates extracted from the MD simulations at 60 °C for the  $(AN)_n$ -LiDFOB ( $n = 30$ ) mixture (from file: 3-v1\_AN-LiDFOB-e50-30-333K\_solvAnion.xyz).<sup>10</sup>

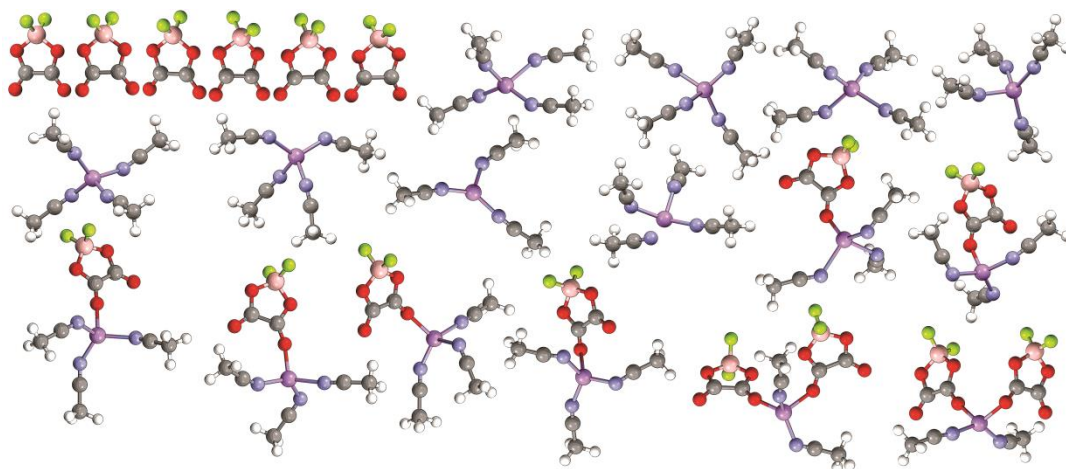


**Figure C13.** Solvates extracted from the MD simulations at 60 °C for the  $(AN)_n$ -LiDFOB ( $n = 30$ ) mixture (from file: 4-v1\_AN-LiDFOB-e50-30-333K\_solvAnion.xyz).<sup>10</sup>

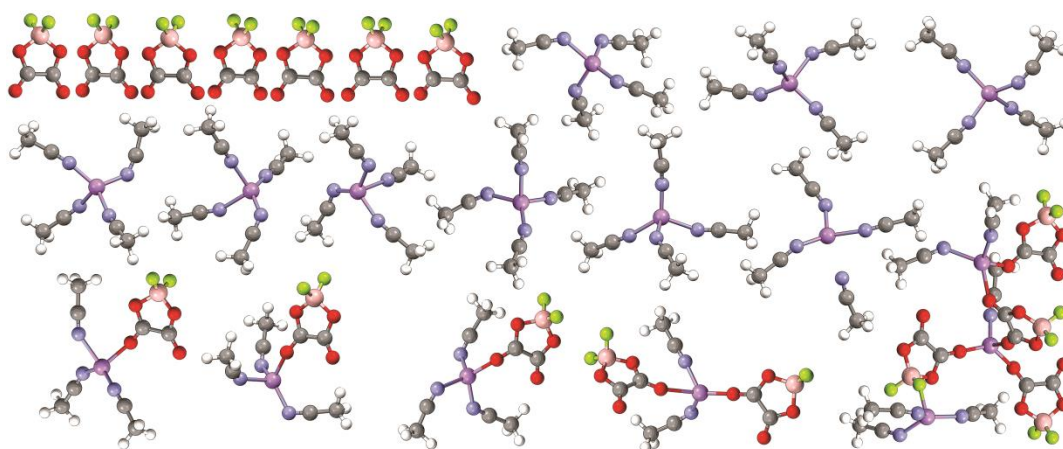


**Figure C14.** Solvates extracted from the MD simulations at 60 °C for the  $(AN)_n$ -LiDFOB ( $n = 30$ ) mixture (from file: 5-v1\_AN-LiDFOB-e50-30-333K\_solvAnion.xyz).<sup>10</sup>

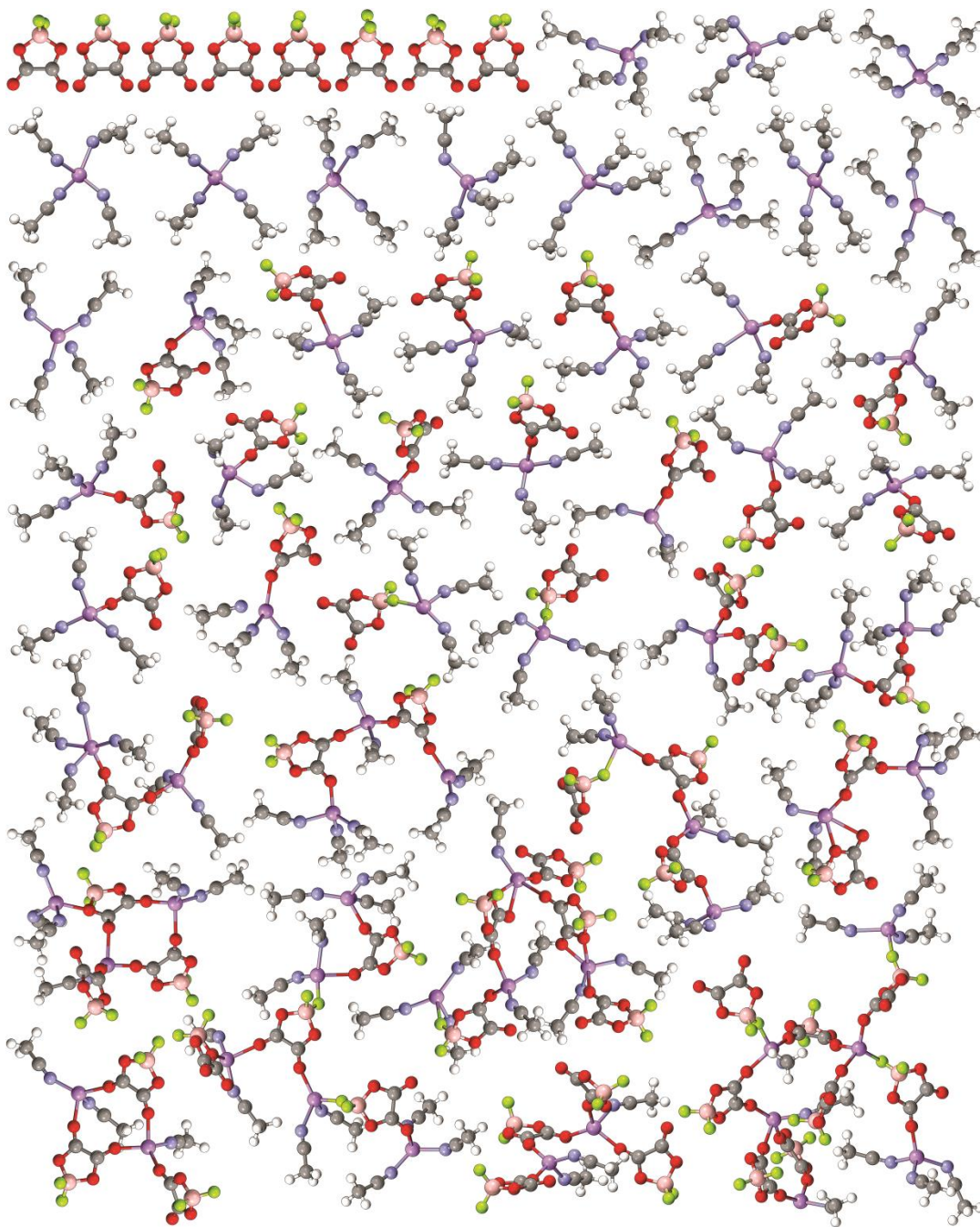


**Figure C15.** Solvates extracted from the MD simulations at 60 °C for the  $(AN)_n$ -LiDFOB ( $n = 10$ ) mixture (from file: 1-v1\_AN-LiDFOB-e50-10-333K\_solvAnion.xyz).<sup>10</sup>

**(AN)<sub>n</sub>-LiDFOB—Version 1 (v2):**

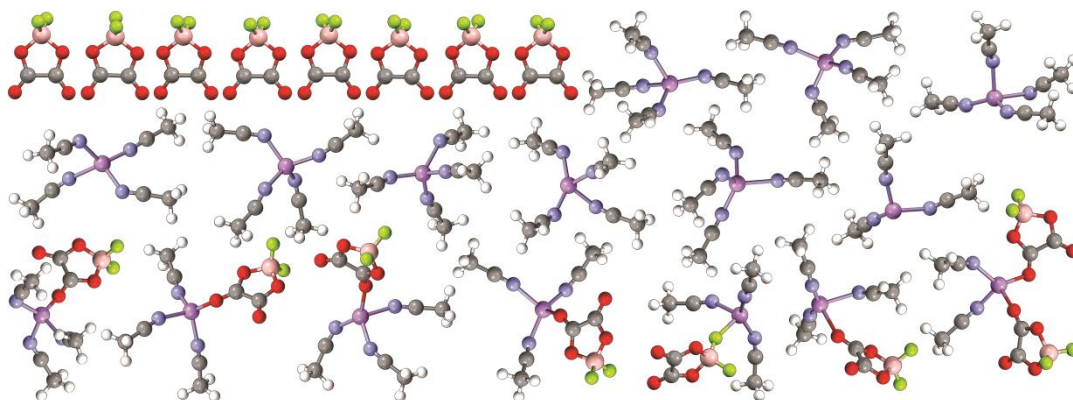


**Figure C16.** Solvates extracted from the MD simulations at 60 °C for the (AN)<sub>n</sub>-LiDFOB (n = 30) mixture (from file: 0-v2\_AN-LiDFOB-e50-30-333K\_solvAnion.xyz) (Li-purple, N-blue, B-tan, F-light green, O-red).<sup>10</sup>

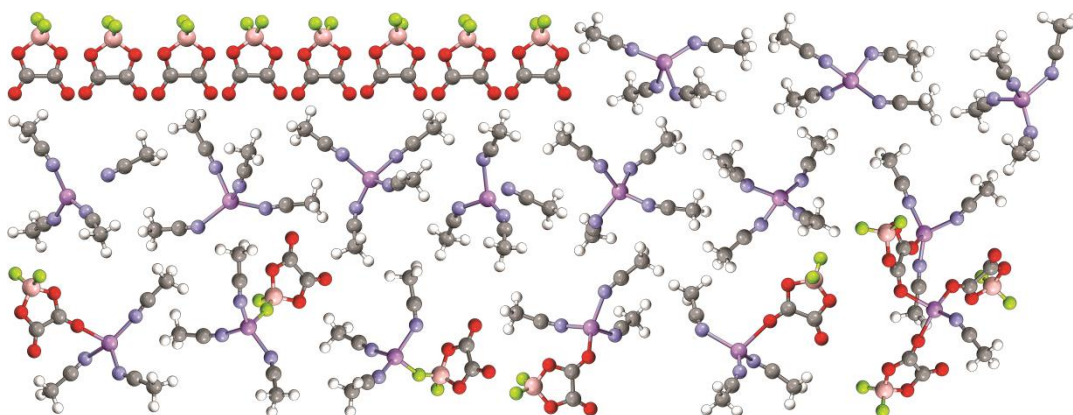


**Figure C17.** Solvates extracted from the MD simulations at 60 °C for the (AN)<sub>n</sub>-LiDFOB (n = 30) mixture (from file: 1-v2\_AN-LiDFOB-e50-30-333K\_solvAnion.xyz).<sup>10</sup>

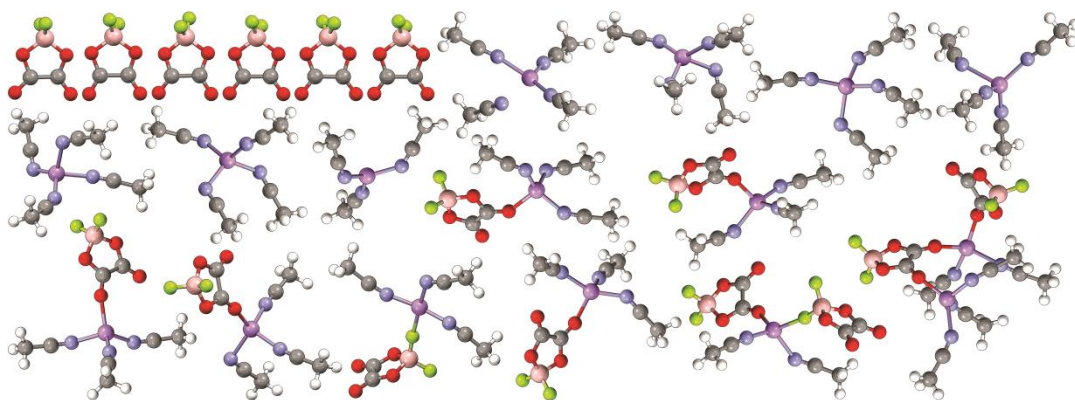


**Figure C18.** Solvates extracted from the MD simulations at 60 °C for the  $(AN)_n$ -LiDFOB ( $n = 30$ ) mixture (from file: 2-v2\_AN-LiDFOB-e50-30-333K\_solvAnion.xyz).<sup>10</sup>

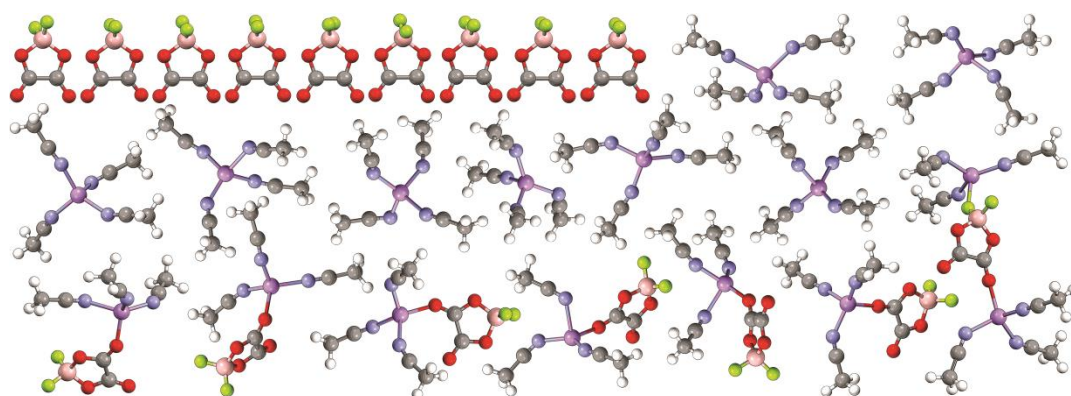


**Figure C19.** Solvates extracted from the MD simulations at 60 °C for the  $(AN)_n$ -LiDFOB ( $n = 30$ ) mixture (from file: 5-v2\_AN-LiDFOB-e50-30-333K\_solvAnion.xyz).<sup>10</sup>

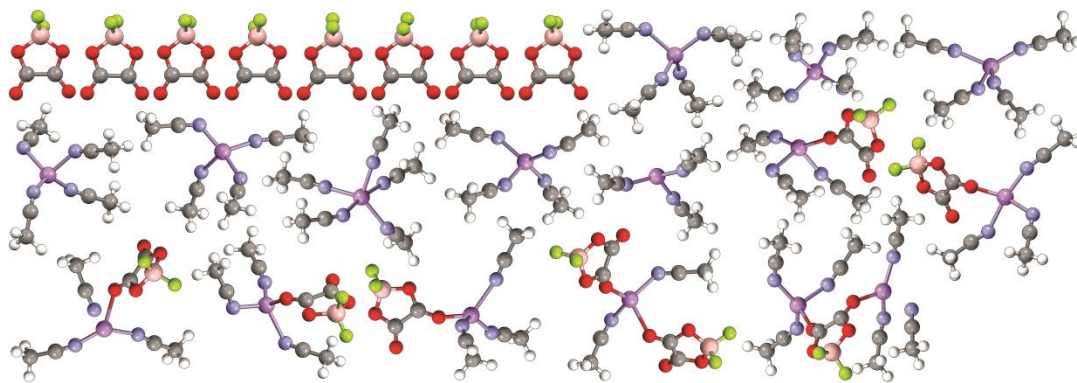
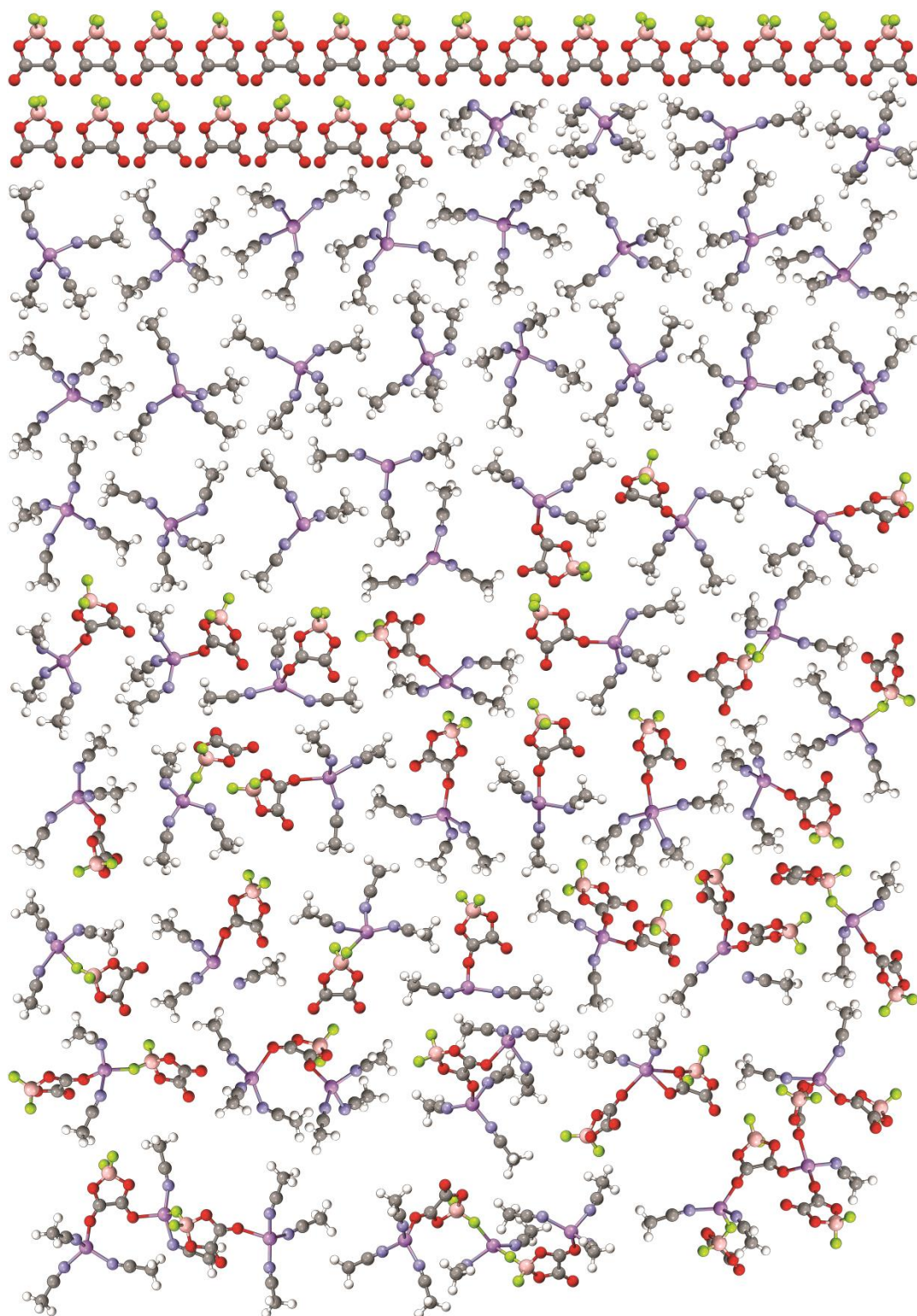
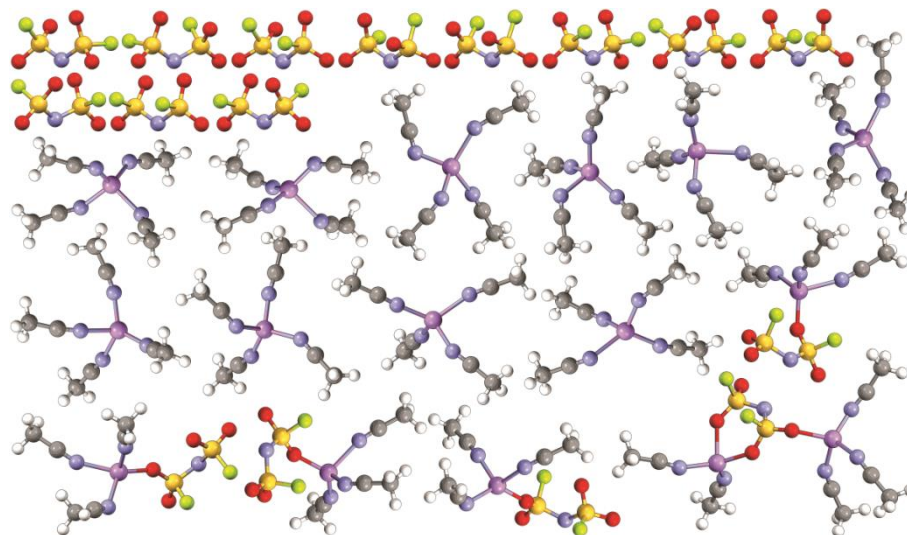


**Figure C20.** Solvates extracted from the MD simulations at 60 °C for the  $(AN)_n$ -LiDFOB ( $n = 30$ ) mixture (from file: 6-v2\_AN-LiDFOB-e50-30-333K\_solvAnion.xyz).<sup>10</sup>

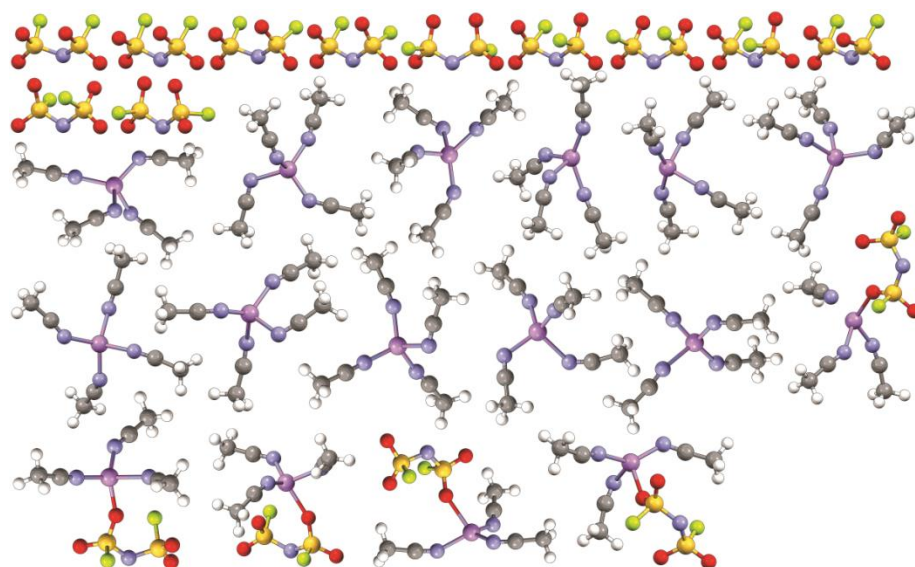
**Figure C21.** Solvates extracted from the MD simulations at 60 °C for the (AN)<sub>n</sub>-LiDFOB (n = 10) mixture (from file: 0-v2\_AN-LiDFOB-e50-10-333K\_solvAnion.xyz).<sup>10</sup>



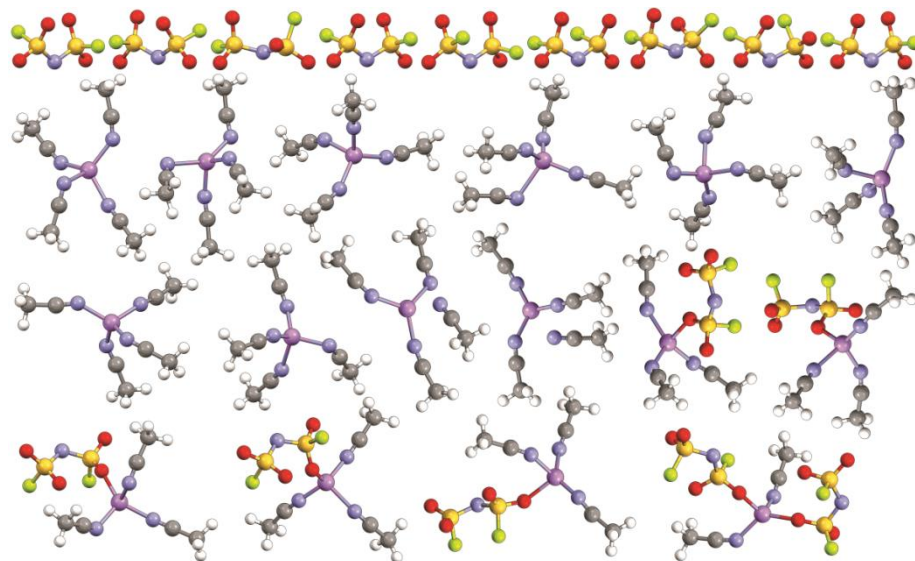
**(AN)<sub>n</sub>-LiFSI:**



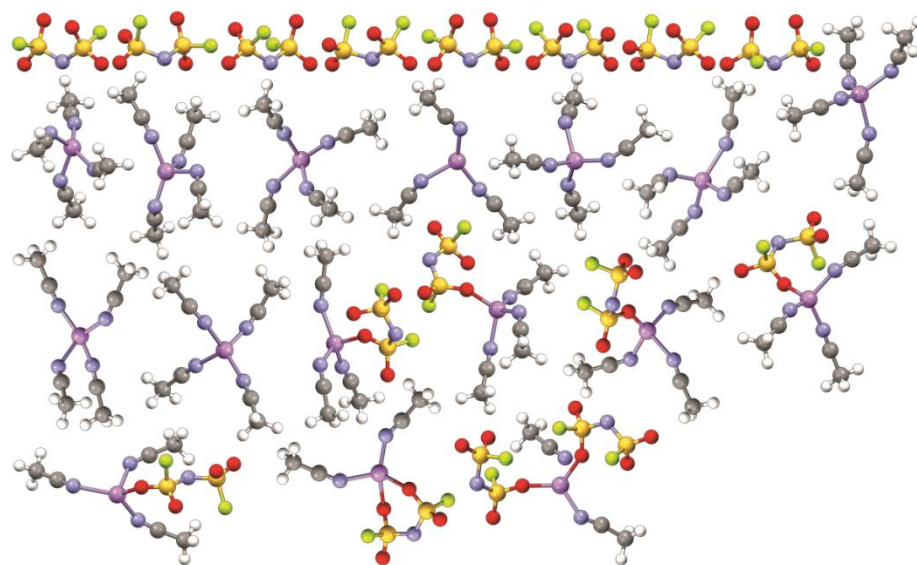
**Figure C22.** Solvates extracted from the MD simulations at 60 °C for the (AN)<sub>n</sub>-LiFSI (n = 30) mixture (from file: 3\_AN-LiFSI-f1e24-30-333K\_solvAnion.xyz) (Li-purple, N-blue, S-yellow, F-light green, O-red).



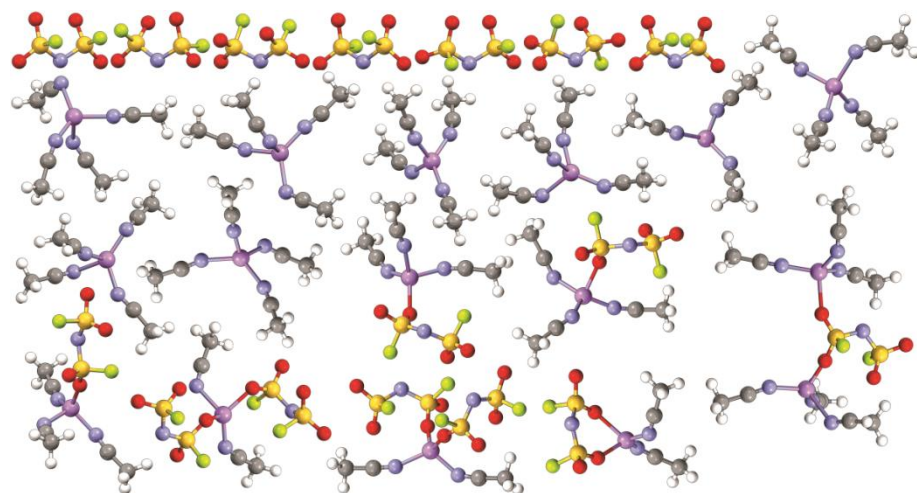
**Figure C23.** Solvates extracted from the MD simulations at 60 °C for the  $(AN)_n$ -LiFSI ( $n = 30$ ) mixture (from file: 4\_AN-LiFSI-f1e24-30-333K\_solvAnion.xyz) (Li-purple, N-blue, S-yellow, F-light green, O-red).



**Figure C24.** Solvates extracted from the MD simulations at 60 °C for the  $(AN)_n$ -LiFSI ( $n = 30$ ) mixture (from file: 0\_AN-LiFSI-f1e24-30-333K\_solvAnion.xyz) (Li-purple, N-blue, S-yellow, F-light green, O-red).

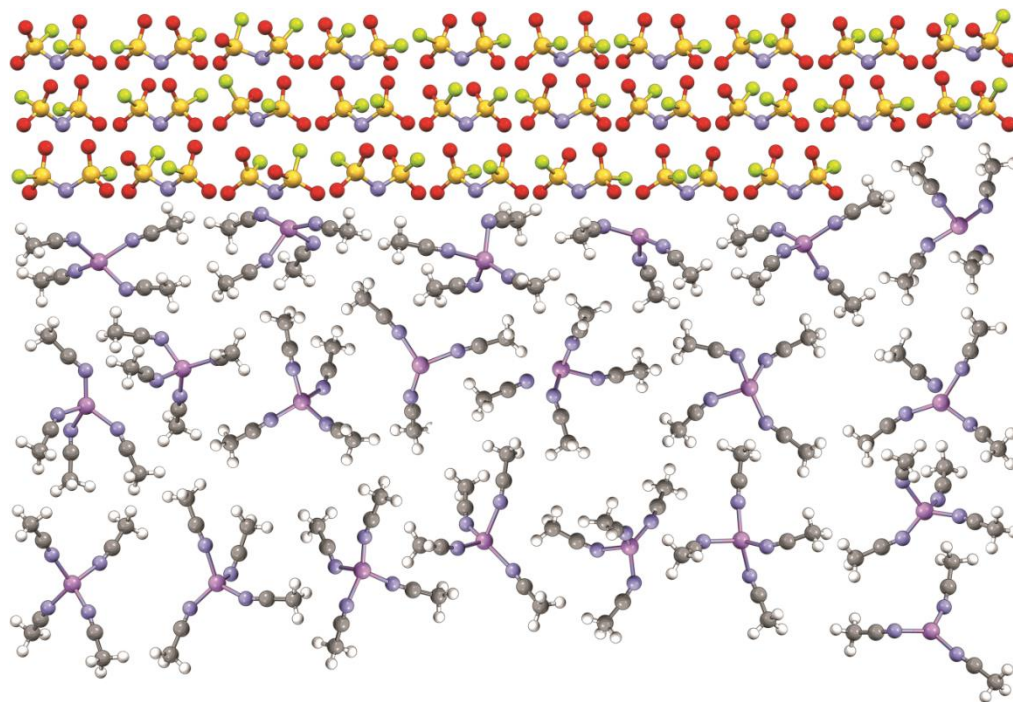


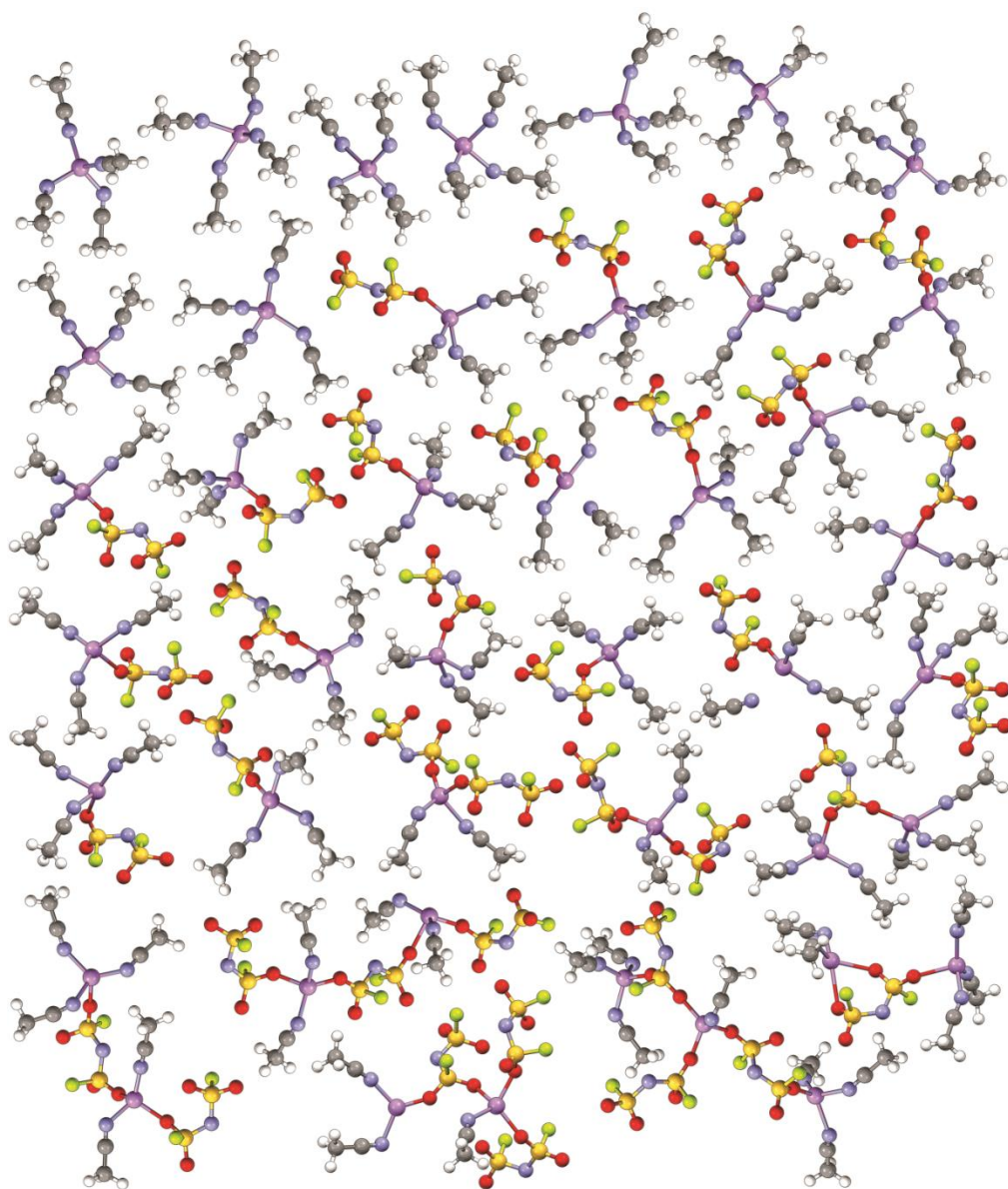
**Figure C25.** Solvates extracted from the MD simulations at 60 °C for the  $(AN)_n$ -LiFSI ( $n = 30$ ) mixture (from file: 2\_AN-LiFSI-f1e24-30-333K\_solvAnion.xyz) (Li-purple, N-blue, S-yellow, F-light green, O-red).



**Figure C26.** Solvates extracted from the MD simulations at 60 °C for the  $(AN)_n$ -LiFSI ( $n = 30$ ) mixture (from file: 1\_AN-LiFSI-f1e24-30-333K\_solvAnion.xyz) (Li-purple, N-blue, S-yellow, F-light green, O-red).

**Figure C27.** Solvates extracted from the MD simulations at 60 °C for the (AN)<sub>n</sub>-LiFSI (n = 10) mixture (from file: 3\_AN-LiFSI-f1e24-10-333K\_solvAnion.xyz) (Li-purple, N-blue, S-yellow, F-light green, O-red).





## References

1. Y. Yokota, V. G. Young Jr., and J. G. Verkade, *Acta Crystallogr.*, **C55**, 196 (1999).
2. D. M. Seo, O. Borodin, S.-D. Han, Q. Ly, P. D. Boyle, and W. A. Henderson. *J. Electrochem. Soc.*, **159**, A553 (2012).
3. D. M. Seo, P. D. Boyle, and W. A. Henderson, *Acta Crystallogr.*, **E67**, m547 (2011).
4. N. R. Brooks, W. A. Henderson, and W. H. Smyrl, *Acta Crystallogr.*, **E58**, m176 (2002).
5. D. M. Seo, P. D. Boyle, and W. A. Henderson, *Acta Crystallogr.*, **E67**, m534 (2011).
6. D. M. Seo, O. Borodin, S.-D. Han, P. D. Boyle, and W. A. Henderson. *J. Electrochem. Soc.*, **159**, A1489 (2012).
7. D. M. Seo, P. D. Boyle, O. Borodin, and W. A. Henderson, *RSC Adv.*, **2**, 8014 (2012).
8. D. M. Seo, P. D. Boyle, and W. A. Henderson, *Acta Crystallogr.*, **E67**, m1148 (2011).
9. D. M. Seo, O. Borodin, D. Balogh, M. O'Connell, Q. Ly, S.-D. Han, S. Passerini, and W. A. Henderson, *J. Electrochem. Soc.*, **160**, A1061 (2013).
10. S.-D. Han, O. Borodin, J. L. Allen, D. M. Seo, D. W. McOwen, and W. A. Henderson, *J. Electrochem. Soc.*, in-press (2013).